Palaeomagnetic and Geochemical Characterisation of Geomagnetic Excursions in the Quaternary

DPhil Thesis

Doctorate in Earth Sciences

Mark Bourne

September, 2013

Supervisors:
Dr Conall Mac Niocaill
Prof. Gideon Henderson

Department of Earth Sciences
Worcester College
University of Oxford

In Memoriam

David Bourne

18 January 1929 – 12 March 2010

Iris Mintrim

22 February 1939 – 21 August 2013

‘But they that wait upon the Lord shall renew their strength; they shall mount up with wings as eagles; they shall run, and not be weary; and they shall walk, and not faint.’ *Isaiah 40:31*

Abstract

Palaeomagnetic and Geochemical Characterisation of Geomagnetic Excursions in the Quaternary

Mark Bourne

Worcester College

University of Oxford

Geomagnetic excursions, brief deviations in geomagnetic field behaviour from that expected during 'normal' secular variation, remain some of the most enigmatic features of geomagnetic field behaviour. This thesis presents high-resolution records of geomagnetic excursions recorded at the Blake-Bahama Outer Ridge in the Western North Atlantic. The highest resolution record yet of the Blake geomagnetic excursion (~125 ka) is measured in three cores from Ocean Drilling Program Site 1062 (ODP Leg 172). These cores have sufficiently high sedimentation rates (>10 cm ka^{-1}) to allow detailed reconstruction of the field behaviour at these sites during the excursions. Previous reconstructions of geomagnetic field behaviour during excursions from marine cores have been limited by low-resolution age models. This thesis discusses a new approach, whereby measurements of excess ^{230}Th ($^{230}Th_{xs}$) are used to constrain relative variations in sedimentation rate. Modifications are suggested to the methods previously used to calculate the concentration of $^{230}Th_{xs}$ and a new MATLAB® program is developed and described that allows rapid and flexible calculation of $^{230}Th_{xs}$. Using this new approach, the duration (6.5±1.3 kyr) and age (129-122 ka) of the Blake excursion are accurately constrained. A palaeomagnetic study is also conducted on two ODP Sites, 1061 and 1062 on the Blake-Bahama Outer Ridge to obtain a high-resolution record of the Laschamp geomagnetic excursion (~41 ka). The Blake excursion is found to be of 'long' duration (6.5±1.3 kyr) whilst the Laschamp excursion is relatively short (<400 years) showing that excursions do not have a characteristic duration, linked to the conductivity of the inner core, but instead

occupy a continuous range of durations. The records of both the Blake excursion and the Laschamp excursion from the Blake-Bahama Ridge sites also show rapid transitions to excursional geomagnetic pole positions (less than 500 years), much faster than often quoted for full geomagnetic reversals. Based on current estimates for reversal durations, this would imply that excursions and reversals are controlled by different processes.

Extended Abstract

Palaeomagnetic and Geochemical Characterisation of Geomagnetic Excursions in the Quaternary

Mark Bourne

Worcester College

University of Oxford

Geomagnetic excursions are brief deviations in geomagnetic field behaviour from that expected during 'normal' secular variation. Geomagnetic excursions are defined as periods of time during which the virtual geomagnetic pole (VGP) deviates by more than 40–45° from the time-averaged position of the geomagnetic pole and are commonly associated with significant decreases in geomagnetic field intensity. Accurate dating of such excursions, and determining their duration(s) from multiple locations, is critical to our understanding of global field behaviour during these deviations. High-resolution, continuous records of field behaviour, captured in marine sedimentary cores, present an opportunity to determine the temporal and geometric character of the field during geomagnetic excursions and provide constraints on the mechanisms producing field variability. This thesis uses Ocean Drilling Program (ODP) sedimentary cores to construct well-dated, high-resolution palaeomagnetic records of two of the most recent geomagnetic excursions.

Previous reconstructions of geomagnetic field behaviour during excursions from marine cores have been limited by low-resolution age models, often based on oxygen isotope stratigraphies. Chapter 3 discusses a new approach, whereby measurements of excess ^{230}Th ($^{230}\mathrm{Th}_{xs}$) are used to constrain relative variations in sedimentation rate. A new MATLAB® program that facilitates fast calculation of this proxy is also presented. Using this new approach, Chapter 4 presents a new well-constrained, high-resolution record of the Blake geomagnetic excursion (∼125 ka) at its type location at the Blake-Bahama

Outer Ridge in the western North Atlantic. Chapter 5 presents a new palaeomagnetic record of the Laschamp excursion ($\sim$41 ka) at the same location, tied to a Greenland δ^{18}O time-scale. $^{230}Th_{xs}$ measurements are also attempted on the Laschamp record in Chapter 6 but significant variations in sediment focussing preclude the use of $^{230}Th_{xs}$ as a sediment rate normalizer during this period at this location. Lastly, in an attempt to construct a global picture of the evolution of the geomagnetic field during the Blake excursion, a number of sites from the Pacific Ocean are subjected to palaeomagnetic analysis in Chapter 7.

Excess ^{230}Th ($^{230}Th_{xs}$) is produced in the water column at a constant rate by the decay of dissolved ^{234}U and removed rapidly to the underlying sediment. $^{230}Th_{xs}$ is therefore a constant flux proxy, and measurements of the concentration of $^{230}Th_{xs}$ have proved to be a useful tool in constraining changes in sedimentation rate, and improving our understanding of the fluxes of other components into marine sediments. To obtain the initial activity of $^{230}Th_{xs}$ ($^{230}Th^0_{xs}$) in sediment: the total measured ^{230}Th must be corrected for the presence of ^{230}Th associated with detrital minerals, for ingrowth from uranium-bearing authigenic phases and also corrected for the decay of $^{230}Th_{xs}$ since deposition. Chapter 3 describes a number of improvements in the way these corrections are applied to obtain more accurate determinations of $^{230}Th^0_{xs}$. A new method for the determination of a local estimate for the detrital $^{238}U/^{232}Th$ activity ratio is presented; a suggestion is made for more appropriate values for the isotopic composition of authigenic uranium; and finally, the assumption of secular equilibrium in detrital material is questioned.

Chapter 3 also presents a new, freely-available MATLAB® script called 'XSage' that can calculate $^{230}Th^0_{xs}$, from user-supplied datasets of uranium and thorium isotope activities from sedimentary samples following the theoretical approach described. 'XSage' can determine variations in sedimentation rate between stratigraphic horizons of known age and thus produce high-resolution age models. Using a Monte Carlo approach, the program calculates uncertainties for these age models and on the durations of intervals between tie-points.

Chapter 4 presents the highest resolution record yet of the Blake geomagnetic excursion (at ∼125 ka), measured in three cores from Ocean Drilling Program (ODP) Site 1062 on the Blake-Bahama Outer Ridge in the western North Atlantic. Whilst the Blake excursion is represented in many cores and palaeomagnetic records, it remains one of the most ambiguous of recent geomagnetic excursions. Although this excursion has a controversial structure and timing, these cores have a sufficiently high sedimentation rate (∼10 cm ka^{-1}) to allow detailed reconstruction of the field behaviour at this site during the excursion.

Palaeomagnetic measurements were conducted on 385 discrete sediment samples from 3 cores from Site 1062. All samples were subjected to full alternating-field demagnetization to constrain the palaeomagnetic directional vector. Rock magnetic measurements, including mass susceptibility and S-Ratio determinations were conducted to ensure the reliability of the palaeomagnetic record. Palaeomagnetic measurements of the cores reveal rapid transitions (< 500 years) between the contemporary stable normal polarity and a single, completely reversed state, which spans a stratigraphic interval of 0.7 m. A relative palaeointensity record during the Blake excursion is also determined by normalizing the natural remanent magnetization using two artificial remanent magnetizations: isothermal remanent magnetization and anhysteretic remanent magnetization. The palaeointensity record shows a significant decrease in field intensity initiating several thousands of years before the directional excursion.

Following the approach described in Chapters 2 and 3, the duration of the reversed state during the Blake excursion is determined by combining an oxygen isotope stratigraphy with measurements of $^{230}Th_{xs}$ to assess variations in the sedimentation rates through the sections of interest. This provides an age and duration for the Blake excursion with greater accuracy than traditional methods and also assigns a constrained uncertainty. The directional excursion is found to occur between 129 and 122 ka, with a duration for the deviation of 6.5±1.3 kyr, comparatively longer than previous determinations of excursion duration, but similar to the duration of the Iceland Basin excursion (∼185 ka) determined using a similar approach at a nearby location. It has been proposed that excursions should not exceed a duration of ∼3 kyr; the inner core has been thought to provide a magnetic inertia that, given sufficient time, will stabilise the new, reversed direction, preventing a return to the original polarity seen during excursions. The long durations of the Blake and Iceland Basin excursions, and their fully reversed field, suggest the existence of a pseudo-stable, reversed dipole field component during the excursion and challenge the idea that excursions are always of short duration.

At a neighbouring location, a palaeomagnetic study is conducted on two ODP Sites, 1061 and 1062 on the Blake-Bahama Outer Ridge (ODP Leg 172) to obtain a high-resolution record of the Laschamp excursion (∼41 ka). Unlike the Blake excursion, the Laschamp excursion is universally recognised as being of short duration (<2000 years) and previously published records also suggest rapid changes in field direction and a concurrent substantial decrease in field intensity associated with this excursion. The Blake-Bahama Ridge sites are characterised by very high sedimentation rates (∼30–40 cm kyr^{-1}) during this time interval, allowing the determination of transitional field behaviour during the excursion. Palaeomagnetic measurements of discrete samples from four cores reveal a single excursional feature, across an interval of 30 cm, associated with a broader palaeointensity low.

The age and duration of the Laschamp excursion is ascertained using a stratigraphy tied to the well-dated $\delta^{18}O$ record from the Greenland ice cores. This high-resolution chronology dates the Laschamp excursion at the Blake Ridge to 41.3 ka, in good agreement with the most recent estimates for the age of the excursion from volcanic lava and sedimentary archives. The excursion is also characterized by rapid transitions (less than 200 years) between a stable normal polarity and a partially-reversed polarity. A relative palaeointensity record is also constructed for the Laschamp excursion interval.

The palaeointensity record, which is in good agreement between the two sites, shows two prominent minima, the first associated with the Laschamp excursion at 41 ka. The record obtained suggests that the directional excursion during the Laschamp at this location was no longer than ~400 years, and may have been as short as 250 years, occurring within a palaeointensity low lasting 2000 years. The Laschamp excursion at this location is therefore much shorter in duration than the Blake and Iceland Basin excursions.

A refinement of the Site 1061 Laschamp interval age model is attempted using $^{230}Th_{xs}$-normalization of the sedimentation rate (Chapter 6). However, analysis of the measured $^{230}Th_{xs}$ concentrations and the use of independent stratigraphic tie-points indicates that the site has been subject to significant variations in lateral transport of sediment (changes in focussing) throughout the Laschamp interval. Variation in sediment focussing is not unexpected during this period. Unlike marine isotope stage (MIS) 5, (during which the Blake excursion occurred), the period 60-30 ka (MIS 3) is characterized by a dynamic, rapidly changing climatic system, particularly in the North Atlantic. $^{230}Th_{xs}$-normalization of sedimentation rates assumes constant focussing and is therefore not applicable during this period at this site. Chapter 6 therefore highlights the importance of ensuring that the degree of focussing has remained constant through time within the interval of study when using $^{230}Th_{xs}$-normalization.

In Chapter 7, a number of ODP cores from the Pacific Ocean were studied in an attempt to move the focus of study away from the North Atlantic and provide a more global perspective on the most recent excursions. Despite the apparent abundance of suitable ODP sites, this study failed to provide any record of the Blake excursion. Poor magnetic remanence and magnetic mineralogy characteristics precluded the isolation of a stable remanence signal in many of the cores.

In summary, this thesis presents high-resolution records of two geomagnetic excursions at the Blake-Bahama Outer Ridge, representing the first steps towards constructing a global dataset of high-quality palaeomagnetic data with precise chronological control.

The long duration of the Blake excursion at the Blake-Bahama Outer Ridge has significant implications for our understanding of the importance of the inner core as a stabilising influence on the geodynamo. However, the existence of the short-duration Laschamp excursion demonstrates that excursions occupy a continuous range of durations. Furthermore, the rapid transitions observed for the Blake and Laschamp excursions correspond to virtual geomagnetic pole transition rates of $>100°$ kyr^{-1}. Current orthodoxy suggests that full reversal transitions can take $\sim$5 kyr, corresponding to a rate of only 18° kyr^{-1}. On the basis of present evidence, any mechanism or mechanisms to explain excursions and reversals must be able to account for (or resolve) the apparent significant difference in transition rate between the two.

Acknowledgements

First and foremost I thank my supervisors Conall Mac Niocaill and Gideon Henderson who have provided invaluable expert support and guidance throughout my D.Phil. I have very much enjoyed my D.Phil and this is in no small part down to their care and advice.

I also owe a large debt of gratitude to Alex Thomas, now at the University of Edinburgh, who has been unfailingly helpful. He has maintained his good humour in the face of unending questions about uranium and thorium geochemistry and has been a constant source of inspiration throughout my D.Phil. I am also grateful to Mads Faurshou Knudsen for his help in preparing the Blake excursion study for publication.

Thanks too to Ben Hickey and Norman Charnley for their advice and assistance in preparing and measuring the samples for the oxygen isotope study; Steve Wyatt for his help in preparing samples, and Andrew Mason for the use of his DONKEY script for processing uranium and thorium measurements. This research used samples provided by the Integrated Ocean Drilling Program (IODP). I thank the Bremen Core Repository and Gulf Coast Repository teams for their kind hospitality and assistance.

The ARM acquisitions would not have been possible without the kind permission of Adrian Muxworthy to use the ARM facilities at Imperial College, London. Many thanks to Jess Adkins, Jerry F. McManus and Franco Marcantonio for their support and kind permission to use their uranium and thorium data to test the XSage program. I apologise to Christopher Kinsley for using him as a guinea-pig to test the XSage program but I am very grateful for all his 'bug-reports'. Lukas Jonkers also made some useful suggestions that improved the XSage script. I have also benefited from discussions with several other people; Maxwell Brown, Andrew Jackson, Richard Harrison, Phil Livermore, and Chuang Xuan. I also thank Cor Langereis and Stuart Robinson, who were kind enough to agree to be my examiners. They provided a thoughtful, thought-provoking and constructive critique of my work and for that I am very grateful.

Throughout my time at Oxford I have been fortunate to meet so many lovely people: Catherine Rushworth and Cara Curran, Martin Sykes, Brendan McCormick, Sam Weatherley and Helen Pillar, Thomas O'Toole, and my long-suffering office mates; Paul Savage, Thomas Jackson, Maeve Eason Hubbard, and Julia Barrott; and lab mates, Laura Gregory and Sarah Dodd; and the members of the Woodroffe Society. I have been very fortunate to have such good company in David Kennerley for the past four years and I thank him for being such a good friend and for always being on hand to give me a historical perspective!

I would also like to thank my parents and brother who have always been there for me, as have Ken and Iris, and my grandparents who first introduced me to geology. Finally, I thank Susannah, who has shared all my ups and downs, for her love, patience and understanding.

This work was supported by a NERC studentship and by NERC grants NER/T/S/2003/00041, NE/G001391/1 and NE/F017316/1.

Contents

Abstract **i**

Extended Abstract **iii**

Acknowledgements **ix**

Contents **xv**

List of Figures **xviii**

List of Tables **xix**

1 Introduction **1**

1.1 Overview 1
1.2 Fundamentals of Magnetism 3
1.3 The Geomagnetic Field 6
1.3.1 Magnetic Directions 6
1.3.2 The Geocentric Axial Dipole Theory 7
1.3.3 Virtual Geomagnetic Poles 11
1.4 Geomagnetic Excursions 12
1.4.1 Defining Geomagnetic Excursions 13
1.4.2 Geomagnetic Excursions in the Brunhes Chron 16
1.4.3 Duration of Geomagnetic Excursions 18
1.4.4 Geometry of Geomagnetic Excursions 21
1.5 The Geodynamo 24
1.5.1 The Magneto-Hydrodynamic Dynamo 25
1.5.2 Numerical Models of the Geodynamo 27
1.5.3 Reversing Dynamos 28
1.5.4 Influence of the Inner Core 31
1.6 Sedimentary Palaeomagnetic Archives 32
1.6.1 Post-Depositional Detrital Remanent Magnetization 33

1.6.2 Flocculation 35
1.6.3 Chemical Remanent Magnetization 37
1.7 Oxygen Isotope Stratigraphy 38
1.8 $^{230}Th_{xs}$ Normalization 39
1.8.1 Uranium Series Nuclides 41
1.8.2 Marine Geochemistry of ^{230}Th 46
1.8.3 Determining $^{230}Th_{xs}$ Concentration 49
1.8.4 Calculating $^{230}Th_{xs}$-normalized Sedimentation Rates 50
1.9 Summary 52

2 Methods **55**
2.1 Introduction 55
2.2 Sampling 56
2.3 Palaeomagnetic Measurements 57
2.3.1 Field-Free Room 57
2.3.2 Measuring Remanence 57
2.3.3 Demagnetization of Remanence 58
2.3.4 Declination Correction 61
2.3.5 Magnetic Susceptibility 62
2.3.6 Isothermal Remanent Magnetization 63
2.3.7 Anhysteretic Remanent Magnetization 65
2.4 Oxygen Isotope Measurements 65
2.5 Uranium-Thorium Measurements 67
2.5.1 Chemistry 67
2.5.2 Spike and Standards 75
2.5.3 Mass Spectrometry 77
2.6 Summary 88

3 Improving $^{230}Th_{xs}$ Normalization **89**
3.1 Introduction 89
3.2 Approach & Assumptions of $^{230}Th_{xs}$ as a Constant Flux Proxy 90
3.2.1 Determination of $^{230}Th_{det}$ 91
3.2.2 Determination of $^{230}Th_{auth}$ 91
3.2.3 $^{230}Th_{xs}$ Normalization Approach 92
3.2.4 Summary of Assumptions 94
3.3 Addressing the Assumptions of $^{230}Th_{xs}$ as a Constant Flux Proxy . . . 95
3.3.1 $(^{238}U/^{232}Th)_{det}$ in Detrital Material 95

3.3.2 Is Detrital Material in Secular Equilibrium? 95
3.3.3 Authigenic $^{234}U/^{238}U$ 96
3.4 The XSage Model Approach 98
3.4.1 Description of Program 100
3.4.2 Monte Carlo Method to Calculate Uncertainties 100
3.4.3 Output of Durations (Correlated Errors) 101
3.4.4 Example Calculations 101
3.5 Summary 105

4 The Blake Excursion 107
4.1 Introduction 107
4.2 Study Site and Sampling 112
4.3 Age Model 112
4.3.1 Composite Depth Scale 112
4.3.2 Oxygen Isotope Stratigraphy 114
4.3.3 Chronology 116
4.4 Palaeomagnetic Methods & Results 117
4.4.1 Palaeomagnetic Directions 119
4.4.2 Core Properties 121
4.4.3 Relative Palaeointensity Proxies 124
4.5 Constraining Sedimentation Rate 126
4.5.1 Focussing 133
4.6 Duration and Age of the Blake Excursion 134
4.7 Discussion 136
4.7.1 Geometry of the Excursional Field 136
4.7.2 Duration of Geomagnetic Excursions 137
4.7.3 Rapid Transitions 138
4.7.4 Stability of the Excursional Field 138
4.8 Conclusions 140

5 The Laschamp Excursion 141
5.1 Introduction 141
5.2 Study Site and Sampling 143
5.3 Age Model 145
5.3.1 Composite Depth Scale 145
5.3.2 Chronology 146
5.4 Palaeomagnetic Methods & Results 149

5.4.1 Palaeomagnetic Directions 149
5.4.2 Core Properties 154
5.4.3 Relative Palaeointensity Proxies 159
5.5 Discussion 162
5.5.1 Timing of the Laschamp excursion 162
5.5.2 Duration of the Laschamp excursion 164
5.5.3 Sensitivity to field intensity 166
5.6 Conclusions 167

6 ^{230}Th$_{xs}$ Normalization at Site 1061 169

6.1 Introduction 169
6.2 ^{230}Th$_{xs}$ Calculations and Results 170
6.3 Discussion 174
6.4 Conclusions 176

7 Pacific Cores 177

7.1 Introduction 177
7.2 Core Choice 178
7.3 ODP Leg 167 181
7.3.1 Depositional Setting 183
7.3.2 Sampling 184
7.3.3 Age Models 185
7.3.4 Palaeomagnetic Measurements 189
7.4 ODP Leg 181 194
7.4.1 Depositional Setting 194
7.4.2 Sampling 196
7.4.3 Palaeomagnetic Measurements 196
7.5 ODP Leg 202 200
7.5.1 Depositional Setting 201
7.5.2 Sampling 201
7.6 Conclusion 202

8 Conclusion 203

8.1 ^{230}Th$_{xs}$-Normalization 203
8.1.1 A Modified Approach 204
8.1.2 XSage Software 204
8.1.3 Sediment Focussing 205

8.2 Geomagnetic Excursions . . . 206
8.2.1 Duration of Geomagnetic Excursions . . . 207
8.2.2 Rapid Transitions . . . 208
8.2.3 Palaeomagnetic Measurements . . . 209
8.2.4 A Global Perspective . . . 209

Bibliography **211**

Appendices **249**

A Free Decay of the Earth's Core **251**
A.1 Introduction . . . 251
A.2 Decay in a Solid Conductor . . . 252
A.3 Decay Time of Earth's Inner Core . . . 254

B Manual for XSage Script **257**
B.1 Overview . . . 257
B.2 Installation . . . 258
B.3 Preparing Data for Use . . . 258
B.4 Running the Script . . . 261
B.5 Results . . . 267
B.6 Known Issues . . . 270

List of Figures

1.1 Fundamental Magnetic Units 4
1.2 Magnetic Direction Vectors 7
1.3 Inclined geocentric dipole model 8
1.4 The Geocentric Axial Dipole 9
1.5 Brunhes Chron geomagnetic excursions 16
1.6 Relative palaeointensity during the Brunhes Chron 17
1.7 VGP paths observed for the Laschamp Excursion 23
1.8 Excursions as aborted polarity reversals 24
1.9 Demonstration of frozen-in-field theorem 27
1.10 The traditional conception of pDRM 34
1.11 Schematic drawing showing flocculation model of DRM acquisition 36
1.12 Schematic drawing of the ^{238}U and ^{232}Th decay chains 41
1.13 Decay of a hypothetical radionuclide 43
1.14 Graph of the decay of the first two radionuclides in a decay series 45
1.15 Schematic drawing of the marine chemistry of ^{230}Th 47

2.1 Schematic of Alternating Field Demagnetization 60
2.2 An example (IRM) acquisition profile 64
2.3 Schematic of Anhysteretic Remanent Magnetization 66
2.4 Schematic example of isotope dilution 76
2.5 Schematic diagram of the Nu Instruments Plasma MC-ICP-MS 79
2.6 Schematic of abundance sensitivity 82
2.7 Uncertainty budget for U and Th isotope concentrations 87

3.1 Mixing relationship between authigenic U and a detrital end-member 97
3.2 Determination of authigenic ^{234}U/^{238}U for the WIND 28K core 98
3.3 Determination of authigenic ^{234}U/^{238}U for ODP Hole 1062E 103
3.4 ^{230}Th$_{xs}$ normalized sedimentation rates for ODP Hole 1062E 104

4.1 Three published records of the Blake excursion 109
4.2 Location and age model of Site 1062 113

4.3 Zijderveld plots of samples from Site 1062 118
4.4 Directional record of the Blake Excursion from Site 1062 120
4.5 IRM acquisition profiles for Site 1062 samples 122
4.6 Rock magnetic properties of Site 1062 123
4.7 RPI record of the Blake excursion from Site 1062 125
4.8 Identification of $(^{238}U/^{232}Th)_{det}$ for Hole 1062E 130
4.9 $^{230}Th^{\circ}_{xs}$ and sedimentation rate for Hole 1062E 132
4.10 VGP latitude record of the Blake Excursion from ODP Site 1062E . . . 139

5.1 Locations of ODP Sites 1060, 1061, and 1062 144
5.2 Age model for ODP Site 1061 147
5.3 Age-depth relationship for ODP Site 1061 148
5.4 Representative Zijderveld diagrams from ODP Sites 1061 and 1062 . . 150
5.5 Directional record of the Laschamp excursion from Site 1061 151
5.6 Directional record of the Laschamp excursion from Site 1062 152
5.7 Rock magnetic properties of Site 1061 155
5.8 Rock magnetic properties of Site 1062 156
5.9 IRM acquisition profiles for Site 1061 and 1062 samples 157
5.10 Modelled IRM Gradient Plots for Site 1061 and 1062 samples 157
5.11 RPI record of the Laschamp excursion from Site 1062 159
5.12 VGP latitude and palaeointensity comparison at Site 1061 163

6.1 Age model for Hole 1061B used to calculate $^{230}Th_{xs}$ 171
6.2 ^{230}Th-normalized sedimentation rates for Site 1061 174

7.1 Location map of the three Pacific legs sampled in this study. 179
7.2 ODP Leg 167 site location map 182
7.3 Site 1017 hole correlation 186
7.4 Age model for Site 1017 187
7.5 Age model for Site 1018 187
7.6 Age model for Site 1019 188
7.7 Zijderveld diagrams for samples from Site 1017 190
7.8 Zijderveld diagrams for samples from Sites 1018 and 1019 191
7.9 Directional record from Site 1017 192
7.10 Directional record from Site 1018 193
7.11 Directional record from Site 1019 194
7.12 ODP Leg 181 site location map 195
7.13 Zijderveld diagrams for samples from Site 1119 197

7.14 Thermal dependency of magnetic susceptibility for Hole 1119B 198
7.15 IRM acquisition profiles for Hole 1119C 199
7.16 ODP Leg 202 site location map 200

A.1 Simple model of magnetic free decay in the inner core 252

List of Tables

1.1 VGP cut-off calculated for latitudinal bands 15

2.1 Isotopic composition of 'Oxford Carbonate Spike' 78
2.2 Isotopic composition of Uranium and Thorium Standards. 79
2.3 Nu Plasma Collector Array 79
2.4 Measurement Configurations of the Collector Array 83
2.5 Uranium-Thorium blank measurement data 87

4.1 Published age and duration estimates for the Blake Excursion. 111
4.2 Measured activities and calculated ^{230}Th components 129
4.3 $^{230}Th^0_{xs}$ and sedimentation rate for Hole 1062E 132
4.4 Marine Isotope Stage (MIS) 5 sedimentation rates 133
4.5 Marine Isotope Stage (MIS) 5 focussing calculations 134

6.1 Measured activities and calculated ^{230}Th components 172
6.2 $^{230}Th^0_{xs}$ and sedimentation rate for Hole 1061B 173
6.3 Variation in Focussing in Hole 1061B 176

7.1 Sampled Pacific Sites 181
7.2 Samples taken from ODP Leg 167 to study the Blake Excursion. 184
7.3 Samples taken from ODP 181 to study the Blake Excursion. 196
7.4 Samples taken from ODP 202 to study the Blake Excursion. 201

Chapter 1

Introduction

1.1 Overview

The Earth's magnetic field is dynamic, continually changing and evolving on time-scales from less than 1 s to more than 10 Myr. When averaged over sufficient time, the geomagnetic field resembles a magnetic dipole, with North and South geomagnetic poles that align with the Earth's rotation axis [*Hospers*, 1953]. Since the early discoveries of rocks recording magnetic polarities in the opposite direction to the modern field [*Brunhes*, 1906; *Matyuama*, 1929], it was suspected that the Earth's field had not always remained in its current configuration. By the early 1950s, it became increasingly clear that at times in the past, the Earth's field had reversed back and forth between two comparably stable polarities with a frequency on the order of 100s or 1000s of years to millions of years [e.g. *Hospers*, 1955]. The relatively stable intervals between reversals became known as chrons and subchrons. The global sequence of reversals is continually being refined using palaeomagnetic measurements from across the globe, forming the basis of magnetostratigraphy, and formalised as the Global Polarity Time Scale (GPTS) [e.g. *Cande and Kent*, 1992, 1995]. However, within the last few decades palaeomagnetic measurements have revealed that at times, during otherwise stable chrons, geomagnetic field behaviour deviates from that expected during 'normal', secular variation for periods of a few thousand years [e.g.

Channell, 2006; *Laj and Channell*, 2007; *Smith and Foster*, 1969; *Tric et al.*, 1991]. These deviations are known as geomagnetic excursions, and are defined as periods of time during which the geomagnetic pole deviates by more than 40–45° from the geographic pole, equivalent to the time-averaged geomagnetic pole position [*Vandamme*, 1994]. Despite continued research, geomagnetic excursions remain an enigmatic feature of geomagnetic field behaviour [*Roberts*, 2008].

Many questions regarding these events are still unanswered and a lack of high-quality, global observations limits our ability to understand their nature and adequately test hypotheses. The geometry of the field during excursions is controversial and the extent to which the field remains dipolar during polarity transitions is not clear [*Laj et al.*, 2006; *Merrill and McFadden*, 1994; *Nowaczyk et al.*, 2012; *Valet et al.*, 2008]. This is linked, in part, to whether excursions are typically global or regional features of geomagnetic field behaviour [*Laj and Channell*, 2007; *Roberts*, 2008; *Roberts and Winklhofer*, 2004]. The answers to these questions may help to determine whether excursions are closely related to full geomagnetic reversals or are instead periods of enhanced secular variation [*Valet et al.*, 2008]. Of particular interest to this study is the timing and duration of excursions. It has been suggested that excursions have a maximum duration of no more than ∼6000 years, a time-scale determined by the conductivity of the Earth's inner core [*Gubbins*, 1999; *Hollerbach*, 1993]. However, estimates for the duration of excursions range from as short as 250 years [*Nowaczyk et al.*, 2012] to as long as 7 kyr [*Knudsen et al.*, 2007] and beyond [*Nowaczyk*, 1997]. Determining whether excursions have a characteristic duration would help to clarify the importance of the inner core as a stabilising influence on the geodynamo. To help answer these questions, accurate dating of such excursions, and determinations of their durations from multiple locations, is critical to our understanding of global field behaviour during these deviations. High-resolution, continuous records of field behaviour, captured in marine sedimentary cores, present an opportunity to determine the temporal and geometric character of the field during geomagnetic excursions and provide constraints on the mechanisms producing field variability.

This thesis uses Ocean Drilling Program (ODP) sedimentary cores to construct well-dated, high-resolution palaeomagnetic records of some of the most recent geomagnetic excursions: the Blake geomagnetic excursion (~125 ka) and the Laschamp geomagnetic excursion (~41 ka). Previous reconstructions of geomagnetic field behaviour during excursions from marine cores have been limited by low-resolution age models, often based on oxygen isotope stratigraphies. In such cases, there is the possibility that unresolved variations in sedimentation rate could hinder attempts to determine accurate age models at higher resolutions. This thesis develops the use of excess ^{230}Th ($^{230}Th_{xs}$), a constant-flux proxy, to determine relative variations in sedimentation rate. By combining traditional stable oxygen isotope stratigraphy with determinations of variations in sedimentation rate using $^{230}Th_{xs}$, it is possible to more accurately constrain the age and duration of short-duration stratigraphic intervals.

This chapter provides an introduction to some of the fundamental concepts underlying this study of geomagnetic excursions and also outlines the current understanding of these events. The first sections of this chapter (Sections 1.2–1.5) introduce the principles of magnetism and geomagnetism and discuss the behaviour of geomagnetic excursions. The later sections (Sections 1.6–1.8) discuss how palaeomagnetic records obtained from marine cores can help to characterize the behaviour of the geomagnetic field during geomagnetic excursions. These include a discussion of the magnetization acquired by sediments (Section 1.6); a means by which a low-resolution age model for a marine core might be achieved (Section 1.7); and the use of $^{230}Th_{xs}$ as a constant flux proxy to refine such an age model by constraining relative changes in sedimentation rate (Section 1.8).

1.2 Fundamentals of Magnetism

The evolution of our understanding of magnetism has resulted in more than one way to view the 'origin' of magnetism and this in turn presents us with multiple ways to define

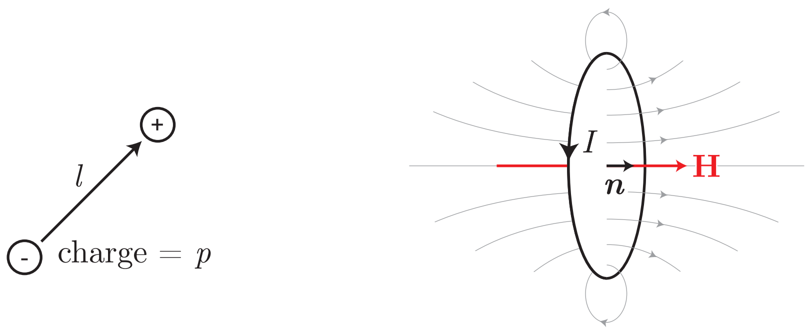

(a) (b)

Figure 1.1: (a) The CGS unit, magnetostatic concept. A pair of monopoles of charge p separated by an infinitesimal distance l. (b) The SI unit, electrodynamic concept. A loop carrying a current, I, generating a magnetic field $\mathbf{H}$.

the terms used in magnetism. Before the introduction of SI (systéme internationale) units, the CGS (centimetre, gram, second) viewed magnetic fields as the result of pair of magnetic charges: a magnetic dipole in a magnetostatic theory analogous to that used in electrostatics. In this case, the 'magnetic moment', $\boldsymbol{m}$, is defined by considering a pair of magnetic poles of strength, p, separated by an infinitesimal distance, $\boldsymbol{l}$, (Figure 1.1a) where:

$$\boldsymbol{m} = p\boldsymbol{l} \qquad [\text{Gauss cm}^3] \quad . \tag{1.1}$$

However, this concept of magnetism has lost favour as it became increasingly clear that magnetic dipoles could not be separated into their two constituent positive and negative charges or 'monopoles'. In line with the modern literature, all terms and units in the rest of this thesis will instead follow the new SI units system.

The electrodynamic, SI, view is that magnetic fields result from loops of electrical current. In this context, a loop of cross section, r, and current, I, will have a magnetic moment, $\boldsymbol{m}$, associated with it, where $\hat{\boldsymbol{n}}$ is the outward normal from the plane of the loop (using the right-hand rule) (Figure 1.1b):

$$\boldsymbol{m} = IA\hat{\boldsymbol{n}} \qquad [\mathrm{A\ m^2}] \quad . \tag{1.2}$$

The net magnetic dipole moment per unit volume, or magnetization (**M**), is calculated by summing the vectors of the individual magnetic moments and dividing by the volume enclosing the constituent magnetic moments, V. Where $\boldsymbol{m}_i$ is the constituent magnetic moment:

$$\mathbf{M} = \frac{\sum_i \boldsymbol{m}_i}{V} \qquad [\mathrm{A\ m^{-1}}] \quad . \tag{1.3}$$

A magnetic field, **H**, is produced by the loop, of radius r, where, at its centre:

$$\mathbf{H} = \left(\frac{I}{2r}\right)\hat{\boldsymbol{n}} \qquad [\mathrm{A\ m^{-1}}] \quad . \tag{1.4}$$

When a material is exposed to a magnetic field, **H**, it acquires a induced magnetization, **M**. The degree to which an applied field generates an induced magnetization in a particular sample is described by the relational factor 'magnetic susceptibility' per unit volume (volume magnetic susceptibility), κ, such that:

$$\mathbf{M} = \kappa\mathbf{H} \qquad [\text{where } \kappa \text{ is dimensionless}] \quad . \tag{1.5}$$

It should be noted that the relationship as written above assumes that the material has an isotropic response to the applied field and therefore κ is a scalar. Magnetic susceptibility per unit mass, χ, can then be calculated by dividing the volume susceptibility by the material's density, ρ:

$$\chi = \kappa/\rho \qquad [\mathrm{m^3\ kg^{-1}}] \quad . \tag{1.6}$$

The magnetic induction, $\mathbf{B}$, is an augmented field that results from the sum of the $\mathbf{H}$ field and the magnetization, $\mathbf{M}$, multiplied by the permeability of free space, μ_0:

$$\mathbf{B} = \mu_0 (\mathbf{H} + \mathbf{M}) \qquad \text{[Tesla, T]} \quad . \tag{1.7}$$

Outside a magnetic material, the magnetization is equal to zero ($\mathbf{M} = 0$) and thus $\mathbf{B}$ and $\mathbf{H}$ describe the same field. In SI units, $\mu_0 = 4\pi \times 10^{-7}$ H/m. This means that the numerical values of $\mathbf{B}$ and $\mathbf{H}$ (in Tesla and A m^{-1} respectively) are quite different even when describing the same field.

Different conventions for $\mathbf{B}$, $\mathbf{H}$ and $\mathbf{M}$ in the cgs and SI unit systems mean that it is relatively more straightforward to convert values for $\mathbf{B}$ fields between the two systems than $\mathbf{H}$ fields. It is therefore common practice for values for $\mathbf{H}$ fields to be given in Tesla following the convention for B fields ($\mu_0\mathbf{H}$).

1.3 The Geomagnetic Field

1.3.1 Magnetic Directions

The main elements of the geomagnetic field at any location are described by a magnetic field vector, $\mathbf{F}$ (Figure 1.2). The direction of the field is defined by two parameters: The inclination, I, is the angle between the field vector and the horizontal where I is positive in the downward direction and the declination, D, the angle between the horizontal component of the field vector, $\mathbf{F}$, and true or geographic north - essentially equivalent to its azimuth. The declination is positive when the field direction is east of true north.

The total field vector, $\mathbf{F}$, may be resolved into two components: the horizontal component, $\mathbf{F_h}$, such that $\mathrm{F_h} = \mathrm{F} \cos I$ and the vertical component, $\mathbf{F_v}$, where $\mathrm{F_v} = \mathrm{F} \cos D$. The field intensity is equal to the magnitude of the magnetic field vector, F.

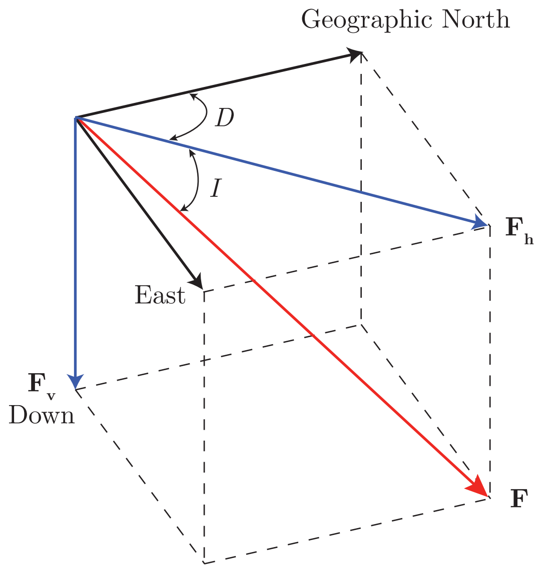

Figure 1.2: Describing the magnetic field Redrawn from *Merrill et al.* [1996].

1.3.2 Geocentric Axial Dipole Theory

Although inspired by the work of Petrus Peregrinus (13th century), William Gilbert [1600] was the first to recognise that the recent Earth's magnetic field approximates, to first order, a dipole field. Spherical harmonic models of the current geomagnetic field show that the majority (80–90%) of the geomagnetic field at the Earth's surface can be described by a dipole field, tilted approximately 11.5° away from the Earth's axis of rotation and passing through the centre of the Earth (Figure 1.3) [*Merrill et al.*, 1996]. The tilted dipole field actually comprises two major components: an axial dipole and an equatorial dipole (corresponding to the g_1^0 and g_1^1 terms respectively in the harmonic expansion). The points at which the tilted geocentric dipole axis intersects the surface of the Earth are termed the geomagnetic poles. Due to the current tilt of the dipole component of the Earth's field, the geomagnetic poles do not coincide with the geographic poles. The geomagnetic poles are theoretical locations calculated from this approximation and do not necessarily coincide with the 'magnetic' poles, points on the Earth's surface where in the inclination of the actual field is vertical. This results from the fact that the Earth's

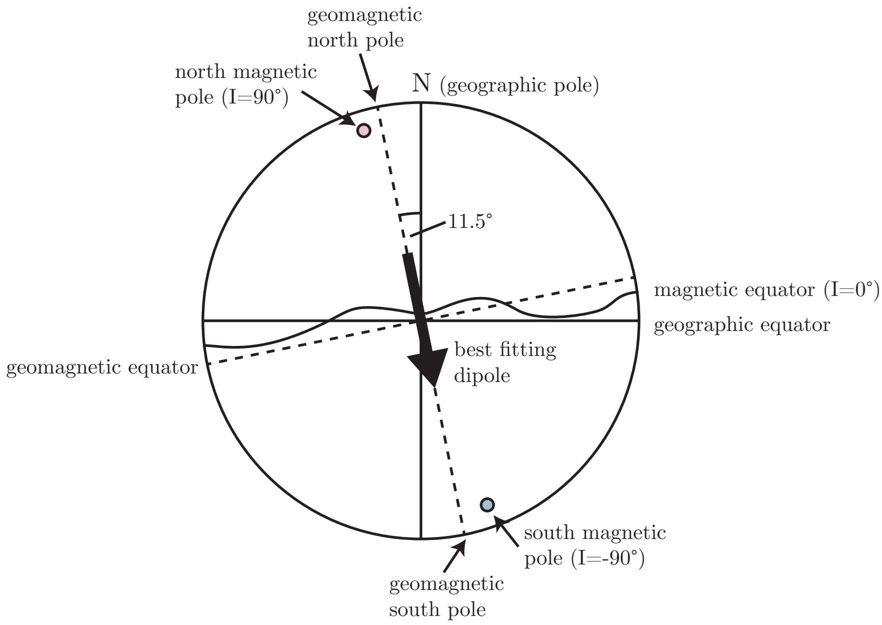

Figure 1.3: Inclined geocentric axial dipole model. The best-fitting inclined geocentric axial dipole (large arrow) is shown in meridional cross section through the Earth; the geographic, geomagnetic and magnetic poles are distinguished and a schematic comparison of the geomagnetic equator and magnetic equator is also shown. Redrawn from *McElhinny* [1973].

field has contributions not only from a dipole field component but also higher-order, non-dipole field components.

Historical records of the geomagnetic field show that both the dipole and non-dipole components of the Earth's field are constantly varying across a range of time-scales [*Jackson et al.*, 2000]. Variation of the geomagnetic field on time-scales greater than a few years is known as 'secular variation'. It is commonly assumed that, when averaged over several thousand years, the Earth's mean field is that of a single magnetic dipole coincident with the Earth's axis of rotation, i.e. the effect of secular variation is 'averaged out'. This assumption is referred to as the geocentric axial dipole (GAD) hypothesis and is one of the foundations upon which palaeomagnetic studies rest (Figure 1.4). Using this model, the vertical and horizontal components of the observed field direction (F_v and F_h

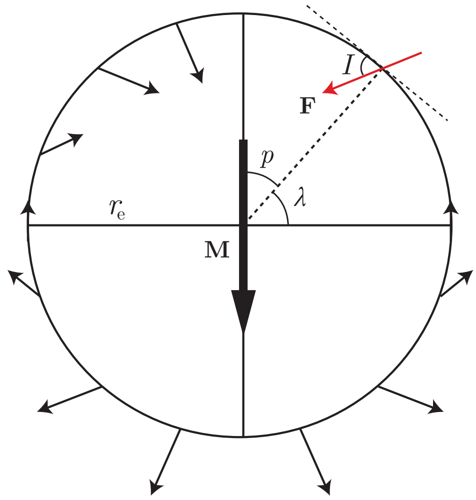

Figure 1.4: Field vectors for the Geocentric Axial Dipole (GAD). Where M is the dipole moment of the geocentric axial dipole; λ is the geographic latitude; and r_e is the mean Earth radius. The inclination, I, is the angle between the local horizontal and the field direction. Redrawn from *Butler* [1992].

respectively) may be determined at any given location:

$$\mathrm{F_v} = \frac{\mathrm{M}\cos\lambda}{r_\mathrm{e}^3} \quad ; \tag{1.8}$$

$$\mathrm{F_h} = \frac{2\mathrm{M}\sin\lambda}{r_\mathrm{e}^3} \quad ; \tag{1.9}$$

where M is the dipole moment of the geocentric axial dipole; λ is the geographic latitude; and r_e is the mean Earth radius. Using trigonometry this simple model gives a systematic relationship between the inclination of the magnetic field lines relative to the horizontal (I) at any latitude (λ). Where:

$$\tan I = \frac{\mathrm{F_v}}{\mathrm{F_h}} = \frac{2 \times \sin\lambda}{\cos\lambda} = 2 \times \tan\lambda \quad . \tag{1.10}$$

Assuming a GAD model, the field intensity at the Earth's surface is also a function of magnetic colatitude:

$$\mathrm{F} = \frac{\mu_0 m}{4\pi r_\mathrm{e}^3}\left(1 + 3\cos^2\theta\right)^{\frac{1}{2}} \quad , \tag{1.11}$$

where m is the moment of the geocentric dipole and θ is the magnetic colatitude.

The robustness of the GAD model is of fundamental importance to the study of the Earth's magnetic field in the past. The first explicit test of the GAD hypothesis was conducted in the mid-1950s [*Hospers*, 1955] and demonstrated that, within a relatively large uncertainty, the main direction of a series of recent lava flows and sediments coincided with that expected from a dipole field. Subsequent studies using the same approach also agreed that when averaged over tens of thousands of years the Earth's field of the last 2 Myr closely approximated a geocentric axial dipole [e.g. *Opdyke and Henry*, 1969]. Other studies corroborated this view, analysing the amount of scatter observed in palaeomagnetic measurements from sites at different latitudes using the spherical statistics of *Fisher* [1953] and comparing it to that expected from palaeosecular variation [e.g. *Creer*, 1962]. *Irving* [1964] presented a range of palaeoclimatic evidence that broadly supported the axial nature of the GAD for the last 2 Myr.

However, it should be noted that the GAD is still very much an approximation. As recognised by *Wilson and Ade-Hall* [1970], many of the palaeomagnetic poles calculated plot to the far-side of the geographic pole by a few degrees, along the great circle from the observation site. This effect is most likely the result of a comparatively weak non-dipole field component [*Wilson*, 1970]. Later work using large palaeomagnetic datasets has been able to resolve this second-order component of the field as equivalent to a persistent axial magnetic quadrupole with a moment estimated to be approximately 4% of that of the dipole field [*McElhinny et al.*, 1996] and equivalent to a maximum offset of 5° [*McElhinny et al.*, 1996]. Overall however, this effect is relatively minor when compared to the uncertainties associated with the magnetic recording mechanism of sediments and the large changes (up to 180°) in geomagnetic pole position during field reversals.

1.3.3 Virtual Geomagnetic Poles

The GAD model may be used to convert an observed magnetic field direction at any location into an equivalent pole position. This approach calculates the expected intercept of the dipole with the Earth's surface assuming that the field direction observed at a location is the result of a pure axial dipole field. As the Earth's field is not a pure axial dipole, this calculated pole position is only a theoretical construct and may not reflect the actual position of the geomagnetic pole. It is thus referred to as a 'virtual geomagnetic pole' or VGP. However, if the mean of a sufficient number of VGPs is used to 'average out' the effect of secular variation, the mean of the VGPs describes the average geomagnetic field and is termed a palaeomagnetic pole.

If the direction at a particular locality (latitude, longitude) $S(\lambda, \phi)$ is known from observation we can calculate the position of the equivalent theoretical VGP, $P(\lambda', \phi')$. The coordinates of P may be calculated as follows:

$$\lambda' = \sin^{-1}\left(\sin\lambda\cos p + \cos\lambda\sin p\cos D\right) \quad \left(-90^\circ \leq \lambda' \leq 90^\circ\right) \quad , \tag{1.12}$$

$$\text{where,} \quad p = \tan^{-1}\left(2\cot I\right) \quad , \tag{1.13}$$

and,

$$\phi' = \begin{cases} \phi + \beta & \text{when } \cos p \geq \sin\lambda'\sin\lambda, \\ \phi + 180 - \beta & \text{when } \cos p < \sin\lambda'\sin\lambda, \end{cases} \tag{1.14}$$

$$\text{where,} \quad \beta = \sin^{-1}\left(\sin p\sin D/\cos\lambda'\right) \quad \left(-90^\circ \leq \beta \leq 90^\circ\right) \quad . \tag{1.15}$$

A virtual geomagnetic pole (VGP) does not necessarily represent a true magnetic pole, rather it is calculated on the assumption that the magnetic field direction at a location is the result of a dipolar field. The rate at which the VGP 'moves' should therefore be understood as a representation of the rate of change of the field direction at the site location rather than the movement of any 'real' pole.

The magnetic field is a vector quantity, with both direction and intensity. Reconstructions of geomagnetic field intensity similarly rely on the dipole hypothesis to calculate a field intensity comparable between sampling localities at different latitudes. The Virtual Dipole Moment (VDM) can be calculated by substituting the estimated field intensity (F) and magnetic co-latitude into equation 1.11.

1.4 Geomagnetic Excursions

Some of the earliest palaeomagnetic measurements revealed magnetic records of a reversed polarity [*Brunhes*, 1906; *Matyuama*, 1929] and by the middle of the last century it was widely recognised that the Earth's geomagnetic field had reversed many times in the past generating a unique sequence of global 'normal' and 'reversed' periods, or 'chrons' that typically have durations of between 0.1 and 1 Ma [*Hospers*, 1955]. This early work became the basis of magnetostratigraphy and the Geomagnetic Polarity Time Scale (GPTS) [e.g. *Cande and Kent*, 1995].

However, palaeomagnetic measurements have also revealed that since the last full reversal, ∼780 ka, the Earth's magnetic field has, for brief intervals, departed from the behaviour expected during 'normal' secular variation [*Laj and Channell*, 2007]. Excursions were first documented in the late 1960s; the first documented excursion was the Blake excursion, identified in seven deep-sea sediment cores from the Blake Outer Ridge in the western North Atlantic [*Bonhommet and Babkin*, 1967; *Smith and Foster*, 1969]. It has since become commonly accepted as a global geomagnetic feature [*Laj and Channell*, 2007]. During excursional intervals, the geomagnetic VGP deviates away from the stable pole and can at times approach or even achieve reversed polarities. Concurrently, the average strength of the geomagnetic field is reduced to a small fraction of the stable field strength [*Channell et al.*, 2009; *Guyodo and Valet*, 1999; *Laj et al.*, 2000, 2004; *Valet et al.*, 2005]. These significant deviations in direction and intensity of the Earth's field have become known as geomagnetic excursions. These periods of time are distinguished from the transitional states during geomagnetic field reversals by the fact that excursions do not ultimately end in a sustained opposite polarity but instead return to the field's initial polarity state within a period of several thousand years [*Merrill and McFadden*, 1994; *Merrill et al.*, 1996]. While geomagnetic excursions have long been recognised in palaeomagnetic records [e.g. *Channell*, 2006; *Laj et al.*, 2006; *Langereis et al.*, 1997; *Lund et al.*, 1998], they remain enigmatic features of the past behaviour of the Earth's magnetic field and the relationship between secular variation, geomagnetic excursions and full geomagnetic reversals is still unclear [*Merrill and McFadden*, 1999; *Roberts*, 2008]. Understanding and accurately constraining these observations is important for constraining models of the geodynamo [e.g. *Wicht*, 2005]. The durations of excursions are of particular interest because they may relate to the stability of magnetic field states and provide information about processes during directional changes in the field [*Gubbins*, 1999; *Hollerbach and Jones*, 1995; *Knudsen et al.*, 2007].

1.4.1 Defining Geomagnetic Excursions

Initial attempts to define excursional field behaviour used arbitrary VGP latitude cut-offs on the basis that that these values tended to delimit the edges of reasonably well-peaked distributions of VGPs (centred around the geographic poles). Excursions were therefore periods of time during which the VGP deviated by more than 40–45° from the time-averaged position of the geomagnetic pole [e.g. *Watkins*, 1973; *Wilson et al.*, 1972]. The use of a constant VGP latitude cut-off (Θ) has since become a relatively universal convention used to analyse palaeosecular variation (PSV) [e.g. *Johnson et al.*, 2008; *Quidelleur et al.*, 1994] and to constrain the duration of intervals identified as excursions [e.g. *Knudsen et al.*, 2007; *Laj et al.*, 2006; *Lund et al.*, 2001a].

A constant VGP cut-off could be argued to allow comparison between different records. However, the constant VGP cut-off approach is not without limitations. In order to define excursional field behaviour it must be stated what might be expected of 'normal' field behaviour, that is, secular variation. Palaeosecular variation (PSV) is mainly studied by analysing the dispersion of VGPs obtained from various localities across the globe [*Irving*, 1964]. The scatter of a set of VGPs is usually described by the angular standard deviations (ASD). Where Δ_i is the angular deviation of the ith VGP from the geographic pole, the ASD of N VGPs is given by:

$$\mathrm{ASD} = \left(\sum_{i=1}^{N} \frac{\Delta_i^2}{(N-1)} \right)^{\frac{1}{2}} \quad . \tag{1.16}$$

The principal assumption made is that secular variation produces characteristic VGP distributions that conform to a Fisherian distribution [*Creer*, 1962; *Fisher et al.*, 1981] centred around the geographic pole for the last 5 Ma. The ASD of VGPs obtained from observations from different latitudes would then be expected to conform to those predicted by a Fisherian distribution. Those VGPs that do not conform to this model are then defined as a deviation from 'normal' secular variation and furthermore, that of this set, those not associated with a full reversal are 'excursional'.

To determine palaeosecular variation, palaeomagnetic field directions from any particular site location must therefore first be converted into their equivalent VGPs. As a result of the spherical transformation between field directions and VGPs, the scatter of the distribution of the VGPs is dependent upon not only the scatter of the palaeomagnetic field directions but also the latitude of the observation site of the field directions [*Cox*, 1970; *Creer*, 1962].

Using synthetic VGP distributions, *Vandamme* [1994] demonstrated that using a constant cut-off angle of 40° is too large to estimate low ASD distributions as the VGP distribution is not sufficiently truncated to remove obviously transitional VGPs. Similarly, such a cut-off angle may be too small to estimate higher ASD, over-truncating the distribution. *Vandamme* [1994] proposed that the cut-off angle (Θ) should vary as a

Min lat	Max lat	Θ	No sites	Mean α_{95}
0.0	4.9	24.6	101	5.5
5.0	14.9	28.5	79	5.0
15.0	24.9	27.4	307	5.2
25.0	34.9	31.4	181	5.2
35.0	39.9	33.4	349	4.9
40.0	49.9	34.1	246	4.3
50.0	59.9	37.8	127	4.6
60.0	90.0	40.0	328	4.2

Table 1.1: VGP cut-off (Θ) calculated for latitudinal bands for the time interval 0-5 Ma from a generalized lava dataset - Normal polarity only. Selection criteria $\alpha_{95} < 10°$, $n \geq 2$ [from *McElhinny and McFadden*, 1997].

function of the expected ASD. Using an iterative process, the appropriate value of Θ may be determined by the following linear relation:

$$\Theta = 1.8\,\mathrm{ASD} + 5 \quad . \tag{1.17}$$

Using a large database of VGPs obtained from lavas, *McElhinny and McFadden* [1997] showed that ASD can vary between approximately 11° and 22° between the equator and the pole corresponding to values of Θ between 25° and 45° respectively (Table 1.1).

It is important to note that although the field is a vector, these definitions use the direction of the field rather than its intensity as the principal means to define excursions. Whilst excursions are also associated with significant decreases in field intensity, quoted durations of excursions rarely determine the limits of excursional intervals using palaeointensity records [*Laj et al.*, 2000]. This is primarily a matter of pragmatism. Sedimentary records can only provide relative palaeointensity changes within a limited interval and thus absolute cut-off values are not always appropriate. *Laj et al.* [2004] define the duration of an excursion, using a palaeointensity record, as the full width of the half maximum of the intensity 'minimum' but do not define the field intensity decrease that constitutes

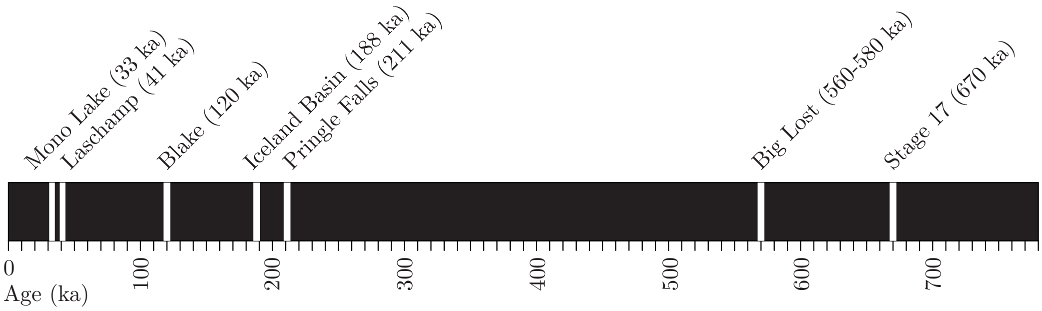

Figure 1.5: Well-documented Geomagnetic excursions in the Brunhes Chron excursions with acceptable age control following *Laj and Channell* [2007].

an intensity 'minimum'. In many cases, it is often difficult to retrieve a palaeointensity curve from sediments due to the difficulties associated with trying to resolve the combined effects of sedimentary controls and palaeofield intensity [e.g. *Tauxe*, 1993]. In any case, although excursions are typically defined by VGP position rather than by intensity, it should not be taken as meaning that field intensity is of lesser importance in examining the nature of geomagnetic excursions.

1.4.2 Geomagnetic Excursions in the Brunhes Chron

The first geomagnetic excursion to be recognised was also one of the most recent; the Laschamp excursion (∼41 ka) was first discovered in the Laschamp and Olby lava flows, part of the Chaîne des Puys volcanic field, in central France [*Bonhommet and Babkin*, 1967]. Volcanic records have since confirmed the presence of the Laschamp excursion [*Cassata et al.*, 2008] and revealed evidence for the occurrence of other excursions [e.g *Laj et al.*, 2011]. However, while volcanic records can provide invaluable absolute ages for geomagnetic events, they are unable to continuously record high-resolution field behaviour during an excursion. The advent of hydraulic piston coring in high sedimentation rate sequences by the Deep Sea Drilling Project (DSDP) in 1979, and subsequently by the Ocean Drilling Program (ODP) and Integrated Ocean Drilling Program (IODP), has presented palaeomagnetists with high-resolution marine records capable of recording short-duration

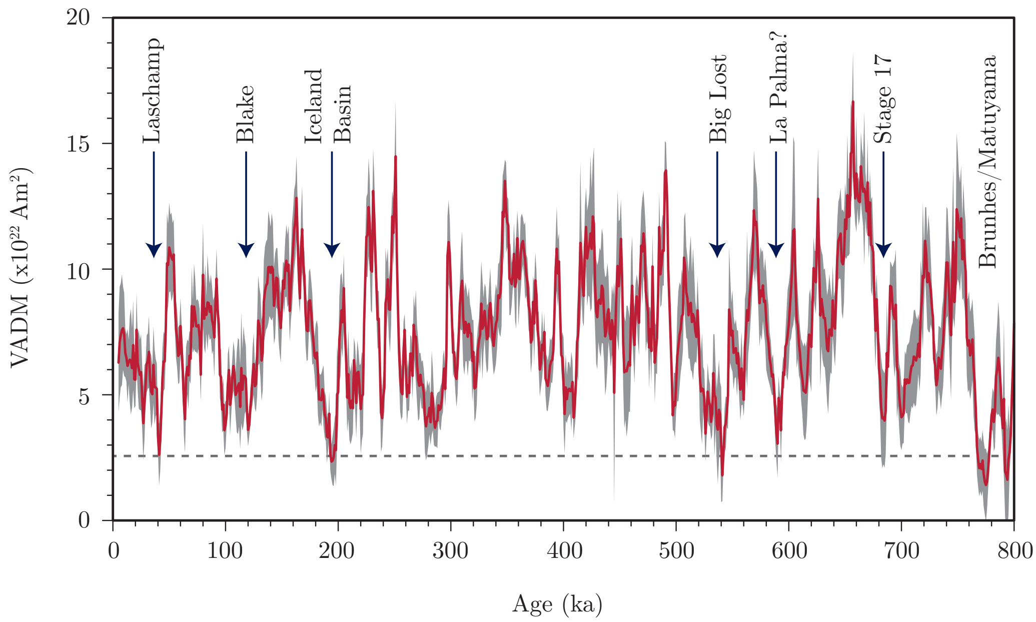

Figure 1.6: An example relative palaeointensity stack (PISO-1500) [*Channell et al.*, 2009]. A virtual axial dipole moment (VADM) is derived from a calibrated stack of palaeointensity records. Excursions (labelled) appear to be more likely when the intensity falls below a threshold value of 2.5×10^{22} A m^2 that appears to trigger excursions and reversals.

excursion events [*Lund et al.*, 2006]. Estimates for the number of excursions since the start of the Brunhes Chron (∼780 ka) from marine core records vary from as few as ∼7 [*Laj and Channell*, 2007] (Figure 1.5) up to as many as 12-17 [*Lund et al.*, 2001a, 2006]. The number and extent of individual excursions is unclear [*Roberts*, 2008]. A survey of the literature by *Langereis et al.* [1997], suggested a total of 12 excursions in the Brunhes Chron, of which 7 were considered 'well-dated'. A later survey by *Laj and Channell* [2007] proposed a similar number of well-constrained excursions. Of these 7 'well-dated' excursions, the best studied are some of the youngest:the Laschamp Excursion (41 ka) [*Bonhommet and Babkin*, 1967; *Bourne et al.*, 2013; *Channell*, 2006; *Guillou et al.*, 2004; *Laj et al.*, 2000; *Nowaczyk et al.*, 2012], the Blake Excursion (∼125 ka) [*Bourne et al.*, 2012a; *Channell et al.*, 2012; *Smith and Foster*, 1969; *Tric et al.*, 1991; *Wollin et al.*, 1971], and the Iceland Basin Excursion (∼187 ka) [*Channell*, 2006; *Knudsen et al.*, 2006].

Relative palaeointensity stacks obtained from sedimentary records show that a significant decrease in geomagnetic palaeointensity is associated with excursional VGPs during excursions [*Channell et al.*, 2009; *Guyodo and Valet*, 1999; *Laj et al.*, 2000, 2004; *Valet et al.*, 2005] (Figure 1.6). Although many of these stacks comprise data principally from the Northern Hemisphere, similar palaeointensity minima are seen in cores from the Southern Hemisphere [*Channell et al.*, 2000]. Field intensity can see as much as a 75% reduction during geomagnetic excursions [*Channell et al.*, 2009]. This reduction in palaeointensity during excursions demonstrates that excursions are an intrinsic feature of the global field and processes occurring in the geodynamo [*Channell et al.*, 2009; *Valet et al.*, 2005].

Evidence for geomagnetic palaeointensity lows are not confined to palaeomagnetic archives. *Elsasser et al.* [1956] showed that the atmospheric production of the cosmogenic nuclide ^{10}Be is modulated by the intensity of the geomagnetic field over millenial time scales. Reconstructions of the geomagnetic field intensity independent of palaeomagnetic measurements have since been derived from sedimentary archives of ^{10}Be [e.g. *Christl et al.*, 2003; *Frank et al.*, 1997; *Ménabréaz et al.*, 2011, 2012] and ice cores [*Muscheler et al.*, 2004, 2005]. This approach has been validated by *Knudsen et al.* [2008] who demonstrated that, when measured within the same sedimentary archive, ^{10}Be and palaeomagnetic anomalies were synchronous. The cosmogenic records show ^{10}Be atmospheric overproduction at excursional intervals and, in particular, at ∼41 ka, indicating a global palaeointensity low corresponding to the Laschamp excursion [*Ménabréaz et al.*, 2011].

1.4.3 Duration of Geomagnetic Excursions

The duration of geomagnetic excursions is poorly constrained [*Roberts*, 2008; *Roberts and Winklhofer*, 2004]. Detailed analyses of recent geomagnetic excursions have tried to determine typical durations for excursions. Estimates for the durations of geomagnetic excursions have ranged from as short as 250 years [*Nowaczyk et al.*, 2012] through 1-2 kyr [*Channell et al.*, 2012; *Laj et al.*, 2000; *Lund et al.*, 2001b] to as long as 7 kyr [*Knud-*

sen et al., 2007] and beyond [*Nowaczyk and Antonow*, 1997]. These discrepancies arise, in part, due to differences in definition (directional vs. intensity records, and the use of VGP cut-offs, see Section 1.4.1) and the fact that different excursions appear to show different characters.

The Laschamp excursion (∼41 ka), has been found in globally distributed marine core records and is now generally recognised as being of relatively 'short' duration (∼2 kyr) [*Channell*, 2006; *Laj et al.*, 2000, 2006; *Lund et al.*, 2001a]. This is on the basis of both directional and intensity variations. The directional excursion may itself be shorter than the intensity reduction and a recent estimate suggests a duration of ∼250 years [*Nowaczyk et al.*, 2012]. A study of Arctic sediments had suggested a much longer duration for the Laschamp excursion [*Nowaczyk and Antonow*, 1997] but it is likely that these sediments have been adversely affected by self reversal and diagenesis [*Channell and Xuan*, 2009; *Xuan and Channell*, 2010].

Initial studies also suggested that the duration of the earlier, Iceland Basin excursion (IBE) (∼185 ka) might also be relatively short (∼2 kyr) [*Laj et al.*, 2006]. However, using a novel geochemical approach to capture variations in sedimentation rate in cores from the North Atlantic, *Knudsen et al.* [2007] demonstrated that the IBE had a longer duration of up to 7 kyr, apparently challenging the idea that excursions would have a short duration. However, the duration of the IBE is debatable, using an almost identical record, *Channell et al.* [2012] suggest a duration closer to 1.5 kyr. The discrepancy arises due to a difference in definition of the limits of the directional excursional interval.

Estimates for the duration and timing of any directional deviation during the Blake excursion vary and the uncertainties are unconstrained. Global relative palaeointensity stacks reveal a broad interval of reduced palaeointensity lasting ∼25 kyr [*Channell et al.*, 2009; *Frank et al.*, 1997; *Valet et al.*, 2005], but the directional excursion is much shorter, with estimates from 1 kyr [*Channell et al.*, 2012] to between 4 and 9 kyr [*Fang et al.*, 1997; *Tric et al.*, 1991; *Tucholka et al.*, 1987]. The difference in durations for even the best-studied excursions and the limited number of excursions studied at sufficiently high resolution, leaves it unclear whether excursional events have a characteristic duration [*Roberts*, 2008].

The rate at which the Earth's field changes direction, and thus the time taken for the field to reverse, is a constraint on the nature of fluid flow in the outer core that generates the geomagnetic field [*Christensen*, 2011]. *Clement* [2004] presented an analysis of records of the last four full geomagnetic reversals that estimated the mean time taken for the VGP to reverse. The duration of the transition zones was found to be 5 ± 1 kyr, corresponding to a rate of latitudinal change of 18° kyr^{-1} (where the transition zone is defined as the period within which the VGP was between 45°N and 45°S).

It has been recently suggested that reversals may be more rapid (occurring within < 1000 years) [*Valet et al.*, 2012]. However, the estimated duration of the transitions is estimated from timescales derived from archaeological secular variation of the non-dipole field rather than direct determination from the archives themselves. *Valet et al.* [2012] states that the suggested 'rapid' polarity reversal might be the result of 'mechanisms other than those governing secular variation'. If this is the case, then it may be misleading to select a recent, non-transitional period of time, apparently governed by secular variation, to determine the duration of any transitional feature.

The rate of change of field direction appears to be significantly faster during excursions. By virtue of the short duration of the Laschamp excursion, during which VGPs from some records reach latitudes beyond 45°S [*Laj et al.*, 2006], the sum of the two transition intervals must be less than 2 kyr. This implies rates of VGP change of at least 90° kyr^{-1}; a rate significantly faster than for reversals. The records of the IBE presented by *Knudsen et al.* [2007], suggest minimum transition rates of ∼30° kyr^{-1}, where transitions take 3 kyr, from a core on the Gardar Drift but far more rapid transition rates of ∼200° kyr^{-1} from a core on the Bermuda Rise. While geometric effects could potentially account for some of the discrepancy between the excursional and full reversal transition rates, the difference is sufficiently great to suggest that polarity transitions may be more rapid during excursional events than during full reversals.

1.4.4 Geometry of Geomagnetic Excursions

Some geomagnetic excursions are undoubtedly global features of geomagnetic field history. Continuous palaeomagnetic records from marine sedimentary archives around the world have been particularly important in demonstrating the global nature of some excursions [*Channell*, 2006; *Channell et al.*, 2012; *Laj et al.*, 2006; *Lund et al.*, 2001b, 2005; *Nowaczyk et al.*, 2012] as have relative palaeointensity stacks from marine sediments [e.g. *Channell et al.*, 2009; *Laj et al.*, 2004; *Valet et al.*, 2005] and ice cores [*Muscheler et al.*, 2005].

Many of the excursional events found in local records have VGPs that plot more than 90° away from the geographic pole and that in some cases achieve a fully reversed polarity [*Laj and Channell*, 2007; *Merrill et al.*, 1996]. *Merrill and McFadden* [1994] suggest the term 'reversal excursion' to describe the subset of 'excursions' that have VGP deviations greater than 90° and that are observed at multiple sites in order to distinguish them relatively minor excursional behaviour. A more subtle distinction, but of vital importance in understanding excursional behaviour, is between reversal excursions and short polarity intervals (i.e. paired full reversals separated by less than 10 kyr). This problem is fundamental to our understanding the cause of excursions. If excursions result from extremes of the same mechanism that causes secular variation it is possible that reversed polarities could be relatively localised features, where the local field in one region may be simultaneously in the opposite polarity to that in another [*Whitney*, 1971]. What constitutes the required amount of evidence to confirm either possibility remains controversial. *Merrill and McFadden* [1994] and *Laj and Channell* [2007], for example, consider the Laschamp excursion as a reversal excursion and a polarity interval respectively. It has been proposed that polarity intervals with durations on the order of 10^5 years long should be termed 'microchrons' as recommended by the IUGS Subcommission on the Magnetic Polarity Time Scale [after *Opdyke and Channell*, 1996]. Here, palaeointensity may hold the key; it seems unlikely that a full, stable polarity reversal can have occurred if the field does not regain intensity following a transition.

Globally reversed VGPs, occurring simultaneously in both hemispheres, indicate a reversed dipole field and may be the result of a completely different mechanism to that controlling secular variation [*Roberts*, 2008]. This could arise from two possibilities. The simplest proposal is that the dipole field component simply rotates away from the Earth's rotation axis [*Merrill and McFadden*, 1994]. In this case, one would expect that the VGPs at all locations would follow the same path for any given excursion. An analysis by *Laj et al.* [2006] appeared to show consistent VGP paths during the Laschamp and Iceland Basin Excursions between a number of widely separated, although mostly North Atlantic, marine sites. These sites showed a broad clockwise loop for the Laschamp excursion. However, sites in the Black Sea fail to show this broad clockwise VGP loop [*Nowaczyk et al.*, 2012], and instead more closely correlate with the VGPs found from volcanic records [*Guillou et al.*, 2004; *Plenier et al.*, 2007] (Figure 1.7). The lack of agreement between these sites suggests that the excursional geometry may be more complicated.

An alternative proposal is that the dipole field intensity collapses, followed by a slight recovery in the reverse direction, before another collapse and recovery in the original direction [*Valet et al.*, 2008]. Such a mechanism is closely aligned with theories that excursions may represent 'aborted' polarity reversals [*Gubbins*, 1999; *Valet et al.*, 2008] where a full reversal would occur if the dipole continued to stabilise in the reversed configuration (Figure 1.8). If this hypothesis is correct, excursion characteristics have the potential to be more spatially and temporally disparate. VGP paths are less likely to be globally consistent and may have different durations and directions [*Brown et al.*, 2007].

Some excursions could result from an increase in the strength of the non-dipole field

This figure has been omitted due to copyright restrictions

Figure 1.7: VGP paths observed for the Laschamp Excursion. (a) The VGP paths from the *Laj et al.* [2006] compilation (colour coded according to the site label for each core. The overall loop pattern is indicated by the orange arrow). (b) The VGP path recorded in the Black Sea [*Nowaczyk et al.*, 2012]. Note that the map in (a) is centred at 90°E, but at 180°E in (b). Also shown for comparison are the volcanic VGPs for the Laschamp excursion (blue rings) [*Cassata et al.*, 2008; *Guillou et al.*, 2004; *Plenier et al.*, 2007].

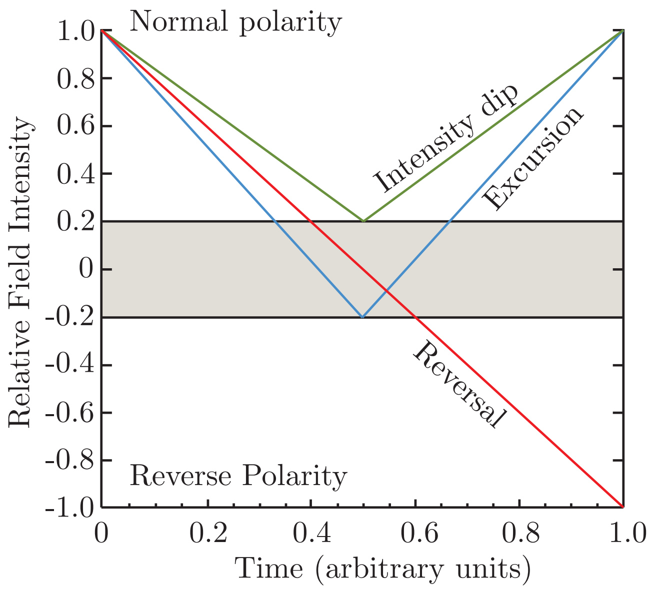

Figure 1.8: Excursions as aborted polarity reversals hypothesis. Excursions are suggested as an intermediary between 'intensity dips' and 'reversals'. A reduction in the dipole field can result in an intensity dip. An excursion can occur if the dipole field recovers in the reverse direction. If the dipole field continues to increase in the reverse direction then a full polarity reversal results. Within an unstable domain (grey band), the dipole may grow in either polarity direction [after *Valet et al.*, 2008].

relative to the dipole field. In this case, excursions would be localized features with non-simultaneous directional characteristics. For the majority of excursions, such a mechanism is unlikely; excursions are typically associated with a decrease in field palaeointensity [*Channell et al.*, 2009]. However, such localized variations in the non-dipole field, more in common with extreme secular variation, may explain the proliferation of some of the less universally recognised excursions [*Roberts*, 2008].

1.5 The Geodynamo

The geomagnetic field is thought to be generated by the flow of electrically conducting material in the Earth's liquid outer core [*Bullard*, 1949; *Elsasser*, 1946]. As a result of the inaccessibility of the Earth's core, numerical modelling of dynamical processes in the core is one of the few means by which we can investigate the principles governing the generation of the Earth's magnetic field.

1.5.1 The Magneto-Hydrodynamic Dynamo

Solving the Earth dynamo problem is certainly not a trivial undertaking. The flow of the electrically conducting material in the core generates a magnetic field, but in turn, the flow is modified by the Lorentz force generated as the material moves through the magnetic field. As a result, the geodynamo requires two sets of coupled governing equations to be solved simultaneously. One set of equations describes the fluid motion, the Navier-Stokes equations, the other describes dynamo action, summarised by the magnetic induction equation. The problem of solving these two sets of equations simultaneously is known as the magneto-hydrodynamic dynamo [*Merrill et al.*, 1996].

The magnetic induction equation alone allows us some degree of physical insight:

$$\partial \mathbf{B}/\partial t = k_m \nabla^2 \mathbf{B} + \nabla \times (\mathbf{v} \times \mathbf{B}) \quad . \tag{1.18}$$

This equation describes how the magnetic field, $\mathbf{B}$, varies with time, t, via diffusion and advection. The first term on the right-side describes the process of magnetic diffusion. Here, k_m is the magnetic diffusivity and is equal to $1/\sigma\mu_o$ (where μ_o is the magnetic permeability and constant in the core, and σ is the electrical conductivity of the core fluid). The last term in the equation describes the interaction of the velocity field, represented by $\mathbf{v}$, with the magnetic field $\mathbf{B}$. Inspection of the magnetic induction equation reveals a symmetry of the equation such that if $\mathbf{B}$ is a solution then so is -$\mathbf{B}$ [*Merrill et al.*, 1979]. This is an important observation as it demonstrates that the equations can support two stable solutions, representing 'normal' and 'reversed' states. Furthermore, the symmetry indicates that the basic equation has no inherent preference for one or the other states; they have identical statistical likelihood. Clearly, however, an energetic barrier resides between the two, inhibiting transitional states, and thus precluding uninhibited switching between the two stable states.

The Earth's field is controlled by the balance of these two terms. The magnetic diffusion term causes the magnetic field to decay with time whilst the advectional term describing the interaction of **B** with **v** can cause field strength to increase or decrease. In the absence of a velocity field, the Earth's field would decay to zero (see Appendix A). Therefore a necessary condition for the Earth's magnetic field to be sustained over time is that the second term must be greater than the first. The ratio of the two terms is expressed using the magnetic Reynolds number, R_m.

$$\frac{\nabla \times (\mathbf{v} \times \mathbf{B})}{k_m \nabla^2 \mathbf{B}} \approx \frac{\mathrm{u}L}{k_m} \equiv R_m \quad , \tag{1.19}$$

where L is an appropriate length dimension and v is the magnitude of a characteristic velocity. Therefore, it is necessary (although not sufficient) that $R_m > 1$ in order for a dynamo to be self-sustaining. If it is assumed that diffusion is negligible such that $R_m >> 1$ then we can consider a simplified view of how the magnetic field may be built up and broken down by fluid motion. Setting the diffusion term to zero, the fluid is infinitely conductive. In this approximation, the magnetic field lines and the fluid appear to be 'frozen together'. This result was first observed by *Alfvén* [1942] and it has since become known as the 'frozen-in-field' theorem. Whilst magnetic diffusion certainly occurs in the core, its high magnetic Reynolds number allows us to use the 'frozen-in-field' theorem to illustrate how convection interacts with the magnetic field [*Bloxham and Gubbins*, 1986]. For example, in the simplified case represented in Figure 1.9, shearing two 'blocks' of material with finite conductivity at a rate greater than that of their magnetic diffusion shears the magnetic field lines. The concentration of magnetic flux is increased, and thus kinetic energy is converted into magnetic field energy. It is worth noting, however, that although the frozen-in-flux theorem is not likely to be strictly true in the Earth's core, the assumption does not significantly detract from numerical models [*Bloxham and Gubbins*, 1986; *Chulliat and Olsen*, 2010].

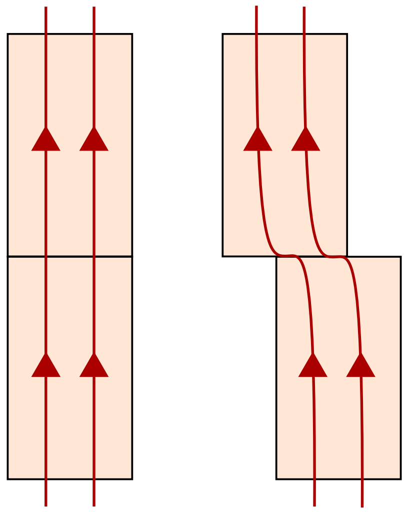

Figure 1.9: Demonstration of frozen-in-field theorem showing two blocks of finite conductivity. The lower block is sheared to the right such that the rate of motion is greater than the rate of magnetic diffusion. The field lines are carried with the block. Within the shear zone at the boundary between the two blocks the magnetic field line density is increased. [after *Merrill et al.*, 1996].

1.5.2 Numerical Models of the Geodynamo

The magnetic induction equation has never been solved in closed form. Thus, numerical models must be employed to investigate its behaviour. Numerical models attempt to solve the equations in a rotating spherical shell of convecting, electrically conducting fluid. *Glatzmaier and Roberts* [1995a] presented the first numerical dynamos model that exhibited chaotic behaviour similar to that of the Earth. Of perhaps most interest is the fact that this first model [*Glatzmaier and Roberts*, 1995a,b] was indeed the first to exhibit self-reversals in a simulation of the Earth's core. Subsequently several workers have replicated many features of the Earth's field behaviour including polarity transitions [e.g. *Christensen and Aubert*, 2006; *Kageyama and Sato*, 1995; *Kuang and Bloxham*, 1997; *Wicht et al.*, 2009].

Dimensionless parameters are commonly used to determine and characterize the simulations. As a result of computational limitations, the parameters used in numerical models of the geodynamo may diverge from realistic values for the Earth's core [*Glatzmaier*, 2002; *Olson*, 2011]. In numerical models the minimum heat input required for convection is lower than the real Earth whilst the relative importance of the fluid viscosity to the magnetic diffusivity in numerical models is about 4-6 orders of magnitude too large. That is, more magnetic field energy is transferred by physical motion of the fluid (rather than by diffusional processes) in numerical models than in the Earth's core. Furthermore, the relative importance of frictional effects at the boundaries of the spherical shell, where liquid is in contact with a solid surface, is about 8-10 orders of magnitude larger in numerical models than in the Earth's core.

Numerical models therefore have inherent uncertainty resulting from the requirement to make debatable assumptions, the limitations of modern computing power, and the uncertainties associated with estimating input parameters [e.g. *Dormy et al.*, 2000]. However, this does not preclude their usefulness in furthering our understanding of plausible processes that could generate the Earth's field. Despite these limitations numerical dynamo models recreate many important dynamic features of the geodynamo perhaps more successfully than we might expect [*Amit et al.*, 2010; *Glatzmaier*, 2002].

Many output parameters are on the same order of magnitude as those estimated for the real Earth indicating that the flow and field dynamics of the models are not too dissimilar to those in reality. For example, the magnetic Reynolds number, R_m, shown in equation 1.19, is found to be large, such that the frozen-in-field theorem is a reasonable approximation [*Bloxham and Gubbins*, 1986]. Numerical models are therefore a useful tool, albeit with limitations [e.g. *Dormy et al.*, 2000], that can help us discern the most likely interpretations of observational data.

1.5.3 Reversing Dynamos

In order to examine how the input parameters influence the geodynamo behaviour, studies have been conducted to systematically vary the input parameters in numerical models [*Christensen et al.*, 1999; *Christensen and Aubert*, 2006]. Of particular interest are those parametric regimes that generate the best representations of the Earth's field [*Amit et al.*, 2010]. That is, a magnetic field that is principally dipolar and, in our case of particular interest, reversing.

One of the most intriguing problems in these numerical dynamo models is that those parameters which are most conducive to dipolar fields do not coincide with those that generate reversing dynamos [*Christensen and Aubert*, 2006]. Typically, the dipolar dominated dynamos produce significantly more stable fields that maintain a single polarity unlike their multipolar equivalents which frequently reverse. Only a few, relatively weak dipole-dominated fields, on the boundary between the dipolar and multipolar dynamo regimes are found to reverse. However, it is important that the relative strength of the dipole should be high during stable polarity chrons, like that of the geomagnetic field.

When comparing the absolute time-scales of the numerical models to that of the geodynamo, the dimensionless model results must be rescaled. In doing so, the resulting output parameters, such as the magnetic Reynolds number R_m may become somewhat reduced in comparison to the real-world value ($R_m \sim 500$) which may affect the reversal dynamics [*Amit et al.*, 2010]. In those models that do represent reversing dipolar dynamos, it is difficult to obtain precise estimates of the duration of polarity transitions short kyr events. However, what is clear from the models is that the duration of polarity transitions is dependent upon the location of the observation [*Wicht*, 2005; *Wicht et al.*, 2009]. At higher latitudes, the duration of polarity transitions is longer than at lower latitudes, although transitions at the equator itself appear to be longer due to the presence of low-latitude flux patches at the core-mantle boundary (CMB). This is not unexpected, there is some evidence for latitudinal dependence in the palaeomagnetic record [*Clement*, 2004] and similarly simple models of the modern field that decrease the dipole component to simulate a reversal show a similar relationship [*Brown et al.*, 2007].

Two extreme examples for the reversal process can be imagined. Firstly, that the strength of the dipole field collapses such that it becomes small relative to the non-dipole field, followed by a subsequent increase in the dipole strength in either its original direction (that is, an excursion) or in the opposite direction to the original field (a full reversal). In this scenario, the strength of the non-dipole field may remain constant or increase or decrease during the dipole collapse. Alternatively, a model could be imagined whereby the direction of the dipole field changes continuously during a polarity transition, rotating such that at the midpoint of a transition, the poles are transferred to the equator. Numerical models of the geodynamo indicate that the former is far more likely than the latter [e.g. *Amit and Olson*, 2010; *Kutzner and Christensen*, 2002]. In order for a decrease in the dipole component and reversed directions to be observed at the surface, reversed flux magnetic field must be generated and transferred to the CMB [*Chulliat and Olsen*, 2010]. Typically, such a process is observed in reversing dynamo models as flow upwellings of magnetic material from the inner core boundary. These interact with the magnetic field lines to produce regions of reversed flux at the CMB [*Aubert et al.*, 2008; *Wicht and Olson*, 2004]. The strength and duration of the upwelling period could potentially increase the likelihood of a reversal rather than an excursion [*Wicht et al.*, 2009]. Following the upwelling, the dipole can recover in either direction [*Kutzner and Christensen*, 2002].

Numerical models show polarity transitions that are associated with intensity lows that are of significantly longer duration than the directional transition [*Glatzmaier and Coe*, 2007; *Olson et al.*, 2009]. This is usually due to a significant long-term decrease in the stability and strength of the dipolar component of the modelled field associated with magnetic upwellings. This is due to the fact that a significant decrease in the dipolar component of the field is required before reversed directions that diverge from dipolar ones are manifested [*Dormy et al.*, 2000]. The model transitional field is therefore dominated by the non-dipolar field during a reversal. This means that polarity transitions observed at the Earth's surface may exhibit different directional and temporal characteristics at different sites [e.g. *Kutzner and Christensen*, 2004]. Indeed, in some scenarios an excursion observed at one location is not necessarily manifested at another or only appears as a period of increased secular variation [*Wicht*, 2005].

1.5.4 Influence of the Inner Core

It is well known that the presence alone of an inner core, as a physical barrier within the outer core, significantly alters the dynamics of the flow within the rotating core [*Proudman*, 1956]. The presence of the inner core results in the appearance of a tangent cylinder (TC) which divides the outer, fluid core into three distinct regions of flow. This result is consistently observed in many numerical models of convection, although the exact difference between dynamics inside and outside the TC is unknown.

Gubbins [1999] proposed a hypothesis to explain why the field rapidly returned to its previous polarity following an excursion, rather than remain in the opposite state, as in a reversal. The conjecture, based upon numerical simulations conducted by [*Hollerbach*, 1993], emphasized the influence of interactions between the inner and outer core on the geomagnetic field. The magnetic field of the liquid outer core could change by fluid flow within 500 years. However, the field in the inner, solid core can only change via a process of diffusion, on a time-scale of approximately 3 kyr (for derivation of this value see Appendix A) [*Hollerbach and Jones*, 1995]. The inner core therefore imposes a magnetic inertia on the system. *Gubbins* [1999] suggested that an excursion, rather than a full reversal, occurs when the magnetic field in the outer core does not persist in a reversed state for sufficient time ($>$ 3 ka) for the inner core's field to also achieve reversal. The implication therefore is that the duration of an excursion should be less than 6 ka: equivalent to the time taken for the field to reverse and then return to its previous polarity in the inner core.

The importance of magnetic diffusion in the inner core may, however, have been overestimated. *Wicht* [2002] examined the results of two comparable 3D dynamo simulations with insulating or conducting inner cores. Running the two simulations *Wicht* [2002] demonstrated that whilst the presence of an inner core has an influence on the geometry of the dynamics, the electrical conductivity of the core has little effect. This was not necessarily an unexpected result. *Schubert and Zhang* [2001] had earlier pointed out that the Earth's inner core only accounts for 4% of the total core volume, and furthermore, only 2% of the total magnetic energy in the core may be attributed to the inner core. Numerical experiments suggest that for the inner core to have a substantial effect on magnetic field generation the ratio of the inner to outer core radius would have to be greater than 0.5 [*Schubert and Zhang*, 2001], although reducing the size of the inner core can also have unexpected effects upon the stability of the flow in the outer core [*Coe and Glatzmaier*, 2006].

1.6 Sedimentary Palaeomagnetic Archives

Sediments present the palaeomagnetist with an opportunity to study past geomagnetic field behaviour, and excursions, in high-resolution, continous archives. Sediments can acquire a magnetic remanence, termed detrital remanent magnetization (DRM), during their formation. In general terms, the relationship between the magnetic signal and depth in the sedimentary unit is thought to record the variations in the ambient magnetic field through time. The process by which the sediment acquires a remanent magnetization is, however, controversial. Whether the magnetic signal is recorded or 'locked-in' at the time of deposition (depositional DRM) or after some time interval (post-depositional DRM) is not clear [e.g. *Carter-Stiglitz et al.*, 2006; *Mitra and Tauxe*, 2009]. Understanding the process by which a field is recorded by sediments is of prime importance in interpreting sedimentary magnetic records.

1.6.1 Post-Depositional Detrital Remanent Magnetization

Early work by *Nagata* [1961] and *Collinson* [1965] presented a basic theory of depositional DRM whereby ferromagnetic grains, settling within a water-like fluid, align their magnetic moments with the ambient magnetic field. Thus, the sediment contains a population of magnetic grains aligned with the contemporary field and the age of the magnetic remanence is equal to that of the sediment medium in which it is recorded.

Depositional DRM has until relatively recently been regarded as relatively unimportant. The most obvious reason for this is that the initial DRM of most sediments is destroyed by bioturbation of the uppermost layers of the sediment. As a result, acquisition of DRM post-deposition has been assigned primary importance. However, this poses the palaeomagnetist with a problem: if the sediment acquires the remanence after initial deposition then there is an offset between the age of the sediment ascertained from sedimentary chronological methods and the age of the magnetic signal recorded within that sediment.

Laboratory redeposition experiments carried out by *Irving and Major* [1964] suggested that water-filled voids in the sediment below the surface could allow the free movement of magnetic grains post-deposition. Magnetic grains at some depth below the surface could therefore freely align with an ambient field of younger age than the sediment itself. Subsequent de-watering of the sediment at depth as a result of compaction would then 'lock-in' the post-depositional DRM (pDRM) (Figure 1.10). Later redeposition experiments seemed to confirm this result [e.g. *Lovlie*, 1974; *Otofuji and Sasajima*, 1981] and the concept of a 'lock-in' depth for the magnetic signal. Subsequent reviews therefore characterized DRM as being dominated by post-depositional DRM [e.g. *Tauxe*, 1993; *Verosub*, 1977].

The existence of pDRM raises the possibility of smoothing in the sedimentary record. If the 'lock-in' of a population of magnetic grains occurs across a depth range then the input magnetic signal will be filtered by the sediment during the recording process [*Roberts*

This figure has been omitted due to copyright restrictions

Figure 1.10: An illustration of the traditional conception of pDRM [*Roberts and Winklhofer*, 2004]. No lock-in of pDRM occurs above δ but below δ pDRM acqusition is initially high and decreases with depth according to some function. Lock-in is complete at the base of this zone, λ.

and Winklhofer, 2004] (Figure 1.10). Measurements from natural records also seem to confirm the existence of a pDRM. Records of palaeosecular variation (PSV), such as those from the Bermuda Rise in the western North Atlantic [*Lund and Keigwin*, 1994], exhibit subdued variability when sediment rates are lower. This smoothing of the PSV record is attributed to a DRM/pDRM acquisition process which, when modelled mathematically, suggests that acquisition occurs within a 10-20 cm lock-in interval. *DeMenocal et al.* [1990] investigated the variations in the relative stratigraphic positions of an oxygen isotope stratigraphic event, an interglacial (marine isotope stage 19.1), and the last full magnetic reversal, the Brunhes-Matuyama (B/M) ($\sim$780 ka). The depth offset between the palaeomagnetic event and the oxygen isotope stratigraphic event was found to be linearly related to sedimentation rate whereby the offset *decreases* with increasing sedimentation rate (for cores with a sedimentation rate greater than 1 cm kyr^{-1}). *DeMenocal et al.* [1990] argue that such a relationship can only be explained by a significant lock-in depth of $\sim$16 cm.

Any particular combination of sedimentation rate and lock-in depth within a core will have an associated degree of smoothing. Modelling of the effect of lock-in depth on smoothing can guide an interpretation of a sedimentary magnetic record (Figure 1.10). *Roberts and Winklhofer* [2004] demonstrated that with a lock-in depth of ~10 cm kyr^{-1}, in which 95% of the magnetic signal is locked-in 5 cm below the surface mixed layer, low sedimentation rate cores (1-3 cm kyr^{-1}) will fail to record 1 kyr-long events, such as excursions. They argue that moderate sedimentation rates (>~10 cm kyr^{-1}) are required to consistently detect short-duration excursions.

1.6.2 Flocculation

Simple calculations to determine the time required for a settling particle's magnetic moment to attain alignment with an ambient field, with a strength on the order of that of the Earth's field, imply that full alignment is achieved by a magnetic grain within a few milliseconds. Of particular interest is that the time taken to align is relatively invariant with respect of the strength of the field. If we assume this to be correct, and that there are no other mechanisms taking place, such calculations imply that no matter the strength of the applied field, the sediment will always have a saturated remanence (i.e. all the grains' magnetic moments are aligned). However, laboratory redeposition experiments carried out to investigate how sediments acquire a DRM demonstrate that the DRM produced is approximately linearly dependent upon the applied field at field-strengths within the range of those expected for the Earth's field [e.g. *Johnson et al.*, 1948]. One explanation for under-saturation of the sediment's magnetization could be that settling particles stick together or ''flocculate' which creates particles with a lower net moment and thus the theoretical time constant of alignment would be longer.

In salt water solutions, van der Waals forces can cause particles to coagulate, a process known as flocculation [*Tauxe et al.*, 2006]. In natural environments where magnetite particles are in the pseudo-single-domain range (i.e. those of interest to the palaeomagnetist) the magnetite particles are likely to be incorporated into larger flocs. Under-saturation

This figure has been omitted due to copyright restrictions

Figure 1.11: Schematic drawing showing flocculation model of DRM acquisition [*Tauxe et al.*, 2006]. Floc forms in both the high-turbulence surface zone and near the benthic boundary layer. Bioturbation and bottom currents resuspend the otherwise stable gel. The DRM is acquired during resuspension and is eventually recorded as sediment accretes into the historical layer.

could be then explained as a result of the fact that the larger flocs are subject to greater viscous drag which inhibits perfect alignment. Furthermore, the irregularly-shaped flocs are themselves made up of clay particles and potentially randomly orientated magnetic grains that lower the net moment of the floc as a whole [*Mitra and Tauxe*, 2009] The size of the flocs and the effect of the van der Waal's forces inhibits free rotation of the grains once deposited.

Katari et al. [2000] and *Tauxe et al.* [2006] present a forceful argument against the role of pDRM in the acquisition of DRM, arguing that the proposed evidence for lock-in depth from natural sediments [e.g. *Channell et al.*, 2004; *DeMenocal et al.*, 1990; *Lund and Keigwin*, 1994] is flawed. Re-evaluation of the variation in stratigraphic position of the B/M boundary by *Tauxe et al.* [1996] using twice the number of records as *DeMenocal et al.* [1990] reduces the apparent lock-in depth to a few centimetres below the sediment surface.

In the flocculation model (Figure 1.11), DRM is probably not acquired during initial settling as this might be expected to produce a saturation remanence; a feature that is not observed in naturally deposited sediments. Instead, the magnetization is acquired during the ubiquitous resuspension of sediment by bioturbation and bottom currents, settling through only a few tens of centimetres back into the 'gel zone' or benthic boundary layer. The DRM would thus be dependent upon the settling distance and the floc size distribution. As time passes, some small fraction of the magnetized sediment in the benthic boundary layer is incorporated into the undisturbed 'historical layer' [*Katari et al.*, 2000]. The sedimentation rate therefore still retains key importance, dictating the length of time sediment remains within the benthic boundary layer before eventual incorporation into the historical layer where the DRM is retained undisturbed.

1.6.3 Chemical Remanent Magnetization

Sediments can also acquire a chemical remanent magnetization (CRM), sometimes referred to as a crystallization remanent magnetization. A CRM results from the formation of a new magnetic mineral in the presence of an external magnetic field. A CRM can arise either by the formation of an entirely new magnetic mineral or by chemical alteration from one mineral phase to another [*Dunlop and Ozdemir*, 1997]. The development of a secondary CRM in a sediment, post-deposition, can obscure or destroy the primary DRM and preclude the isolation of a palaeomagnetic signal contemporary with the age of the sediment in which it is recorded [*Roberts et al.*, 2013]. In high-sedimentation rate marine sediments, one of the principal means by which a CRM may be formed is via the dissolution of magnetite and other iron oxides and the authigenic growth of iron sulphides including pyrite and greigite [*Berner*, 1984; *Roberts et al.*, 2013; *Rowan and Roberts*, 2006]. This arises in regions with high rates of organic matter deposition [e.g. *Tarduno et al.*, 1998; *Yamazaki and Solheid*, 2011], where detrital iron minerals react with H_2S, formed by bacterial sulphate reduction under anoxic conditions [*Berner*, 1984].

1.7 Oxygen Isotope Stratigraphy

Oxygen isotope stratigraphy is now a relatively routine method by which sedimentary archives may be dated by comparison to a global record. This section provides a brief overview of the general principles of oxygen isotope stratigraphy.

There are three naturally occurring isotopes of oxygen. Of these, ^{16}O is by far the most abundant (99.76%), followed by ^{18}O (0.2%) and ^{17}O (0.04%). Oxygen isotope stratigraphy relies upon the variation in the ratio of ^{18}O to ^{16}O in geological records. By convention, the ratio of ^{18}O to ^{16}O is usually cited as per mil (‰) differences relative to a standard. Carbonate samples are reported as ‰ deviation relative to the isotopic composition of the Vienna Pee-Dee Belemnite standard[1] (V-PDB) via the following equation:

$$\delta^{18}O = \left[\frac{(^{18}O/^{16}O)_{sample} - (^{18}O/^{16}O)_{V\text{-}PDB}}{(^{18}O/^{16}O)_{V\text{-}PDB}}\right] \times 10^3 \quad ‰ \quad . \tag{1.20}$$

Marine fauna such as foraminifera that have calcareous shells incorporate oxygen from the water in which they reside. The $\delta^{18}O_{calcite}$ of foraminiferal tests is dependent upon the temperature and $\delta^{18}O$ of the water in which the calcite is formed [*Epstein et al.*, 1953; *Urey et al.*, 1951].

One of the primary drivers of variation in $\delta^{18}O$ of seawater is temperature dependent fractionation between the heavier $H_2{}^{18}O$ and lighter $H_2{}^{16}O$ isotopologues during evaporation [*Craig and Gordon*, 1965]. Within the hydrological cycle, seawater is generally evaporated at lower latitudes and precipitated at high latitudes. Fractionation during evaporation preferentially transfers the lighter $H_2{}^{16}O$ isotopologue into water vapour leaving the seawater relatively enriched in the heavier $H_2{}^{18}O$.

During glacial periods, the $H_2{}^{16}O$-enriched precipitate at high latitudes is retained in ice sheets rather than being returned to the ocean. When ice-sheets are large, this

[1] The original standard was made from crushed belmnite (*Belemnitella americana*) from the Cretaceous Peedee formation in South Carolina. The original material has since been used up entirely, and other standards calibrated to PDB are used as an intermediate reference standard.

results in a substantial enrichment in ^{18}O relative to ^{16}O in seawater. This is recorded as a measurable increase in the $\delta^{18}O_{seawater}$ value. Thus, the ratio of $\delta^{18}O$ recorded in the calcite shells of benthic foraminifera (which are not also subject to local surface salinity variations, unlike planktic species) is dependent upon both the temperature and the volume of water stored globally as ice [*Shackleton*, 1967].

Because changes in ice-volume and temperature occur synchronously on glacial to interglacial time-scales, variation in $\delta^{18}O_{calcite}$ produces a globally consistent signal. More positive values of $\delta^{18}O_{calcite}$ occur during glacial intervals and more negative values during interglacial periods [*Emiliani*, 1955].

$\delta^{18}O$ records can therefore provide us with a means for correlating marine records with a common time-scale. $\delta^{18}O$ records from multiple sites can be used to produce an average record or 'stack' [e.g. *Imbrie et al.*, 1984; *Lisiecki and Raymo*, 2005]. Stacking local sites increases the signal-to-noise ratio, thereby allowing common features between different locations to produce a global record. The $\delta^{18}O$ record itself does not give absolute age determinations. However, by employing independent absolute age techniques to particular sites, or by tuning $\delta^{18}O$ records to assumed orbital forcing, distinctive features in the $\delta^{18}O$ record can be dated.

By comparing a locally measured oxygen isotope stratigraphy with a global stack of known age and attempting to discern features from the measured stratigraphy in the global stack, it is possible to assign ages to the stratigraphic section. Typically this results in recognition of a few well-dated 'tie-points' at which sudden changes occur in the $\delta^{18}O$ value as a result of relatively rapid and substantial climatic change between glacial and interglacial stages.

1.8 $^{230}Th_{xs}$ Normalization

The durations of geomagnetic excursions are thought to be less than 6000 years. To date excursions precisely and determine their durations, accurate, high-resolution age models are of primary importance. Alone, oxygen isotope stratigraphy cannot resolve millennial-scale fluctuations in sedimentation rate between known tie-points. The resolution is limited by the quality of the measured isotope record and by the ~20 kyr or longer spacing of major climatic shifts which produce the isotopic intervals. Thus, when used alone, oxygen isotope stratigraphy requires the assumption of a constant sedimentation rate within relatively long duration intervals. These limiting factors make it difficult to reduce the uncertainty surrounding the duration of excursions [*Knudsen et al.*, 2007] .

One approach that has been used in marine cores to improve age models derived from stratigraphic dating methods, such as oxygen isotope stratigraphy, is the use of $^{230}Th_{xs}$ as a constant-flux proxy [*Francois et al.*, 2004; *Henderson and Anderson*, 2003]. $^{230}Th_{xs}$ has been used, for instance, to assess lateral sediment advection in the central equatorial Pacific Ocean [*Marcantonio et al.*, 2001]; to assess the changing fluxes of windblown dust from the Sahara during the Holocene [*Adkins et al.*, 2006]; and to assess possible changes in sedimentation rate during Heinrich events in the North Atlantic [*McManus et al.*, 1998].

$^{230}Th_{xs}$ is produced by the decay of dissolved and oceanographically uniform ^{234}U in the water column. The rate of production is dependent on the concentration of uranium in the water column and on its isotopic composition, both of which are thought to have remained constant over the past few hundred-thousand years [*Henderson*, 2002]. This highly insoluble ^{230}Th, produced at a constant rate, is efficiently scavenged from the water column and transported to the underlying sediment by sinking particles [*Bacon and Anderson*, 1982] such that the vertical flux of ^{230}Th to the sea-floor is assumed to be equal to production in the overlying water column [*Bacon et al.*, 1985]. This component of ^{230}Th in the sediment is termed 'excess' thorium ($^{230}Th_{xs}$) because it is not supported by the decay of sedimentary uranium. Typically, concentrations of both uranium and thorium isotopes are measured from samples taken downcore. By measuring the concentration of $^{230}Th_{xs}$ in the sediment we can determine relative variations in total

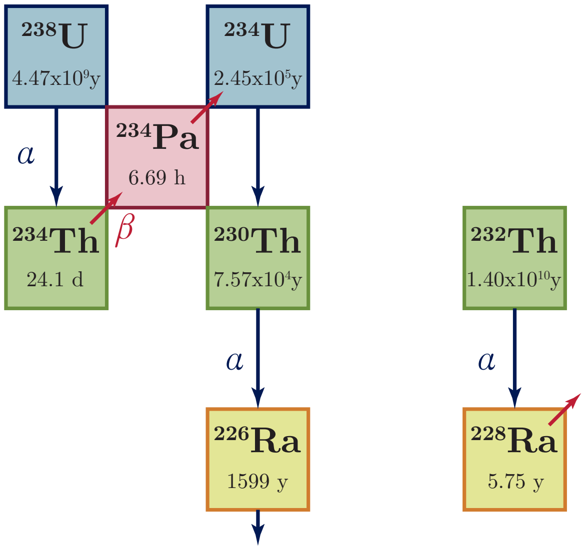

Figure 1.12: Schematic drawing of the ^{238}U and ^{232}Th decay chains with half-lives indicated [*Bourdon et al.*, 2003].

sediment flux. The following sections outline the basics of radioactive decay series and briefly discusses the principle of ^{230}Th$_{xs}$ normalization. A more thorough discussion of ^{230}Th$_{xs}$ normalization may be found in Chapter 3.

1.8.1 Uranium Series Nuclides

^{230}Th is a radioactive isotope (half-life: 75.69±0.23 kyr [*Cheng et al.*, 2000]) and a member of the ^{238}U decay series (Figure 1.12). The long-lived parent nuclide, ^{238}U, radioactively decays, through two short-lived daughters, to form ^{234}U, which itself alpha decays to form ^{230}Th.

Radioactive Decay

Rutherford and Soddy [1902] demonstrated that the rate of decay of an unstable parent nuclide is proportional to the number of atoms (N) remaining at any time t. Such that:

$$-\frac{dN}{dt} \propto N \quad . \tag{1.21}$$

The proportionality above may be expressed as an equality by using a constant of proportionality, λ, termed the decay constant. Each radioactive nuclide has a characteristic decay constant. The units of the decay constant are in reciprocal time.

$$-\frac{dN}{dt} = \lambda N \quad , \tag{1.22}$$

where λN is termed the 'activity' (A) of a radioactive nuclide. Rearranging and integrating,

$$-\int \frac{dN}{N} = \lambda \int dt \quad , \tag{1.23}$$

to find,

$$-\ln N = \lambda t + C \quad , \tag{1.24}$$

where C is a constant of integration. At $t = 0$, N is equal to the initial number of atoms, i.e. $N = N_0$. Thus,

$$C = -\ln N_0 \quad . \tag{1.25}$$

Substituting into Equation 1.24, we obtain

$$-\ln N = \lambda t + -\ln N_0 \quad , \tag{1.26}$$

$$\begin{aligned} \ln N - \ln N_0 &= -\lambda t \\ \ln \frac{N}{N_0} &= -\lambda t \\ \frac{N}{N_0} &= e^{-\lambda t} \\ N = N_0 e^{-\lambda t} & \quad . \end{aligned} \tag{1.27}$$

This is the basic equation describing radioactive decay for any radioactive nuclide. N is the number of atoms left after time, t, from an initial number, N_0. Figure 1.13 shows

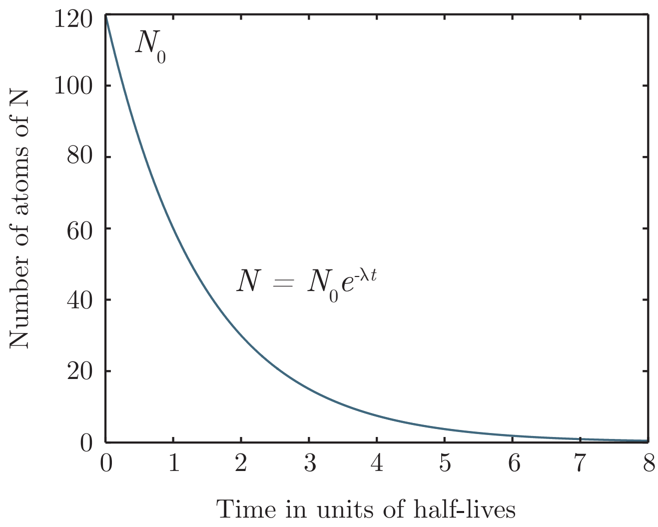

Figure 1.13: Decay of a hypothetical radionuclide (N) with time measured in units of half-lives.

how the number of atoms for a hypothetical radionuclide (N) decreases exponentially with time. As $t \to \infty$, $N \to 0$.

The half-life ($T_{1/2}$) is the time required for half of the initial number of atoms to decay. That is, when $t = T_{1/2}$, the value of N is halved, $N = \frac{1}{2}N_0$. By substituting this definition into Equation 1.27 we can determine how the half-life relates to the decay constant, λ.

$$\begin{aligned} \frac{1}{2}N_0 &= N_0 e^{-\lambda T_{1/2}} \\ \ln\frac{1}{2} &= -\lambda T_{1/2} \\ \ln 2 &= \lambda T_{1/2} \\ T_{1/2} = \frac{\ln 2}{\lambda} &= \frac{0.693}{\lambda} \quad . \end{aligned} \tag{1.28}$$

Decay Series

The daughter nuclide to which a parent nuclide decays may itself be radioactive. This is the case with the nuclides of interest in the uranium decay series. In this process, a parent

(N_1) decays to a radioactive daughter (N_2), which itself decays to a second daughter (N_3).

$$N_1 \rightarrow N_2 \rightarrow N_3$$

From Equation 1.22, the rate of decay of N_1 is:

$$-\frac{dN_1}{dt} = \lambda_1 N_1 \quad . \tag{1.29}$$

The rate of decay of the daughter nuclide, N_2, is the difference between the rate at which it is formed by decay of the parent, N_1, and its own decay rate. Thus,

$$-\frac{dN_2}{dt} = \lambda_1 N_1 - \lambda_2 N_2 \quad , \tag{1.30}$$

where λ_1 and λ_2 are the decay constants of radionuclides 1 and 2 respectively, and N_1 and N_2 are similarly the number of atoms of each remaining after time, t. Substituting Equation 1.27 into 1.29 and rearranging, we determine:

$$\frac{dN_2}{dt} + \lambda_2 N_2 - \lambda_1 N_1^0 e^{-\lambda_1 t} = 0 \quad , \tag{1.31}$$

where N_1^0 is the initial number of atoms of radionuclide 1. This is a first order linear differential equation, first solved by *Bateman* [1910].

$$N_2 = \frac{\lambda_1}{\lambda_2 - \lambda_1} N_1^0 \left(e^{-\lambda_1 t} - e^{-\lambda_2 t}\right) + N_2^0 e^{-\lambda_2 t} \quad . \tag{1.32}$$

The first term on the left-hand side in the equation represents the number of atoms of N_2 that have been formed by the decay of N_1, but have themselves not yet decayed. The second term is the number of atoms, N_2, that are left after the decay over time of some initial N_2^0. In many contexts, there are no initial atoms N_2^0. This allows us to simplify

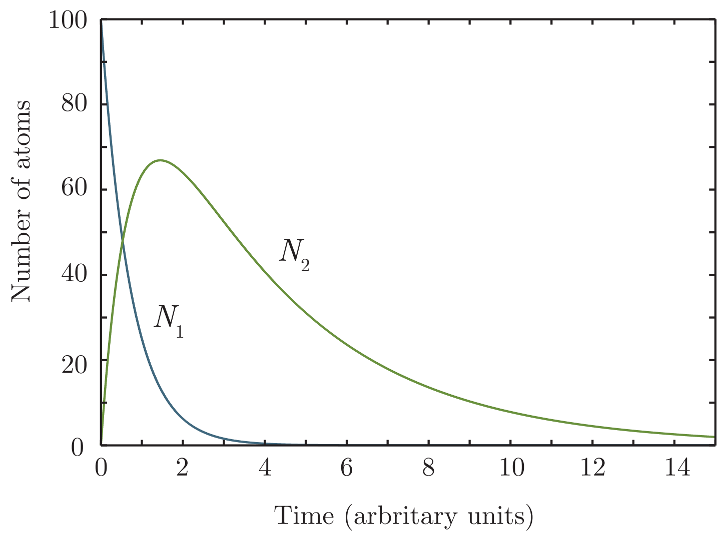

Figure 1.14: The first two radionuclides in a radioactive decay series showing the change in number of atoms of parent (N_1) and first daughter (N_2) with time. The parent has a half-life of one time unit; the first daughter has a longer half-life of 5 time units. Initially only atoms of the parent are present, N_1^0.

the above equation:

$$N_2 = \frac{\lambda_1}{\lambda_2 - \lambda_1} N_1^0 \left(e^{-\lambda_1 t} - e^{-\lambda_2 t}\right) \quad . \tag{1.33}$$

Figure 1.14 shows how the numbers of atoms of the first two radionuclides in a hypothetical decay series change over time.

Secular Equilibrium

For the decay chains arising from ^{238}U and ^{232}Th, the parent isotopes have much longer half-lives than their respective daughter isotopes such that the number of parent atoms remains almost constant for several half-lives of the daughter isotopes, where $\lambda_1 \ll \lambda_2$. In such cases, $e^{-\lambda_2 t}$ will tend to zero faster than $e^{-\lambda_1 t}$ as t increases. Equation 1.33 may therefore be simplified to:

$$N_2 \approx \frac{\lambda_1}{\lambda_2 - \lambda_1} N_1^0 e^{-\lambda_2 t} \quad , \tag{1.34}$$

and therefore, from Equation 1.27:

$$\frac{N_2}{N_1} = \frac{\lambda_1}{\lambda_2 - \lambda_1} = \text{constant} \quad . \tag{1.35}$$

Furthermore, because $\lambda_1 \ll \lambda_2$ we can simplify further:

$$\frac{N_2}{N_1} = \frac{\lambda_1}{\lambda_2} \quad \text{or} \quad \lambda_1 N_1 = \lambda_2 N_2 \quad . \tag{1.36}$$

Equation 1.36 indicates that the activities of all the nuclides in a decay chain initiated with a long-lived parent are the same (i.e $A_1 = A_2$). This situation is termed 'secular equilibrium', where the rate of the decay of the daughter is equal to that of the parent.

The ^{238}U decay chain comprises a parent with a very long half-life (^{238}U) and a series of intermediate short-lived daughters (^{234}Th, ^{234}Pa) before another longer-lived daughter (^{234}U) (Figure 1.12). Under conditions of secular equilibrium, the number of radiogenic ^{234}U atoms that have accumulated by series decay can be treated as though the initial parent ^{238}U decays directly to ^{234}U.

1.8.2 Marine Geochemistry of ^{230}Th

This section summarizes the marine geochemistry of ^{230}Th and outlines the principles which underlie the use of ^{230}Th$_{xs}$ as a constant flux proxy. Figure 1.15 provides a generalized overview of the aspects of marine geochemistry relevant to ^{230}Th$_{xs}$ normalization.

Continental Weathering and Uranium

Within the mineral lattices of crustal rocks older than 10^6 years, the uranium decay series nuclides are all in secular equilibrium. During weathering of these rocks, the balance of secular equilibrium is disturbed [*Chabaux*, 2003]. More soluble uranium isotopes are released from the lattice preferentially compared to the relatively insoluble thorium isotopes. Insoluble ^{230}Th and ^{232}Th are therefore only transported from the continents

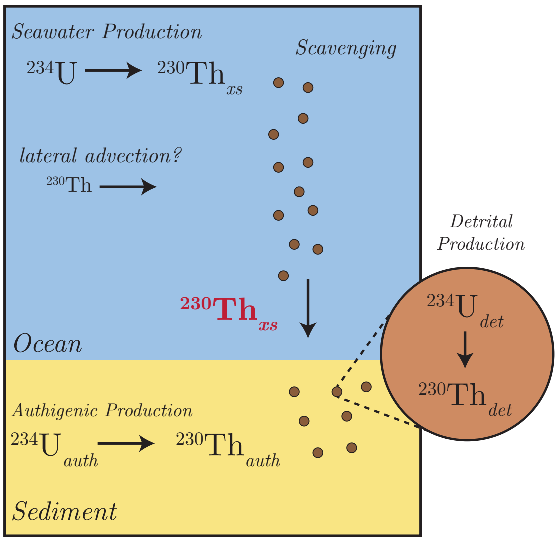

Figure 1.15: Schematic drawing of the marine chemistry of ^{230}Th. Refer to text (Section 1.8.2) for explanation.

to the sea in the form of 'detrital' ^{230}Th and ^{232}Th where they are held in the mineral lattices of particulate dust or riverine particles. Uranium is also transported in 'detrital' form but the dominant supply to seawater is in dissolved form from continents by river runoff [*Palmer and Edmond*, 1993].

Furthermore, α-recoil during the decay of ^{238}U ejects the immediate daughter ^{234}Th from the mineral lattice, which in turn rapidly decays to ^{234}U. Thus, ^{234}U is released preferentially into the waters relative to ^{238}U such that the (^{234}U/^{234}U) activity ratio in continental surface waters is greater than the secular equilibrium value (i.e. >1.0) [*Henderson and Anderson*, 2003; *Robinson et al.*, 2004].

Production of ^{230}Th in the Water Column

^{230}Th in the water column is produced by the decay of dissolved ^{234}U. Dissolved uranium has a long residence time (320–560 years) in the ocean relative to the timescale of circulation and is therefore well mixed in the ocean [*Dunk et al.*, 2002]. Dissolved uranium also behaves conservatively; its concentration in seawater is proportional to the salinity.

Seawater uranium has a (^{234}U/^{238}U) ratio of 1.147, resulting from the preferential weathering of ^{234}U. In seawater with a salinity of 35 ‰, the activity of ^{234}U is 2.835 dpm kg^{-1} equivalent to ~2910 dpm m^{-3} [*Robinson et al.*, 2004]. The production rate of ^{230}Th per unit volume, β_{230}, is dependent upon the concentration of its parent, ^{234}U, in the water and the rate of decay of the parent.

$$\beta_{230} = \lambda_{230} \times \left[{}^{234}\mathrm{U}\right] \quad , \tag{1.37}$$

where λ_{230} is the decay constant of ^{230}Th.

The concentration of ^{234}U, and therefore production rate, is understood to have remained constant for at least the last ~400 kyr [*Henderson*, 2002]. Modelling studies have demonstrated that lateral advection of ^{230}Th is low, with 70% of the ocean floor receiving a ^{230}Th flux within 30% of that expected from production [*Henderson et al.*, 1999].

Scavenging of ^{230}Th from the Water Column

Uranium and thorium exhibit very different chemical behaviour in seawater. Unlike uranium, thorium is extremely insoluble and highly particle reactive [*Bacon and Anderson*, 1982]. As a result, ^{230}Th is rapidly adsorbed onto the surfaces of particulate matter following its production in the water column by the decay of dissolved ^{234}U. This process is typically referred to as scavenging. The rapid scavenging of ^{230}Th means that it has a very short residence time in the water column (~20 years) [*Henderson and Anderson*, 2003]. The resulting flux of scavenged ^{230}Th into the sediment, j_{230} is therefore approximated to the total production rate in the water column above (P_{230}) [*Bacon*, 1984]:

$$j_{230} \approx P_{230} = \beta_{230} \times z \quad , \tag{1.38}$$

where z is the depth of the overlying water column. This approximation has been validated by more recent modelling [*Henderson et al.*, 1999; *Marchal et al.*, 2000] and sediment trap [*Yu et al.*, 2001] studies to within ∼30%. On the basis of average sinking velocities for suspended particles of 500-1000 m yr^{-1} [e.g. *Marchal et al.*, 2000], the very short residence time (∼20 years) of ^{230}Th argues against any more than limited lateral transport of ^{230}Th before it is removed as particles on the seafloor [*Francois et al.*, 2007; *Siddall et al.*, 2008].

Rapid removal from the water column isolates the scavenged ^{230}Th from its parent, ^{234}U. This component of ^{230}Th is therefore termed excess ^{230}Th ($^{230}Th_{xs}$). Following burial, the concentration of $^{230}Th_{xs}$ in the sediment is only dependent upon its own decay.

1.8.3 Determining $^{230}Th_{xs}$ Concentration

As the supply of $^{230}Th_{xs}$ to the sediment is constant, its concentration in the sediment is dependent upon the rate of sedimentation [*Francois et al.*, 2004]. A higher rate of sedimentation effectively 'dilutes' the constant supply of $^{230}Th_{xs}$, resulting in an inverse relationship between sediment $^{230}Th_{xs}$ and accumulation rates [*Krishnaswami*, 1976].

Scavenging is not, however, the only source of ^{230}Th into the sediment (see Figure 1.15). Sedimentary ^{230}Th consists of three components: scavenged ^{230}Th ($^{230}Th_{xs}$), detrital ^{230}Th ($^{230}Th_{det}$), and authigenic ($^{230}Th_{auth}$). Detrital ^{230}Th is that locked in the mineral lattices of lithogenic particles within the sediment and in secular equilibrium with ^{238}U. Authigenic ^{230}Th is produced from the decay of authigenic U that is either adsorbed on oxides or precipitated in anoxic or subanoxic sediments after diffusion from bottom waters [*Klinkhammer and Palmer*, 1991].

Therefore, to determine the $^{230}Th_{xs}$ (of use as a constant flux indicator) from the total ^{230}Th content of the sediment, contributions from $^{230}Th_{det}$ and $^{230}Th_{auth}$ must be subtracted from the total measured activity of ^{230}Th, such that:

$$^{230}Th_{xs} = ^{230}Th_{meas} - ^{230}Th_{det} - ^{230}Th_{auth} \quad . \tag{1.39}$$

The initial $^{230}\mathrm{Th}_{xs}$ concentration can then be calculated by correcting for its own decay since the time of sediment deposition:

$$^{230}\mathrm{Th}_{xs}^{\circ} = ^{230}\mathrm{Th}_{xs} e^{\lambda_{230} t} \quad . \tag{1.40}$$

Chapter 3 describes in detail the approach by which $^{230}\mathrm{Th}_{xs}$ values are calculated and the use of $^{230}\mathrm{Th}_{xs}^{0}$ as a constant-flux proxy.

1.8.4 Calculating $^{230}\mathrm{Th}_{xs}$-normalized Sedimentation Rates

The concentration of $^{230}\mathrm{Th}_{xs}^{0}$ in the sediment may be used to determine relative variations in total sedimentation rate. The higher the concentration of $^{230}\mathrm{Th}_{xs}^{0}$, the lower the sedimentation rate. To calculate a linear relationship between the concentration of $^{230}\mathrm{Th}_{xs}^{0}$ and the sedimentation rate, the two must be examined within an interval constrained by tie-points of known age and depth, taken from a traditional stratigraphy. The average concentration of $^{230}\mathrm{Th}_{xs}^{0}$ in the sediment within the tie-point constrained interval can be calculated and related to the average sedimentation rate. The variation in sedimentation rate is calculated using relative variations in concentration of $^{230}\mathrm{Th}_{xs}^{0}$ above and below the average to modify the average sedimentation rate determined between the stratigraphic tie-points. In this approach, the sedimentation rate for each depth interval is calculated using the following expression:

$$\mathrm{F}_n = \mathrm{F}_a \times \frac{\overline{\mathrm{Th}}}{\mathrm{Th}_n} \quad . \tag{1.41}$$

where F_n is the sedimentation rate for the sample interval; Th_n is the concentration of $^{230}\mathrm{Th}_{xs}^{0}$ in that sample interval; F_a is the average sedimentation rate in cm kyr^{-1} between the tie-points; and $\overline{\mathrm{Th}}$ is the depth-interval-weighted average concentration of $^{230}\mathrm{Th}_{xs}^{0}$ between the tie-points.

Chapter 3 describes in detail the means by which $^{230}\mathrm{Th}_{xs}^{0}$ may be used to calculate sedimentation rates, the underlying assumptions and associated uncertainties.

Focussing

This ^{230}Th-normalization approach assumes that ^{230}Th is scavenged from the seawater in the vertical water column above the site and then rapidly exported to the seafloor by large, sinking particles. If we assume that there is no lateral transport of sediment material to or from a site then, between two dated horizons at depths z_2 and z_1, the total $^{230}\mathrm{Th}^0_{xs}$ inventory in the sediment should equal the production, P, of ^{230}Th in the overlying water column integrated over the time interval (t_2–t_1) corresponding to that between the two dated horizons. Where $^{230}\mathrm{Th}^0_{xs}$ is the $^{230}\mathrm{Th}_{xs}$ activity corrected for its own decay since deposition and ρ is the dry sediment density.

$$\int_{z_1}^{z_2} {}^{230}\mathrm{Th}^0_{xs}\rho \,\mathrm{d}z = \int_{t_1}^{t_2} P \,\mathrm{d}t \quad , \tag{1.42}$$

where production is dependent upon the ^{234}U activity in seawater (for a salinity of 35 ‰^{234}U activity is $\sim$2910 dpm m^{-3} [*Robinson et al.*, 2004]) and the depth of the water column above the site.

However, if lateral transport of sediment material has occurred, the total $^{230}\mathrm{Th}^0_{xs}$ in the sediment will not equal the integrated production in the water column above, either due to the addition or removal of sediment from the site. To determine the degree to which focussing or winnowing of sediment has taken place at a given site, *Suman and Bacon* [1989] defined a 'focussing factor' (Ψ):

$$\Psi = \int_{z_1}^{z_2} \left({}^{230}\mathrm{Th}^0_{xs}\rho\right) / \left(P(t_2 - t_1)\right) \,\mathrm{d}z \quad . \tag{1.43}$$

Where $\Psi = 1$, no syndepositional redistribution has occurred. Where $\Psi > 1$, focussing is likely to have occurred (i.e. sediment from elsewhere has been added to the sediment at the measured site), whilst when $\Psi < 1$ winnowing is assumed. The focussing factor is often calculated when $^{230}Th_{xs}$ normalization methods are used [e.g. *Francois et al.*, 2004; *Higgins et al.*, 1999; *Loubere et al.*, 2004; *Marcantonio et al.*, 2001].

Although the formulation of Equation 1.43 provides potential for a focussing factor less than 1, typically focussing factors measured are greater than 1 [e.g. *Higgins et al.*, 1999; *Loubere et al.*, 2004; *Marcantonio et al.*, 2001]. In part, this is likely due to the bias in choosing drill-site locations that have high accumulation rates. Such sites are more likely to be sediment sinks with lateral input of sediment from surrounding areas.

1.9 Summary

Our understanding of the geodynamo is dependent upon accurate and reliable observations that can be used to constrain and critique models and hypotheses about the mechanisms generating the Earth's magnetic field. Although marine sediment cores have been extremely important in revealing the existence and number of geomagnetic excursions [*Lund et al.*, 2006], the cause and nature of geomagnetic excursions remains uncertain [*Roberts*, 2008]. The focus of current research is directed towards obtaining high resolution sedimentary excursion records with good age control from sites with sedimentation rates sufficiently high (>10 cm kyr^{-1}) to record excursional behaviour in detail.

This thesis attempts to characterize the behaviour of the geomagnetic field during excursional events. Rock magnetic and palaeomagnetic measurements are used to determine reliable records of two geomagnetic excursions, the Blake Excursion (∼125 ka) and the Laschamp excursion (∼41 ka) from high sedimentation rate marine cores. Using a combination of conventional stratigraphic methods and the novel use of $^{230}Th_{xs}$ as an indicator of relative variation in sedimentation rate, high-resolution age models are constructed to allow robust temporal analysis of the two excursions.

The methods used to obtain and date palaeomagnetic records from marine cores are described in Chapter 2. Chapter 3 discusses in detail the approach used to determine relative variations in sedimentation rate using $^{230}Th_{xs}$ as a constant flux proxy. It suggests some improvements to the corrections used to determine $^{230}Th_{xs}$ and presents a new MATLAB program that can be used to calculate $^{230}Th_{xs}$ and age models for marine sediment cores. Chapter 4 presents a new, high-resolution palaeomagnetic record of the Blake geomagnetic excursion from the Bahama Outer Ridge contourite in the western North Atlantic. Chapter 4 also demonstrates the use of $^{230}Th_{xs}$ to more accurately constrain the duration of this geomagnetic excursion. Chapter 5 follows a similar approach and presents a record of the Laschamp geomagnetic excursion at a neighbouring site on the Blake Ridge. Chapter 6 presents $^{230}Th_{xs}$ data that was used to try and improve the age model for the Laschamp excursion record from Site 1061. Finally, in an attempt to characterize the global behaviour of the Blake excursion, a number of sites from the Pacific Ocean were studied and the results of these investigations are presented in Chapter 7.

Chapter 2

Methods

2.1 Introduction

This chapter describes the experimental methods used throughout this thesis. Following sample collection, the experimental methods may be divided into two principal components: (i) the methods carried out to characterize the palaeomagnetic properties of the sediments and (ii) the methods used to determine an age model for the palaeomagnetic measurements. The palaeomagnetic section comprises methods with two main objectives: firstly, to measure the Characteristic Remanent Magnetization (ChRM) that describes the palaeomagnetic vector recorded by the sediment sample and secondly, to determine rock magnetic properties that may influence the efficiency of acquisition or the reliability of the recorded signal. Methods employed to determine an age model for the palaeomagnetic records may also be divided into two objectives. The first objective is to determine a stratigraphy from which absolute ages with appropriate uncertainties may be derived. In this thesis, only one such stratigraphy, using oxygen isotope analysis, is determined by direct measurements carried out by the author. Secondly, mass spectrometry is employed to determine the concentration of $^{230}Th_{xs}$ in the sediment which is used as a proxy for relative variations in sedimentation rate between stratigraphic bounds of known age.

2.2 Sampling

Sampling was undertaken at two Integrated Ocean Drilling Program (IODP) core repositories on a number of occasions. In general, cores drilled from the Atlantic Ocean are stored at the Bremen Core Repository, based at the the Center for Marine Environmental Sciences (Marum) at the University of Bremen. Cores from the Pacific Ocean are stored at the Gulf Coast Repository (GCR) associated with Texas A&M University in College Station, Texas.

Ocean Drilling Program cores are stored at the repositories as core-halves. One half is used as the 'working' half, available for research purposes. The other half is designated as an 'archive' half and is only available at the discretion of the repository staff. The vast majority of samples were taken from 'working' halves, although in a few cases, where sampling of the 'working' half was precluded by previous sampling, the 'archive' half was used. At the core repository, the cores are maintained at a temperature of 4.4°C.

Discrete samples were taken as $20 \times 20 \times 20$ mm cubes from the radial centre of the split cores to avoid core-edge distortion associated with drilling. When the core is retrieved during a cruise, it is cut into sections 1.5 m in length. Samples were therefore not taken from intervals within 5 cm of the core-breaks and intervals where the sediment was obviously disturbed. Standard, hollow Perspex cubes were pushed into the mud, ensuring that each cube was oriented parallel to the core side and perpendicular to the core surface. The cubes were then extracted from the core using a wire tool. Typically, samples were taken at increased resolution across intervals believed to coincide with excursional features on the shipboard palaeomagnetic measurements. All the samples were kept refrigerated at the University of Oxford to prevent the samples from drying out by loss of water vapour.

Samples are identified by their Leg number, Site number, Hole identifier, Core number, Core type, Core section, and depth interval in the core section. The depth interval is always assumed to be 20 mm and so the depth given is the mid-point of the perspex cube. This is given in a four-digit form, where 1000 is equivalent to 100.0 cm. For example, a sample identification of Leg 172, Hole 1061A, 3H1-0100 should be interpreted as representing a sample removed from the interval between 9.0 and 11.0 cm below the top of Section 1 in core 3H of Hole 1061A from Leg 172. Where the 'H' indicates that the cores sampled were Hydraulic Piston Cores, as was the case for all samples in this thesis.

2.3 Palaeomagnetic Measurements

2.3.1 Field-Free Room

All palaeomagnetic measurement and demagnetization procedures were carried out in field-free rooms at the Department of Earth Sciences at the University of Oxford. Field-free rooms are constructed with multiple layers of transformer steel lining the walls. This affords protection against ambient fields. In 2010, the department was relocated from a premises on Parks Road to the current building on South Parks Road. The Oxford palaeomagnetic laboratory was therefore relocated to the new premises and a new field-free room built.

The first set of palaeomagnetic measurements (those in Chapter 4) were conducted in the older field-free room. The rest of the palaeomagnetic measurements were conducted in the new field-free room. Within the new room, the measured ambient field was 0.27 μT, corresponding to a $\sim$98% reduction in field intensity compared to that immediately outside the room.

2.3.2 Measuring Remanence

Measurements of the samples' magnetization were carried out using a 2G Enterprises DC-SQUID Cryogenic magnetometer at the University of Oxford. This device uses three super-conducting quantum interference devices (SQUIDs) to measure the magnetization.

SQUIDS measure the magnetic flux in a closed loop of super-conducting material. The physics of SQUIDs is beyond the scope of this thesis but may be found elsewhere [e.g. *Collinson*, 1983; *Fagaly*, 2006].

Typical intensity sensitivity of the 2G magnetometer is approximately 6×10^{-10} Am^{-2}. Measurement of inclination is accurate to within 1°, whilst declination is typically accurate to within 5°.

2.3.3 Demagnetization of Remanence

Given sufficient time, the magnetic remanence of a grain will reach magnetic equilibrium with an external field [*Néel*, 1949]. The time taken to achieve equilibrium is termed the relaxation time, τ:

$$\tau = \frac{1}{\mathrm{C}} \exp\left(\frac{\mathrm{vH}_{cr}\mathrm{M}_s}{2kT}\right) \quad , \tag{2.1}$$

where C is a frequency factor, v is the volume of the grain, H_{cr} is the grain's coercivity, M_s is the spontaneous magnetization, k is the Boltzmann constant and T is the absolute temperature. For single domain magnetite grains under geological conditions, the temperature is sufficiently low such that the relaxation time exceeds the age of the Earth and the remanence is stable.

There are two principal means of demagnetizing samples: thermal and alternating field (AF) demagnetization. In both cases, demagnetization is achieved by changing the external conditions to reduce the relaxation times of the sample grains to laboratory timescales (i.e. seconds-minutes). In AF demagnetization, samples are subjected to fields that are stronger than the constituent grains' coercivities such that the magnetization rapidly aligns with the applied field. Thermal demagnetization, on the other hand, increases the temperature term on the bottom of the exponent thereby reducing the relaxation time of constituent grains. When the sample is heated and cooled in a zero field there is no external field for the grains' magnetic moments to realign to and the resulting net magnetization is zero. For the vast majority of samples, AF demagnetization was used to isolate the ChRM. However, for a few samples for which AF demagnetization was unsuccessful, thermal demagnetization was attempted.

Alternating Field Demagnetization

A sample may be demagnetized by exposure to a decaying alternating field which is smoothly reduced to zero (Figure 2.1). By applying fields along three perpendicular axes the net effect of the applied field has no preferred orientation. In any natural sample, there will be a population of grains with a range of different coercivities. The magnetic moments of grains with coercivities less than the alternating field will align themselves with the field. As the field decreases smoothly, those grains with coercivities just above that of the alternating field will have their moments fixed in the direction of the field. As the field reverses, the remaining mobile moments will similarly reverse. Those grains with coercivities just above that of the following half-cycle will again have their moments fixed in the direction of the field. In this way, populations of grains with similar coercivities will be remagnetized in alternating directions. The result is that the magnetic moments of grains with coercivities less than the peak alternating field are effectively randomized -resulting in a net magnetization of zero.

By repeating the process with progressively higher peak fields and measuring the remaining remanence between steps, individual components of the total NRM magnetization may be determined until the highest coercivity grains are completely demagnetized.

AF demagnetization has a number of advantages over thermal demagnetization: the samples are not chemically or compositionally altered by being subjected to an alternating field; stepwise demagnetization is almost completely automated and may be carried out on the same equipment as the measurement of magnetization; and it is relatively quick to undertake.

All samples demagnetized using stepwise AF demagnetization were subjected to applied AF peak fields of 3, 6, 9, 12, 15, 20, 25, 30, 35, 40, 50, 60, 70, 80, 90, and 100 mT.

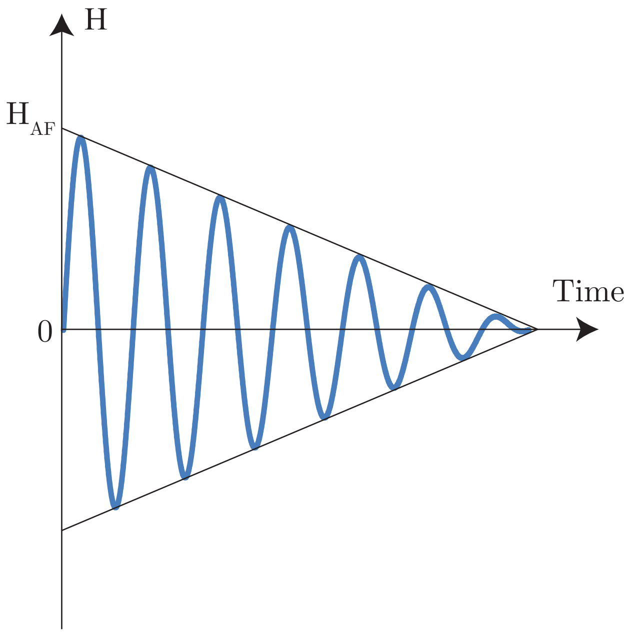

Figure 2.1: The alternating field (AF) intensity is smoothly reduced from a peak value (H_{AF}) to zero. This effectively randomizes the magnetization of a grains with coercivities less than the peak field.

All demagnetization steps were performed using the in-line, triaxial, alternating field demagnetizer of the 2G Enterprises DC-SQUID cryogenic magnetometer within shielded rooms at the University of Oxford.

Thermal Demagnetization

The method of thermal demagnetization employs the application of heat to demagnetize a sample. When a magnetized grain is subjected to heat, the increased thermal energy causes the remanent magnetic moments to precess around their average directions. At the grain's Curie temperature, T_c, the magnetic moments become randomly oriented and the material is paramagnetic, such that there is no remanent magnetization. If the sample is then cooled in a zero field, the net remanent magnetization will be zero.

If the sample is heated to a temperature less than T_c in a zero field then only some of the magnetic moments will be randomized, such that the sample is only partially demagnetized. Subsequent cooling to room temperature in a zero field allows this partial magnetization to be measured.

Before thermal demagnetization, sediment samples were carefully removed from their plastic sample cubes and wrapped in aluminium foil and their orientation marked in permanent ink. Samples were heated in an MMTD oven at the University of Oxford. The oven has a Helmholtz coil [*Collinson*, 1983] around the entrance to the sample chamber to further reduce the internal ambient field to less than 1 μT. For each demagnetization step, the samples were held at peak temperature for 35 minutes before cooling to room temperature. To readily detect any potentially spurious remanence acquired in the oven, the sample orientation was systematically alternated when placed in the oven.

2.3.4 Declination Correction

In many of the cores, the ChRM directions showed progressive trends in declination along core. This was taken as an indication that the cores had been twisted during the drilling process. Furthermore, as the cores were not oriented, there was no agreement between individual core sections, reflected by large apparent jumps in declination between core sections in the raw data.

However, useful information may still be extracted if it is assumed that the record conforms to a geocentric axial dipole model (GAD). In this case, the mean direction of the record is oriented towards the geographic North Pole (0°). The declination data was corrected using the following method. For each core section, a 'best-fit' regression line was determined for the declination values. Declination values which showed a deviation greater than 45° from the previous data point were excluded from the determination of a best-fit line. Each data point was then corrected by setting the deviation of the data from the best-fit line as its deviation about 0°.

2.3.5 Magnetic Susceptibility

Magnetic susceptibility is a measure of the response of a sample to an applied field (see Section 1.2). The low-field magnetic susceptibility measurements were made using a Geofyzika KLY-2 KappaBridge at the University of Oxford. The Kappabridge is not kept in the field-free room but is placed on a wooden work-bench.

Low Temperature Susceptibility

The samples were measured in their plastic cubes following demagnetization in the Kappabridge at room temperature. The Kappabridge measures volume magnetic susceptibility (per unit volume, κ) 'in-field' assuming a volume of 10 cm^3 (Equation 1.5). As the samples are 8 cm^3 volume, the measured value is multiplied by 10/8 to account for the difference in volume. To calculate the magnetic susceptibility per unit mass (χ, Equation 1.6) the calculated volume susceptibility was multiplied by the volume of the sample and divided by the sample mass.

Sensitivity is equal to 4×10^{-8} SI (four orders of magnitude smaller than the measured values). Random error is therefore essentially negligible.

High Temperature Susceptibility

Measurement of susceptibility as a function of temperature can provide information about the magnetic mineralogy of a sample. Samples for which high temperature magnetic measurements were made were prepared by reducing them to a fine powder. Approximately 0.5 cm^3 of sample powder was then placed into a cleaned, narrow glass test tube. Using the CS-2 apparatus and KLY-2 Kappabridge, the samples' magnetic susceptibility was monitored as the samples were heated in air from room temperature up to 700°C and subsequently cooled back to room temperature. The temperature is monitored by a thermocouple placed within the powder.

2.3.6 Isothermal Remanent Magnetization

An isothermal remanent magnetization (IRM) is achieved by exposing the sample to a strong field for a short period of time. Stepwise application of isothermal remanant magnetization may be used to determine the coercivity spectrum of a sample and thereby its constituent magnetic grain mineralogy [*Kruiver et al.*, 2001; *Robertson and France*, 1994]. To determine IRM acquisition profiles, selected samples were subjected to progressive forward- and back-field IRM acquisition using a Molspin Pulse Magnetizer at the University of Oxford. These samples were demagnetized at 100 mT and their magnetization measured to ensure that their initial remanence was negligible. The samples were then subjected to forward fields of 5, 10, 15, 20, 25, 30, 40, 50, 70, 90, 120, 150, 200, 250, 300, 400, 500, 600 and 800 mT. The samples' magnetizations were measured out-of-field between each step using the 2G magnetometer. Subsequently the same series of fields were applied in the opposite direction (back-field). The resulting curves show the progressive magnetization of each sample tending towards a maximum value after exposure to fields of increasing strength. As the samples are exposed to reverse fields, their remanence decreases to zero before then developing a magnetization in the reverse direction (Figure 2.2).

Remanence Coercivity (H_{cr})

The remanence coercivity (H_{cr}) is the 'reverse' field required to reduce a 'forward' saturation remanence to zero (see Figure 2.2). Typically samples dominated by low-coercivity magnetite have H_{cr} values ranging from approximately 30 to 70 mT; higher-coercivity magnetic minerals such as haematite have H_{cr} values exceeding 100 mT [*McElhinny et al.*, 1999]. This parameter is concentration-independent to a first-order approximation [*Dekkers*, 1997].

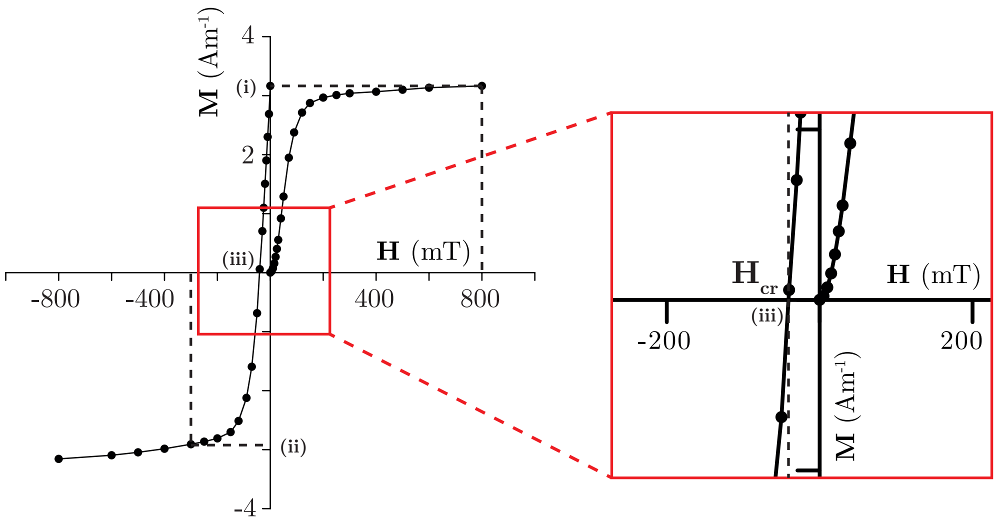

Figure 2.2: An example isothermal remanent magnetization (IRM) acquisition profile. (i) The magnetization achieved by an applied 'forward' IRM of 800 mT; (ii) the magnetization achieved by a 'reverse' IRM of 300 mT; and (iii) the H_{cr} is the 'reverse' field required to reduce a 'forward' saturation remanence to zero.

S-Ratio

The S-Ratio is a magnetic parameter that can be used to diagnose the presence of particular magnetic minerals [*King and Channell*, 1991]. It principally provides a measure of the proportion of high coercivity ('hard') remanence to low coercivity ('soft') remanence carriers and is typically calculated by dividing the magnetization acquired in a back-field of 300 mT by that acquired in a forward-field of 1000 mT (i.e. 1 T). Due to limitations on the maximum applied field achievable by the pulse magnetizer, the 'S-Ratio' was calculated using a 800 mT forward-field (Equation 2.2, see Figure 2.2).

Where:

$$\text{S-Ratio} = -\frac{\text{IRM}_{300mT}}{\text{IRM}_{800mT}} \quad . \tag{2.2}$$

A value nearing 1 indicates that a reverse field of 300 mT has been sufficient to produce an equivalent magnetization to that produced by an 800 mT field in the forward direction. If this is the case, the principal remanence carriers have a low coercivity mineralogy [*McElhinny et al.*, 1999]. A value significantly less than 1 would imply that high coercivity remanence carriers such as haematite are present.

The IRM acquisition curves showed that in some cases saturation isothermal remanent magnetization (SIRM) was not achieved by application of an 800 mT field (90-98% saturation). To determine the SIRM, the acquisition curves were modelled using IRMUNMIX [*Heslop et al.*, 2002] assuming a two component mixture of one lower and one higher coercivity component. The model can then be used to calculate an estimate for the SIRM.

2.3.7 Anhysteretic Remanent Magnetization

An anhysteretic remanent magnetization (ARM) is induced in a sample by the application of a large alternating field whose intensity is reduced to zero whilst a smaller constant direct-current (DC) bias is simultaneously applied (Figure 2.3) [*Collinson*, 1983]. Thus the sample is effectively exposed to an asymmetric AF field. An ARM was induced in all samples using a 100 mT peak field and a 0.1 mT bias field. The ARM was applied using a DTECH-2000 AF demagnetiser which can induce ARMs at Imperial College, London.

2.4 Oxygen Isotope Measurements

Oxygen isotope measurements on the carbonate tests of foraminifera may be employed to determine a stratigraphy which may be used to assign ages to depth intervals in the cores. To extract the planktonic foraminiferal tests from the sediment samples, each sample was submerged in deionized water and mechanically agitated until suspension of the sediment was achieved. The sediment suspension was then sieved and the 63 μm fraction retained. This fraction was subsequently dried in an oven at 50°C. Specimens in this fraction were picked that showed good levels of preservation.

Oxygen isotope analyses were conducted using a Finnigan automated Kiel IV acidification unit and a dual inlet Delta V isotope ratio mass spectrometer at the Department

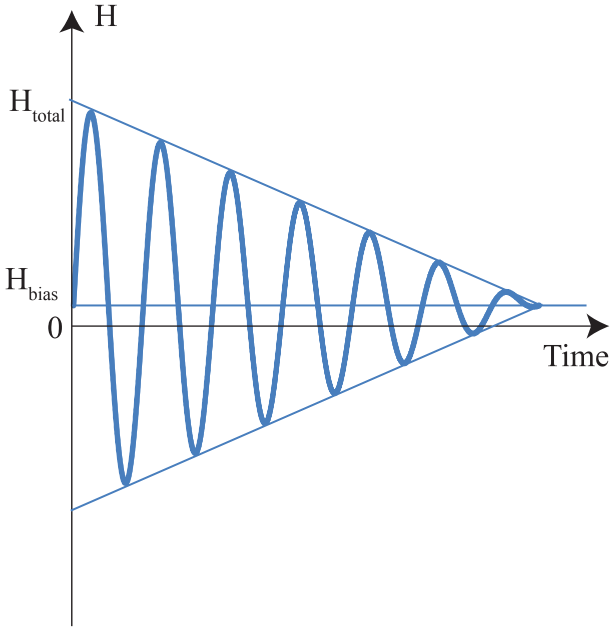

Figure 2.3: Whilst the alternating field (AF) intensity is smoothly reduced from a peak value (H_{AF}) to zero, the DC bias field is maintained at a constant throughout the process (H_{bias}). This gives an ARM magnetization to grains with coercivities less than the total peak field.

of Earth Sciences, University of Oxford. Purified phosphoric acid (H_3PO_4) is automatically added to the foraminiferal tests in an evacuated vial at high temperature in order to achieve complete digestion of the $CaCO_3$:

$$2H_3PO_{4(aq)} + 3CaCO_{3(s)} \rightleftharpoons Ca_3(PO_4)_{2(s)} + 3H_2O_{(g)} + 3CO_{2(g)} \quad . \tag{2.3}$$

The resulting CO_2 and H_2O gases are cooled using liquid nitrogen at -190°C while any non-condensible gases are removed. The CO_2 is then released at -90°C, whilst the water is completely retained. The gaseous CO_2 molecules are then ionized by electron impact and separated by the analyzer into three ion beams corresponding to $^{12}C^{16}O^{16}O$, $^{13}C^{16}O^{16}O$ and $^{12}C^{16}O^{18}O$ (with molecular masses of 44, 45 and 46 respectively) and a small component of molecules containing ^{17}O. The ratio of the intensity of the 46 to 44 ion beam is equal to the $^{18}O/^{16}O$ ratio of the sample CO_2.

All measurements are given in standard delta notation in per mil (‰) relative to the

Vienna PeeDee Belemnite (V-PDB) carbonate standard. Where:

$$\delta^{18}\mathrm{O} = \left[\frac{(^{18}\mathrm{O}/^{16}\mathrm{O})_{sample} - (^{18}\mathrm{O}/^{16}\mathrm{O})_{V\text{-}PDB}}{(^{18}\mathrm{O}/^{16}\mathrm{O})_{V\text{-}PDB}}\right] \times 10^3 \quad ‰ \quad . \tag{2.4}$$

Isotopic values were related to the V-PDB standard by repeated measurements of laboratory reference standards of the National Bureau of Standards NBS-19 (δ^{18}O=-2.2‰; δ^{13}C=1.95‰) and NBS-18 (δ^{18}O=-23‰; δ^{13}C=-5.0‰). The external analytical precision of the Delta V has been determined by repeated measurement of NBS-19. 321 measurements (May 2007 to June 2008) indicate an analytical precision of ±0.04‰ (2σ) for δ^{13}C and ±0.1‰ (2σ) for δ^{18}O [*Burgess et al.*, 2010]. Analytical precision for replicate standard measurements ($n = 13$) of δ^{18}O in NBS-19, made internally with the measurements in Chapter 4, was ±0.18‰ (2σ).

2.5 Uranium-Thorium Measurements

2.5.1 Chemistry

Laboratory Conditions

All sediment chemistry was conducted at the Department of Earth Sciences at the University of Oxford. In 2010, the department was relocated from a premises on Parks Road to the current building on South Parks Road. All chemistry conducted to examine the Blake excursion (Chapter 4) was undertaken in the laboratories at the old department building. Subsequent work attempting to characterize the Laschamp excursion (Chapter 5) was undertaken at the new premises. The following description of the laboratory method is applicable for both sites.

To avoid external contamination of samples, all chemistry was conducted under clean-lab conditions. The clean lab is over-pressured with class 1000 HEPA-filtered air. Within the clean lab, all users wear Tyvek over-suits and clean shoes confined to the laboratory.

Latex gloves were worn at all times. Chemistry in the lab, including column chemistry, was undertaken in a laminar-flow clean-hood.

Some of the sample preparation prior to clean-lab chemistry was undertaken in a 'non-clean' lab. This is because it is preferable for the samples to be taken into the clean-lab in suspension, rather than as free particulates, to prevent cross-contamination with other users. This included the drying of and weighing of samples.

Cleaning Procedure

To avoid contamination of the samples, Teflon beakers are cleaned using the following procedure:

- The Teflon beakers and lids are rinsed with de-ionised water three times. Each time the beakers and lids are filled to the top and poured cleanly to ensure no residual drips are left in the bottom or on the sides of the beakers. The beakers are then filled roughly 1/3 full of 2 Molar reagent grade hydrochloric acid (HCl). The beakers are then left to reflux on the hotplate overnight at a temperature of 120°C with the lids on.
- The beakers are removed from the hotplate and the acid is discarded. The Teflon is then rinsed again with DI water, following the procedure above. To check for scratches and unwanted residue, the beakers are rotated whilst holding a small amount of water to see whether the meniscus catches. If it does, the Teflon is either not used or stage 1 is repeated. The water is then poured away. The Teflon is subsequently placed in a large glass vat and submerged in 7.5 Molar reagent-grade nitric acid (HNO_3). The vat is subsequently covered and placed on a hotplate overnight at 120°C.
- The vat is removed from the hotplate and allowed to cool. The beakers and lids are removed from the vat, rinsing each with Milli-Q (resistivity: 18.2 MΩ) three times. The beakers are then filled roughly 1/3 full of 10 M distilled HCl. The beakers are

then placed, with their lids on, onto the hotplate and left to reflux overnight again at 120°C.

- The beakers are removed from the hotplate the following day and allowed to cool. The acid is discarded and the Teflon is rinsed three times using Milli-Q. The Teflon is then left to air-dry, open-side down on a clean lab wipe in a laminar flow hood.

All non-Teflon plasticware and drying crucibles are leached in 3% HNO_3 and rinsed with Milli-Q before use. The columns are heated overnight in distilled 7 M HNO_3.

Weighing

The sediment samples and spike solutions were weighed using a Sartorius analytical balance readable to 0.00001 g, at a precision better than ±0.0001 g (less than 0.1% of the mass of the sample). In both cases, the 'target' mass for the spike and for the sample was 0.1 g each.

Prior to weighing, aliquots of the sediment were heated overnight in a 'non-clean' lab at 110°C to drive off any water and allow a dry-mass to be measured. The sediment samples were weighed out onto a small tray of aluminium foil and subsequently transferred into clean PFA Teflon beakers and any residue on the foil was rinsed into the beakers using a small amount of Milli-Q. The sample powders, now in suspension, were then taken to the clean lab.

Weighing of the spike solution was performed under clean-lab conditions into a Teflon beaker. A 'double-accounting' method was used whereby both the beaker and the spike-solution bottle were weighed before and after the transfer of spike. The spike was weighed at least three successive times to ensure reproducibility. To reduce the biasing effects of static [see Fig. 2.7 in *Thomas*, 2006], the internal deionization function of the balance was used to deionize the beakers and spike bottle.

Sample Digestion

The use of a spike relies on complete equilibration with the sample to be analysed. This in turn requires that the sample be completely dissolved. Dissolution or 'digestion' of marine sediments is complicated by the fact that the sediment comprises a mixture of both silicates and carbonates. The two components have different chemical behaviours that unfortunately make dissolution with a single solvent impossible [*Potts*, 1987]. All acids used are quartz distilled from reagent grade. Water used for chemistry is 18.2 MΩ Milli-Q.

Nitric acid (HNO_3) can dissolve calcium carbonate material with relative ease:

$$CaCO_{3(g)} + 2HNO_{3(aq)} \rightarrow Ca(NO_3)_{2(aq)} + H_2O_{(l)} + CO_{2(g)} \quad . \tag{2.5}$$

Silicates, however, are relatively unaffected by the addition of Nitric acid (HNO_3) and require the addition of hydrofluoric acid (HF) to break strong Si-O bonds [*Langmyhr and Sveen*, 1965]:

$$SiO_{2(s)} + 4HF_{(l)} \rightleftharpoons SiF_{4(g)} + 2H_2O_{(l)} \quad . \tag{2.6}$$

This produces the volatile gas SiF_4, liberating silicon from the mixture. However, the addition of HF to a solution containing calcium ions (Ca^{2+}) unfortunately results in the formation of extremely insoluble calcium fluoride (CaF_2) salts.

$$Ca^{2+}_{(aq)} + 2F^{-}_{(aq)} \rightarrow CaF_{2(s)} \quad . \tag{2.7}$$

To reduce the production of fluorides and ensure complete dissolution of sample material, perchloric acid ($HClO_4$) is added to the solution. Perchloric acid is a strong mineral acid which is highly dissociated in water. Hydrofluoric acid is a weak acid with a low dissociation constant ($K_a = 7.2 \times 10^4$). Thus, in aqueous form it has the equilibrium:

$$HF_{(l)} + H_2O_{(l)} \rightleftharpoons F^-_{(aq)} + H_3O^+_{(aq)} \quad . \tag{2.8}$$

Following Le Chatelier's Principle, the addition of H_3O^+ ions via the dissociation of perchloric acid, drives the equilibrium to the left. As a result, the HF remains primarily undissociated. The HF is therefore in the correct form to react with the silicates (liquid) and fewer fluorides ions are in solution and thus available to react with the calcium ions.

Perchloric acid also forms an azeotropic mixture with water which boils at 203°C. This high boiling temperature (higher than that of HF and HNO_3) allows significant heating of the entire mixture, driving off any remaining HF and SiF_4.

Subsequent repeated addition and drying-down of concentrated nitric acid further ensures that all the HF and SiF_4 is driven off and that any remaining fluorides are converted to soluble nitrates [*Anderson and Fleer*, 1982].

$$CaF_{2(s)} + 2HNO_{3(aq)} \rightleftharpoons Ca(HNO_3)_{(aq)} + 2HF_{(l)} \quad . \tag{2.9}$$

Initially, the digestion procedure used followed that of *Thomas* [2006], which is a modification of a method developed by S. Wyatt (Oxford University), in which sample dissolution is attempted in one beaker. Initially HNO_3 was added to the sample to dissolve the carbonate material in the sediment. Subsequently HF was added to dissolve the silicate content with perchloric acid, used to inhibit fluroide production and drive off any fluorides produced. However, this process was extremely time-consuming as, inevitably, some fluorides were produced in sediments with high carbonate content.

Subsequently a new procedure was developed whereby the two components of the sediment (the silicate and carbonate material) are dissolved in separate containers. The dissolved carbonate solution is separated from the sample before HF is added to reduce the production of fluorides. This procedure was developed by Alex Thomas and Chris Kinsley at Oxford University. The following is therefore a modification of the digestion procedure of *Thomas* [2006] but essentially follows the same principles.

- The sample material is weighed into a white PFA Teflon beaker. 1 ml of MilliQ water is added to form a suspension. The sample is then sonicated to break up the sediment.

- To dissolve the carbonate fraction, 2 ml of 15 M HNO_3 is added to each PFA beaker. The solution fizzes as carbon dioxide is released.

- The beaker is then capped and heated for two hours at 120°C on a hotplate to dissolve any remaining carbonate material and oxidise organic material before the addition of perchloric acid. Then the remaining sediment mixture is poured into a leach-cleaned centrifuge tube. The mixture is then centrifuged.

  As much of the solution as possible is then carefully pipetted out of the beaker and into a separate pre-spiked PEF beaker (see Section 2.5.2). This is to remove as much calcium as possible from the silicate fraction before HF is added.

  2 ml of 7.5 M HNO_3 is then added to the mixture to rinse the silicate fraction. The mixture is then centifuged again and the resulting solution is then pipetted off into the corresponding spike beaker.

- 2 ml of 15 M HNO_3 is then added to the silicate fraction and the mixture is returned to the original PFA beaker. The centrifuge tube is rinsed with a further 1 ml of 15 M HNO_3 which is also poured into the PFA beaker.

- 1 ml of $HClO_4$ is added to each silicate sample beaker. The silicate beakers are then heated, uncapped, at 110°C on a hotplate. This is undertaken with the perchloric scrubber activated in the laminar flow hood to prevent formation of explosive perchloric salts in the extraction system. 1 ml of HF is added to dissolve the silicate material.

- The sample is subsequently dried down taking care to keep the sample damp to avoid the formation of insoluble residues [*Potts*, 1987]. Whilst the beaker is still hot on the hotplate, a further 0.5 ml $HClO_4$ and 1 ml HF is added to each beaker and the temperature increased to 180°C. The second addition of HF is to account for the fact that during the reaction with silicates (Equation 2.6) the molarity of the acid is diluted by the production of water. The sample is then allowed to dry down.

- The dried sample is then redissolved in 2 ml 15 M HNO_3 and dried down at 180°C twice over. The high temperature (> 140°C) is to ensure that all of the HF is driven off, whilst repeated addition of HNO_3 ensures that all remaining fluorides are converted to nitrates.
- The spiked, dissolved carbonate solution is then poured into the silicate fraction beaker. The spike beaker is rinsed with 1 ml 15 M HNO_3 which is also poured into the sample beaker. The dissolved sample is then dried down at 150°C on the hotplate and made back up with 4 ml of 7.5 M HNO_3. Subsequently, the sample beaker is capped and allowed to reflux overnight to ensure full equilibration of the two dissolved fractions and the spike.
- The result of this complete process is a dissolved solution in nitrate form, ready for elemental separation via column chemistry.

Elemental Separation

Elemental separation is very important prior to mass spectrometry. The sample is introduced into the mass spectrometer in dissolved form. If a sample contains high dissolved total solids then it can clog the nebuliser or affect the stability of the plasma. Simply reducing the total concentration of the solution would reduce the ability of the machine to measure the U and Th accurately. By separating the U and Th from the rest of the matrix, and Fe in particular, the U and Th may be run at a high enough concentration to ensure accurate measurement of the desired isotopes. U is collected separately from Th as U has a much higher concentration (by a factor of $\sim 10^4$) in the sediment than Th. Accurate measurement of U and Th together is therefore prevented by the limited dynamic range of the mass spectrometer.

The column procedure used is that of *Thomas* [2006], which itself is derived from a protocol developed by *Robinson et al.* [2004], based on that of *Chen et al.* [1986]. This approach uses the differing interactions of U and Th with an anion-exchange resin. In 7.5 M HNO_3, Th has a high affinity for the resin and U is moderately adhered to the resin whilst other matrix components, such as Fe, are easily removed. Addition of 6 M HCl elutes Th from the column whilst U maintains a strong affinity to the resin and is retained in the column. The U still retained by the column is then eluted by the addition of Milli-Q. By applying this technique carefully, the U and Th may be separated from one another into two 'cuts'.

The separation procedure was as follows:

- A batch of Dowex 'Biorad AG1-X8' 100–200 mesh resin was rinsed by vigorous shaking in a beaker of Milli-Q. The Milli-Q was then decanted from the resin, and the process was repeated with fresh Milli-Q a further two times. The same process was then repeated with 6 M HCl, and then again with Milli-Q. The resin was left in suspension following the final stage.
- 2 ml Teflon Biorad columns, were filled with 2 ml of the cleaned resin slurry. They were then washed with 10 ml Milli-Q, 10 ml 6 M HCl and a further 10 ml Milli-Q to remove any contaminant U and Th.
- The columns were then prepared by conditioning with 10 ml (2×5 ml) of 7.5 M HNO_3. The samples were subsequently loaded directly from the sample beaker.
- The columns were then washed with 4 ml (2×2 ml) of 7.5 M HNO_3 , the first 2 ml is added to the sample beaker and then poured from the beaker into the column.
- The columns were then converted by 1.5 ml (4×0.25 ml, 4×0.5 ml) of 6 M HCl. At this point, a Teflon sample beaker was placed under the columns to collect the Th cut. Elution of Th is then achieved by the addition of 6 ml (2×1 ml, 2×2 ml) of 6 M HCl, the U is retained on the columns.

- Lastly the U cut was eluted from the columns. Another Teflon sample beaker was placed under the columns to collect the U cut. This was achieved by the addition of 10 ml (2×1 ml, 2×4 ml) Milli-Q.
- Both cuts were then dried down. Then 0.2 ml of 15 M HNO_3 was added to each cut and dried down again. Finally the cuts were dissolved in 42 μl of 7.5 M HNO_3 for storage before mass spectrometry. 958 μl Milli-Q was added to the sample prior to mass spectrometry to make up a 1 ml sample in a solution of 2% HNO_3.

2.5.2 Spike and Standards

Isotope Dilution & Concentration

The aim of the mass spectrometry is to determine the concentrations of isotopes of U and Th in the sediment to allow the determination of the concentration of $^{230}Th_{xs}$. The principal mode of operation of a mass spectrometer is to simultaneously measure multiple isotopes to allow accurate determination of isotope ratios. Measurement of a ratio is more accurate as any fluctuations in the ion beam strength ('plasma flicker') are similar for both isotopes.

Isotope dilution is the method whereby a spike of known isotopic composition is added to the sample, allowing conversion of measured isotope ratios to concentrations of the individual isotopes. ^{236}U is used to determine the amount of sample uranium isotopes and ^{229}Th is used to determine the amount of sample thorium isotopes. ^{236}U and ^{229}Th are both isotopes that do not occur naturally and therefore the samples, prior to spike addition, are assumed not to contain either isotope. The spike is added to the samples and well-equilibrated before measurement. By knowing the number of atoms of the spike isotope added to the sample, and the measured ratio of the spike isotope to the sample isotopes of interest, the amount of sample isotopes may be calculated. As the spike is not entirely pure, the amount of sample isotope determined must also be corrected for any addition of the same isotope from the spike.

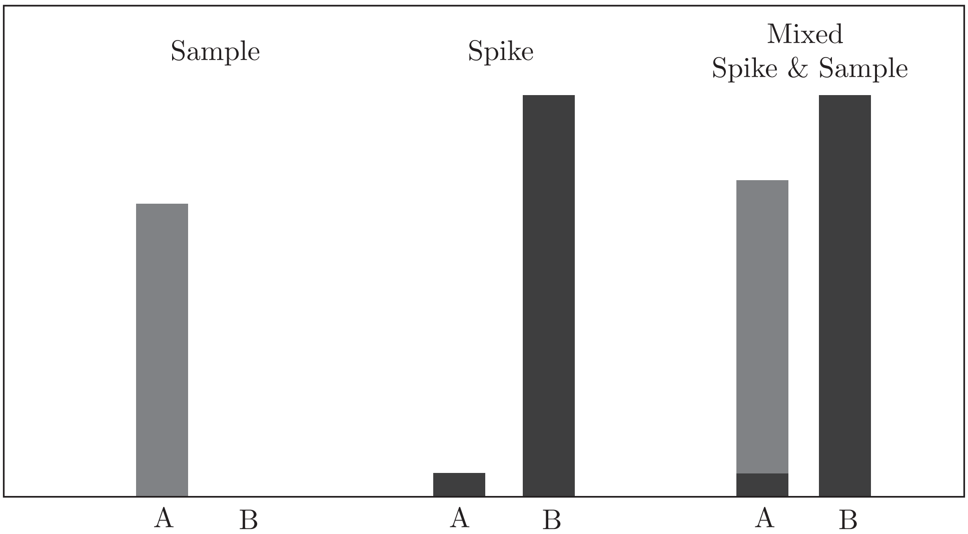

Figure 2.4: Schematic example of isotope dilution. The sample and the spike contain two isotopes ‘A’ and ‘B’ of the same element. The sample contains the naturally occurring isotope ‘A’, but does not contain isotope ‘B’, which does not occur naturally. The spike contains a large amount of isotope ‘B’ but only a very small amount of isotope ‘A’.

Figure 2.4 shows a schematic example of isotope dilution. The measured atom ratio (R_M) from the spike (*sp*) and sample (*sa*) mixture is:

$$R_M = \left[\frac{A}{B}\right]_M = \frac{A_{sa} + A_{sp}}{B_{sp}} \quad . \tag{2.10}$$

The amount of isotopes A and B added as part of the spike (A_{sp} and B_{sp} respectively) are known from the mass of spike added to the sample and the calibrated composition of the spike.

We can therefore calculate the amount of isotope A attributable to the sample (A_{sa}):

$$A_{sa} = (R_M \times B_{sp}) - A_{sp} \quad . \tag{2.11}$$

A mixed spike, ‘Oxford Carbonate Spike’, containing both ^{236}U and ^{229}Th was used to make measurements of U and Th concentrations in the sediment samples. By using a spike containing both isotopes, the concentrations of both U and Th can be determined in the same sample. To reduce uncertainty, a spike is used that has a mass of spike isotope close to the mass of the isotope of interest in the sample [*De Bièvre and Debus*, 1965]. The composition of the sediment spike is such that using a total spike mass equivalent to that of the sample sediment mass provides such a state. The calibration of the spike was performed by Andrew Mason at Oxford University. The composition of the sediment spike is summarised in Table 2.1.

Standards

Uranium and thorium standards were measured routinely during mass spectrometry to ensure maintenance of accurate and reproducible isotope ratio determination. Two standards were used and are summarised in Table 2.2.

CRM-145 is a uranium concentration and isotopic solution standard made from a high purity metal, available from the New Brunswick Laboratory, NJ, USA. The $^{238}U/^{235}U$ activity ratio is similar to that of natural samples at 137.849.

The thorium standard, ThIS-2-250, is a University of Oxford laboratory standard. The artificial standard was mixed from solutions of ^{232}Th (High Purity Standards Lot # 0724812), ^{230}Th (IRMM 060), ^{229}Th (Eckert&Ziegler Lot # 30216.01 and 'Oak Ridge Th229') [*Mason and Henderson*, 2010]. The $^{232}Th/^{230}Th$ activity ratio is equal to 249.67 and the $^{232}Th/^{229}Th$ ratio is 0.77116.

2.5.3 Mass Spectrometry

The Mass Spectrometer

The mass spectrometer used throughout this study for the determination of U and Th isotope concentrations is a Nu Instruments multi-collector inductively-coupled-plasma mass spectrometer (MC-ICP-MS) (Fig. 2.5). The Nu Plasma is a variable-dispersion, double-focusing instrument [*Belshaw et al.*, 1998]. The sample and standard solutions are injected into the nebulizer which sheers the liquids into small droplets forming an

Table 2.1: Isotopic composition of 'Oxford Carbonate Spike'. Measured by Andrew Mason, University of Oxford, 2 Feb 2011.

Oxford Carbonate Spike						
Isotope	Atomic Mass	λ (yr^{-1})	Natural *Atom %*	Spike *Atom %*	*Conc. (g/g)*	*2 s.e. ‰*
229Th	229.031755	8.7740×10^{-05}	0.0	0.99598	2.3943663×10^{-10}	2.4
230Th	230.033127	9.1577×10^{-06}	4.1631973×10^{-06}	0.00006		
232Th	232.038054	4.9500×10^{-11}	0.999996	0.00396		
233U	233.039628	4.3594×10^{-06}	0.0	0.0		
234U	234.040946	2.8263×10^{-06}	5.4877631×10^{-05}	3.8647974×10^{-11}		
235U	235.043924	9.8458×10^{-10}	7.2526835×10^{-03}	4.2057328×10^{-05}		
236U	236.045562	2.9622×10^{-08}	0.0	0.99972753682218	9.0959080×10^{-08}	0.8
238U	238.050784	1.5510×10^{-10}	0.992692	0.00023040581098		

Standard	$^{238}U/^{235}U$	$^{235}U/^{234}U$	$^{238}U/^{234}U$	$^{232}Th/^{230}Th$	$^{230}Th/^{229}Th$
CRM-145	137.849	137.29	18924.7	n/a	n/a
ThIS-2-250	n/a	n/a	n/a	249.67	0.77116

Table 2.2: Isotopic composition of Uranium and Thorium Standards.

Collector	F	F	F	F	F	F	AXIAL	F	F	IC	F	IC	F	IC	F
Mass	+7	+5	+4	+3	+2	+1	0	-1	-2	-3	-4	-5	-6	-7	-8

Table 2.3: Nu Plasma Collector Array. The ‘Axial’ and ‘F’ collectors are Faraday cups, the ‘IC’ collectors are ion counters. The numbers in the second row refer to the number of effective mass units away from the Axial collector [following *Robinson et al.*, 2004]

This figure has been omitted due to copyright restrictions

Figure 2.5: Schematic diagram of the Nu Instruments Nu Plasma MC-ICP-MS, from *Rehkämper et al.* [2001].

aerosol. The aerosol is then passed into the ICP torch and rapidly dried to a solid and then heated to a gas. As the atoms pass through the plasma, at a temperature of ~6000°C, they lose a single electron to form a positive ion. The resulting ion beam is focussed by an electrostatic analyser (ESA), ensuring that all ions have the same velocity. This prevents the large spread of initial ion energies in the beam from affecting the mass separation of the isotopes. A magnet separates the ion beams by their mass/charge (m/z) ratio. The isotope beams of interest are then dispersed by two quadrupole lenses, which together form a variable 'zoom' lens. The zoom lens is used to align the isotopes of interest with the collector array.

The Collector Array

The collector array is equipped with 12 Faraday cups and 3 electron multipliers (ion counters) (Table 2.3). The Faraday cups are used for the measurement of relatively large ions beams ($>10^{-12}$ A $\approx 6 \times 10^{6}$ counts s^{-1}). Incoming positive ions generate a current by attracting a flow of electrons from ground to the collector across a high (10^{11} Ω) resistance. The resultant change in voltage is amplified and detected. The detectors therefore measure the intensity of the incoming beam rather than 'counting' individual ions. As Faraday cups are limited in sensitivity and dynamic range, smaller ion beams ($<10^{-13}$ A $\approx 6 \times 10^{5}$ counts s^{-1}) are measured using the electron multipliers. An incoming positive ion results in a release of electrons when it strikes the first dynode of the multiplier. The electrons cascade to the next dynode, where they release a larger pulse of electrons. The electrons continue to multiply as they cascade through a series of dynodes before they are detected as a narrow pulse at the detector. Thus, the effect of a single ion is amplified such that it may be counted by a detectable pulse of electrons.

Relative Gain

As the Faraday cups and ion counters have different sensitivities, a correction must be made for isotope ratios in which one isotope has been measured in an ion counter (IC) and the other in a Faraday cup. The difference between the response of the ion counter and the Faraday cup is referred to as the 'gain', where:

$$\mathrm{gain} = \frac{\mathrm{I}_{IC}}{\mathrm{I}_{Faraday}} \quad . \tag{2.12}$$

To determine the relative gain, a gain measurement step may be included in the mass spectrometry routine. By measuring a standard of known isotopic ratios across an ion counter and a Faraday cup an external correction may be made for the relative gain.

Mass Bias

The mass of an ion can significantly affect its transfer from the ion source. Mass bias results from two causes: the space charge effect [*Gillson et al.*, 1988] and nozzle dispersion [*Heumann et al.*, 1998]. Of these two, the space charge effect is thought to have the greatest influence. The space charge effect occurs when positive ions are brought together in narrow region of space. The positively charged ions repel one another and some are deflected away from the main ion beam. This disproportionately affects lighter ions as they are more easily deflected. The ion beam therefore has a lower proportion of the lighter isotopes than the original sample.

For isotopes with high mass (including U and Th), where the relative difference in mass is small, this effect is assumed to be linearly related to the difference in mass between the isotopes. The real isotope ratio (R_{Real}) may be determined from the measured ratio (R_{Meas}) using the following relationship:

$$\mathrm{R}_{Real} = \mathrm{R}_{Meas}\,(1 + \varepsilon\Delta\mathrm{M}) \quad , \tag{2.13}$$

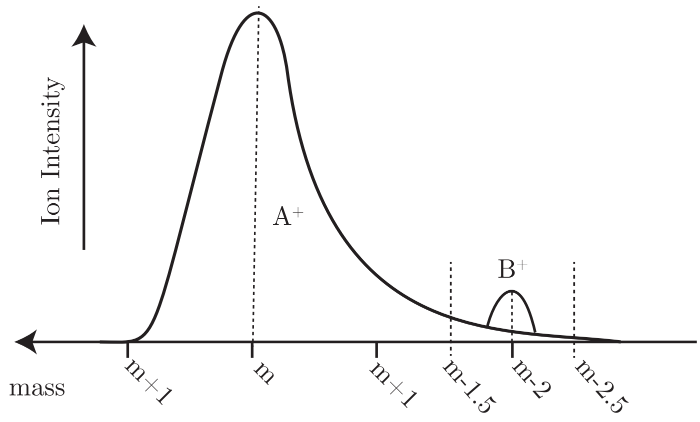

Figure 2.6: Schematic showing abundance sensitivity effect. The 'tail' of the high intensity beam of isotope 'A', mass, m, extends across lighter mass units, contributing to the measurement at of isotope 'B' at m-2. To correct for this contribution, measurement is made at m-1.5 and m-2.5 and extrapolated to calculate the contribution at m-2.

where ΔM is the difference in mass units between the isotopes and ε is an empirically determined linear factor (the mass bias per unit mass). The mass bias effect is corrected by measurement of a standard. A known isotope ratio of the standard is then used to determine ε and thus to correct the measured sample isotope ratios.

Abundance Sensitivity

The vacuum within the mass spectrometer is not perfect. A small proportion of the ions may therefore interact with gaseous atoms within the flight tube. Many of these ions are deflected such that they collide with the walls of the flight tube and are absorbed by baffles. However, some of the ions interact with the atoms such that their flight is merely slowed. When this occurs, their deflection by the magnet is significantly greater than for the rest of the ions of the same isotopic mass. This effect widens the ion beam, creating a 'tail' that extends across lighter mass units. This is particularly a problem when measuring an isotope of relatively low concentration in a solution containing an isotope of high concentration but of slightly greater mass (Fig. 2.6).

Collector:	F(+1)	AXIAL	F(-1)	F(-2)	IC(-3)
Uranium					
Sample Measurement	^{238}U		^{236}U	^{235}U	^{234}U
Abundance Sensitivity					233.5
					234.5
Thorium					
Sample Measurement			^{232}Th		^{230}Th
		^{232}Th			^{229}Th
Abundance Sensitivity					230.5
					229.5
					229.5
					228.5
		^{232}Th			
Gain Measurement	^{238}U			^{235}U	^{234}U

Table 2.4: Measurement Configurations of the Collector Array.

To correct for abundance sensitivity, a step is included in the measurement whereby the ion beams are aligned such that the intensity at the mass units 1/2 amu above and below the low concentration isotope may be measured. The measurement at these two points is attributed entirely to the 'tail' of the higher mass isotope and a exponential approximation is made to determine the contribution from the tail to the signal measured across the mass unit of interest.

Uranium

The collector configuration for all measurements using the mass spectrometer is presented in Table 2.4. Measurements of uranium samples are conducted in three principal stages:

1. *Memory measurement*: this is a measurement made before the sample is introduced but when 2% nitric wash is passing through the system. The collector configuration is the same as for the sample measurement.

2. *Sample measurement*: this also includes a measurement of the background (i.e. the

values registered by the collectors when they are isolated from any beam - the 'zero' point).

3. *Abundance sensitivity measurement*: made using the sample solution, in multiple configurations.

The sample measurements are made in a static mode with ^{238}U, ^{236}U, and ^{235}U focused in Faraday collectors, and ^{234}U in IC(-3) (Table 2.6). Samples are bracketed by CRM-145 standards to correct for mass bias and ion counter gain. CRM-145 standards are also run as 'dummy' samples to assess the reproducibility of the measurements.

To improve the accuracy of this approach, the samples and standards are run at equivalent concentrations to ensure that beam-size effects are minimized. Maximum precision is achieved by running the samples at the highest possible concentration. The concentration of the solution is limited by the maximum voltage that can be recorded on the Faraday collectors (10 V). In this case, the most abundant, and therefore limiting, isotope is ^{238}U. Samples are diluted such that the ^{238}U concentration is roughly equivalent to 9 V on the Faraday collector.

Abundance sensitivity resulting from the 'tail' of the ^{238}U beam is internally assessed and corrected for by measurement of the beam 1/2 amu above and below ^{234}U in IC(-3), using the ^{238}U beam in the sample configuration as a reference beam. Machine drift is accounted for by normalizing the ^{235}U/^{234}U to the mean ^{235}U/^{234}U of the standards. All the samples are then normalized to the drift-corrected standards' known ratio of 137.29 (Table 2.2). This applies an external correction for ion counter gain and mass bias. The ^{238}U/^{236}U ratio is externally corrected for mass bias with the ^{238}U/^{235}U ratio of the standard (137.849, Table 2.2). From equation 2.13:

$$\varepsilon = \left(\frac{^{238}\mathrm{U}/^{235}\mathrm{U}_{meas}}{137.849} - 1\right)/3 \quad , \tag{2.14}$$

and,

$$^{238}\mathrm{U}/^{236}\mathrm{U}_{real} = \frac{^{238}\mathrm{U}/^{236}\mathrm{U}_{meas}}{1 + (\varepsilon \times 2)} \quad . \tag{2.15}$$

The ^{238}U and ^{234}U concentrations in activities per gram (dpm g^{-1}) may then be determined using the isotope dilution approach (Section 2.5.2), with corrections for the contributions from the spike.

Thorium

Measurements of thorium samples are conducted in four stages:

1. *Memory measurement*: this is a measurement made before the sample is introduced but when 2% nitric wash is passing through the system. The collector configuration is the same as for the sample measurement.
2. *Sample measurement*: this also includes a measurement of the background (i.e. the values registered by the collectors when they are isolated from any beam - the 'zero' point).
3. *Abundance sensitivity measurement*: made using the sample solution, in multiple configurations.
4. *Gain Measurement*: evaluates the difference in sensitivity between the ion counter and the Faraday collectors using the standard.

The thorium sample measurement is conducted in a two-step routine. This is because the ion counters are separated by the equivalent of two mass units, whilst two of the isotopes of interest ^{229}Th and ^{230}Th are of low concentration (and therefore best measured using an ion counter) but are only one mass unit apart. A measurement of ^{232}Th is made in both steps and used to normalize the ^{230}Th/^{229}Th ratio between steps. The ^{232}Th concentration is matched between standards and samples and diluted such that the ^{232}Th is roughly equivalent to 9 V on the Faraday collector. Thorium standards were run as 'dummy' samples to assess the reproducibility of the measurements.

Abundance sensitivity resulting from the 'tail' of the ^{232}Th beam is internally assessed and corrected for by measurement of the beam 1/2 amu above and below both ^{229}Th and ^{230}Th in IC(-3), and measurement of the ^{232}Th beam as a reference beam.

The isotopes ^{229}Th and ^{230}Th are both measured in an ion counter and therefore no correction is required for relative gain between the detectors (see Relative Gain). However, ^{232}Th is also of interest as it is used for correcting for the detrital component of $^{230}Th_{xs}$. ^{232}Th is measured in a Faraday cup. To account for the relative gain (and mass bias), a separate gain measurement is made externally using the standard CRM-145. The use of a uranium standard for the gain correction allows measurement of the gain directly before further thorium analysis with a reduced potential for memory effects [*Thomas et al.*, 2006]. The standard is measured with ^{235}U directed into a Faraday cup, F(-2). In this configuration, ^{234}U falls in the ion counter, IC(-3) and ^{238}U in F(+1). The known ratios of $^{238}U/^{235}U$ and $^{235}U/^{234}U$ in the CRM-145 standard (Table 2.2) are then used to correct the relative sensitivities of the ion counter and Faradays.

The ^{230}Th and ^{232}Th concentrations in activities per gram (dpm g^{-1}) may then be determined using the isotope dilution approach (Section 2.5.2), with corrections for the contributions from the spike.

Blanks

Total procedural blanks were run along side all uranium and thorium samples (Table 2.5). An empty Teflon beaker was used as the blank in all cases. Some of the thorium blank contamination is attributable to initial preparation of the samples outside of the clean lab. The uranium blanks are typically ∼0.03% of the uranium in the sample, whilst the thorium blanks contribute ∼0.01% with respect to the sample thorium.

Run Date	Blank #	Hole	^{238}U (pg)	2σ	^{232}Th (pg)	2σ	^{230}Th (pg)	2σ
13/04/10	Blank 1	1062E	58.91	1.28	117.00	108.21	3.98	3.96
06/08/10	Blank 2	1062E	110.00	0.89	61.90	50.06	0.07	0.08
		—–Department move——						
16/01/13	Blank 1	1061B	67.10	0.54	47.30	36.52	-0.79	-0.70
16/01/13	Blank 2	1061B	66.60	0.54	17.30	7.47	-0.88	-0.54
		Pre-move average:	84.45	1.08	89.45	79.14	2.02	2.02
		Post-move average:	66.85	0.54	32.30	21.99	0.83	0.62
		Compilation Average:	75.65	0.81	60.88	50.56	1.14	1.06

Table 2.5: Table showing the total procedural blanks run along side sediment samples.

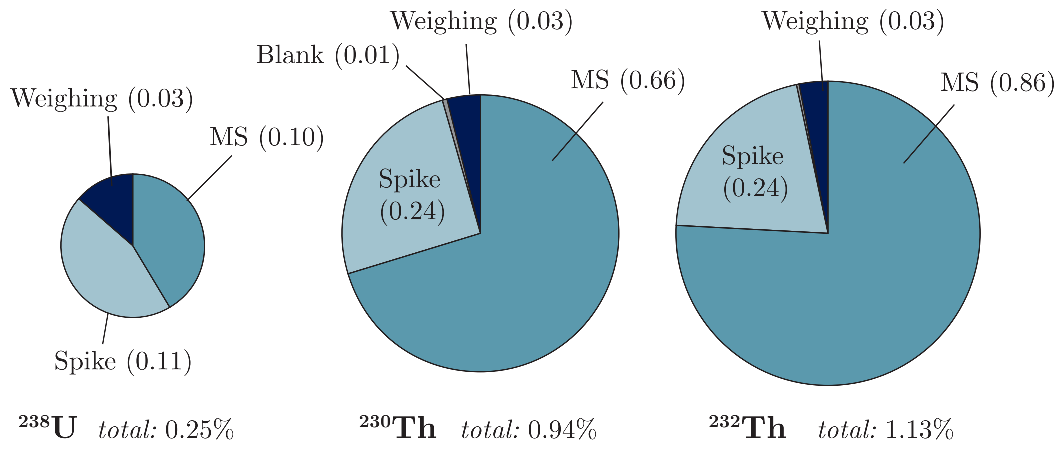

Figure 2.7: Uncertainty budget for measurement of uranium and thorium concentrations, where MS (Mass Spectrometry) is the uncertainty attributable to the uncertainty associated with the raw measurement and corrections made to account for biasing effects of the mass spectrometer. All values are given in percentage 2σ.

Uncertainties

The uncertainty budgets for the concentrations of ^{238}U, ^{230}Th and ^{232}Th, derived by the above methods, are shown in Figure 2.7. The average total uncertainties (2σ) are 0.25% for ^{238}U, 0.94% for ^{230}Th, and 1.13% for ^{232}Th. Due to the high concentrations of uranium and thorium in the sediment samples, the blank uncertainty is negligible (contributing 0.0002% uncertainty for ^{238}U, 0.006% for ^{230}Th, and 0.002% for ^{232}Th). In any case, the contribution of the uncertainty in the concentrations derived by mass spectrometry to the total uncertainty in the derived relative sedimentation rate are much smaller than those attributable to the supplied absolute age constraints.

2.6 Summary

The methods outlined above provide the data required to fulfil the principal aims of (i) retrieving the palaeomagnetic record of the geomagnetic field (ii) characterizing the palaeomagnetic properties of the sediments and (iii) determining an age model for the palaeomagnetic measurements. The measurements of uranium and thorium isotope concentrations in the sediment samples provide the means by which we may make determinations of the different components of the ^{230}Th, including ^{230}Th$_{xs}$. The ^{230}Th$_{xs}$ may then be used to determine relative variations in sedimentation rate. The calculations by which the sedimentation rate may be derived are discussed in Chapter 3.

Chapter 3

Improving ^{230}Th$_{xs}$ Normalization

This chapter appears in a modified form as:

'Bourne, M. D., Thomas, A. L., Mac Niocaill, C., Henderson, G. M., [2012b]. Improved determination of marine sedimentation rates using ^{230}Th$_{xs}$. *Geochemistry Geophysics Geosystems*, 13, Q09017.'

3.1 Introduction

Measurements of excess ^{230}Th (^{230}Th$_{xs}$) have proved to be a useful tool in constraining changes in sedimentation rate, and improving our understanding of the fluxes of other components into marine sediments. Using the uranium and thorium activities determined by mass spectrometry (see Section 2.5.3) we can calculate ^{230}Th$_{xs}$ and determine relative variations in sedimentation rates.

To obtain the initial activity of ^{230}Th$_{xs}$ (^{230}Th$^{0}_{xs}$) in sediment, the total measured ^{230}Th must be corrected for the presence of ^{230}Th associated with detrital minerals, for ingrowth from uranium-bearing authigenic phases and then also corrected for the decay of ^{230}Th$_{xs}$ since deposition. This chapter describes a number of improvements in the way these corrections are applied to obtain more accurate determinations of ^{230}Th$^{0}_{xs}$: presenting a new method for the determination of a local estimate for the detrital ^{238}U/^{232}Th activity ratio; suggesting more appropriate values for the isotopic composition of authigenic uranium; and questioning the assumption of secular equilibrium in detrital material.

This chapter also describes a new, MATLAB® program called 'XSage' that can calculate ^{230}Th$^{0}_{xs}$, from user-supplied datasets of uranium and thorium isotope activities from sedimentary samples following the theoretical approach described. 'XSage' can determine variations in sedimentation rate between stratigraphic horizons of known age and thus produce high-resolution age models. Using a Monte Carlo approach, the program calculates uncertainties for these age models and on the durations of intervals between tie-points. Data measured for the study of the Blake excursion (see Chapter 4) is used to demonstrate the application of the XSage program.

3.2 Approach & Assumptions of ^{230}Th$_{xs}$ as a Constant Flux Proxy

To calculate the ^{230}Th$_{xs}$ contribution to the measured total ^{230}Th concentration in deep-sea sediment, corrections for other sources of ^{230}Th must be made. These comprise ^{230}Th associated with detrital material (^{230}Th$_{det}$) and that produced in the sediment by the decay of authigenic uranium, added to the sediments shortly after sedimentation in reducing environments (^{230}Th$_{auth}$) [see Section 1.8.3 and *Francois et al.*, 2004; *Henderson and Anderson*, 2003]. Because ^{230}Th is radioactive, the calculated ^{230}Th$_{xs}$ must also be corrected for its own decay to give the ^{230}Th$_{xs}$ at the time of deposition (^{230}Th$^{0}_{xs}$):

$$^{230}\mathrm{Th}^{0}_{xs} = e^{\lambda_{230}t} \times \left[^{230}\mathrm{Th}_{meas} - ^{230}\mathrm{Th}_{det} - ^{230}\mathrm{Th}_{auth}\right] \quad , \tag{3.1}$$

where λ_{230} is the decay constant of ^{230}Th and t is the age of the sediment.

Corrections for detrital and authigenic sources of ^{230}Th rely on a number of assumptions. The following sections outline the conventional approach to calculating and using determinations of $^{230}Th_{xs}$ and the assumptions typically required to calculate $^{230}Th_{xs}$.

3.2.1 Determination of $^{230}\mathbf{Th}_{det}$

Detrital ^{230}Th is that locked in the mineral lattices of lithogenic particles within the sediment [*Chabaux*, 2003]. To calculate $^{230}Th_{det}$, the ^{232}Th content of the sediment is assumed to come entirely from detrital material in the sediment and the activity of uranium associated with this detrital component is calculated using an assumed $^{238}U/^{232}Th$ for the detrital material, $(^{238}U/^{232}Th)_{det}$. An assumption is then made that detrital ^{230}Th is in secular equilibrium with this uranium such that $^{238}U_{det}{=}^{230}Th_{det}$ [*Francois et al.*, 2004; *Henderson and Anderson*, 2003]:

$$^{230}Th_{det} =^{238} U_{det} = (^{238}U/^{232}Th)_{det} \times^{232} Th_{meas} \quad . \tag{3.2}$$

Here and throughout this chapter, all references to isotopic values and ratios are given as activities (see Section 1.8.1).

3.2.2 Determination of $^{230}\mathbf{Th}_{auth}$

^{230}Th is also produced from the decay of authigenic U that is either adsorbed on oxides or precipitated in anoxic or subanoxic sediments after diffusion from bottom waters [*Klinkhammer and Palmer*, 1991]. Any ^{238}U not accounted for by the detrital component is assumed to be authigenic uranium [*Henderson and Anderson*, 2003]. By assuming that that the incorporation of authigenic uranium occurs at the time of sediment deposition, at a 'known' $^{234}U/^{238}U$ ratio, and that the authigenic uranium has not subsequently been lost from the sediment (e.g. via oxidation and subsequent dissolution) we may determine the amount of ^{230}Th produced by the decaying authigenic uranium. As the initial authigenic uranium is not in secular equilibrium (i.e. $^{234}U \neq^{238} U$), the correction accounts for the ^{230}Th produced by the decay of the component of ^{234}U in secular equilibrium and the ^{230}Th produced by the decay of the excess component of ^{234}U above the equilibrium value:

$$^{230}\mathrm{Th}_{auth} = \left(^{238}\mathrm{U}_{meas} - ^{238}\mathrm{U}_{det}\right) \times \left[\left(1 - e^{-\lambda_{230}t}\right) + \frac{\lambda_{230}}{\lambda_{230} - \lambda_{234}}\left(\left(\frac{^{234}\mathrm{U}}{^{238}\mathrm{U}}\right)_{init} - 1\right)\left(e^{-\lambda_{234}t} - e^{-\lambda_{230}t}\right)\right] \quad . \tag{3.3}$$

where $(^{234}\mathrm{U}/^{238}\mathrm{U})_{init}$ is the initial ^{234}U/^{238}U ratio of the authigenic uranium, assumed to be that of seawater (=1.147).

3.2.3 ^{230}Th$_{xs}$ Normalization Approach

The calculated ^{230}Th$^{0}_{xs}$ may be used in two, subtly different, ways. The first uses the measured ^{230}Th$^{0}_{xs}$ values as a vertical flux proxy. The flux of other components from the water column into marine sediments can be assessed by measuring their concentration relative to that of ^{230}Th$^{0}_{xs}$ and by assuming that the measured ^{230}Th$^{0}_{xs}$ is equal to its production in the overlying water column. This approach gives an estimate for the instantaneous flux for that component at the time that the measured sediment was laid down. It has been used, for example, to assess changing fluxes of ice-rafted debris into North Atlantic sediments during Heinrich events [*McManus et al.*, 1998] and to assess the changing fluxes of windblown dust from the Sahara during the Holocene [*Adkins et al.*, 2006].

A critical assumption of the above is that there is minimal lateral movement of ^{230}Th in the water column. This appears reasonable based on sediment trap [*Yu et al.*, 2001] and modelling [*Henderson et al.*, 1999] studies, although it has been questioned recently based on sediment thicknesses observed from seismic data [*Lyle et al.*, 2005]. Furthermore, at some locations, lateral movement of ^{230}Th in the water column can be more than 30% of a water column's production [*Henderson et al.*, 1999].

The second, alternative approach is to use the concentration of ^{230}Th$^{0}_{xs}$ in the sediment to determine relative variations in total sedimentation rate between tie-points. In the ideal case, the concentration of $^{230}\text{Th}^0_{xs}$ in the sediment is expected to be inversely proportional to the sedimentation rate: the higher the sedimentation rate, the lower the concentration of $^{230}\text{Th}^0_{xs}$, the sediment effectively 'diluting' the $^{230}\text{Th}^0_{xs}$, supplied at a constant rate from the overlying water column. The relative variation in sedimentation rate is calculated using relative variations in concentration of $^{230}\text{Th}^0_{xs}$ to modify an average sedimentation rate determined between stratigraphic tie-points of known age. In this approach, the sedimentation rate for each depth interval is calculated using the following expression:

$$\text{F}_n = \text{F}_a \times \frac{\overline{\text{Th}}}{\text{Th}_n} \quad . \tag{3.4}$$

where F_n is the sedimentation rate for the sample interval; Th_n is the concentration of $^{230}\text{Th}^0_{xs}$ in that sample interval; F_a is the average sedimentation rate in cm kyr^{-1} between the tie-points; and $\overline{\text{Th}}$ is the depth-interval-weighted average concentration of $^{230}\text{Th}^0_{xs}$ between the tie-points. In practice, the dated tie-points will also have associated uncertainties, potentially in both depth and age. This approach has been used in the past to determine the durations of short geomagnetic events [*Knudsen et al.*, 2007].

Using $^{230}\text{Th}^0_{xs}$ in this second way, to constrain relative sedimentation rates, requires an additional assumption that sediment focussing throughout the interval of interest is constant. It is therefore important that the sedimentary environment remained broadly constant between the tie-points used by the $^{230}\text{Th}_{xs}$ normalization. Independent methods must be used to check that potential variation in focusing is minimal relative to changes in sedimentation rate, such that the uncertainty introduced by focusing does not obscure any variation in the sedimentation rate. Such independent methods might include: sortable silt analysis to assess changes in sediment transport [e.g. *McCave and Hall*, 2006; *McCave et al.*, 1995]; measuring the magnetic properties of the sediment to investigate potential variations in grain size [e.g. *Banerjee et al.*, 1981; *Stanford et al.*, 2011]; or physical inspection of core material to assess changes in sediment type. The use of intermediate tie-points or stratigraphic analysis, whereby variation in focusing can be constrained between multiple dated stratigraphic intervals, may also provide some indication of whether focusing is variable at a site with time or changes in climate.

3.2.4 Summary of Assumptions

In summary, either approach using $^{230}Th_{xs}$ relies on five principal assumptions:

1. An assumed $(^{238}U/^{232}Th)_{det}$ in detrital material.
2. Detrital material is in secular equilibrium $^{238}U_{det}$=$^{230}Th_{det}$.
3. Authigenic U has an initial $^{234}U/^{238}U$ of seawater (=1.147), forms at time of sediment deposition, and does not dissolve or mobilize in the sediment column.
4. No lateral transport of ^{230}Th in the water column.
5. A known age model with accurately dated tie-points.

If relative variation in $^{230}Th^{0}_{xs}$ is to be used to constrain relative variations in sedimentation rate then this requires a further assumption that:

6. Sediment focusing is constant between tie-points.

Note also that because the variation in sedimentation rate is derived from relative variation in $^{230}Th^{0}_{xs}$, assumption (4) may be modified to 'no *change in* lateral transport of ^{230}Th in the water column' when assessing relative sedimentation rate changes.

In this chapter, I will discuss uncertainties in the first three of these assumptions, and describe a piece of new, freely-available MATLAB® software, 'XSage', that enables the user to insert appropriate uncertainties into a self-consistent calculation of $^{230}Th^{0}_{xs}$ and sedimentation-rate histories from Th and U measurements, also taking into account uncertainties in the input linear age model. The XSage model is designed principally to improve the use of $^{230}Th_{xs}$ data to refine changes in sedimentation rates between tie-points, but it also has potential to improve the use of $^{230}Th_{xs}$ as a constant-flux proxy.

3.3 Addressing the Assumptions of $^{230}Th_{xs}$ as a Constant Flux Proxy

3.3.1 $(^{238}U/^{232}Th)_{det}$ in Detrital Material

The assumption of known $(^{238}U/^{232}Th)_{det}$ often involves the use of 'appropriate' basin wide ratios [e.g *Henderson and Anderson*, 2003], which may lead to systematic inaccuracies where the local sediment differs from the assumed value.

A more localized estimate of $(^{238}U/^{232}Th)_{det}$ may be achieved if the absence of authigenic uranium can be identified at some depths in the measured core. Measured $^{238}U/^{232}Th$ at these depths can then be assumed to represent the detrital end member. Identification of sediment with no authigenic uranium can be made if the $^{234}U/^{238}U$ of the sediment is measured, as is commonly the case. Incorporation of authigenic uranium into sediment will elevate the $^{234}U/^{238}U$ above 1, due to the excess ^{234}U in seawater and sediment porewater [*Ku*, 1965; *Robinson et al.*, 2004]. The $^{238}U/^{232}Th$ of samples with $^{234}U/^{238}U$ less than 1 may therefore be used to provide a better constraint on the local $(^{238}U/^{232}Th)_{det}$. XSage follows this new approach by allowing the user the option to identify sediment samples without an authigenic uranium component. These samples are then used to estimate the local $(^{238}U/^{232}Th)_{det}$ based on their $^{234}U/^{238}U$ ratios and determine an appropriate uncertainty.

3.3.2 Is Detrital Material in Secular Equilibrium?

Some deep-sea sediments have $^{234}U/^{238}U$ below 1 [*Ku*, 1965]. This observation indicates that the assumption that the detrital component is in secular equilibrium (i.e. $(^{234}U/^{238}U)_{det} = 1$) is invalid. $^{234}U/^{238}U$ measured in marine sediments can be as low as ~ 0.96 due to the loss of roughly 4% of the daughter ^{234}U from the sediment grains by alpha-recoil [*DePaolo et al.*, 2006; *Ku*, 1965]. The $^{230}Th/^{238}U$ in such sediment,

$(^{230}Th/^{238}U)_{det}$, is therefore likely to be even lower. Assuming that a further 4% of daughter ^{230}Th is lost because of the second alpha decay involved in the formation of ^{230}Th, $(^{230}Th/^{238}U)_{det}$ could be as low as 0.92 (i.e. 1×0.96^2). We therefore propose a modification to the detrital correction, where $\sim 0.96 \pm 0.04$ (i.e. the range 0.92-1.00) is the value for $(^{230}Th/^{238}U)_{det}$:

$$^{230}Th_{det} = (\sim 0.96 \pm 0.04) \times (^{238}U/^{232}Th)_{det} \times ^{232}Th_{meas} \quad . \tag{3.5}$$

This modification to the calculation of $^{230}Th_{det}$ assumes that the disequilibrium of $(^{230}Th/^{238}U)_{det}$ is maintained through time and does not evolve either towards secular equilibrium, or to lower values by additional recoil loss. That the authigenic component may have $^{234}U/^{238}U$ elevated above that of seawater (see below) indicates that recoil products may well be lost from detrital phases and hence that return to secular equilibrium is unlikely, although further disequilibrium cannot be ruled out. Therefore, the potential for bias on $^{230}Th^0_{xs}$ normalization between age tie points will be limited but accumulation rates calculated independently of tie-points and comparisons between sites may be affected. XSage allows the user to specify the degree of disequilibrium with an associated uncertainty but uses a default value of 0.96 ± 0.04 for $(^{238}U/^{232}Th)_{det}$.

3.3.3 Authigenic $^{234}U/^{238}U$

Addition of authigenic uranium to a detrital end-member should follow a simple mixing relationship (Figure 3.1). Typically the authigenic end-member is assumed to have a $(^{234}U/^{238}U)_{init}$ ratio equal to that of seawater (=1.147) [*Andersen et al.*, 2010; *Robinson et al.*, 2004]. To investigate this assumption, we revisit a down-core ^{230}Th record that was measured from the south-western Indian Ocean to reconstruct the history of deep water flow into that basin over the last 140 kyr [*Thomas et al.*, 2007]. This core, WIND 28K, was collected during RRS Charles Darwin cruise CD129 at 51°46'E 10°9'S, in 4157 m

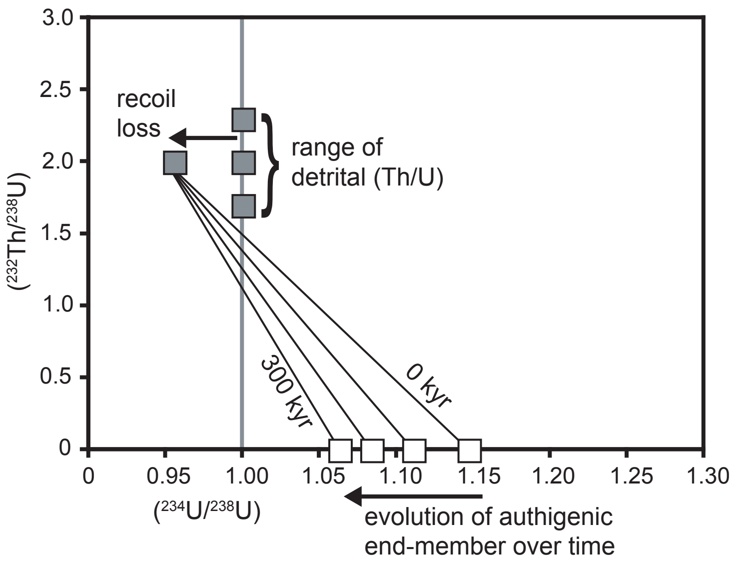

Figure 3.1: Detrital components (grey squares) shown schematically with uranium isotopes at secular equilibrium (grey line) and after recoil loss, with a $^{234}U/^{238}U$ ratio of 0.96. The authigenic component (white squares), consisting of uranium only, initially has a seawater $^{234}U/^{238}U$ of 1.147 (at 0 kyr) but evolves over time after deposition as the excess ^{234}U decays. Multiple mixing lines show the expected evolution through time of the relationship between the detrital component and the evolving authigenic component.

water depth.

Down-core data from WIND 28K are not well described by mixing lines based on assumed $^{234}U/^{238}U$ at seawater values (Figure 3.2). Better agreement to the data is possible if the authigenic component has $^{234}U/^{238}U$ higher than seawater. This additional excess ^{234}U could be due to the maintenance of a $^{234}U/^{238}U$ deficit in the detrital phase and thus higher $^{234}U/^{238}U$ in sediment pore waters than in seawater. This is supported by $^{234}U/^{238}U$ activity ratios of pore water from ODP Site 984A in the North Atlantic, which have higher than seawater values, in the range 1.2-1.6 [*Maher et al.*, 2004]. The observation of $^{234}U/^{238}U$ greater than 1.147 in the authigenic phase in WIND 28K and in pore waters from ODP Site 984A raises the possibility that this feature may occur more generally. It may therefore be appropriate to use a $(^{234}U/^{238}U)_{init}$ value greater than 1.147 in Equation 3.3.

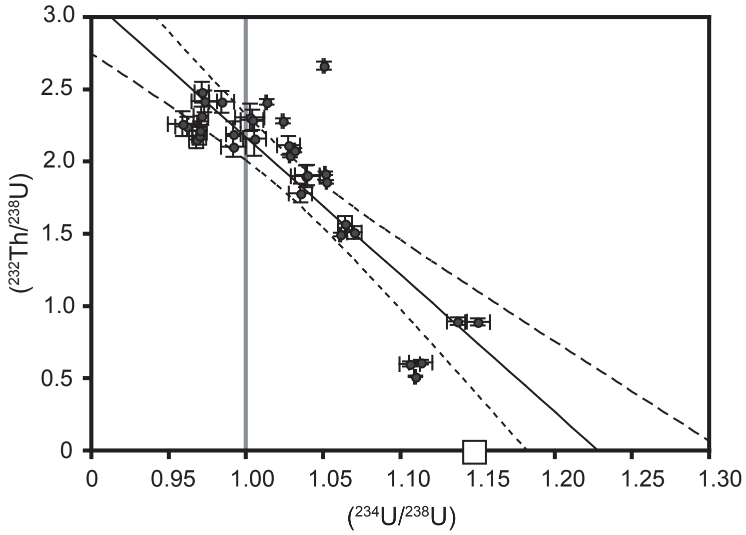

Figure 3.2: Down core data from the 140 ka WIND 28K record from the Indian Ocean [*Thomas et al.*, 2007] (dark grey circles). Best-fit mixing line (black line with dashed lines indicating 2σ uncertainty) suggests that an authigenic component with $^{234}U/^{238}U$ equal to that of seawater (= 1.147, white square) is inappropriate and that the $^{234}U/^{238}U$ of the authigenic component is likely to be greater than that of seawater.

The impact of a higher $(^{234}U/^{238}U)_{init}$ on the $^{230}Th^0_{xs}$ correction will be to increase the apparent $^{230}Th_{auth}$ component for samples which have a significant authigenic uranium content. This correction will become increasingly important as sample age increases. For samples where the relative $^{230}Th^0_{xs}$ content is lower (shallower core depths, higher authigenic uranium) these additional corrections may become significant. XSage provides an opportunity to choose an appropriate value for $(^{234}U/^{238}U)_{init}$ with an associated uncertainty.

3.4 The XSage Model Approach

The uncertainty on the $^{230}Th_{xs}$ activity in any one sample is dependent upon the uncertainty of the measured uranium and thorium activities as well as upon the assumptions used to determine the proportion of the total sample ^{230}Th accounted for by $^{230}Th_{det}$ and

^{230}Th$_{auth}$.

1. The uncertainty on ^{230}Th$_{det}$ is controlled by the uncertainties associated with the assumed (^{238}U/^{232}Th)$_{det}$ activity ratios and the degree to which the detrital material is thought to be in secular equilibrium.

2. The uncertainty on any authigenic component, ^{230}Th$_{auth}$; is dependent upon the detrital component ^{238}U$_{det}$; on the assumed value for (^{234}U/^{238}U)$_{init}$; and the time since sediment deposition.

3. In all cases, corrections for decay of ^{230}Th$_{xs}$ since deposition mean that the uncertainty on the age of the sample (which is dependent upon the ages and depths, and associated uncertainties, of the tie-points) plays a role in the final uncertainty on the ^{230}Th$^0_{xs}$ activity of the sample.

In each case the relative importance of each input uncertainty is not only dependent upon the size of the input uncertainties themselves but also on the relative proportions of the three thorium components in the sample's total ^{230}Th. Furthermore, if the ^{230}Th$^0_{xs}$ activity is used as a modifier on the average sedimentation rate, to obtain variations in sedimentation rate between tie-points, and hence on the age model, each calculated sedimentation rate from a single sample is dependent upon the ^{230}Th$^0_{xs}$ activities of all the samples, as well as the average linear sedimentation rate determined from the ages and depths of the tie-points.

The complexity and inter-dependence of the various equations therefore makes the use of classical error propagation difficult when attempting to determine the uncertainty on calculated sedimentation rates, age models and interval durations. Instead, the XSage MATLAB® script uses a Monte Carlo iterative approach to calculate a range of possible answers and subsequently determine average values for the final ^{230}Th$^0_{xs}$ activities, sedimentation rates, and ages, with estimates of all their associated uncertainties.

3.4.1 Description of Program

When using XSage, the user supplies measured ^{238}U, ^{230}Th and ^{232}Th (and optionally ^{234}U) activities for samples from the interval of interest. Using tie-points of known depth and age and user-defined ratios of $(^{238}U/^{230}Th)_{det}$ and $(^{238}U/^{232}Th)_{det}$ and $(^{234}U/^{238}U)_{init}$ (see Equations 3.3 and 3.5), the script can then calculate for each sample depth: the detrital component, $^{230}Th_{det}$; the component formed by the decay of authigenic uranium (if present), $^{230}Th_{auth}$; and the initial excess component, $^{230}Th^0_{xs}$.

Using the relative variation in the calculated $^{230}Th^0_{xs}$ between samples, the script then calculates the variations in sedimentation rate through the core relative to the average sedimentation rate (calculated from the tie-points). The normalized sedimentation rates are then also used to determine an age-depth relationship for the core section. $^{230}Th^0_{xs}$ is subsequently iteratively recalculated using the new age-model in the time-dependent corrections for decay.

3.4.2 Monte Carlo Method to Calculate Uncertainties

The Monte Carlo simulation models the inputs as probability distributions. For each iteration the script randomly samples appropriate values from the probability distributions for the measured ^{238}U, ^{230}Th and ^{232}Th activities of the samples, the ages and depths of the tie-points, and the user-defined values of the $(^{234}U/^{238}U)_{init}$, $(^{238}U/^{230}Th)_{det}$ and $(^{238}U/^{232}Th)_{det}$ activity ratios (see Equations 3.3 and 3.5). The measured activity ratios and user-defined ratios are modelled as Gaussian probability distributions using standard deviations provided by the user. The Monte Carlo simulation can optionally model the age and depths of the tie-points as 'top-hat' distributions whereby the uncertainties provided set the minima and maxima for the ages and depths and the probability of any value between the bounds is equally likely. Alternatively the ages and depths can be modelled as independent Gaussian probability distributions. When running the script, the user can specify the size of the uncertainties and which of the above may vary between each iteration (in order to better understand the error 'budget' of the final uncertainty). It should be recognised that any uncertainties calculated by the XSage script only capture the uncertainties in the calculations and supplied data and not the potential for unrecognised sedimentation rate variation due to under-sampling or the potential for variations in lateral redistribution of sediment and/or ^{230}Th. Thus uncertainty in focusing must be accounted for independently following the XSage calculation of the uncertainties associated with the measurements, tie-points and assumed ratios.

3.4.3 Output of Durations (Correlated Errors)

$^{230}Th^0_{xs}$-normalization is particularly useful for determining accurate ages and durations of events that have durations much shorter (i.e. thousand-year durations) than the resolution afforded by standard stratigraphical and chronological techniques such as oxygen isotope stratigraphy. XSage allows the user to specify intervals of particular interest. This is important as the uncertainty on the duration of any such interval of interest is not necessarily as large as that implied by the uncertainties on the ages of its two bounding depths. This is because the ages of the two depths are strongly correlated such that, for example, if one increases, it is likely that the other does too whilst the duration may not change significantly. If intervals of interest are specified then, to estimate the uncertainty on their duration, the duration of each interval is calculated during each iteration and the resulting answers are used to directly determine average durations and their uncertainty.

3.4.4 Example Calculations

Here I present an example, using measured uranium and thorium isotope activities in a marine core to demonstrate the utility of the XSage programme. In Chapter 4, measurements of $^{230}Th^0_{xs}$ (see Table 4.2) are used to determine relative sedimentation rates in a marine core from the Blake-Bahama Ridge (Ocean Drilling Program, Leg 172, Hole 1062E) [*Bourne et al.*, 2012a]. A record of thorium-normalized sedimentation rate is determined throughout Marine Isotope (MIS) Stage 5. Using the thorium-normalized sedimentation rates allows the determination of the duration of the Blake excursion, that occurred during MIS 5e. In the following, this data is used to demonstrate how XSage may be used to calculate normalized sedimentation rates and an age model with associated uncertainties.

Using XSage, we can compare the normalized sedimentation rates calculated firstly by the commonly applied approach, as described in Section 3.2, and then, secondly, using the modifications proposed in this paper in Section 3.3. In both cases, the linear age model is constrained by the same two dated boundaries obtained from oxygen isotope stratigraphy: the younger marks the transition from MIS 5 to MIS 4 at 13.64±0.35 metres below sea floor (mbsf), which is assigned an age of 72.0±1.5 ka; and the older age constraint, at 20.20±0.40 mbsf marks the transition from MIS 6 to MIS 5 and is assigned an age of 135.0±1.5 ka (see Section 4.3.3 and *Bourne et al.* [2012a]).

For our first calculation, we follow the standard approach and assume that the $(^{238}U/^{232}Th)_{det}$ ratio is equal to a basin-wide estimate of Atlantic detrital material of 0.6 ± 0.1 [*Henderson and Anderson*, 2003] and that the detrital material is in secular equilibrium such that $^{238}U_{det}$=$^{230}Th_{det}$. Lastly, we assume that $(^{234}U/^{238}U)_{init}$, the $^{234}U/^{238}U$ of any authigenic end-member, is equal to that of sea-water (1.147). Any corrections for decay use the linear time scale derived from the average sedimentation rate between the two tie-points.

For the second calculation, following the adjusted protocol of this paper, we use the mean $^{238}U/^{232}Th$ of samples with $(^{234}U/^{238}U)$ less than 1 to provide a better constraint on the local $(^{238}U/^{232}Th)_{det}$ and its uncertainty. These suggest 0.55 ± 0.16 to be a better estimate of the local $(^{238}U/^{232}Th)_{det}$. Alpha-recoil from detrital material is accounted for, as in Equation 3.5. In this case, a seawater value for $(^{234}U/^{238}U)_{init}$ of 1.147 appears to be a reasonable assumption for the authigenic end-member (Figure 3.3). Corrections for decay are made iteratively by XSage using thorium-normalized age models.

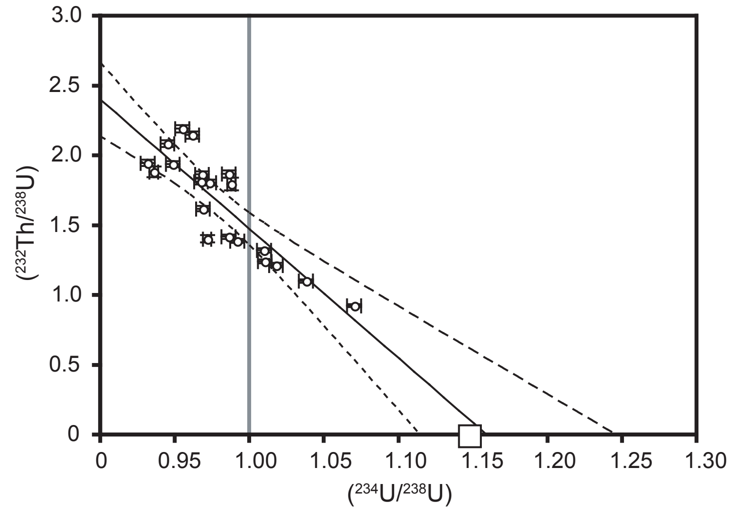

Figure 3.3: Down core data from ODP Hole 1062E from the Atlantic Ocean [*Bourne et al.*, 2012a] (white circles). The best-fit mixing line (black line with dashed lines indicating with 95% confidence intervals) suggests that an authigenic component with $^{234}\mathrm{U}/^{238}\mathrm{U}$ equal to that of seawater (= 1.147, white square) is appropriate in this case, in contrast to that shown in Figure 3.2.

For both calculations, XSage calculates each of the components that comprise the total $^{230}\mathrm{Th}$, including $^{230}\mathrm{Th}^0_{xs}$, as well as an age model determined using thorium-normalized sedimentation rates. For this core, the calculated $^{230}\mathrm{Th}^0_{xs}$ activities for each sample are similar in both calculations. The $^{230}\mathrm{Th}^0_{xs}$ activities differ by no more than 5% between the two approaches. The differences between the two sets of sedimentation rates are therefore also limited (~2%) (Figure 3.4). As a result, the age models for the two calculations are similar.

This similarity is principally due to the fact that, in this case, the concentration of $^{230}\mathrm{Th}^0_{xs}$ varies relatively little such that the thorium-normalized sedimentation rate does not vary significantly about the average sedimentation rate between the tie-points. Using the linear decay correction in the first calculation is therefore a reasonable approximation of the iterative calculation.

Previous published measurements have tended to avoid sediments where the authi-

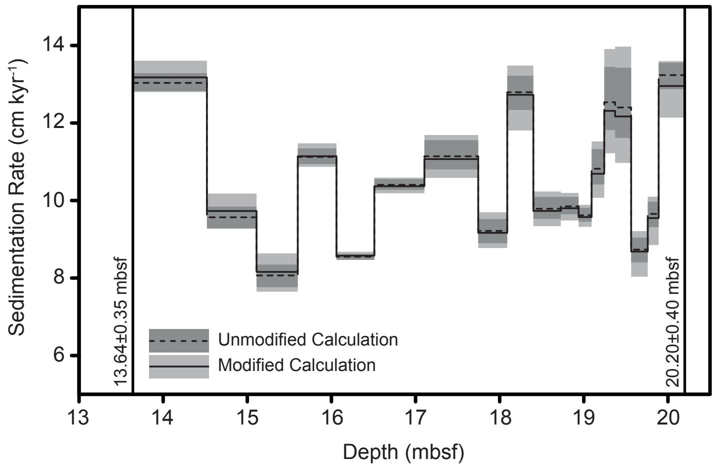

Figure 3.4: Thorium-normalized sedimentation rates calculated using XSage for ODP Hole 1062E [*Bourne et al.*, 2012a]. Results given, with 95% confidence intervals, for rates calculated using the unmodified approach (dashed line, dark grey band) and using the modified approach suggested in this paper (solid line, light grey band).

genic or detrital corrections amount to a significant proportion of the total ^{230}Th, because their associated uncertainties are poorly constrained. Therefore, the corrections are relatively minor. However, our revised approach, with better estimation of uncertainties, opens the possibility of using sites in the future where the authigenic correction is larger (where the age of the sediment is greater) or at sites with a larger detrital input.

XSage also provides uncertainties on all calculated values. This allows us to examine how the input uncertainties in our calculations propagate to the final answer. Compared to the traditional approach of the first calculation, the modified thorium excess approach takes into account more of the uncertainties associated with the thorium normalization method, in particular that associated with the potential for alpha-recoil from detrital material. As a result, the uncertainties on the sedimentation rates are increased by at least 50%, more accurately reflecting the uncertainties inherent in the calculation and its assumptions.

Thus, in any case, the revised approach does more accurately reflect the uncertainties in the method whether or not the absolute value for the $^{230}Th^0_{xs}$ changes significantly between the two calculations.

XSage is available for download at http://climotope.earth.ox.ac.uk/research/xsage, along with additional documentation. A manual for the use of XSage is included in this thesis in Appendix B.

3.5 Summary

Normalization using $^{230}Th^0_{xs}$ presents investigators with an opportunity to more accurately determine sediment fluxes and to better constrain age models. This chapter suggests a number of improvements to the corrections applied to the total measured ^{230}Th used to obtain $^{230}Th^0_{xs}$ activities:

1. The determination of a localized estimate of $(^{238}U/^{232}Th)_{det}$ by identifying samples that are unlikely to contain authigenically derived uranium (those in which $^{234}U/^{238}U$ is greater than 1) and taking the mean of their $^{238}U/^{232}Th$.
2. The assumption that the detrital component is in secular equilibrium is invalid. The detrital correction should be modified by a factor of 0.96±0.04 to account for the recoil of two alpha decays between ^{238}U and ^{230}Th.
3. The value for $(^{234}U/^{238}U)_{init}$ used in the correction for ^{230}Th derived from authigenic uranium may be higher than the 1.147 of seawater as evidenced by mixing lines from core data. This excess ^{234}U potentially arises from the maintenance of a $(^{234}U/^{238}U)$ deficit in the detrital phase.

Finally, the MATLAB routine 'XSage' allows the rapid calculation of $^{230}Th^0_{xs}$ activities using measured total uranium and thorium isotopic activities. It allows the calculation of sedimentation rates, age models and can produce an estimate and uncertainty on the duration of an individual horizon using a Monte Carlo approach. Furthermore it allows flexible and quick comparison between different approaches and assumptions.

Chapter 4

The Blake Excursion

This chapter appears in a modified form as:

'Bourne, M., Mac Niocaill, C., Thomas, A. L., Knudsen, M. F., and Henderson, G. M., [2012a] Rapid directional changes associated with a 6.5 kyr-long Blake geomagnetic excursion at the Blake-Bahama Outer Ridge. *Earth and Planetary Science Letters*, 333–334, 21–34.'

4.1 Introduction

The Blake excursion was first documented by *Smith and Foster* [1969] in seven deep-sea sediment cores from the Blake Outer Ridge in the western North Atlantic. It has since become commonly accepted as a global geomagnetic feature occurring between the Laschamp and Iceland Basin excursions [*Laj and Channell*, 2007]. However, whilst the Blake excursion is represented in many cores and palaeomagnetic records it remains one of the most ambiguous of the recent geomagnetic excursions. What is clear though is that, like other polarity transitions, the Blake excursion is associated with an interval of significantly reduced geomagnetic field intensity. Global relative palaeointensity stacks reveal a long duration interval of reduced palaeointensity lasting ($\sim$25 kyr), demonstrating that the excursion is an intrinsic feature of the global field [*Channell et al.*, 2009;

Frank et al., 1997; *Valet et al.*, 2005; *Ziegler et al.*, 2011].

Previous studies of the timing and duration of the Blake event are compiled in Table 4.1. Although the field intensity is well-constrained, estimates for the duration and timing of any directional deviation during the Blake excursion vary and the uncertainties are unconstrained. Radiometric dating of lavas suggest reversed directions at 123±7 ka [*Zhu et al.*, 2000] and 120±12 ka [*Singer et al.*, 2013] and a reef carbonate record places the beginning of a reversed event at 132.8±1.3 ka [*Ménabréaz et al.*, 2010] (Table 4.1). *Tric et al.* [1991] provide one of the most detailed marine records of a 'Blake' event (Fig. 4.1a), identifying a double event in a core from the Nile River Fan in the Eastern Mediterranean (following work by *Tucholka et al.* [1987]). Using oxygen isotope stratigraphy and tephrochronology, *Tric et al.* [1991] found the event within marine isotope stage (MIS) 5e and calculated an upper bound for the excursion's duration of 4.5 kyr.

However, even within the Mediterranean, cores suggest durations ranging from 3.5–8.6 kyr [*Tucholka et al.*, 1987]. This discrepancy is most likely the result of three factors: the potential for unrecognised variations in sedimentation rates between widely spaced age-constrained boundaries and the combined effects of limited resolution and significant magnetic remanence lock-in depths at low-sedimentation rates (< 10 cm kyr^{-1}) [*Roberts and Winklhofer*, 2004]. Palaeomagnetic records from cores on the Yermack Plateau in the Arctic suggested a relatively long duration of up to ∼10 kyr [*Nowaczyk et al.*, 1994]. However, these Arctic sediments have since been identified as potentially subject to a chemical remanent magnetization (CRM) that can result in self-reversal [*Channell and Xuan*, 2009] and thus these records are potentially unreliable.

Some of the previous records that suggest the most complex field behaviour during the Blake excursion, such as those of *Zhu et al.* [1994] and *Fang et al.* [1997], have been obtained from sections from the western Loess Plateau of China (Fig. 4.1b and c). In both of these records, the Loess appears to record multiple reversed periods with an

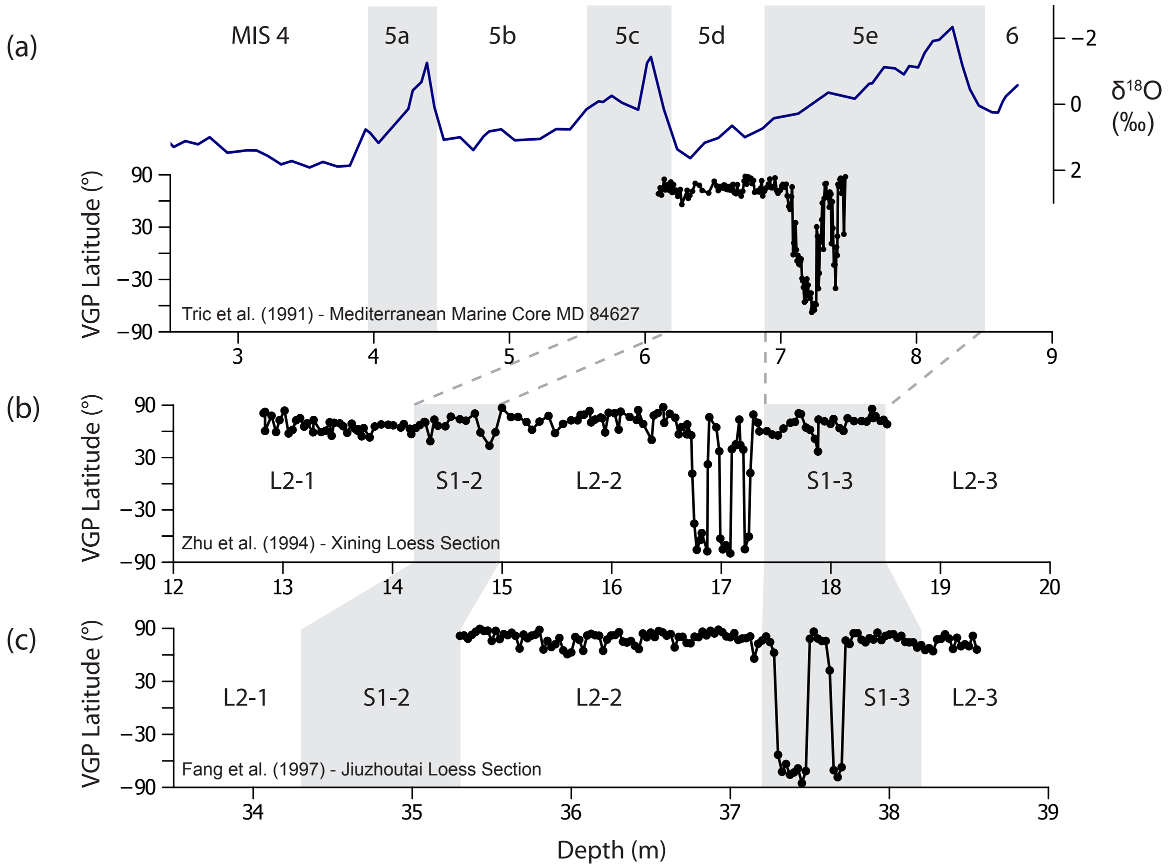

Figure 4.1: Three of the highest resolution records of the Blake excursion from the literature. (a) δ^{18}O stratigraphy for Mediterranean core MD 84627 with Marine Isotope Stages (MIS) identified, and below, the VGP latitude curve from the same core [*Tric et al.*, 1991]. (b) VGP latitude record from Xining Loess section, with palaeosol (grey bars) and loess stratigraphy correlated to MIS (dashed lines) [*Zhu et al.*, 1994]. (c) VGP latitude record for Jiuzhoutai Loess section and section stratigraphy [*Fang et al.*, 1997].

estimated total duration of ∼5 kyr. Yet dating loess records is not trivial; age models for loess rely on thermoluminescence dating and correlating palaeosol horizons and magnetic parameters with global isotope curves [e.g. *Evans and Heller*, 2001; *Fang et al.*, 1997; *Heslop et al.*, 2000; *Kukla et al.*, 1988]. The limited resolution of age models means that average sedimentation rates are used over relatively long intervals.

As noted by *Parés et al.* [2004], on examination the two Loess records are significantly different. Most importantly, the reversed directions appear in different stratigraphic horizons in the sections. *Zhu et al.* [1998] and *Parés et al.* [2004] demonstrated that there are ambiguities in the faithfulness of loess palaeomagnetic records of the Blake excursion after failing to find the event in many sections in the Chinese Loess Plateau. *Parés et al.* [2004] attribute the absence of the event to delayed magnetization acquisition and a previously unrecognised CRM. Similar difficulties have been faced in attempting to determine the timing of the Matuyama-Brunhes reversal in Chinese Loess [*Spassov et al.*, 2003]. In the face of these difficulties and inconsistencies, it is hard to be confident in either of the two loess records of the Blake and the field behaviour they describe.

More recently, *Osete et al.* [2012] have found a doubly-reversed event in a radiometrically dated speleothem from a cave in northern Spain. The age of the event is estimated here to be between 116.5±0.7 kyr and 112.0±1.9 kyr, younger than many of the estimates determined using astronomically-tuned sedimentary records.

Excursional field behaviour during the Blake excursion therefore remains ambiguous. A coherent global picture of the excursion is limited by the quality of previous records and the difficulties in dating marine records. It is difficult to discern whether previously observed anomalous directions within this period of low field intensity correspond to a global directional excursion feature or represent localised fluctuations apparent during a period of reduced dipole intensity.

Location	Medium*	Site	Lat.	Long.	Dating	Sed. Rate (cm kyr^{-1})	Duration (kyr)	Age / MIS (ka)	Principal Reference
New Mexico	B	Laguna Basalt	35.1	252.3	K/Ar	-	-	128±33	1
Hawaii	B	Hawaii	19.7	155.1	Ar/Ar	-	-	132±32	2
NE China	B	Jilin Province	42.1	128.0	Ar/Ar	-	-	123±7	3
Tahiti	RC	IODP310 M0005	17.8	-149.6	U/Th	-	-	133±1/5e	4
Xining, W China	L	Xining	36.6	101.8	TL*	9.8	5.3	5d	5
W. Plateau, China	L	Lanzhou	36.0	103.8	TL*	2	5.5	5e	6
Blake Ridge, Caribbean	MS	RC10-49	16.6	-79.5	d18O	3.4	5	-	7
Blake Ridge, Caribbean	MS	A179-4	16.6	-74.8	d18O	2.4	7	5e	7
E. Mediterranean	MS	MD84641	33.0	31.4	d18O	2.3	3.5	-	8
W. Mediterranean	MS	KET8004	39.7	12.4	d18O	6.4	8.6	5e/5d	8
W. Mediterranean	MS	KET8022	40.6	10.3	d18O	5.5	6.4	Spans 5e	8
E. Mediterranean	MS	MD84640	33.1	-32.9	d18O	8	4	end of 5e	8
E. Mediterranean	MS	MD84627	32.2	32.3	d18O	10.5	4.5	end of 5e	8,9
W. Mediterranean	MS	DED8707	39.7	-12.4	d18O	10.5	4	5e	9
Yermack Plateau, Arctic	MS	PS 1533-3 SL	82.0	15.2	d18O	2	10	Start 5e	10
Yermack Plateau, Arctic	MS	PS 2212-3 KAL	82.1	15.9	d18O	6	10	Start 5e	10
Amazon Fan	MS	ODP 942A/946A	5.7	-49.1	d18O	100	-	5e	11
Northern Spain	S	C8	43.0	-4.4	U-Th	0.7	4.5	114	12

Table 4.1: Age and duration estimates for the Blake Excursion. *B: Basalt, L: Loess, MS: Marine sediment, TL: Thermoluminescence dating and correlation using magnetic susceptibility. RC: Reef carbonate, S: Speleothem. References: (1) *Champion et al.* [1988], (2) *Holt and Kirschvink* [1996], (3) *Zhu et al.* [2000], (4) *Ménabréaz et al.* [2010] - note that date is the start of excursion, (5) *Zhu et al.* [1994], (6) *Fang et al.* [1997], (7) *Smith and Foster* [1969], (8) *Tucholka et al.* [1987], (9) *Tric et al.* [1991], (10) *Nowaczyk et al.* [1994], (11) *Cisowski and Hall* [1997] (12) *Osete et al.* [2012].

4.2 Study Site and Sampling

This chapter presents a new palaeomagnetic record of the Blake excursion, at the highest resolution yet achieved, using discrete samples obtained from Ocean Drilling Program (ODP) Site 1062 on the Bahama Outer Ridge (Fig. 4.2a, 28° 14.8'N, 74° 25.0'W). ODP Leg 172 has been invaluable in demonstrating the existence of multiple excursions during the Brunhes chron [*Lund et al.*, 1998, 2001a]. Using published shipboard long-core measurements for ODP Leg 172 [*Shipboard Scientific Party*, 1998a], three holes from the Bahama Outer Ridge were selected for this study (Site 1062, Holes B, D and E). A new high resolution chronology for the Blake excursion at Site 1062 is derived using $^{230}Th_{xs}$ measurements coupled to an oxygen isotope stratigraphy.

Discrete cubic samples (~7 cm^3 sample volume) were taken from the three holes at the ODP repository in Bremen. In all, 78 samples were taken from Hole 1062B (16.25–25.40 mbsf), 157 from Hole 1062D (10.37–34.08 mbsf) and 151 from Hole 1062E (8.50–27.53 mbsf). Within the excursional interval, sampling was undertaken at 2.5 cm intervals so that this record is virtually continuous. Considering the average sedimentation rate (~10 cm kyr^{-1}) the individual samples represent an average of 200 years.

4.3 Age Model

4.3.1 Composite Depth Scale

Although the three holes at Site 1062 are close to one another, gaps in recovery mean that a composite depth scale is required to compare equivalent intervals between them. The procedure employed shipboard to develop a composite depth scale links the holes using constant depth offsets at selected tie-points. [*Shipboard Scientific Party*, 1998b]. However, the limitation of using linear depth offsets is that not all prominent features within the individual holes are aligned. Within the interval studied here, correlation of decimetre-scale

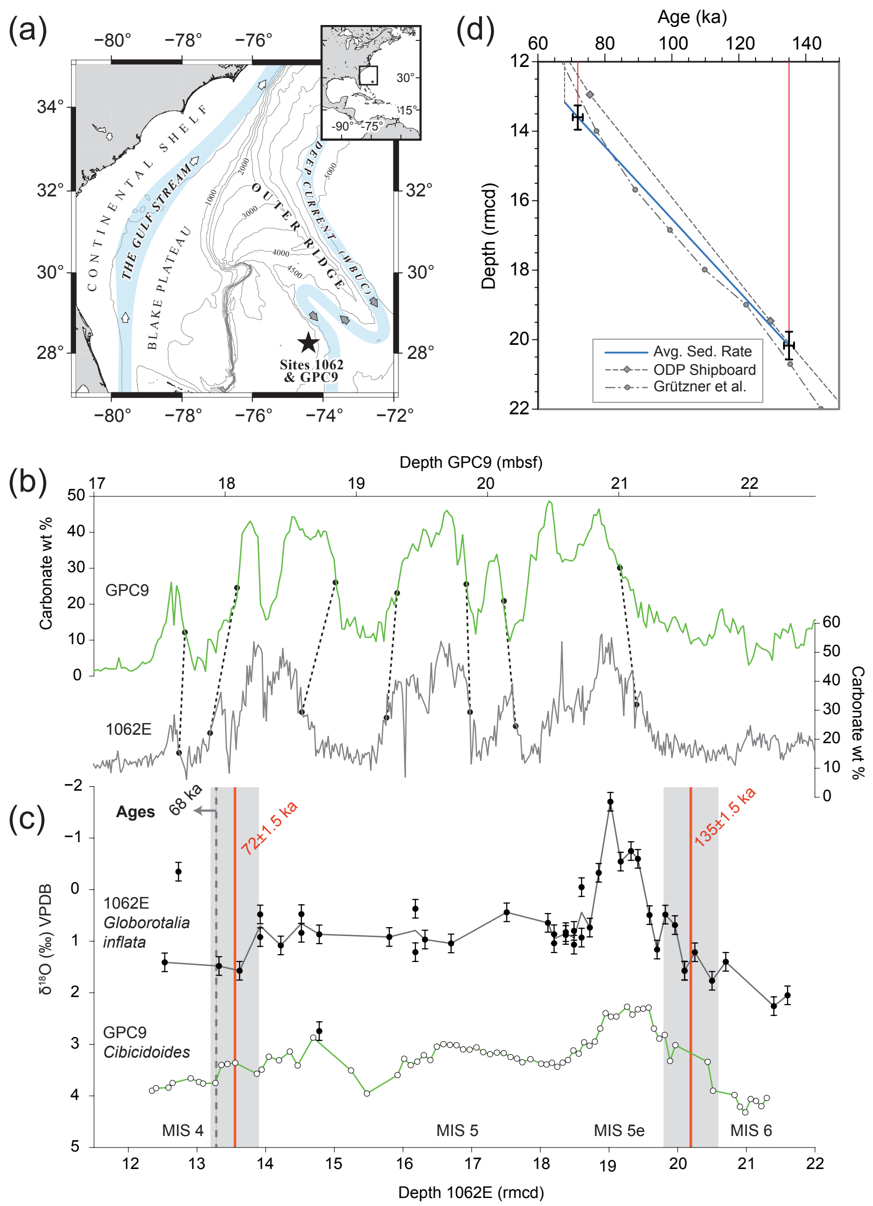

Figure 4.2: (a) Location of Site 1062 and GPC9 (WBUC - Western Boundary Undercurrent). Bathymetry data taken from 'The GEBCO One Minute Grid, version 2.0, http://www.gebco.net'. (b) Carbonate records from GPC9 [*Keigwin et al.*, 1994] and Hole 1062E [*Giosan et al.*, 2001]. Correlated features used as tie-points marked by grey dashed lines. 1062E Depth in 'rmcd' (see text) equivalent to metres below seafloor (mbsf). (c) Hole 1062E and GPC9 $\delta^{18}O$ records on Hole 1062E depth scale (rmcd). $\delta^{18}O$ measured with respect to the Vienna PeeDee Belemnite carbonate standard in delta notation (‰). Age constraints in the $\delta^{18}O$ stratigraphy for the MIS 6/5 & MIS 5a/4 transitions are marked in red with assumed depth uncertainties shown by the grey bars. Last appearance of *Globorotalia tumida flexuosa* (68 ka) marked with grey arrow. (d) Age-depth plot of Hole 1062E. Age constraints used in this study are marked in red. Solid blue line assumes average sedimentation between selected age constraints, dashed grey lines show previous age models [*Grützner et al.*, 2002; *Shipboard Scientific Party*, 1998a].

features in the shipboard magnetic susceptibility record was found to be poor. Thus, to determine the precise relationship between samples in neighbouring holes, a more refined correlation was developed across the studied interval. A new cross-correlation of the holes was created by comparing records of three sedimentological parameters measured shipboard that are independent of magnetic field direction: L*, a measure of the lightness of the sediment; gamma ray count; and magnetic susceptibility. Features in Holes 1062B and D are correlated to those in Hole 1062E. All subsequent depths from Holes 1062B, D and E are quoted in 'revised metres composite depth' (rmcd) which is their equivalent depth in Hoe 1062E (mbsf). Note therefore, that for Hole 1062E, 'rmcd' is the same as 'mbsf'.

4.3.2 Oxygen Isotope Stratigraphy

Age models for the holes exist from shipboard and later work but have been refined by two separate approaches for this study. In the absence of isotope data, *Grützner et al.* [2002] derived age models for the holes at Site 1062 by tuning variations of estimated carbonate content to the orbital parameters. Although variations in carbonate content show a first-order trend associated with glacial-interglacial cycles for some Leg 172 sites [*Chaisson et al.*, 2002], variance in sedimentological parameters may be affected by local, rather than global, factors.

To refine the chronology, two separate approaches are used in this study. We have cross-correlated Hole 1062E with a benthic δ^{18}O record in a neighbouring piston core, Knorr 31 GPC9 (28°14.7'N, 74°26.4'W, 4758 m) [*Keigwin et al.*, 1994] and measure a planktic δ^{18}O record in Hole 1062E itself.

Hole 1062E is correlated with Knorr 31 GPC9 using the variations in estimated carbonate content derived from diffuse spectral reflectance [*Giosan et al.*, 2001]. GPC9 has a measured carbonate content record and a measured oxygen isotope record from analyses of benthic foraminifera *Cibicidoides* spp. [*Keigwin et al.*, 1994] (Figure 4.2b). On the basis of our correlation between the two holes, the GPC9 benthic δ^{18}O record is placed on the Hole 1062E depth scale in Figure 4.2c.

To further confirm this δ^{18}O chronology, the oxygen isotopes of planktonic foraminifera from Hole 1062E were also measured. Following magnetic analysis, each sample was submerged in deionised water and mechanically agitated until suspension of the sediment was achieved. The sediment suspension was then sieved and the 63 μm fraction retained. This fraction was subsequently dried in an oven at 50°C. Specimens of the planktonic *Globorotalia inflata* were the most consistently present species throughout the studied hole interval and were therefore chosen for analysis. Benthic foraminifera were rare. Due to the small volume of sediment per sample ($\sim$7 cm^3), only a limited number of samples contained sufficient specimens for analysis. Oxygen isotope analyses were conducted using a Kiel IV attached to a Delta V isotope ratio mass spectrometer at the University of Oxford. All measurements are given in standard delta notation in per mil (‰) relative to the Vienna PeeDee Belemnite (V-PDB) carbonate standard. Isotopic values were related to the V-PDB standard by repeated measurements of National Bureau of Standards NBS-19 and NBS-18 (with δ^{18}O values of -2.2‰ and -23.2‰ respectively). Analytical precision for replicate standard measurements (n=13) of δ^{18}O in NBS-19, made concurrently with Hole 1062E analyses, was $\pm$0.09‰ (1σ).

In total, 53 samples from Hole 1062E were analysed. Three well-preserved specimens of *G. inflata* were used for each stable isotopic measurement and 10 samples were repeated to check the reproducibility of the results and assess the potential for seasonal bias. Two measurements, at 12.73 and 14.78 rmcd, were identified as anomalous and are probably the result of diagenetic alteration of fractured shells. These measurements were disregarded from further analysis. The results of the δ^{18}O analysis are shown in Figure 4.2c.

4.3.3 Chronology

Biostratigraphy conducted during the ODP expedition identified the last appearance of *Globorotalia tumida flexuosa* (68 ka) to be at a minimum depth of 13.23 rmcd in Hole 1062E [*Shipboard Scientific Party*, 1998a]. Using this biostratigraphic datum as a guide, we correlate the GPC9 and Hole 1062E oxygen isotope curves to the global record.

To construct the age model, two age-constrained boundaries are derived from the oxygen isotope records (Fig. 4.2c.). The younger age constraint, the transition from marine isotope stage (MIS) 5 to MIS 4 is placed at 13.64±0.35 rmcd. This value, with a conservative estimate for the uncertainty, encompasses the transition to more positive values in both the Hole 1062E and GPC9 δ^{18}O records. This depth is assigned an age of 72.0±1.5 ka [*Cutler et al.*, 2003; *Lisiecki and Raymo*, 2005]. For the older age constraint, the change to more negative isotopic values at 20.20±0.40 rmcd is correlated with the transition from MIS 6 to MIS 5 and is assigned an age of 135±1.5 ka [*Cheng et al.*, 2009; *Drysdale et al.*, 2009; *Henderson et al.*, 2001; *Kawamura et al.*, 2007; *Thomas et al.*, 2009]. The assigned ages and uncertainties represent the best estimates for these climatic transitions using published ages determined by uranium-series dating of carbonate material such as corals and stalagmites.

Although broadly consistent with the age-models determined on-board the ODP cruise ship [*Shipboard Scientific Party*, 1998a] and later by *Grützner et al.* [2002] (using variations in magnetic susceptibility and carbonate content respectively), the δ^{18}O stratigraphy reveals that the transition between MIS 5 and MIS 4 occurs a little deeper in the core (13.64±0.35 rmcd) than suggested by the carbonate content record (12.96 rmcd) (Fig. 4.2d.). The δ^{18}O transition between MIS 6 and 5 (20.20±0.40 rmcd) is consistent with that suggested by the carbonate record (20.58 rmcd).

4.4 Palaeomagnetic Methods & Results

All samples were subjected to stepwise alternating-field (AF) demagnetization at applied peak fields of 3, 6, 9, 12, 15, 20, 25, 30, 35, 40, 50, 60, 70, 80, 90 and 100 mT. All measurement and demagnetization steps were performed using a 2G Enterprises DC-SQUID cryogenic magnetometer with an in-line, triaxial, alternating field (AF) demagnetizer in a shielded room at the University of Oxford.

Typical orthogonal demagnetization diagrams of discrete samples from Holes 1062B, D and E are shown in Figure 4.3. The vast majority of samples displayed a steeply inclined remanent magnetization component which was typically removed from each sample by peaks fields between 9 and 25 mT. This is most likely an isothermal remanent magnetization (IRM) induced by exposure of the sediment to the magnetized steel core barrel during drilling. This is a common feature of samples from oceanic boreholes and was first noticed in Deep-Sea Drilling Project (DSDP) cores [*Ade-Hall and Johnson*, 1976].

Principal component analysis (PCA) was used to determine the characteristic remanent magnetization (ChRM). Following removal of the drilling-induced overprint, the majority of samples (80%) display a single, high-stability ChRM. Typically, less than 10% of the total remanence remained after application of the 80 mT peak field. These samples all had ChRMs with maximum angular deviation (MAD) values less than 5°. The high-stability component of magnetization determined suggests that the sediment retains an excellent record of past changes in field direction.

The remaining samples exhibited more complex behaviour; a few samples displayed a randomly oriented low intensity component of remanence that was easily removed by the lowest peak field, 3 mT. This was interpreted as a viscous overprint that was probably acquired during storage. A further group of samples also exhibited a component above 80-90 mT which appeared to have no preferred direction, accounting for 1-5% of the total remanence. At this level, the low signal to noise ratio obscures natural remanence directions.

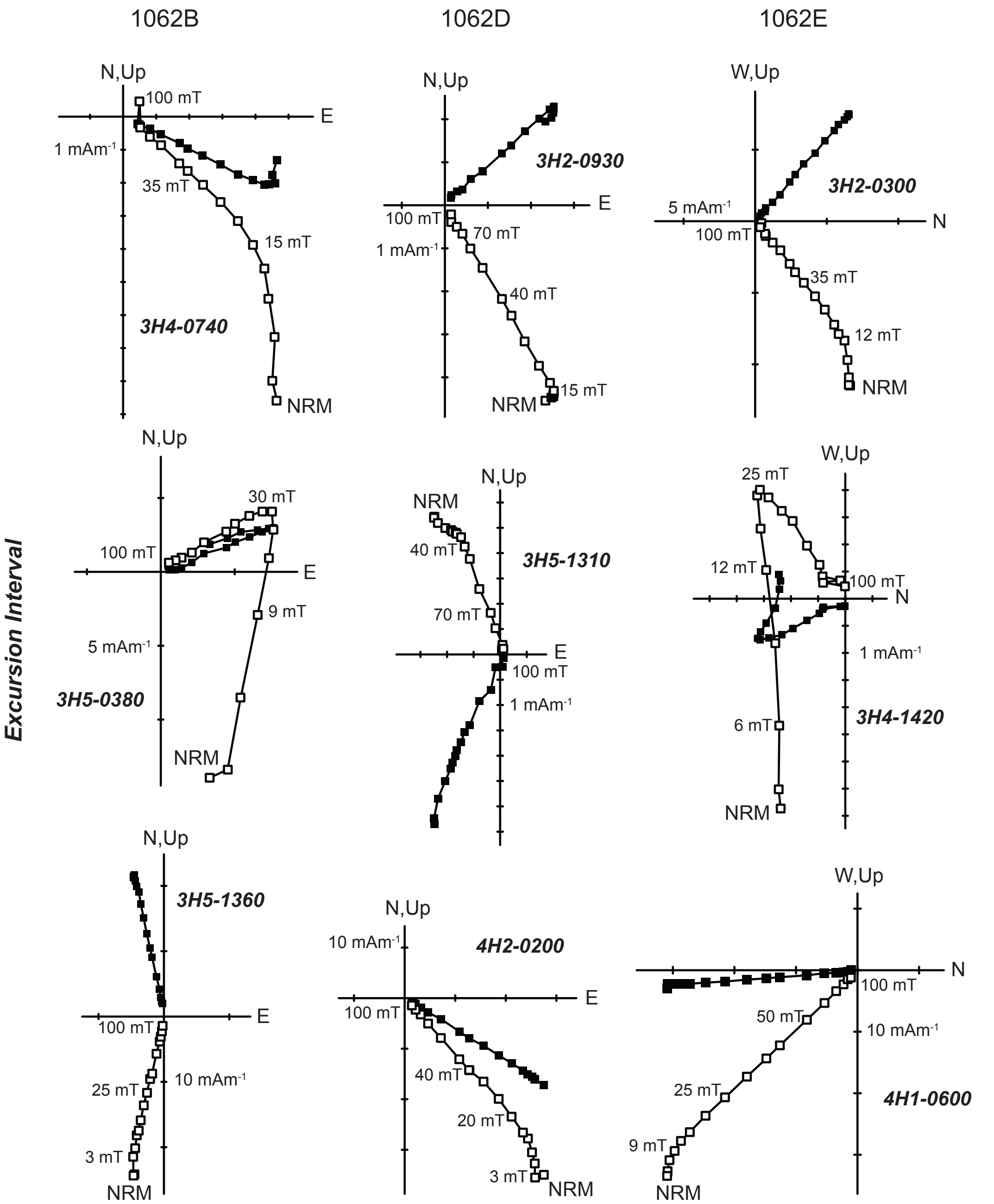

Figure 4.3: Typical orthogonal demagnetization plots for samples from Holes 1062B, D and E. The top and bottom rows are representative of samples younger and older than the excursional interval (middle row) respectively. Sample declinations are unoriented. Magnetization of sample in milli-Amps per metre (mAm^{-1}). Applied alternating-field (AF) demagnetization field strength in milli-Tesla (mT). Open (solid) squares represent the projection of the magnetic vector onto the vertical (horizontal) plane.

Samples from intervals during the transitions between polarities often displayed the most complex behaviour accompanied by significantly reduced NRM intensities. In these intervals, the ChRMs were more ambiguous: 17 MAD values exceeded 10° but none of the samples used in later analysis had MAD values greater than 15°. Only seven samples failed to yield directions fulfilling the above criteria and were subsequently rejected. In general, their ChRMs were not in disagreement with the rest of the record but their MAD values were greater than 15°.

4.4.1 Palaeomagnetic Directions

All core sections were originally extracted unoriented. Furthermore, the ChRM directions showed progressive trends in declination along core. This was taken as an indication that the cores had been twisted during the drilling process. To examine changes in latitude in the virtual geomagnetic pole it is assumed that the records conform to a geocentric axial dipole model (GAD) whereby the Earth's field approximates a dipole aligned along the axis of rotation. All core sections (∼1.5 m length) were oriented such that the mean declination outside the excursional interval is oriented towards the geographic North Pole (0°) [*Knudsen et al.*, 2006].

The resulting three records of palaeomagnetic direction (Fig. 4.4) are remarkably similar and all exhibit a period of excursional behaviour spanning 0.7 m. The average non-excursional inclinations of 46° in Hole 1062B and 43° in both Holes 1062D and 1062E compare well with the expected inclination of 47° for the sites' latitude predicted by the GAD model.

In all three records, the inclination changes rapidly at ∼19 rmcd marking the initiation of the directional excursion (Fig. 4.4b). A brief peak in positive inclinations is immediately followed by an abrupt change to negative inclinations, reaching a maximum of −55 to −65°. Simultaneously, the declinations swing to 180° (Fig. 4.4c). This initial transition occurs within 500 years. Within the excursional interval, Hole 1062B exhibits shallower

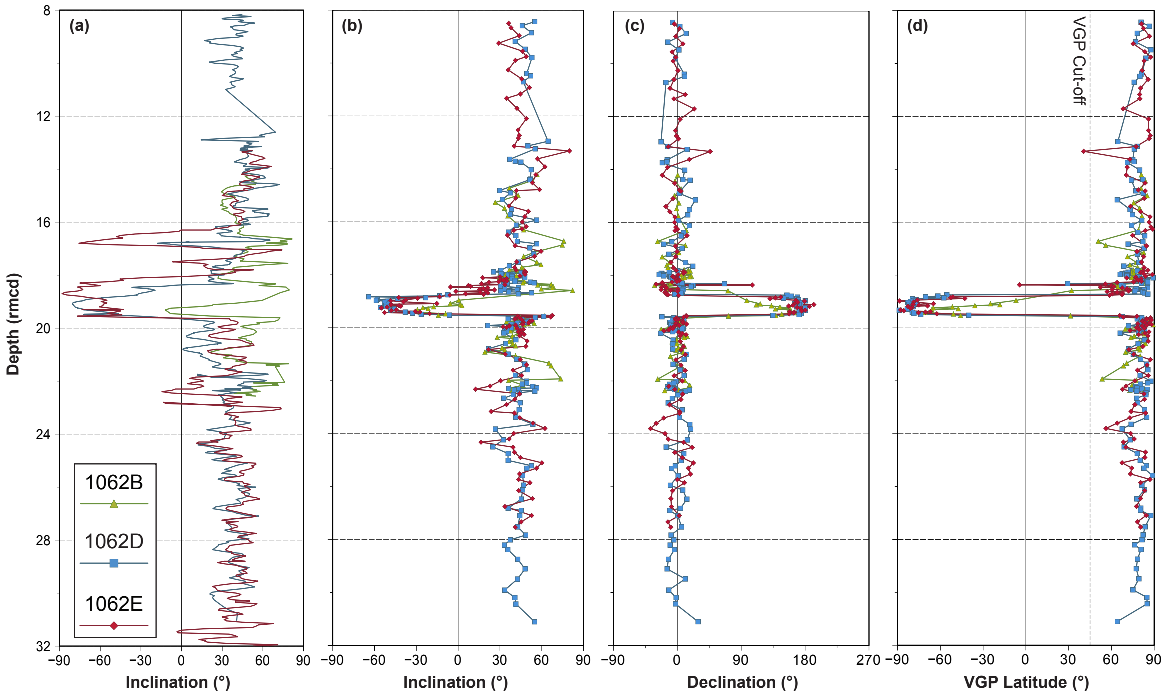

Figure 4.4: (a) Inclinations of the ChRMs of samples from Holes 1062B,D and E against depth (rmcd) measured from split-cores on-board ship [*Shipboard Scientific Party*, 1998a], and (b) from discrete samples (this study). (c) Corrected declinations of discrete samples. (d) Calculated latitude of the virtual geomagnetic poles (VGPs) for all samples. VGP cut-off co-latitude used to define limits of directional excursion marked by dashed line at 45°.

inclinations than the other two holes. Virtual geomagnetic poles (VGPs) were calculated for each sample using the direction vectors of the respective ChRMs (Fig. 4.4d). The record shows a rapid transition to fully reversed directions before an equally rapid return to northern latitudes. The limited number of transition VGPs precludes discussion of VGP paths. During non-excursional intervals the variation in the VGP latitude is within that expected of secular variation.

In general, the directions derived from the discrete samples are consistent with earlier continuous split-core measurements [*Shipboard Scientific Party*, 1998a] although a second, younger, anomalous feature at ∼17 rmcd apparent in the Hole 1062E split-core record is not replicated in the discrete samples measurements (Fig. 4.4a). The magnetizations of the samples within this interval are indistinguishable from those outside it.

4.4.2 Core Properties

Isothermal Remanent Magnetization (IRM) Acquisition

To confirm that the geomagnetic field behaviour has been faithfully recorded, it is important to constrain the effects of the mineralogical properties of the sediment cores. Stepwise application of isothermal remanant magnetization may be used to determine the coercivity spectrum of a sample and thereby its constituent magnetic grain mineralogy. After complete demagnetization, a series of 32 representative samples, 16 each from Holes 1062D and 1062E, were subjected to progressive forward-field IRM acquisition using a Molspin Pulse Magnetizer at the University of Oxford. The samples' magnetizations were measured out-of-field between each step using the 2G magnetometer. Subsequently, the samples were subjected to an equivalent series of fields in the opposite direction (back-field) (Figure 4.5).

The IRM acquisition curves showed that in some cases saturation isothermal remanent magnetization (SIRM) was not achieved by application of an 800 mT field (90-98% saturation). To determine the SIRM, the acquisition curves were modelled using IRMUNMIX [*Heslop et al.*, 2002] assuming a two component mixture of one lower and one higher coercivity component. The model can be used to calculate an estimate for the SIRM. The remanence coercivity (H_{cr}), the 'reverse' field required to reduce a 'forward' saturation remanence to zero, varies between 30 and 40 mT (Fig. 4.6a). The S-Ratio = -$IRM_{0.3T}$/SIRM was subsequently calculated for all samples. The majority of samples had an S-Ratio greater than 0.85, and no samples measured had an S-Ratio less than 0.7 (Fig. 4.6b). This indicates that low-coercivity remanence carriers, in this case probably magnetite grains, consistently dominate the magnetic signal. The lack of variation in the H_{cr} values and S-ratios with depth suggests that there has been little change in magnetic grain provenance and mineral composition during the studied time interval. Within the reversed direction interval the S-Ratio value is greater than 0.9 indicating that the contribution of any higher coercivity component is minor.

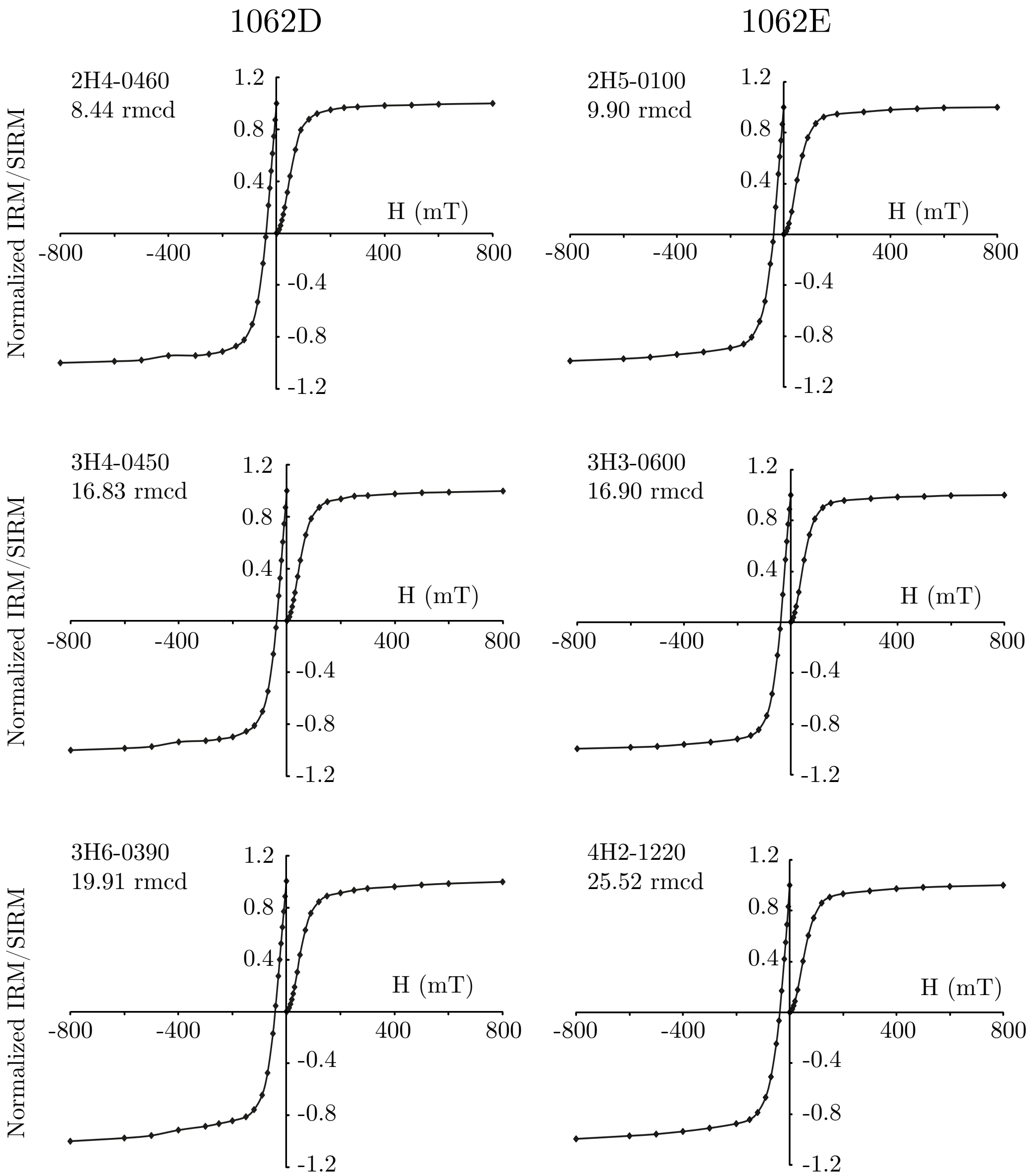

Figure 4.5: Example isothermal remanent magnetization (IRM) acquisition profiles for samples from Holes 1062D and E.

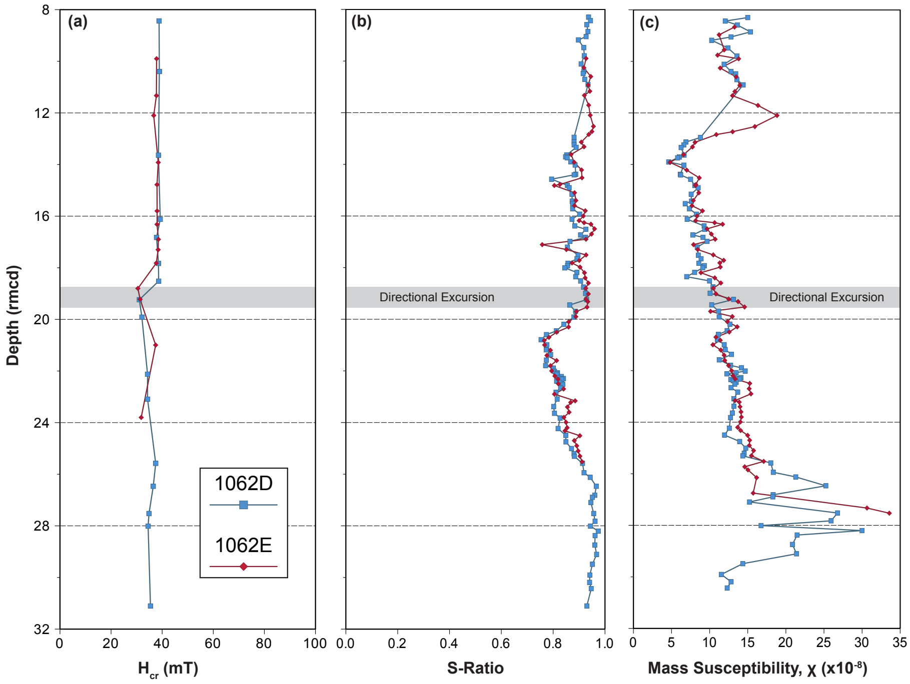

Figure 4.6: (a) Remanence coercivity (H$_{CR}$ of measured samples in milli-Tesla (mT) from Holes 1062D and E against depth (rmcd). (b) S-Ratio (dimensionless - S-Ratio = -IRM$_{0.3T}$/IRM$_{0.8T}$). (c) Mass specific magnetic susceptibility (χ). (10^{-8} m^3 kg^{-1}). Directional excursional interval highlighted by grey-shaded bar defined as in Figure 4.4.

Magnetic Susceptibility

The magnetic susceptibility of the sediments is dependent upon the concentration, grain-size and mineralogy of the remanence carriers. The IRM acquisition results indicate that the average magnetic mineralogy in the samples does not vary substantially with depth. Therefore variation within the susceptibility record can be used to estimate changes in the size and concentration of the magnetic grains. The low-field magnetic susceptibility of representative samples was measured using a Geofyzika KLY-2 KappaBridge at Oxford (Fig. 4.6c). The magnetic susceptibility of the samples shows little variation with depth and is particularly consistent across the excursional interval. Therefore, variation in the intensity of the cores' ChRM is unlikely to be the result of changes in the concentration or grain-size of the remanence carriers.

Grain Size

The ratio of anhysteretic remanence magnetic susceptibility (χ_{ARM}/χ) to low field magnetic susceptibility may be used to investigate first-order variations in grain-size [*Banerjee et al.*, 1981]. The magnitude of the ARM is relatively more sensitive to the finer grain-size fraction while low-field magnetic susceptibility (χ) is particularly sensitive to the coarser grain fraction [*King et al.*, 1982]. Thus an increase in the proportion of fine to coarse grain magnetite is reflected in shift towards higher χ_{ARM}/χ ratios. An ARM was induced in roughly half of the samples with a 100 mT peak AF field and a 0.1 mT bias field using a DTECH-2000 AF unit which can induce ARMs at Imperial College London. The ARM acquired was subsequently demagnetized at 30 mT.

The excursional interval is characterized by high values of χ_{ARM}/χ (due to high ARM intensities) representing a higher proportion of fine magnetic grains (Fig. 4.7a). This feature was also recognized in the same interval by *Schwartz et al.* [1996] in piston cores from the Blake Outer Ridge. Further study of the piston cores by *Schwartz et al.* [1997] demonstrated that high values of χ_{ARM}/χ and ARM associated with high S-ratios are most likely indicators of bacterial magnetite content. In such cases, high values of χ_{ARM}/χ were indicative of the presence of a very fine grained (single domain) magnetite component with high ARM intensities rather than an overall reduction in the size of the clastic magnetite component.

4.4.3 Relative Palaeointensity Proxies

Sedimentary records have the potential to record variations in the relative palaeointensity of the Earth's field [e.g. *Tauxe*, 1993]. The magnitude of the ChRM is dependent upon a combination of: the magnetic mineralogy of a sample; the concentration of magnetic grains; and the strength of the original field. Although absolute palaeointensity can not be determined, the relative palaeointensity (RPI) variation may be obtained by accounting for the effects of magnetic grain mineralogy and concentration.

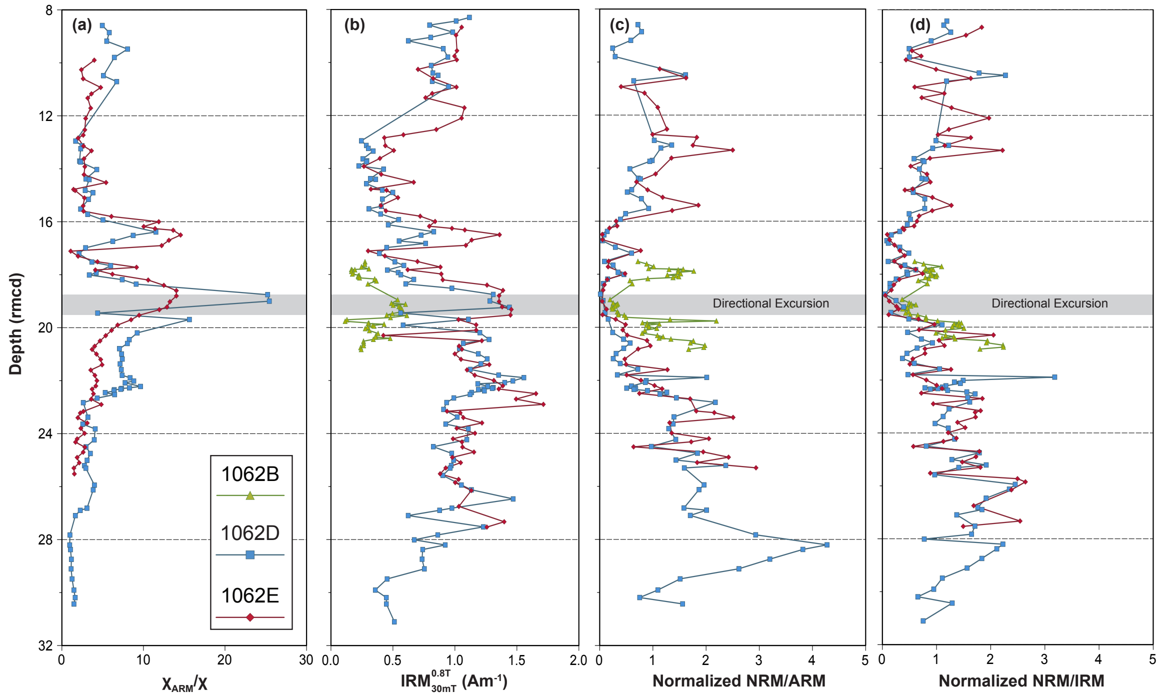

Figure 4.7: (a) Anhysteretic magnetic susceptibility divided by the measured magnetic susceptibility (χ_{ARM}/χ) for samples from Holes 1062D and E. (b) Intensity of applied isothermal remanent magnetization (at 0.8 T) following AF demagnetization at a peak-field of 30 mT. Relative palaeointensity records (c) and (d) for Holes 1062B, D and E derived by dividing the natural remanent magnetizations by the measured anhysteretic and isothermal magnetizations respectively (normalized such that the average values for the records are equal to 1). Directional excursional interval highlighted by grey-shaded bar defined as in Figure 4.4.

The NRM is normalized using the ARM and IRM measurements (Fig. 4.7c and d). After samples had been subjected to an applied magnetization, they were subsequently demagnetized at 30 mT (Fig. 4.7b) and the intensities of the remanent NRM, IRMs and ARMs after demagnetization at 30 mT were used to calculate the NRM/ARM and NRM/IRM palaeointensity proxies.

The significant variation in χ_{ARM}/χ suggests that we should approach the interpretation of the relative palaeointensity proxies with a degree of caution [*Tauxe*, 1993]. However, the relative palaeointensity proxies do exhibit a high degree of consistency, both between the individual holes and between the two methods employed to determine relative palaeointensity. Furthermore, the corroboration of the record by three independent holes is evidence that each has, to a reasonable extent, faithfully recorded the intensity of the local palaeomagnetic field.

In general, the relative palaeointensity proxies show a steady decrease in field intensity from a maximum of 3 or 4 times the average intensity in our record. The field eventually collapses to a significant minimum at 19 rmcd, coinciding with directional excursion. As the field direction returns to normal polarity, the intensity also begins to recover, but this return occurs over an interval of several metres above the directional excursion. Although these general trends are in agreement with palaeointensity stacks [e.g. *Ziegler et al.*, 2011], the potential for sedimentary influences must limit our confidence in any quantification of the relative intensity changes.

4.5 Constraining Sedimentation Rate

To determine an age and duration for the event in our cores we must first constrain the sedimentation rate. Alone, the oxygen isotope stratigraphy cannot resolve millennial-scale fluctuations in sedimentation rate between the two age-constrained stratigraphic bounds. However, unlike records of the Blake excursion from other marine cores, we do not have to assume an average sedimentation rate within a broad interval in the stratigraphy. Instead, using the excess ^{230}Th approach [*Francois et al.*, 2004; *Henderson and Anderson*, 2003] we can reconstruct sedimentation rate variations relative to the average sedimentation rate between the age-constrained bounds. Following the approach described in Chapter 3, an accurate age and duration for the Blake excursion in our record may be determined along with precise uncertainties. Thus, the chronology employed to estimate the age and duration of the excursion does not suffer from the limited resolution that has hindered many earlier attempts to estimate the ages and durations of short duration events in the past.

^{230}Th is produced in the water column by the decay of dissolved ^{234}U. Unlike ^{234}U, ^{230}Th is highly insoluble. As a result, it is rapidly adsorbed onto the surfaces of sinking particles and transported to the underlying sediment: a process known as 'scavenging' [*Bacon and Anderson*, 1982]. This component of the ^{230}Th in the sediment is termed 'excess' thorium ($^{230}Th_{xs}$) as it is not supported by any corresponding uranium component.

The flux of $^{230}Th_{xs}$ to the seafloor is dependent only upon the depth of the overlying water column and the concentration of ^{234}U in seawater, both of which are unlikely to have varied considerably over the last several hundred thousand years [*Henderson*, 2002]. Modelling the variability of the flux of $^{230}Th_{xs}$ into the sediment via scavenging using an ocean general circulation model [*Henderson et al.*, 1999] indicates that the flux at the location of Site 1062 is likely to have been relatively constant and equivalent to its production rate in the water column. The concentration of the $^{230}Th_{xs}$ in the sediment is therefore dependent upon the sedimentation rate. By measuring the concentration of $^{230}Th_{xs}$ in the sediment we can determine relative variations in total sediment flux. We assume a simple reciprocal relationship whereby a doubling of the sedimentation rate would halve the measured $^{230}Th_{xs}$ concentration.

The relatively high average sedimentation rate between the age-constrained bounds ($\sim$10 cm kyr^{-1}) suggests that there is some lateral input of material to the site. Our method assumes that the degree of syndepositional lateral redistribution or 'focussing' of sediment remains constant at the site throughout this interval. The Blake Outer Ridge and surrounding sediments owe their existence to the influx and deposition of terrigenous sediments carried from the north by the deep, geostrophic Western Boundary Undercurrent (WBUC) [*Heezen et al.*, 1966]. The Gulf Stream flows rapidly northwards along the western margin of the Blake Plateau separating the ridge from the potential sediment source of the eastern margin of the continent [*Heezen et al.*, 1966]. ODP Site 1062, south of the Blake Outer Ridge and east of the Blake Plateau, is therefore in a relatively 'sheltered' location. The lack of variation in magnetic grain mineral composition and concentration throughout our studied interval (Fig. 4.6) suggests that the sedimentary environment remained relatively constant during our sampled interval.

Scavenging is not, however, the only source of ^{230}Th into the sediment. To determine the contribution of ^{230}Th$_{xs}$ to the total ^{230}Th content of the sediment, contributions from ^{230}Th supported by detrital U (^{230}Th$_{det}$) and ^{230}Th ingrown from authigenic U (^{230}Th$_{auth}$) must be subtracted from the total measured activity of ^{230}Th, such that:

$$^{230}\mathrm{Th}_{xs} =^{230} \mathrm{Th}_{meas} -^{230} \mathrm{Th}_{det} -^{230} \mathrm{Th}_{auth} \quad . \tag{4.1}$$

^{230}Th measurements were conducted on 18 samples spanning the MIS 5 interval of Hole 1062E. For each sample measured, 0.1 g of dry sediment was dissolved following the method outlined in *Thomas et al.* [2007]. For two of the samples, a further 0.1 g of sediment was dissolved independently to test repeatability. U and Th were then chemically separated from the solution via anion chromatography [*Robinson et al.*, 2004]. The samples were spiked with a mixed ^{229}Th and ^{236}U spike and concentrations of the isotopes ^{234}U and ^{238}U were measured statically and ^{230}Th and ^{232}Th were subsequently measured dynamically, on a Nu Instruments ICP-MS at the Department of Earth Sciences, University of Oxford [*Mason and Henderson*, 2010] (see Section 2.5) (Table 4.2). Subsequent analysis of the measured isotope activities was then conducted using the XSage program (see Chapter 3).

The detrital component of the total measured ^{238}U was calculated and used to determine the detrital input of ^{230}Th. ^{238}U$_{det}$ is calculated by assuming that all of the ^{232}Th in the sample is of detrital origin and using an appropriate value for (^{238}U/^{232}Th)$_{det}$.

$$^{230}\mathrm{Th}_{det} = \left(\frac{^{230}\mathrm{Th}}{^{238}\mathrm{U}}\right)_{det} \times^{238} \mathrm{U}_{det} = \left(\frac{^{230}\mathrm{Th}}{^{238}\mathrm{U}}\right)_{det} \times \left[\left(\frac{^{238}\mathrm{U}}{^{232}\mathrm{Th}}\right)_{det} \times^{232} \mathrm{Th}\right] \quad . \tag{4.2}$$

To estimate (^{238}U/^{232}Th)$_{det}$, samples unlikely to have a thorium contribution from the decay of authigenic uranium were identified. The distribution of measured ^{238}U/^{232}Th

Sample ID	Depth	Measured Activities								XSage Calculations					
	(rmcd)	^{238}U	2 s.e.	^{234}U	2 s.e.	^{232}Th	2 s.e.	^{230}Th	2 s.e.	$^{230}Th_{det}$	2 s.d.	$^{230}Th_{auth}$	2 s.d.	$^{230}Th_{xs}$	2 s.d.
3H1-0920	15.6	0.95	0.003	0.91	0.005	2.04	0.018	3.89	0.026	1.13	0.20			2.76	0.20
3H2-0020	16.2	1.86	0.012	1.81	0.003	2.62	0.043	5.19	0.066	1.45	0.25	0.21	0.17	3.53	0.12
3H2-0600	16.78	1.90	0.005	1.92	0.005	2.52	0.019	5.64	0.033	1.39	0.24	0.28	0.17	3.96	0.09
3H2-1000	17.18	1.12	0.008	1.10	0.005	2.09	0.023	3.97	0.039	1.15	0.20			2.82	0.21
3H3-0020	17.7	0.92	0.001	0.88	0.005	2.02	0.019	4.59	0.032	1.11	0.20			3.47	0.20
3H3-0400	18.08	0.90	0.002	0.85	0.005	1.88	0.016	3.81	0.025	1.04	0.18			2.77	0.18
3H3-1210	18.89	1.14	0.016	1.12	0.003	2.05	0.048	3.56	0.069	1.13	0.20			2.43	0.21
3H4-0180	19.36	1.81	0.004	1.79	0.005	2.55	0.020	4.44	0.028	1.41	0.25	0.25	0.20	2.78	0.07
3H4-0400	19.58	1.50	0.004	1.53	0.005	1.84	0.017	3.31	0.024	1.01	0.18	0.33	0.15	1.97	0.05
3H4-0800	19.98	1.13	0.003	1.09	0.005	2.11	0.020	3.68	0.027	1.17	0.20			2.51	0.21
3H4-1055	20.24	1.04	0.001	1.01	0.005	1.89	0.016	3.48	0.022	1.04	0.18			2.44	0.18
3H4-1220	20.4	1.05	0.001	1.01	0.005	1.79	0.015	3.44	0.023	0.99	0.17			2.45	0.17
3H4-1365	20.55	1.10	0.003	1.04	0.003	2.08	0.464	3.32	0.872	1.15	0.20			2.18	0.21
3H5-0020	20.7	1.13	0.001	1.05	0.005	2.20	0.017	3.09	0.019	1.22	0.21			1.87	0.21
3H5-0125	20.81	1.21	0.002	1.14	0.005	2.34	0.018	3.18	0.019	1.30	0.23			1.88	0.23
3H5-0400	21.08	2.77	0.004	2.96	0.005	2.58	0.020	4.95	0.030	1.42	0.25	1.00	0.22	2.53	0.07
3H5-0520	21.2	2.41	0.003	2.50	0.005	2.66	0.021	4.43	0.027	1.47	0.26	0.68	0.23	2.27	0.07
3H5-0660	21.34	2.12	0.003	2.14	0.005	2.65	0.023	3.59	0.024	1.46	0.26	0.47	0.23	1.66	0.07

Table 4.2: Measured isotope activities and ^{230}Th components calculated using XSage. Isotopic activities given in dpm g^{-1}

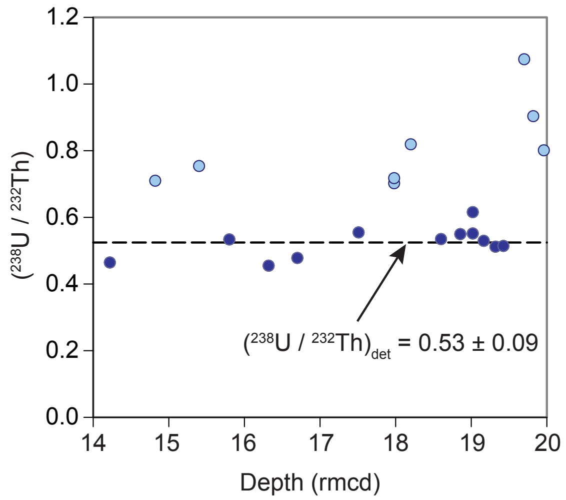

Figure 4.8: The distribution of measured $^{238}U/^{232}Th$ ratios from our samples. One group of samples has consistent low values averaging 0.53 ± 0.09 (dark blue circles), interpreted as the value for $(^{238}U/^{232}Th)_{det}$. The remaining, higher uranium group (light blue circles) are identified as those that have had varying contributions of authigenic uranium in addition to the detrital ^{238}U.

ratios from all the samples includes one group with consistently low values averaging 0.53 ± 0.09 (Fig. 4.8). The remaining samples have a range of values greater than 0.7. The first group is interpreted to represent those samples with limited or no authigenic uranium component, the higher uranium group are therefore identified as those that have had varying contributions of authigenic uranium in addition to the detrital input. A value of 0.53 ± 0.09 is therefore used for $(^{238}U/^{232}Th)_{det}$, consistent with the range typical for Atlantic sediments [=0.6±0.1 *Henderson and Anderson*, 2003].

If ^{230}Th were in secular equilibrium with ^{238}U in marine detrital material, $(^{230}Th/^{238}U)_{det}$ would equal 1, however, $(^{230}Th/^{238}U)_{det}$ may be less than 1 due to alpha recoil from smaller particles [*Osmond and Ivanovich*, 1992]. The deviation of the system from equilibrium is estimated by averaging the measured $^{234}U/^{238}U$ ratios from samples thought to be free of authigenic uranium ($= 0.98 \pm 0.02$). The $(^{230}Th/^{238}U)_{det}$ ratio is likely to be lower than this due to further alpha recoil during the decay of ^{234}U to ^{230}Th. Therefore, $(^{230}Th/^{238}U)_{det}$ is estimated by doubling the deviation of the measured $^{234}U/^{238}U$ average from secular equilibrium to give a $(^{230}\mathrm{Th}/^{238}\mathrm{U})_{det}$ ratio of 0.96 ± 0.04.

Any remaining ^{238}U not accounted for by lithogenic material is assumed to be of authigenic origin. The component of ^{230}Th produced by the decay of authigenic ^{238}U in each sample ($^{230}\mathrm{Th}_{auth}$) is given by [*Henderson and Anderson*, 2003]:

$$\begin{aligned} ^{230}\mathrm{Th}_{auth} = & \left(^{238}\mathrm{U}_{tot} - ^{238}\mathrm{U}_{det}\right) \\ & \times \left[\left(1 - e^{-\lambda_{230}t}\right) + \frac{\lambda_{230}}{\lambda_{230} - \lambda_{234}}\left(\frac{^{234}\mathrm{U}}{^{238}\mathrm{U}}_{init} - 1\right)\left(e^{-\lambda_{234}t} - e^{-\lambda_{230}t}\right)\right] \quad , \end{aligned} \tag{4.3}$$

where λ is the decay constant in yr^{-1}, t is the age (derived from the δ^{18}O stratigraphy), and $(^{234}\mathrm{U}/^{238}\mathrm{U})_{init}$ is the initial ^{234}U to ^{238}U ratio in seawater (=1.147) [e.g. *Robinson et al.*, 2004]. The current $^{230}\mathrm{Th}_{xs}$ activity may then be determined using Equation 1.39. The initial $^{230}\mathrm{Th}_{xs}$ concentration was then calculated by correcting for its own decay:

$$^{230}\mathrm{Th}^{\circ}_{xs} = ^{230}\mathrm{Th}_{xs}e^{\lambda_{230}t} \quad . \tag{4.4}$$

The sedimentation rate, $\mathrm{F}_{(n)}$ (in cm kyr^{-1}) for each sample interval may then be determined using the following expression:

$$\mathrm{F}_n = \mathrm{F}_a \times \frac{\overline{\mathrm{Th}}}{\mathrm{Th}_n} \quad , \tag{4.5}$$

where Th_n is the concentration of $^{230}\mathrm{Th}_{xs}$ in sample n; F_a is the average sedimentation rate in cm kyr^{-1} between the two boundaries of known age and $\overline{\mathrm{Th}}$ is the weighted average concentration of $^{230}\mathrm{Th}_{xs}$ between the boundaries. This assumes a simple reciprocal relationship whereby the variation in the initial concentration of initial $^{230}\mathrm{Th}_{xs}$ about the weighted average initial $^{230}\mathrm{Th}_{xs}$ is proportional to the variation of the sedimentation rate about the average between the boundaries.

The average sedimentation rate between the boundaries (72–135 ka) is 10.4 cm kyr^{-1}. Our thorium data (Figure 4.9, Table 4.3) indicate that the standard deviation of the

Sample						Interval			
ID	Depth (rmcd)	$^{230}Th^0_{xs}$ (dpm g^{-1})	2 s.d.	Age (ka)	2 s.d.	Upper (rmcd)	Lower (rmcd)	Sed. Rate (cm kyr^{-1})	2 s.d.
3H1-0920	14.22	5.62	0.46	76.5	3.6	13.64	14.52	13.02	0.26
3H2-0020	14.82	7.57	0.38	81.9	3.6	14.52	15.11	9.65	0.30
3H2-0600	15.40	8.95	0.40	88.4	3.7	15.11	15.60	8.17	0.29
3H2-1000	15.80	6.59	0.55	92.7	3.7	15.60	16.06	11.11	0.23
3H3-0020	16.32	8.50	0.60	98.0	3.7	16.06	16.51	8.60	0.09
3H3-0400	16.70	7.02	0.55	102.1	3.7	16.51	17.11	10.42	0.17
3H3-1210	17.51	6.61	0.64	109.6	3.8	17.11	17.75	11.07	0.38
3H4-0180	17.98	7.89	0.38	114.3	3.8	17.75	18.09	9.27	0.35
3H4-0400	18.20	5.68	0.27	116.3	3.8	18.09	18.40	12.87	0.50
3H4-0800	18.60	7.52	0.70	119.9	3.9	18.40	18.73	9.73	0.29
3H4-1055	18.86	7.45	0.65	122.6	3.9	18.73	18.94	9.82	0.24
3H4-1220	19.02	7.61	0.63	124.3	3.9	18.94	19.09	9.61	0.20
3H4-1365	19.16	6.84	0.71	125.7	3.9	19.09	19.24	10.70	0.45
3H5-0020	19.32	5.97	0.73	127.0	3.9	19.24	19.37	12.26	0.76
3H5-0125	19.43	6.06	0.78	127.9	3.9	19.37	19.56	12.09	0.83
3H5-0400	19.70	8.34	0.38	130.6	4.0	19.56	19.76	8.77	0.37
3H5-0520	19.82	7.58	0.37	131.9	4.0	19.76	19.89	9.65	0.41
3H5-0660	19.96	5.60	0.31	133.2	4.0	19.89	20.02	13.07	0.55

Table 4.3: Calculated $^{230}Th^0_{xs}$ activity (dpm g^{-1}) and thorium normalized sedimentation rate for Hole 1062E.

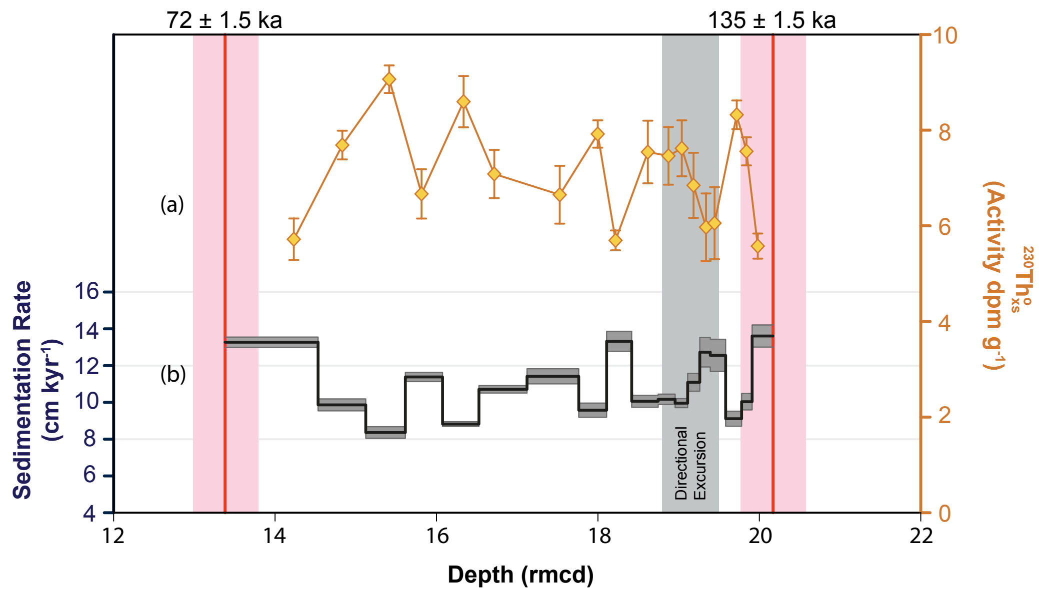

Figure 4.9: (a) Calculated $^{230}Th^{\circ}_{xs}$ (orange diamonds) in decays per minute per gram (dpm g^{-1}) with 2σ uncertainty in Hole 1062E (rmcd). (b) $^{230}Th^{\circ}_{xs}$-normalized sedimentation rate (solid line) between the two age constraints marked in red (72 and 135 ka in cm kyr^{-1}) with depth uncertainty envelopes in pink. Grey envelope indicates 2σ uncertainty on sedimentation rate.

Interval	Mean Sed. Rate (cm kyr^{-1})	Focussing Factor (Ψ)
MIS 5	10.41	4.24
MIS 5a–d	*10.34*	(4.24)
MIS 5e	*10.46*	(4.24)

Table 4.4: Sedimentation rates calculated using MIS 5 boundaries only (72 ka and 135 ka). Focussing is assumed constant across the whole of MIS 5 (hence bracketed focussing factors for intermediate intervals). Italicized numbers indicate values calculated using $^{230}Th_{xs}$-normalization.

rate is only 1.6 cm kyr^{-1} and therefore that the sedimentation rate is rather constant during MIS 5, despite climatic changes. The constancy of sedimentation rate allows us to confidently calculate a duration for the Blake excursion from the new high-resolution record and to assess the uncertainty on this duration.

4.5.1 Focussing

Any variation in focussing could have a significant impact on the final age model. To address this concern, the data is analysed using an intermediate dated tie-point within the studied interval to gain a quantitative estimate of the potential variation in focussing. Assuming constant focussing throughout stage 5 and using only the two tie-points that bound stage 5 (72–135 ka), we can calculate the average sedimentation rates for stages 5a–d and 5e using the $^{230}Th_{xs}$-normalization method.

The focussing factor is calculated by comparing the integral of the expected production of $^{230}Th_{xs}$ from the overlying water column with respect to time, to the total $^{230}Th^0_{xs}$ measured in the samples between the depths corresponding to that time interval. Using the dry bulk density measured on-board ship of 0.74 g cm^{-3} [*Shipboard Scientific Party*, 1998a] and Equation 1.43, we calculate a focussing factor (Ψ) of 4.2 across MIS 5 (Table 4.4).

Using a third stratigraphic boundary within MIS 5, we may investigate to what extent the focussing does remain constant throughout MIS 5. Taking the third boundary at the

Interval	Mean Sed. Rate (cm kyr^{-1})	Focussing Factor (Ψ)
MIS 5	10.41	4.24
MIS 5a–d	10.51	4.30
MIS 5e	10.17	4.10

Table 4.5: Sedimentation rates calculated using MIS 5 and MIS 5e boundaries. Sedimentation rates determined from stratigraphic boundaries. Focussing factors may now be calculated for intermediate intervals.

end of MIS 5e (18.37 rmcd) and assuming an age of 117 ± 1.5 ka [*Kawamura et al.*, 2007], we can calculate the focussing factor for two intervals, (i) MIS 5a–d and (ii) MIS 5e, using the same $^{230}Th_{xs}$ data and method as before (Table 4.5). In MIS 5a–d the focussing factor is $\Psi = 4.30$, whilst in 5e, $\Psi = 4.10$. This would suggest that the focussing factor within MIS 5 may vary by up to 15% from the average.

The reduced focussing in MIS 5e relative to MIS 5a–d results in an overestimate of the sedimentation rate in 5e when we use the $^{230}Th_{xs}$-normalization method, where constant focussing is assumed across all of MIS 5. The duration of the excursional interval in this core, occurring within MIS 5e, may therefore be longer than we have already suggested. An additional 15% uncertainty is therefore added onto our duration estimate to account for this additional source of uncertainty. Without applying the extra stratigraphic constraint, the age calculated for the end of MIS 5e (18.37 rmcd) using only the start and end of MIS 5 and the $^{230}Th_{xs}$ constrained sedimentation rate is 117.9 ka. The difference between this calculated age and that of *Kawamura et al.* [2007] is well within the age uncertainties of the ages used for the stratigraphic boundaries.

4.6 Duration and Age of the Blake Excursion

For the sake of comparison with previous studies of excursions, a conventional co-latitude VGP cut-off is used whereby the duration of an excursion is the period of time the VGP spends more than 45° from the geographic north pole (assumed to be equivalent to the long-term time-averaged VGP position) [*Merrill and McFadden*, 1994]. Following this definition, the Blake excursion spans 0.7 m (the interval 18.8–19.5 rmcd). If we instead examine the deviation of VGPs away from 'normal' secular variation using the adaptive approach of *Vandamme* [1994], we obtain a VGP cut-off value from our data of 27° co-latitude. Due to the rapid change between reversal states, the use of this alternative cut-off value defines a very similar excursion interval. Assuming a constant sedimentation rate, between the boundaries, of 10.4 cm kyr^{-1} the duration of the directional excursional interval would be 6.7 kyr. Using the refined, thorium-corrected sedimentation rates, the duration of the excursional interval is 6.5±1.3 kyr, with the event occurring between 128.5±4.0 ka and 122.0±3.9 ka (note that while the ages have a larger uncertainty, they co-vary, such that the duration has a relatively low uncertainty). To precisely constrain the uncertainties on the duration and age of the excursion, we use a Monte-Carlo method in which the input isotopic data are assigned normal distribution probability density functions and the age and depths of the age-constrained boundaries are varied randomly between maxima and minima. The uncertainty on the duration estimate is principally controlled by potential variation in focussing and the uncertainties assigned to the age and depths of the boundaries.

The new chronology for the Site 1062 holes is in good agreement with the most precise radiometric age for the start of the excursion (132.8±1.3 ka) [*Ménabréaz et al.*, 2010]. However, the stratigraphic relationship between MIS 5e and the excursional event provides an easier way to compare this record with previously published marine core and loess records because previous records have assumed different chronologies for the oxygen isotope record. In the Site 1062 record, the Blake excursion is almost exactly coeval with MIS 5e and the changes in inclination span the entire MIS 5e interval. Mediterranean cores at a similar latitude show that the local directional excursion occurred towards the end of the MIS 5e [*Tric et al.*, 1991; *Tucholka et al.*, 1987], and Arctic records similarly show the excursion coinciding with MIS 5e [*Nowaczyk et al.*, 1994].

If 'lock-in' has occurred at depth below the sediment surface, the age of the measured magnetic signal would be younger than the sediment in which it was recorded and thus the stratigraphic chronology would overestimate the age of the excursion. By studying a core with a relatively high sedimentation rate, ~10 cm kyr^{-1}, the likelihood of there being a significant 'lock-in' depth is reduced [*Roberts and Winklhofer*, 2004]. The sharp transitions between polarity states in the Site 1062 record suggest that 'lock-in' of the magnetic signal occurs across a limited depth range throughout the record of the excursion. The sedimentation rate is also relatively constant. Thus, even if there is a 'lock-in' depth, it is likely to be constant, such that while the age of the excursion may be less, the calculated duration of the excursion is unlikely to change significantly.

4.7 Discussion

This study provides the highest resolution record yet analysed of the Blake geomagnetic excursion. The agreement between the 3 holes indicates that the Site 1062 sediments are excellent recorders of the palaeomagnetic field, yielding high-quality palaeomagnetic vectors with low MAD values.

4.7.1 Geometry of the Excursional Field

The holes from Site 1062 record a fully reversed field, consistent with some previously obtained records of the Blake excursion [e.g. *Fang et al.*, 1997; *Zhu et al.*, 1994]. However, unlike the records of the Blake excursion from the Mediterranean [*Tric et al.*, 1991] and Chinese loess [*Fang et al.*, 1997; *Zhu et al.*, 1994], the holes from Site 1062 do not record multiple reversed intervals separated by normal polarity intervals.

Although cores that record only a single reversed interval have generally been attributed to the filtering of the magnetic signal by low sedimentation rate cores [*Tric* *et al.*, 1991; *Tucholka et al.*, 1987], the high sedimentation rate (~10 cm kyr^{-1}) of the Site 1062 holes, the high resolution of the new record, and the recording of rapid polarity transitions imply that the geomagnetic signal from Site 1062 is well-resolved. Furthermore, the relatively constant sedimentation rate and long duration of the excursion suggest that a hiatus in the Site 1062 record, which could encompass a normal polarity interval during the excursion, is unlikely and was similarly not found in previous age models (Figure 4.2d) [*Grützner et al.*, 2002].

The record obtained in this chapter therefore calls the global existence of multiple reversed intervals into question and suggests that such behaviour should not be considered as characteristic of the Blake excursion.

4.7.2 Duration of Geomagnetic Excursions

The record from Site 1062 indicates that the geomagnetic field deviated from directions that might be expected during 'normal' secular variation for 6.5±1.3 kyr. This duration is within previous estimates for the duration of the Blake excursion (3.5–8.6 kyr) [*Fang et al.*, 1997; *Tric et al.*, 1991; *Zhu et al.*, 1994] but is robust due to the high sedimentation rate and ^{230}Th$_{xs}$ constrained chronology. Although the duration of the Blake excursion's expression in the directional record may vary between locations, the internal process that caused the excursion must therefore have had a relatively 'long' minimum duration of ~6 kyr to create the signal found in our record.

The duration of the Blake excursion is therefore significantly longer than that determined for the Laschamp excursion (~2 kyr) [*Laj et al.*, 2000, 2006] at a number of global sites, including the North Atlantic, and is comparable with the duration of the Iceland Basin excursion (IBE) (6.8±0.5 kyr) [*Knudsen et al.*, 2007] recorded at Site 1063 in the North Atlantic. Directional excursions therefore occupy a broad range of durations and can feature a reversed polarity field state for more than ~3 kyr without this resulting in a full polarity reversal.

4.7.3 Rapid Transitions

Unlike previous records of the Blake excursion [*Tric et al.*, 1991; *Tucholka et al.*, 1987], Site 1062 fails to record the transitional field in any detail despite a relatively high sedimentation rate ($\sim$10 cm kyr^{-1}). Furthermore, the Site 1062 record of the Blake excursion implies rapid and complete reversals in field direction within periods of less than 500 years corresponding to a VGP transition rate of $\sim 180°$ kyr^{-1}. The rapid transition rate in this record suggests that a long duration for the Blake excursion is compatible with much shorter duration estimates for other excursions such as the Laschamp whereby the difference in duration of the event arises as a result of the length of time the field remains in a fully reversed state rather than differences in the durations of the transitions. Furthermore, this rate of change is similar to that observed for the IBE transitions in the North Atlantic [*Knudsen et al.*, 2007] and notably faster than that during reversals. During a reversal, the single polarity transition takes $\sim$5 kyr, corresponding to a rate of only 18° kyr^{-1} [*Clement*, 2004]. The rapidity of the transitions observed in high resolution records of excursions is a particularly striking feature, providing clues about the mechanism that generates field change (Fig. 4.10). Any mechanism or mechanisms to explain excursions and reversals must therefore be able to account for the significant difference in transition rate between the two.

4.7.4 Stability of the Excursional Field

Recent simulations of field reversals, using a time-varying observational model of the geomagnetic field for the last 7000 years [*Korte*, 2005], assume a decreased dipole strength to be the cause of transitional fields [*Brown et al.*, 2007; *Valet and Plenier*, 2008]. Excursions are simulated in these models by setting the strength of the dipole to a reduced value for a set time interval. The axial dipole field strength must be decreased significantly (to around 20%) before large excursional events are observed in the simulations [*Brown et al.*, 2007]. Such a decrease in intensity is observed in this study's record for the Blake,

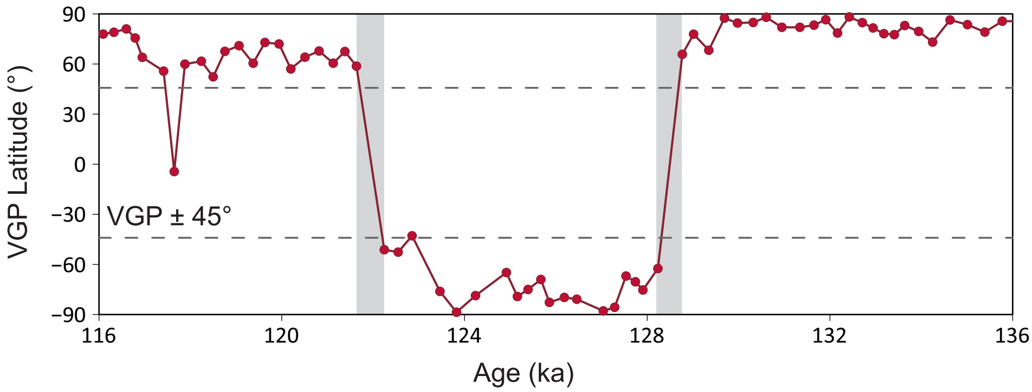

Figure 4.10: VGP latitude record of the Blake Excursion from ODP Site 1062E. Transition zones (VGP within ±45°) highlighted in grey.

and similarly during other polarity transitions [*Ziegler et al.*, 2011], whereby the relative palaeointensity decreases over a significantly longer duration interval before the directional excursion is recorded, and its subsequent increase in strength occurs after the field direction has returned to its intial polarity. However, it is difficult to imagine how a time-varying non-dipole field could maintain fully reversed directions for such a long duration as that found for the Blake excursion in our record (6 kyr+).

Valet and Plenier [2008] simulate excursions in a similar model by decreasing the axial dipole strength to zero and then increasing it back to its initial state - a situation equivalent to that of a full reversal. This approach explores therefore the possibility that a geomagnetic excursion could represent an 'aborted' polarity interval [*Valet et al.*, 2008]. However, they could only simulate directional records with VGPs in high southerly latitudes by adding a short interval of a weakly reversed dipole field before the return of the field to its initial state. This suggests that an extended duration interval with fully reversed directions, such as that found in our Blake record, must represent a short period when there is a weak, reversed polarity dipole field. This study's record does not, however, document an increase in field intensity within the directional excursion, which implies that the strength of the dipole must still be minimal and that this interval still represents an unstable field state.

4.8 Conclusions

- Combining a $\delta^{18}O$ stratigraphy and the ^{230}Th excess method, this new high-resolution palaeomagnetic record of the Blake excursion at ODP Site 1062 indicates that the geomagnetic field deviated from directions expected during 'normal' secular variation for 6.5±1.3 kyr between 129 and 122 ka. This is within the range of previous estimates of the duration of the Blake excursion (3.5–8.6 kyr) at other sites, but previous estimates have generally relied on average sedimentation rates across broad depth intervals.
- The relatively long duration for the Blake excursion at Site 1062 is evidence that excursions do not necessarily have short durations (i.e. < 3 kyr) but instead occupy a continuous range of durations. Furthermore, the maintenance of fully reversed directions for a long duration implies the presence of a weakly reversed dipole during the excursion.
- However, despite the length of the Blake excursion, the record of the event at Site 1062 is characterized by rapid polarity transitions (< 500 years) that are significantly faster than those observed during reversals.
- The ^{230}Th-excess method shows great promise in constraining the duration of short (kyr) events for other records where sedimentation rates may potentially vary more significantly than at Site 1062.
- To understand further the true nature of the global geomagnetic field during the Blake excursion, high quality records are required from a number of locations from across the globe particularly from the southern hemisphere [*Roberts*, 2008]. This new record provides the first steps toward a global dataset of high-quality palaeomagnetic data with precise chronological control for the Blake excursion.

Chapter 5

The Laschamp Excursion

This chapter has been submitted in a modified form as:

'Bourne, M., Mac Niocaill, C., Thomas, A. L., and Henderson, G. M., [2013] High-resolution record of the Laschamp geomagnetic excursion at the Blake-Bahama Outer Ridge. *Geophysical Journal International, in press.*'

5.1 Introduction

Of all the excursions during the Brunhes Chron, the Laschamp excursion is the most widely recognized. The Laschamp excursion was first discovered in the Laschamp and Olby lava flows, part of the Chaîne des Puys volcanic field, central France [*Bonhommet and Babkin*, 1967]. Reversed and transitional directions in these flows, with correspondingly low field intensities, have since been dated by a number of authors [e.g. *Guillou et al.*, 2004; *Plenier et al.*, 2007; *Singer et al.*, 2009]. The most recent radioisotopic dating of the Laschamp and Olby flows using K-Ar, ^{40}Ar/^{39}Ar and ^{238}U-^{230}Th methods indicate an age for the Laschamp Excursion of 40.7±0.95 ka [*Singer et al.*, 2009]. Lavas from the Auckland volcanic field in New Zealand provide evidence that the Laschamp excursion was a global event [*Cassata et al.*, 2008], where ^{40}Ar/^{39}Ar dating of lavas recording excursional directions suggests an age of 39.1±4.1 ka.

While volcanic records can provide invaluable numerical ages for geomagnetic events, they are unable to continuously record high-resolution field behaviour during an excursion and accurately constrain the duration of excursions. Such continuous palaeomagnetic records can be derived, however, from marine sedimentary archives and have been important in demonstrating the global nature of the Laschamp excursion [*Channell*, 2006; *Channell et al.*, 2012; *Laj et al.*, 2006; *Lund et al.*, 2001b, 2005; *Nowaczyk et al.*, 2012]. Excursional directions have been found in marine sediments from the Irminger Basin, off the coast of Greenland [*Channell*, 2006], to the southern Indian Ocean [*Laj et al.*, 2006]. Relative palaeointensity stacks obtained from sedimentary records reveal that a significant decrease in geomagnetic palaeointensity is associated with excursional VGPs during the Laschamp excursion [*Channell et al.*, 2009; *Guyodo and Valet*, 1999; *Laj et al.*, 2000, 2004; *Valet et al.*, 2005]. Although many of these stacks are from the Northern Hemisphere, a similar palaeointensity minimum is seen in cores from the Southern Hemisphere [*Channell et al.*, 2000].

Alternative approaches may also be used to reconstruct variations in the strength of the palaeomagnetic dipole [for a full review see *Roberts et al.*, 2013]. Inversion of high-resolution marine magnetic anomaly records also show a minimum in palaeointensity within the Laschamp interval [*Gee et al.*, 2000]. However, evidence for a geomagnetic intensity minimum during this period is not confined to palaeomagnetic archives. *Elsasser et al.* [1956] demonstrated that the atmospheric production of the cosmogenic nuclide ^{10}Be is modulated by geomagnetic field intensity over millennial time scales. Since that early work, reconstructions of the geomagnetic field intensity, independent of palaeomagnetic measurements, have been derived from sedimentary ^{10}Be archives [e.g. *Christl et al.*, 2003; *Frank et al.*, 1997; *Ménabréaz et al.*, 2011, 2012] and ice cores [*Muscheler et al.*, 2004, 2005; *Raisbeck et al.*, 2006]. Reconstruction of the palaeomagnetic dipole for the last 200 ka using a sedimentary record of ^{10}Be production [*Frank et al.*, 1997] shows a broadly similar pattern to that predicted by analysis of relative palaeomagnetic data [*Ziegler* *et al.*, 2011]. An increase in ^{10}Be production at ∼41 ka, recorded in Pacific sediments, suggests a palaeointensity minimum [*Ménabréaz et al.*, 2011, 2012] coincident with the Laschamp excursion [*Singer et al.*, 2009].

Duration estimates for the Laschamp excursion palaeointensity minimum, reconstructed from both ^{10}Be and palaeomagnetic records, tend to fall between 1 and 2 kyr [e.g. *Laj et al.*, 2004; *Lund et al.*, 2005; *Ménabréaz et al.*, 2012]. On the other hand, recent estimates of the duration of the directional excursion, from high-resolution sedimentary records from the Black Sea [*Nowaczyk et al.*, 2012] and the Bermuda Ridge [*Channell et al.*, 2012] suggest that it lasted no more than ∼500 years. Estimates for the duration of the Laschamp excursion determined in Arctic sediments have tended to be significantly longer [*Nowaczyk and Antonow*, 1997; *Nowaczyk and Knies*, 2000] and, although the possibility of unusual field behaviour at high latitudes can not be completely discounted, it is likely that these 'amplified' excursion records are the result of modification of the original detrital remanent magnetization (DRM) by a self-reversed chemical remanent magnetization (CRM) [*Channell and Xuan*, 2009; *Xuan and Channell*, 2010].

This chapter presents a high-resolution palaeomagnetic record of the Laschamp geomagnetic excursion from cores on the Blake-Bahama Outer Ridge in the North Atlantic Ocean. The duration of the Laschamp excursion is determined using a high-resolution stratigraphy linked to millennial-scale variation in the δ^{18}O record from the Greenland ice cores [*Johnsen et al.*, 1992; *Svensson et al.*, 2006, 2008]. This enables us to provide an age and duration for the Laschamp excursion with greater accuracy than could be achieved using previously published age models for these Blake-Bahama Outer Ridge sites [*Grützner et al.*, 2002; *Keigwin and Jones*, 1994].

5.2 Study Site and Sampling

The Blake-Bahama Outer Ridge is a hemipelagic sediment drift located in the western North Atlantic Ocean, characterized by high sedimentation rates (∼10s of cm kyr^{-1}).

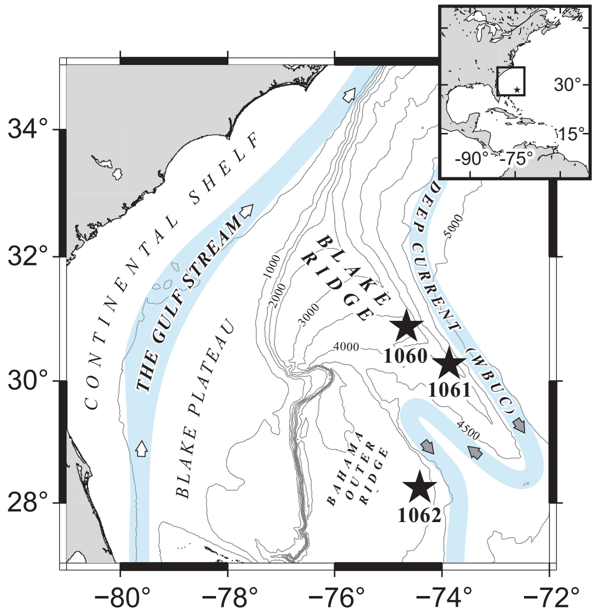

Figure 5.1: Location of Ocean Drilling Program (ODP) Sites 1060 (water depth: 3481 m), 1061 (4047 m), and 1062 (4772 m) on the Blake Ridge and Bahama Outer Ridge. Bathymetry data are from 'The GEBCO One Minute Grid, version 2.0, http://www.gebco.net'.

Early studies of cores from the Blake Ridge sediments identified the Laschamp interval as a palaeointensity minimum, but failed to observe excursional directions [*Schwartz et al.*, 1996, 1998]. Later drilling returned cores with higher sedimentation rates that recorded a directional excursion. These were then placed on an age model determined by correlating variations in carbonate content to the GISP2 ice core chronology [*Keigwin and Jones*, 1994; *Lund et al.*, 2005]. The Laschamp excursion was similarly identified in sister cores from Ocean Drilling Program (ODP) Leg 172 on the Blake Ridge by shipboard palaeomagnetic measurements of half-cores [*Lund et al.*, 1998; *Shipboard Scientific Party*, 1998a] and later u-channel investigations of the same cores [*Lund et al.*, 2001b]. Using the shipboard and u-channel palaeomagnetic measurements, two sites were selected for detailed, discrete sampling: Site 1061 (29° 58.5'N, 73° 36.0'W), located at the tip of the Blake Ridge, and Site 1062 (28° 14.8'N, 74° 25.0'W), located on the Bahama Outer Ridge approximately 210 km south-west of Site 1061 (Fig. 5.1). Site 1062 includes holes drilled on both the western and eastern side of a single mud wave, ~1 km apart [*Shipboard*

Scientific Party, 1998a]. As the holes represent a transect across a single mud wave, they were assigned, unusually, to the same site number despite the multiple drilling locations.

Discrete cubic samples (8 cm^3) were collected from two holes (1061B and 1061C) from Site 1061 at the IODP repository in Bremen. In all, 100 samples were taken from Hole 1061B (between 0.15 and 8.79 mbsf). Unfortunately, sampling from Hole 1061C was hindered by previous u-channel sampling in some core sections and only 21 samples were taken [between 8.90 and 13.12 m below sea-floor (mbsf)]. The sampled interval from Hole 1061C does not include the directional excursion interval.

Discrete samples were also collected from three holes from Site 1062: eastern Holes 1062A, D and western Hole E. 68 samples were taken from Hole 1062D (between 4.41 and 10.01 mbsf), 47 samples from Hole 1062E (between 4.62 and 8.25 mbsf) and 47 samples from Hole 1062A (between 3.00 and 8.02 mbsf) corresponding to the intervals of interest including the Laschamp Excursion ($\sim$41 ka). Samples were taken at varying resolution, but at the highest resolution, up to every 2 cm. Each sample effectively integrates a stratigraphic interval of 50-70 yr.

5.3 Age Model

5.3.1 Composite Depth Scale

The ODP metres composite depth (mcd) scale for cores from Site 1061 was found to provide a good correlation between Holes 1061B and 1061C. The palaeomagnetic records from all holes from Site 1061 are subsequently given on the ODP Site 1061 mcd. The eastern holes from Site 1062, A and D, and the western Hole 1062E have different ODP mcd [*Shipboard Scientific Party*, 1998a]. The 'MATCH 2.3.1' protocol of *Lisiecki and Lisiecki* [2002], which utilizes dynamic programming, was used to determine the best correlation between the shipboard magnetic susceptibility records from the eastern and western Site 1062 holes. The protocol compares possible alignments of the records to determine a realistic and optimal match. Using 'MATCH', the eastern hole was correlated to the western hole and a good match was achieved between the two, which was later confirmed by subsequent palaeomagnetic measurements. The palaeomagnetic records from all holes at Site 1062 are therefore given on the ODP Hole 1062E (western) mcd.

It was not possible to determine an independent, high-resolution correlation between Site 1061 and 1062 using variations in carbonate content, gamma ray count or magnetic susceptibility. This reflects the different sedimentological regimes between the Blake Ridge (Site 1061) and the Bahama Outer Ridge (Site 1062). Relative palaeointensity (RPI) proxies derived from the two sites are similar and therefore, for the sake of comparing the two records, a coarse correlation is presented between major RPI features below.

5.3.2 Chronology

High terrigenous sedimentation rates and carbonate dissolution at depth leaves insufficient foraminifera at Site 1061 (4047 m water depth) to readily conduct oxygen isotope analysis or ^{14}C-dating. Site 1061 cannot therefore be dated directly. Previous age models determined for Blake Ridge sites tuned variations in estimated carbonate content to orbital parameters [*Grützner et al.*, 2002; *Keigwin and Jones*, 1994]. Although variations in sedimentological parameters have a first-order trend associated with glacial-interglacial cycles for some Leg 172 sites [*Chaisson et al.*, 2002], their variance may be affected by local, rather than global, factors [*McCave*, 2002]. *Channell et al.* [2012] recently presented a new δ^{18}O chronology for Site 1063 (also from Leg 172) on the nearby Bermuda Rise (33° 41.2'N 57° 36.9'W). Unfortunately, it was not possible to find a suitable parameter that could be correlated from Sites 1061 and 1062 to Site 1063 at sufficiently high resolution to provide an accurate age for the Laschamp excursion.

To overcome these difficulties, an age model based on planktonic foraminifera is transferred from neighbouring Site 1060 [*Hoogakker et al.*, 2007; *Vautravers et al.*, 2004]. Site

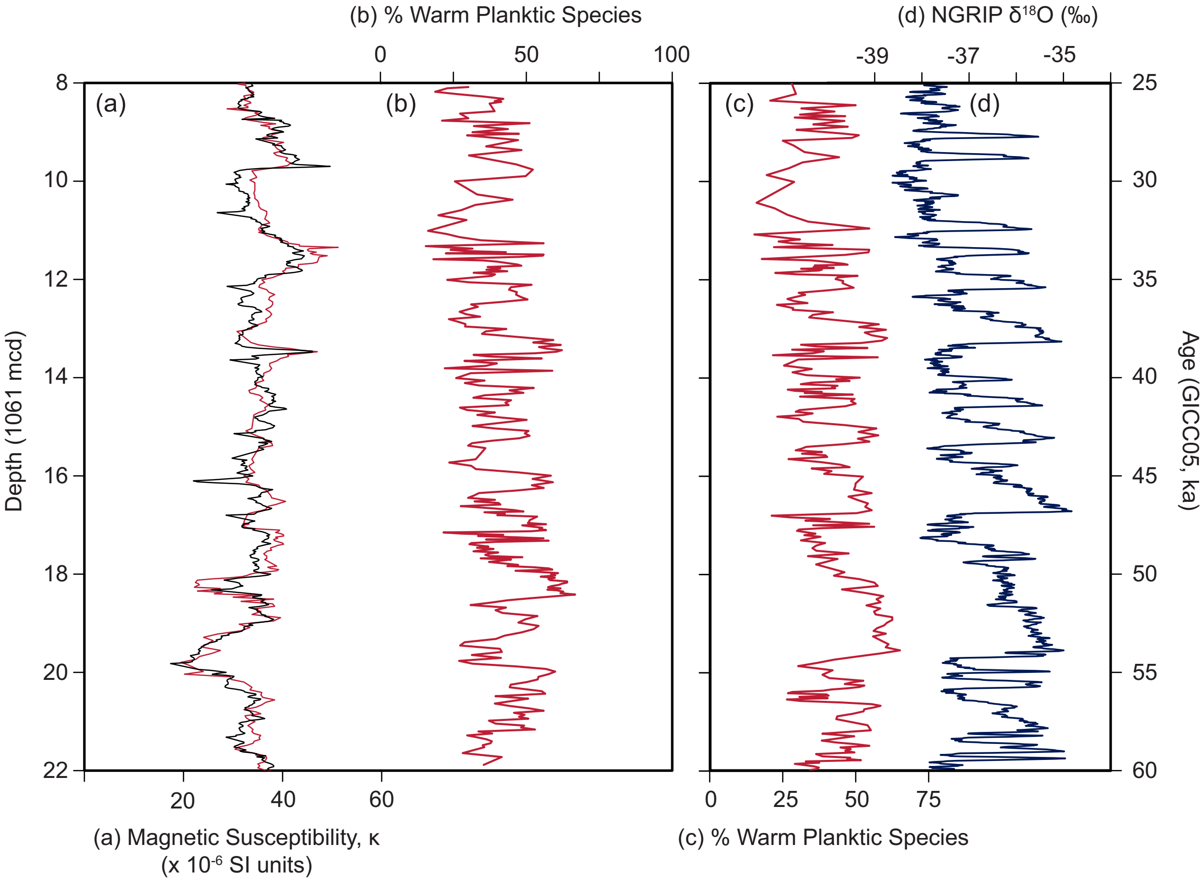

Figure 5.2: Site 1061 chronology: (a) correlation of shipboard magnetic susceptibility records [*Shipboard Scientific Party*, 1998a] between Sites 1060 (red) and 1061 (black) on the Site 1061 depth scale (mcd). (b) Variations in the percentage of warm planktonic foraminiferal species transferred from Site 1060 [*Vautravers et al.*, 2004] onto the Site 1061 depth scale (mcd) and (c) onto the GICC05 age model [*Andersen et al.*, 2006; *Svensson et al.*, 2006] by correlation to (d) the NGRIP $\delta^{18}O$ record [*Andersen et al.*, 2004]. Correlations were achieved automatically using the 'MATCH 2.3.1' protocol of *Lisiecki and Lisiecki* [2002].

1060 is ~120 km north-west of Site 1061 and is also situated on the crest of the Blake Ridge (3480 m water-depth). At a shallower water depth than Site 1061, Site 1060 is less subject to carbonate dissolution and thus an age model can be constructed for this site. To transfer the age model for Site 1060 to Site 1061, the shipboard magnetic susceptibility record of the Site 1060 ODP composite mcd splice [*Shipboard Scientific Party*, 1998a] is correlated to the magnetic susceptibility record of Hole 1061C (mcd). The 'MATCH' protocol of *Lisiecki and Lisiecki* [2002] was again used to determine the best correlation between the two records. The two records are similar and a match between the two was

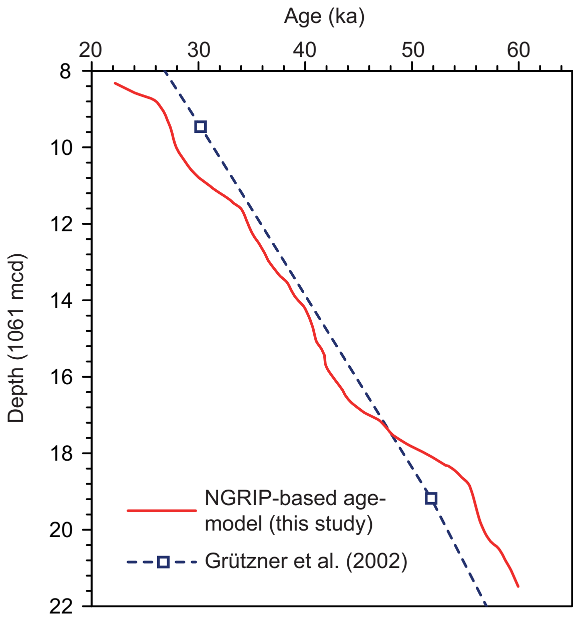

Figure 5.3: Age-depth models for Site 1061. A new age-depth relationship, tied to the NGRIP GICC05 chronology [*Andersen et al.*, 2006; *Svensson et al.*, 2006], (red solid line) is compared to the previous, low-resolution age model for Site 1061 [*Grützner et al.*, 2002] (blue dashed line).

achieved (Fig. 5.2a).

Following the approach of *Vautravers et al.* [2004] and *Hoogakker et al.* [2007], variations in the percentage of warm planktonic foraminferal species at Site 1060 (thought to reflect sea-surface temperatures) are correlated to $\delta^{18}O$ from the NGRIP ice core from Greenland [*Andersen et al.*, 2004] using the 'MATCH' protocol (Fig. 5.2b–d). This procedure assumes that West Atlantic sea-surface temperature and central Greenland temperature varied synchronously. For this study, ages are assigned using the GICC05 age scale for the Greenland ice cores [*Andersen et al.*, 2006; *Svensson et al.*, 2008] (not the older SFCP04 age scale [*Shackleton et al.*, 2004] as used by *Hoogakker et al.* [2007]). However, the assigned ages are within the uncertainty of those given by *Hoogakker et al.* [2007]. This chapter's new age model for Site 1061 linked to NGRIP is compared to the previous, low-resolution age model [*Grützner et al.*, 2002] for this site in Figure 5.3. Within the studied interval, the age models differ by no more than 2 kyr.

5.4 Palaeomagnetic Methods & Results

All of the discrete samples were subjected to a 17-step alternating field (AF) demagnetization procedure. After initial measurement of the natural remanent magnetization (NRM) the samples were subjected stepwise to AFs with maximum amplitudes of 3, 6, 9, 12, 15, 20, 25, 30, 35, 40, 50, 60, 70, 80, 90, and 100 mT. All measurement and demagnetization steps were performed using a 2G Enterprises DC-SQUID cryogenic magnetometer with an in-line triaxial AF demagnetizer in a shielded room at the University of Oxford.

Representative orthogonal demagnetization diagrams from Sites 1061 and 1062 are shown in Fig. 5.4. Many samples have a low coercivity component that was typically removed by AF demagnetization at 20 mT. This low coercivity component was assumed to be an isothermal remanent magnetization (IRM) induced by exposure to the magnetized steel core barrel during drilling and is a common feature of material obtained by oceanic drilling [*Acton et al.*, 2002; *Ade-Hall and Johnson*, 1976].

The resulting demagnetization vectors were analysed using principal component analysis (PCA) to determine the characteristic remanent magnetization (ChRM) direction for the samples [*Kirschvink*, 1980]. Removal of the drilling-induced overprint revealed a stable, single ChRM. All samples analysed from Sites 1061 and 1062 had maximum angular deviation (MAD) values less than 6°, with the majority having MAD values less than 2°. However, three samples from Hole 1062E had MAD values greater than 6° within an interval characterized by low palaeomagnetic intensity (2–3$\times10^{-3}$ Am^{-1}).

5.4.1 Palaeomagnetic Directions

Discrete sample measurements from Site 1061 and 1062 cores agree well with the expected inclination for a geocentric axial dipole (GAD) at the site latitudes (44°). As a result of the drilling process, cores were not oriented. Any measurement of declination must therefore reflect relative variations in azimuth. Progressive trends in declination along the full length of individual cores were taken as an indication that the cores twisted

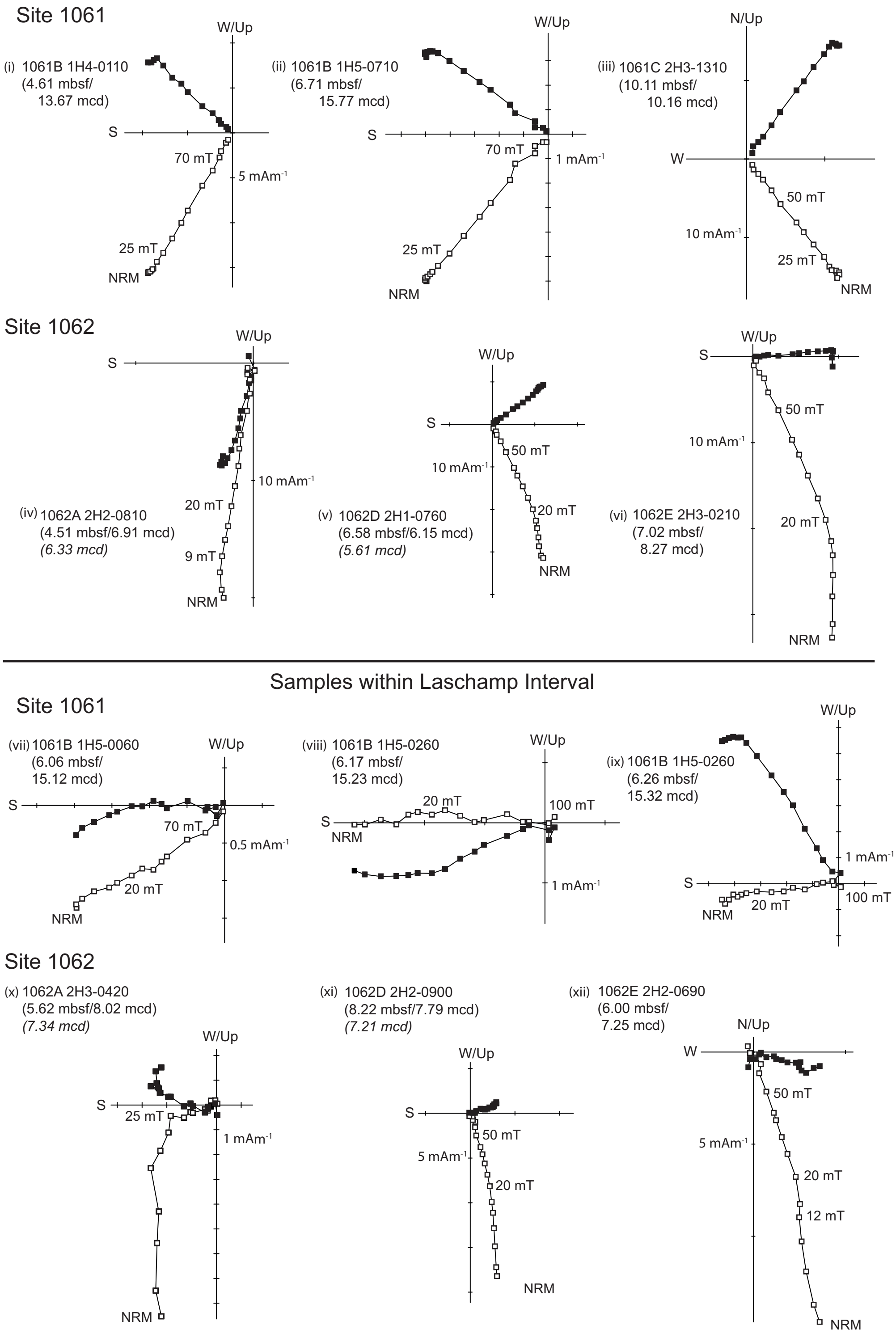

Figure 5.4: Representative orthogonal AF demagnetization diagrams from ODP Sites 1061 and 1062. Sample declinations are uncorrected. Magnetizations are in milli-Amperes per metre (mAm^{-1}). Open (solid) squares represent the projection of the magnetic vector onto the vertical (horizontal) plane. Italicized mcd values for samples from Holes 1062A and 1062D indicate equivalent depths in Hole 1062E. Samples (vii) to (xii) are from within the Laschamp interval. See Figures 5.5 and 5.6 for the depth position of the samples in down core plots.

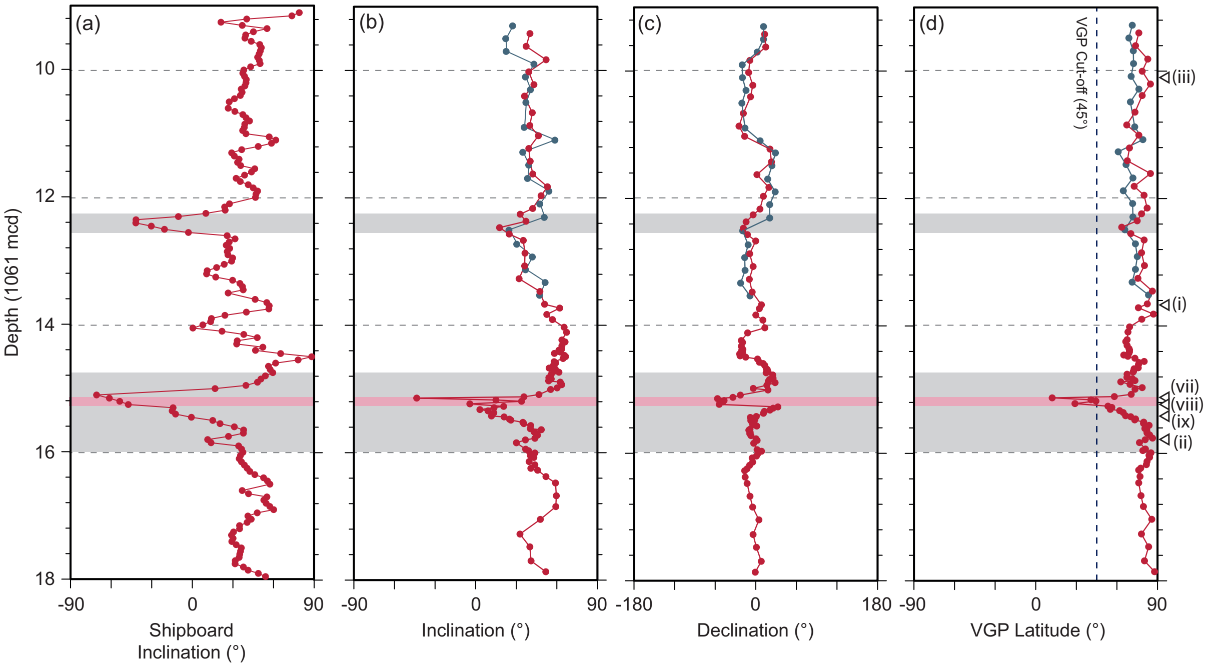

Figure 5.5: (a) NRM inclinations of samples from Hole 1061B measured from split-cores onboard ship [*Shipboard Scientific Party*, 1998a] and (b) ChRM inclinations for discrete samples from Holes 1061B (red) and 1061C (blue) from this study. (c) Corrected ChRM declinations for discrete samples. (d) Calculated latitude of the virtual geomagnetic poles (VGPs) for all samples. The VGP cut-off co-latitude used to define the limits of the directional excursion is marked by a dashed line at 45°. The directional excursion is highlighted by the pink bar and grey shaded bars indicate low palaeointensity intervals as seen in Fig. 5.11. The numbered arrows indicate the depth of the representative samples from Fig. 5.4.

during extraction. To correct for this effect, I follow general practice and assume that the records conform to a GAD model, whereby the average field direction at the site (excluding excursional behaviour) is directed towards the geographic North Pole. The cores were subsequently oriented such that the mean declination outside the excursional interval is oriented towards the geographic North Pole (0°) [e.g. *Bourne et al.*, 2012a; *Knudsen et al.*, 2006].

Hole 1061B records field behaviour during the Laschamp interval. Samples were taken every 2–3 cm, resulting in effectively continuous sampling. The major feature in the shipboard data is a substantial shallowing and slight reversal of inclination at 15.2 mcd (Fig. 5.5b). Two relatively broad 'shoulders' of higher than expected inclina-

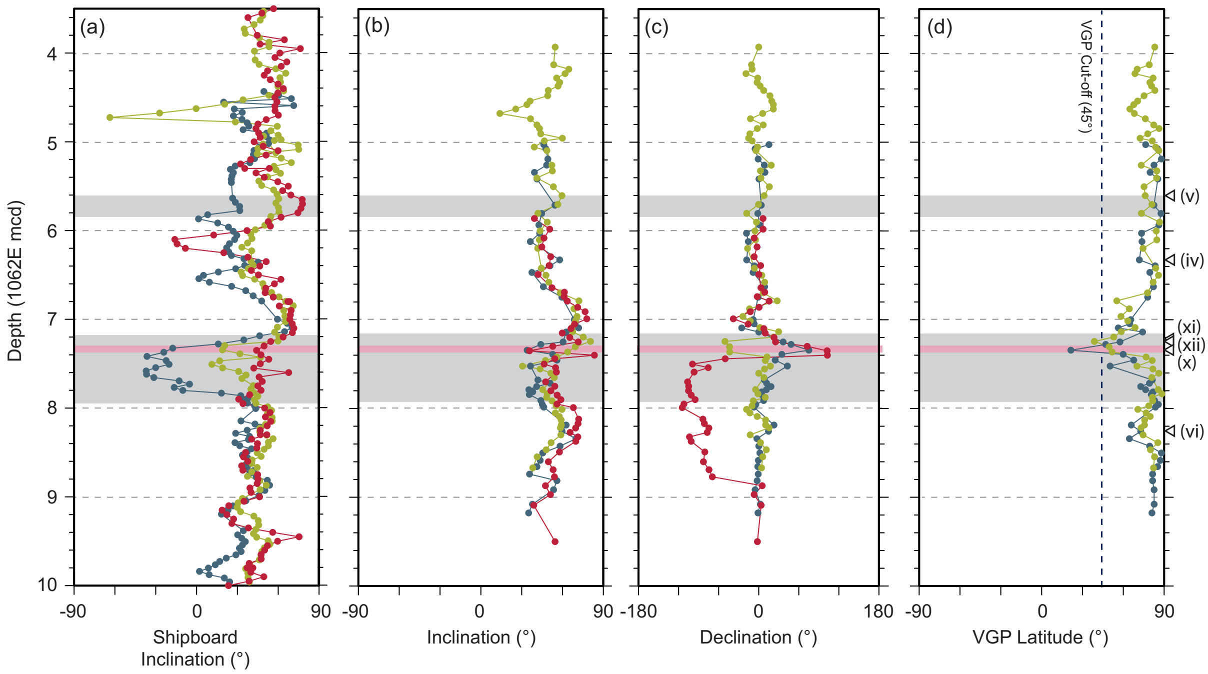

Figure 5.6: (a) NRM inclinations of samples from Holes 1062A (blue), 1062D (green), and 1062E (red) measured from split-cores on-board ship [*Shipboard Scientific Party*, 1998a] and (b) ChRM inclinations from discrete samples from this study. (c) Corrected ChRM declinations for discrete samples. (d) Calculated VGP latitude for all samples. The VGP cut-off co-latitude used to define the limits of the directional excursion is marked by a dashed line at 45°. The directional excursion is highlighted by the pink bar. Grey shaded bars indicate low palaeointensity intervals as seen in Fig. 5.11. The numbered arrows indicate the depth of the representative samples from Fig. 5.4.

tions (up to 70°) precede and follow the excursional interval. A less severe inclination shallowing also occurs at 12.4 mcd. Although the discrete samples also record two shallowing events, they fail to replicate the more steeply reversed inclinations associated with the Laschamp interval found in the shipboard measurements (−70° and −40° respectively) (Fig. 5.5a). Discrepancies between the long-core and discrete sample measurements have been seen before at this site and appear to be the result of biases arising from the long-core measurement process [*Acton et al.*, 2002; *Brachfeld et al.*, 2004; *Lund et al.*, 2001b; *Roberts et al.*, 1996].

Declination records from Holes 1061B and 1061C are in good agreement with each other (Fig. 5.5c). Within the same interval as the inclination deviation in Hole 1061B, the declination also changes by up to 90° at ∼15.2 mcd. A second interval of similar duration at ∼14.2 mcd exhibits a second deviation towards the same direction but of lesser magnitude (∼40°).

On the basis of the shipboard inclination records from Site 1062, the shallow inclinations previously identified as the Laschamp excursion occur at 7.35 mcd (Fig. 5.6a). The discrete sample measurements (Fig. 5.6b) from Site 1062 also agree well with the expected inclination for a geocentric axial dipole (GAD) at the site but they again fail to replicate the shallower (0°) inclinations associated with the Laschamp interval in the shipboard measurements. However, there is evidence for slight but rapid deviations from the GAD direction in all three holes, 1062A, D and E, within this 20 cm interval. Between 7.4 and 6.6 mcd and between 8.5 and 8.0 mcd two 'shoulders' of higher than expected inclinations (up to 85°) precede and follow the excursional interval in a manner similar to that observed at Site 1061.

Declinations from Holes 1062A and D deviate within the same interval as the shallowing inclination (Fig. 5.6c). The records from these two cores are in good agreement with each other, with in-phase changes in declination between the cores. Similar to Hole 1061B, the declinations from the two cores deviate by up to a maximum of ∼90° at 7.44 mcd. The records from holes 1062A and D also have similar behaviour to that observed from Hole 1061B following the first deviation. The amplitude of this declination variation during the excursion is slightly different between the two cores but this may be attributable to differences in resolution.

Hole 1062E records large declination swings. The most striking features are found in sections 2H2 and 2H3 of Hole 1062E. At 7.5 and 8.8 mcd, positions not near core breaks, the measured declination changes by up to ∼100°. This occurs at depths not associated with the Laschamp interval and is replicated in the shipboard measurements from Hole 1062E. There are no equivalent features in holes 1062A or D in either the continuous shipboard measurements or in this study's discrete measurements. Inspection of the cores does not reveal any strong evidence for physical disturbance or change in lithology. However, the absence of corroboration by the other two cores and any noticeable concurrent change in inclination in Hole 1062E suggests that these apparent changes in declination may have resulted from core twisting during drilling. Hole 1062E is therefore not used in further analysis of the directional behaviour of the geomagnetic field at this location.

5.4.2 Core Properties

Isothermal Remanent Magnetization (IRM) Acquisition

Stepwise application of an isothermal remanent magnetization (IRM) can be used to determine the coercivity spectrum, and thereby the constituent magnetic mineralogy, of sediments [*Kruiver et al.*, 2001; *Robertson and France*, 1994] (Figs. 5.7, 5.8). Following complete AF-demagnetization, 32 of the samples (16 each from Holes 1061B and 1062D) were subjected to progressive forward-field IRM acquisition using a Molspin Pulse Magnetizer at the University of Oxford (Fig. 5.9) up to the maximum applied field of the device (800 mT). The IRM was measured between each step using the same magnetometer as for the NRM measurement. A backfield IRM was then imparted with the same fields but in the opposite direction to the initial IRM.

The S-ratio is the ratio between the SIRM and the IRM imparted in a 300 mT backfield [*King and Channell*, 1991]. It is used to indicate the relative proportions of low and high coercivity magnetic minerals. The acquisition curves were modelled using the IRM-CLG spreadsheet program [*Kruiver et al.*, 2001]. The curves were best modelled as two-component mixtures comprising one 'low' and one 'high' coercivity component (Fig. 5.10). The modelled curves suggest that there is a 3-7% contribution to the IRM from the higher-coercivity component. The majority of the samples did not appear to attain complete saturation following application of an IRM at 800 mT. However, the majority of 'S-ratios' calculated using the IRM acquired at 800 mT differ by less than

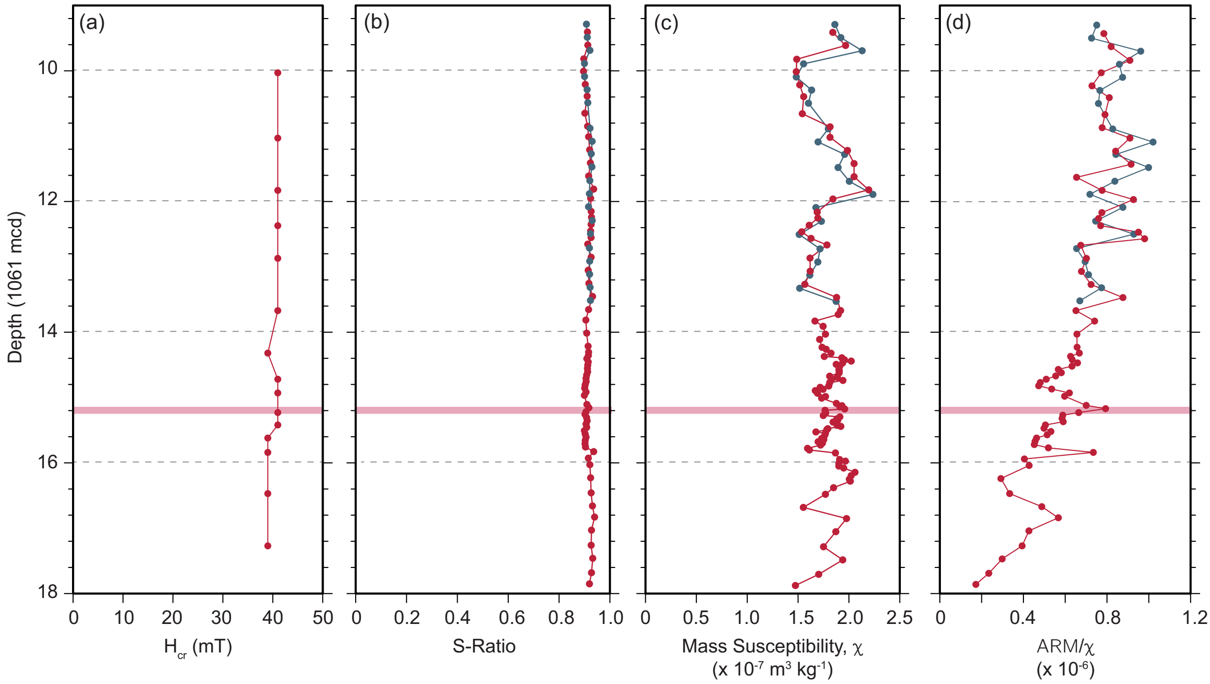

Figure 5.7: (a) Coercivity of remanence (H_{cr}) of measured samples from Hole 1061B. (b) S-ratio (where S-ratio$=-\mathrm{IRM}_{0.3\mathrm{T}}/\mathrm{IRM}_{0.8\mathrm{T}}$ for samples from Holes 1061B (red) and 1061C (blue). (c) Mass specific magnetic susceptibility (χ). (d) Anhysteretic magnetization divided by the measured magnetic susceptibility (ARM/χ). Directional excursion interval highlighted by pink bar defined as in Fig. 5.5.

0.2 from S-ratios estimated for the modelled curves. Subsequently reported 'S-ratios' are those where the S-ratio= -$\mathrm{IRM}_{300\ mT}/\mathrm{IRM}_{800\ mT}$.

All the samples have an S-ratio greater than 0.85, with the majority greater than 0.90 (Fig. 5.7b, 5.8b). The limited variability in the S-ratio indicates that the high coercivity component contribution, and therefore the relative concentration of low-coercivity remanence carriers, varies by less than an order of magnitude [*Frank and Nowaczyk*, 2008; *Heslop*, 2009]. The coercivity of remanence (H_{cr}), which is the backfield required to reduce a saturation IRM (SIRM) to zero, is essentially constant in both cores at ~40±2 mT (Figs. 5.7a, 5.8a). The low variability of the coercivity of remanence and S-ratio with depth indicates that there has been no significant change in magnetic mineral composition within the studied time interval. It is therefore unlikely that there has been any major change in magnetic mineral provenance, a conclusion also reached by [*Schwartz*

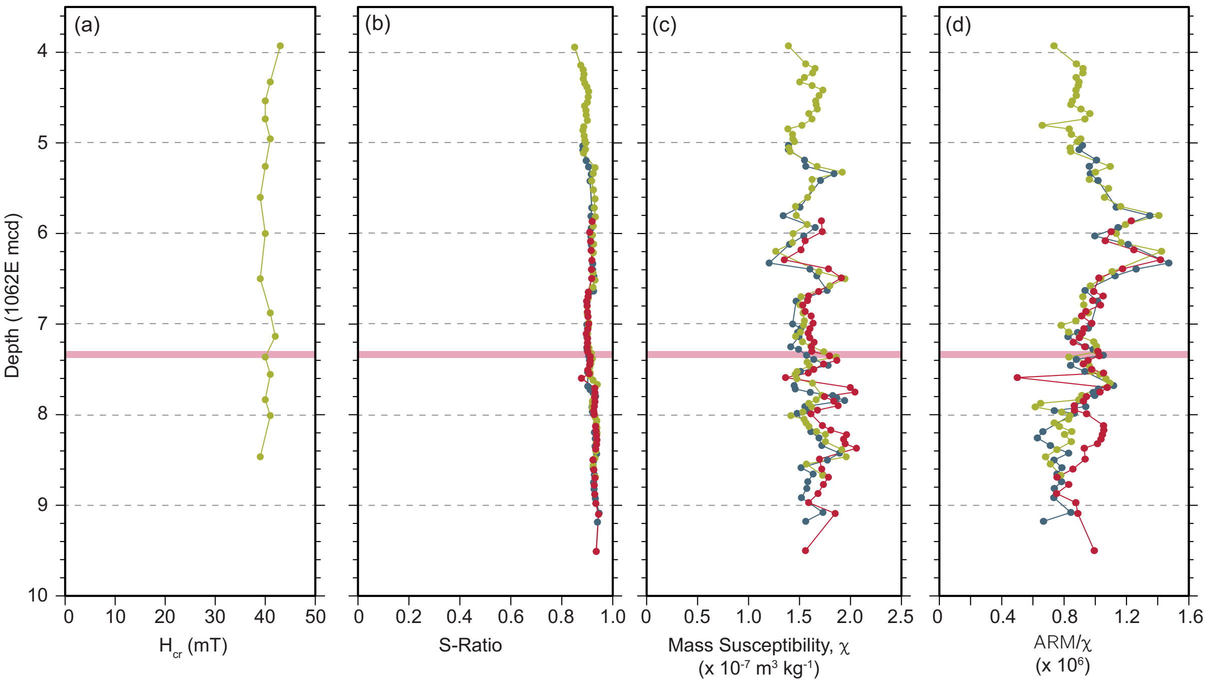

Figure 5.8: (a) Coercivity or remanence (H_{cr}) of measured samples in from Hole 1062D. (b) S-ratio for samples from Holes 1062A (blue), 1062D (green), and 1062E (red). (c) Mass specific magnetic susceptibility (χ). (d) Anhysteretic remanent magnetization divided by the measured magnetic susceptibility (ARM/χ). The directional excursion interval is highlighted by the pink bar as in Fig. 5.6.

et al., 1997]. Detailed rock magnetic analysis of samples from Blake-Bahama Outer Ridge cores, including energy dispersive analysis and X-ray diffraction studies suggest that the principal remanence carrier within the studied interval is most likely a low-titanium titanomagnetite with potentially some degree of maghaemitization [*Schwartz et al.*, 1997, 1998].

Magnetic Susceptibility

The magnetic susceptibility depends on the concentration, grain size and mineralogy of the remanence carriers. The results of the IRM acquisition experiments demonstrate that the magnetic mineralogy of the samples does not vary through time in the studied cores. The magnetic susceptibility of the sediment can therefore be used as a proxy for the concentration of magnetic grains in the sediment. The low-field magnetic susceptibility

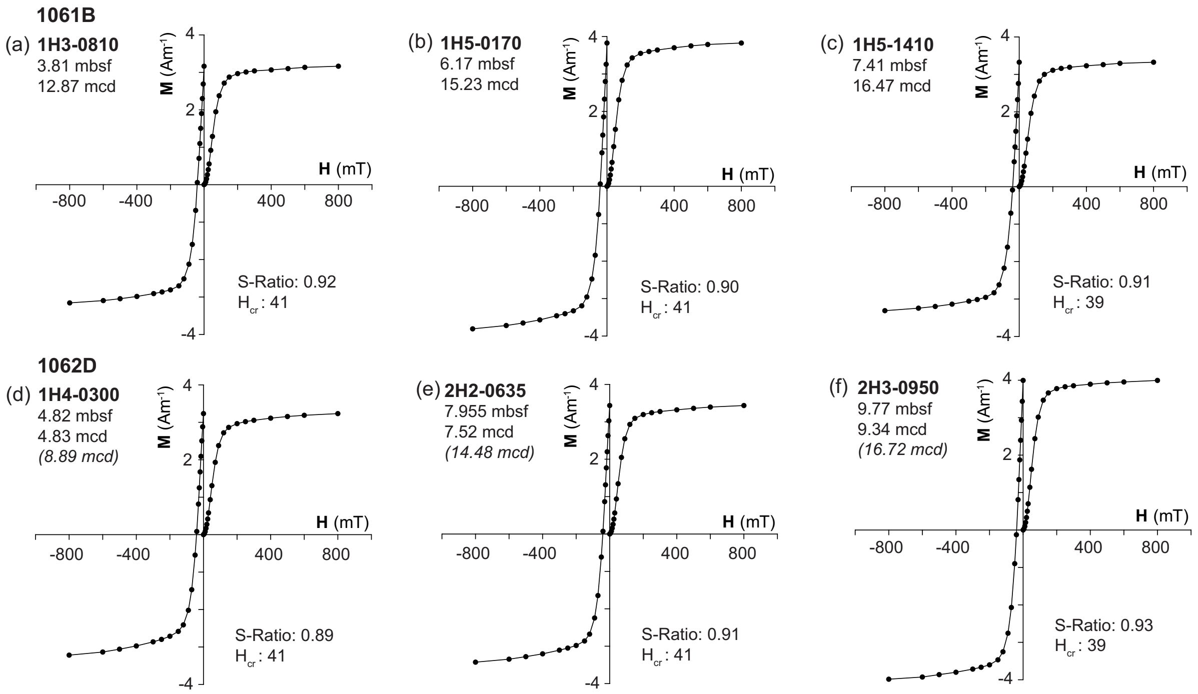

Figure 5.9: Examples of isothermal remanent magnetization (IRM) acquisition and backfield demagnetization curves from (a–c) Holes 1061B and (d–f) 1062D. Italicized mcd depths in (d–f) indicate equivalent depths in Hole 1062E.

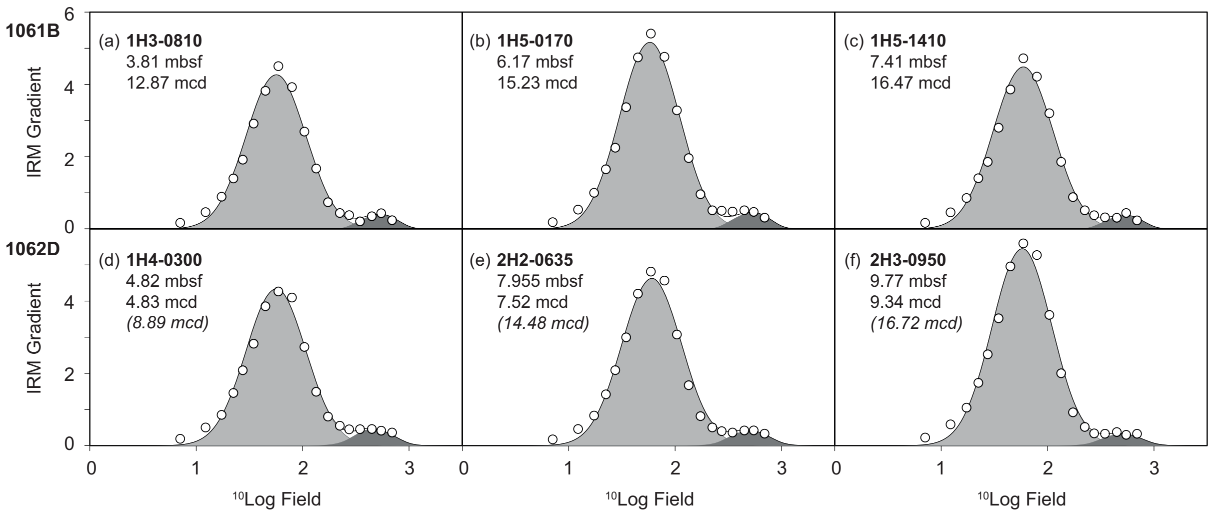

Figure 5.10: IRM gradient plots showing examples of modelled two-component IRM acquisition curves. The samples shown are the same as those in Figure 5.9. Open symbols show the bulk IRM distribution, and the solid line represents the combined signals of the modelled 'low' (light grey shading) and 'high' (dark grey) coercivity components.

of all samples was measured using an AGICO KLY-2 Kappabridge magnetic susceptibility meter at Oxford. The magnetic susceptibility varies by a factor of 60% within the range 0.8–1.4$\times10^{-7}$ m^3 kg^{-1} (Fig. 5.7c, 5.8c). As magnetic mineralogy is likely to have been relatively constant through time in these drift sediments [*Schwartz et al.*, 1997], these fluctuations in bulk susceptibility reflect some variability in the concentration and size of the magnetic particles over 1-5 kyr timescales.

Grain Size

The period 60-30 ka, MIS 3, is characterized by a dynamic, rapidly changing climatic system, particularly in the North Atlantic [*Dansgaard et al.*, 1993; *Rahmstorf*, 2002]. The drift sediments at the Blake-Bahama Ridge are created by deposition of material by the contour-hugging Western Boundary Undercurrent (Fig. 5.1) [*Heezen et al.*, 1966]. Bulk grain-size variation studies suggest that the vigour of the bottom-water flow was significantly increased between 60 and 35 ka, with associated increased variability [*Hoogakker et al.*, 2007; *Johnson et al.*, 1988]. It is therefore possible that magnetic grain size may also have varied throughout this interval.

The ratio of anhysteretic remanence magnetization to low-field magnetic susceptibility (ARM/χ) can be used to investigate first-order magnetic grain-size variation [*Banerjee et al.*, 1981] even in situations where high-coercivity components may contribute to the magnetization [*Frank and Nowaczyk*, 2008]. The magnitude of the ARM is relatively more sensitive to the finer grain-size fraction while low-field magnetic susceptibility (χ) is particularly sensitive to the coarser grain fraction [*King et al.*, 1982]. Thus, an increased relative proportion of fine- to coarse-grained magnetite is indicated by higher ARM/χ ratios [*King et al.*, 1983; *Schwartz et al.*, 1996]. An ARM was induced in the samples with a peak AF of 100 mT and a 0.1 mT direct current bias field using a DTECH-2000 AF unit at Imperial College London. The ARM was subsequently demagnetized at 20 mT.

ARM/χ for Holes 1061B and C is shown in Fig. 5.7d. Hole 1061B shows a steady

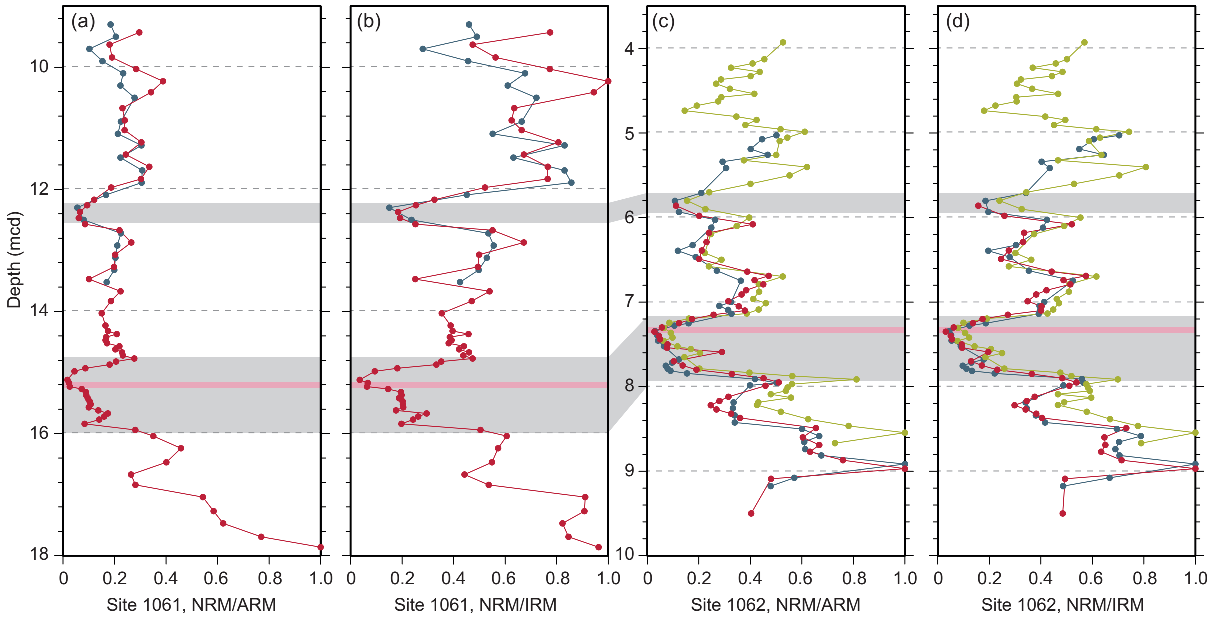

Figure 5.11: Relative palaeointensity proxies: from Holes 1061B (red) and 1061C (blue) derived by dividing the NRM by (a) the measured ARM and (b) IRM (normalized such that the maximum values for the records are equal to 1). Similarly, from Holes 1062A (blue), 1062D (green), and 1062E (red) normalized using (c) the measured ARM and (d) IRM. The grey shaded bars indicate a coarse correlation between major RPI features and the pink bars indicate the position of the directional excursion.

progression in time from lower ARM/χ values at the bottom of the record to significantly higher ARM/χ values at the top of the record. This trend indicates a decrease in the relative proportion of smaller magnetic grains through time. The ARM/χ record from Hole 1062D does not contain such a distinctive trend but between 5.5 and 6.5 mcd there is a double peak feature, suggesting two successive intervals with an increased proportion of finer magnetic grains. In both holes, the ARM/χ records are characterized by short-term variation of up to 30%.

5.4.3 Relative Palaeointensity Proxies

Excursions are not only directional features. Constraining the palaeointensity of the geomagnetic field is important if we are to understand excursional field behaviour [e.g. *Valet et al.*, 2008; *Wicht and Olson*, 2004] and the relationship to cosmogenic nuclide production [*Muscheler et al.*, 2005]. Sedimentary palaeomagnetic records can only provide estimates of relative palaeointensity (RPI) rather than absolute field variation [*Roberts et al.*, 2013; *Tauxe*, 1993]. Regardless, RPI can give important insight into the relationships between field orientation and intensity [*Valet et al.*, 2005]. Following *Tauxe* [1993], the NRM is normalized using ARM and IRM to account for changes in magnetic particle concentration. After imparting the ARM or IRM, samples were demagnetized and the remanent NRM, IRM and ARM after demagnetization at 20 mT were used to calculate the NRM/IRM and NRM/ARM palaeointensity proxies. All the records were normalized such that the maximum RPI is set equal to 1.

If changes in grain size are not accounted for by normalizing the NRM, they could adversely affect the estimate of relative palaeointensity [*Tauxe*, 1993]. Previous studies of sediments from the Blake-Bahama Outer Ridge have found that, despite normalizing the NRM, up to 25% of apparent low frequency palaeointensity variation may be attributable to grain size changes [*Schwartz et al.*, 1996]. To investigate how well environmental effects have been eliminated from the palaeointensity record, the squared coherence of the NRM/ARM and NRM/IRM with the grain size indicator, ARM/χ [*Tauxe*, 1993; *Tauxe and Wu*, 1990], is calculated using a multi-taper technique [*Bendat and Piersol*, 1986; *Thomson*, 1982]. The squared coherence between the NRM/ARM and ARM/χ, and NRM/IRM and ARM/χ, in Hole 1061B have average values of 0.64 and 0.41 respectively, indicating significant contamination of the palaeointensity record at Hole 1061B by changes in grain size.

The result of this contamination may be seen in the the NRM/ARM record for Hole 1061B, where the high NRM/ARM between 16 and 18 mcd is exaggerated relative to the rest of the record. The same feature in the NRM/IRM record for Hole 1061B and in the Site 1062 records is less dramatic. The over-estimation of this feature in the Hole 1061B NRM/ARM record is most likely an artefact, resulting from the higher proportion of finer magnetic grains within this interval.

However, normalization of the NRM was far more successful for Hole 1062D. The squared coherence between the NRM/ARM and ARM/χ, and NRM/IRM and ARM/χ, in holes from Site 1062 have average values of less than 0.15 and 0.10 respectively, indicating that the effects of grain size variation on the Site 1062 palaeointensity records are negligible. The two relative palaeointensity proxies, NRM/IRM and NRM/ARM are also in good agreement (Fig. 5.11). Although the two intervals with an increased proportion of finer magnetic grains at Site 1062 (between 5.5 and 6.5 mcd) coincide with an apparent RPI minimum, this RPI minimum is also seen at Site 1061 where there is no such feature in the ARM/χ record.

The impact of grain size changes on the RPI record from Hole 1061B means that this record must be treated with caution and highlights the complications resulting from environmental factors at the Blake-Bahama Outer Ridge [*Schwartz et al.*, 1996]. However, more confidence may be placed in the records from Site 1062. Much of the record from Site 1061 is in agreement with the more robust Site 1062 record and this broad agreement is employed to provide a coarse correlation between the two sites; Site 1061 on the Blake Ridge and Site 1062 on the Bahama Outer Ridge. Agreement between the RPI records despite the differences in sedimentological parameters, which precludes high-resolution correlation of the records, suggests that many of the major features in the RPI record are not primarily artefacts of sedimentological parameters.

All the records show a broad decrease in field intensity after $\sim$18 mcd (on the Site 1061 mcd scale), long before the directional excursion (Fig. 5.11). At 16 mcd, the field intensity drops relatively quickly to a broad, 1.2 m-wide minimum, at approximately one-third of the average field strength. Towards the end of this broad minimum, the field intensity drops to its lowest value, which corresponds to the main directional excursion. With the return to normal polarity, the field intensity rapidly recovers. This return to higher intensity is maintained until a second rapid drop to a minimum at 12.5 mcd. This coincides with a slight deviation in the inclination towards the equator, although this is not translated into a major deviation in VGP latitude. By 12 mcd, the field is back on a trajectory of recovery and the field intensity subsequently remains high until 9.6 mcd. This pattern is broadly similar to many observed in North Atlantic cores that span the Laschamp interval [*Laj et al.*, 2000, 2004, 2006] within uncertainties in the age models (Fig. 5.12) and confirms the results of previous studies of neighbouring cores [*Lund et al.*, 2005; *Schwartz et al.*, 1998].

5.5 Discussion

These measurements of discrete samples provide a record of the Laschamp excursion from ODP Sites 1061 and 1062. By linking the Blake Ridge palaeomagnetic record to the NGRIP GICC05 age model [*Andersen et al.*, 2006; *Svensson et al.*, 2008], the timing and duration of the Laschamp excursion at the Blake Ridge can be accurately constrained.

5.5.1 Timing of the Laschamp excursion

To define the excursion, it is assumed that any deviation of the VGP beyond a co-latitude of 45° from the geographic pole represents excursional behaviour [*Merrill and McFadden*, 1994]. The record from ODP Site 1061 dates the midpoint of the Laschamp excursion at 41.3 ka, where the midpoint is taken as the halfway point in time between the start and end of the excursional deviation. This is in good agreement with the most recent numerical age for the Laschamp excursion of 40.70±0.95 ka [*Singer et al.*, 2009] and other recent sedimentary records of the excursion [*Channell et al.*, 2012; *Nowaczyk et al.*, 2012]. The directional excursion to low VGP latitudes occurs at the end of the palaeointensity minimum and is associated with a sudden drop to the lowest field intensity. However, recovery of the field intensity following this directional excursion is rapid (within 1 kyr). Despite this rapid recovery, the field direction does not return entirely to its original direction, instead it maintains a slightly lower latitude (but not excursional)

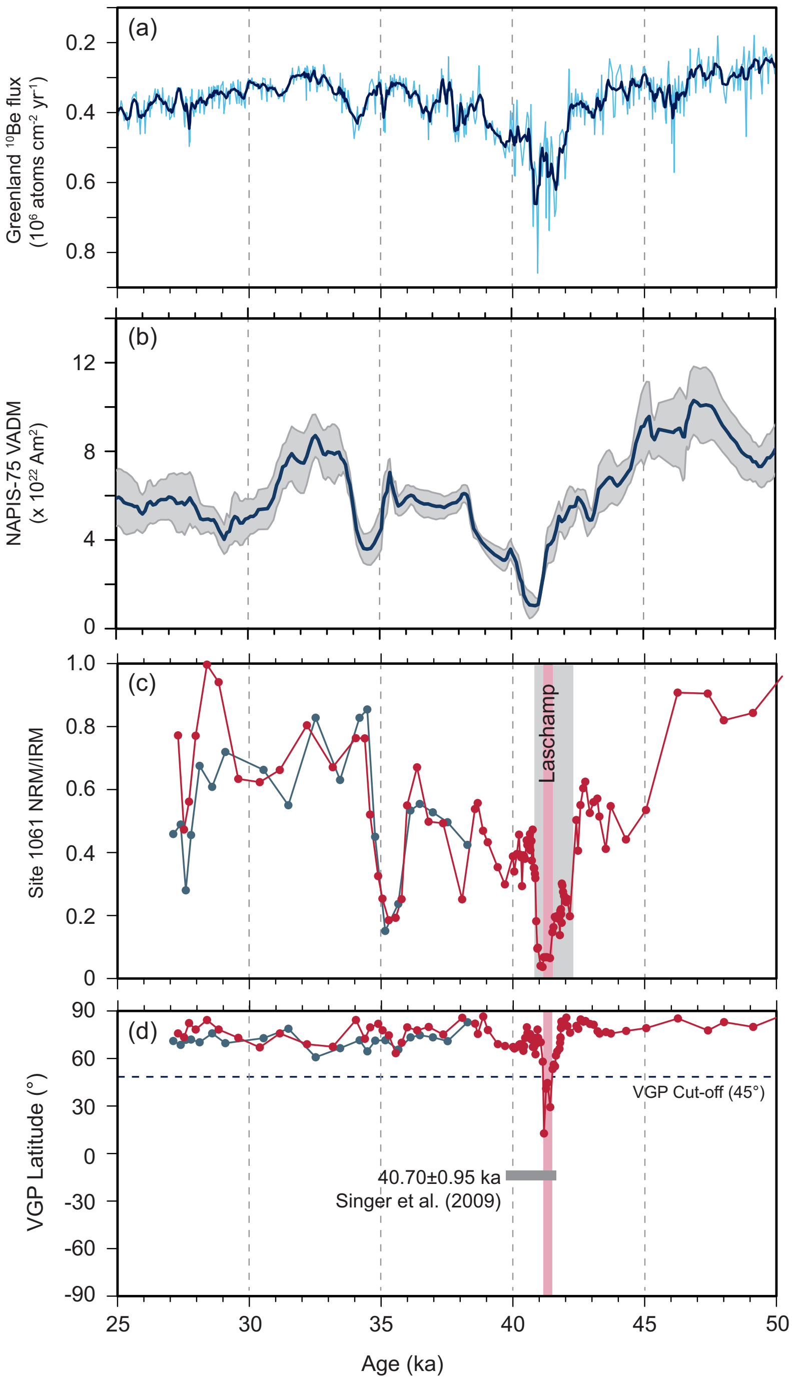

Figure 5.12: (a) Greenland ^{10}Be flux [*Muscheler et al.*, 2004], where the darker line is a 5-point weighted average. (b) The North Atlantic palaeointensity stack (NAPIS-75) [*Laj et al.*, 2000]. (c) The NRM/IRM record from Site 1061. (d) The VGP latitude record of the Laschamp excursion from Site 1061 compared to the mean age of the radiometrically dated French lavas [*Singer et al.*, 2009]. All records are placed on the Greenland GICC05 age model apart from the NAPIS-75 VADM stack, which is given on the GISP2 age model. Age offsets between some of the palaeointensity features can be accounted for within the age uncertainties of the different age models [*Svensson et al.*, 2006, 2008].

VGP for another few thousand years following the recovery in intensity (Fig. 5.12). The broad palaeointensity minimum associated with the Laschamp Excursion in the Blake Ridge record is in good agreement with atmospheric production records of the cosmogenic nuclide ^{10}Be [*Muscheler et al.*, 2005] (Figure 5.12).

5.5.2 Duration of the Laschamp excursion

The duration of the palaeointensity minimum associated with the Laschamp excursion is widely recognized as 'short' (less than 2 kyr) [*Laj et al.*, 2000; *Lund et al.*, 2005]. The duration of the directional deviation of the Laschamp excursion has been recently estimated to be less than 500 years [*Channell et al.*, 2012; *Nowaczyk et al.*, 2012]. Using the 45° cut-off of the first approach, the excursion in Hole 1061B spans an interval of 0.10 m (between 15.25 and 15.15 mcd), which corresponds to a duration of 240 years (Fig. 5.12). Alternatively, an adaptive approach may be used to determine when the VGP deviates beyond that expected due to secular variation [*Vandamme*, 1994]. Performing this iterative calculation on the record from Hole 1061B an excursional VGP co-latitude of 34.4° was determined. Using this approach, the excursional interval in Hole 1061B spans 0.19 m (between 15.32 mcd and 15.12 mcd), which corresponds to a longer duration of 440 years.

Directional records of the excursion at Sites 1061 and 1062 exhibit only a short deviation to low VGP latitudes, away from what might be expected during 'normal' secular deviation. Hole 1061B records VGPs that only reach 12°, whereas Hole 1062A records the lowest VGP latitude of 21°. Nearby records of the Laschamp excursion from the Blake Ridge [*Lund et al.*, 2005] and Site 1063 on the Bermuda Ridge [*Channell et al.*, 2012], exhibit VGPs that reach high southern latitudes. It has been suggested that smoothing can arise due to a post-depositional remanent magnetization (pDRM) lock-in process [*Roberts and Winklhofer*, 2004]. However, at such high sedimentation rates (>40 cm kyr^{-1}), there is unlikely to be a significant associated lock-in depth.

Each 2 cm-width sample measurement within the excursional interval represents an integrated signal of at least 50 years. Even with such high sedimentation rates and sampling resolution, the record from the Blake Ridge is potentially incomplete, indicating a short directional Laschamp excursion, close to 250 years in duration. The absence of fully reversed VGPs therefore reinforces previous short-duration estimates of the excursional duration [*Nowaczyk et al.*, 2012]. The directional excursion sits within a broader, ~2 kyr palaeointensity minimum. However, within this minimum, the lowest field intensity associated with the directional excursion is also recorded over a short (~500 years) interval.

Previously published data from Site 1062 [*Bourne et al.*, 2012a] on the Bahama Outer Ridge and Site 1063 [*Channell et al.*, 2012; *Knudsen et al.*, 2006, 2007] on the Bermuda Ridge provide high-resolution records of other excursions. Although estimates for the duration of the directional Blake [*Bourne et al.*, 2012a; *Channell et al.*, 2012] and Iceland Basin excursions vary [*Channell et al.*, 2012; *Knudsen et al.*, 2007], they all exceed the duration of the Laschamp excursion. High-resolution, discrete sample records analysed using ^{230}Th-normalization methods suggest a duration of 6.5 ± 1.3 kyr for the Blake excursion (as described in Chapter 4). Similarly, using ^{230}Th-normalization, *Knudsen et al.* [2007] estimated the duration of the Iceland Basin excursion to be 6.8 ± 0.5 kyr. Although estimates for the durations of these other excursions vary at these nearby locations, the duration of the Laschamp directional excursion is clearly shorter than either the Blake or the Iceland Basin excursions. Furthermore, unlike the short-duration Laschamp excursion at Site 1062, the Blake excursion at Site 1062 is characterized by fully-reversed polarity VGPs that cluster around the south geographic pole for several thousand years before a rapid return to normal polarity directions [*Bourne et al.*, 2012a; *Smith and Foster*, 1969]. This difference in duration might support the assertion that the Laschamp represents a different category of excursion (Class I) to the Blake excursion (Class II) [*Lund et al.*, 2001a].

5.5.3 Sensitivity to field intensity

Palaeomagnetic records have documented the existence of a later excursion, named the 'Mono-Lake' excursion, following the Laschamp excursion [*Bonhommet and Zähringer*, 1969; *Denham and Cox*, 1971; *Liddicoat and Coe*, 1979]. Although the record of the 'Mono-Lake' is contentious at its type locality [*Cox et al.*, 2012; *Zimmerman et al.*, 2006], there is clear evidence of an excursional interval following the Laschamp at a number of other locations including sedimentary records from the Irminger Basin [*Channell*, 2006] and the Black Sea [*Nowaczyk et al.*, 2012], and volcanic records from the Auckland Volcanic Field, New Zealand [*Cassata et al.*, 2008; *Cassidy and Hill*, 2009], Hawaii [*Teanby et al.*, 2002] and Tenerife [*Kissel et al.*, 2011]. Estimates for the age of this event range from 32 ka [*Cassata et al.*, 2008] to 34.5 ka [*Nowaczyk et al.*, 2012].

According to the Blake Ridge record, a directional excursion is only apparent at the end of the RPI minimum associated with the Laschamp excursion when the field intensity drops to its lowest value. Despite high-sedimentation rates, there is no evidence for another, later, directional excursion. At ~35.5 ka the field intensity is reduced to the same level as the RPI minimum just before the Laschamp directional excursion. Although this reduction in field intensity is commonly attributed to the 'Mono-Lake' excursion [*Laj et al.*, 2000, 2004], on the chronology used in this study it is slightly older than the estimates for the Mono-Lake event at other locations. This later minimum is shorter than the Laschamp excursion minimum. Unlike the Laschamp palaeointensity minimum, the field does not then weaken further and there is no evidence for a directional excursion at this time, merely a slight shallowing of inclination in the Hole 1061B record. It is often observed that directional behaviour of the geomagnetic field is closely linked to the field intensity [e.g. *Laj and Channell*, 2007; *Valet and Meynadier*, 1993; *Valet et al.*, 2005]. Here, the directions observed are highly dependent upon the severity of the intensity drop. Despite a significant fall in palaeointensity at ~35.5 ka, the absence of any directional excursion suggests that even this intensity decrease is insufficient to dramatically change the local field direction.

5.6 Conclusions

By applying a chronology linked to the NGRIP δ^{18}O record, this chapter presents a palaeomagnetic record from the Blake Ridge at ODP Sites 1061 and 1062 tied to a strong associated chronology. The Laschamp Excursion occurred at 41.3 ka, in good agreement with the most recent estimates for the age of the excursion from volcanic lava and sedimentary archives [*Channell et al.*, 2012; *Nowaczyk et al.*, 2012; *Singer et al.*, 2009], and contemporaneous with a ^{10}Be production peak [*Ménabréaz et al.*, 2011; *Muscheler et al.*, 2004]. The estimate for the duration of the Laschamp directional excursion presented here (~250 years) is shorter than the duration of the Blake and Iceland Basin excursions (0.9–6.8 kyr) [*Bourne et al.*, 2012a; *Channell et al.*, 2012; *Knudsen et al.*, 2007].

Unlike the Blake excursion at the same location, Sites 1061 and 1062 fail to record fully reversed polarity directions associated with the Laschamp excursion [*Bourne et al.*, 2012a]. This is attributed to smoothing of the sedimentary record compounded by the shortness of the Laschamp excursion [e.g. *Roberts and Winklhofer*, 2004]. The difference in character of the Laschamp compared to the Blake and Iceland Basin excursions supports the assertion by *Lund et al.* [2001a] that the Laschamp excursion represents a different category of excursion that is more closely aligned with secular variation processes. Directional field behaviour is closely linked to geomagnetic field intensity. A significant global drop in field intensity, where the field intensity collapses to a minimum, is observed for all excursional directions recorded in the Blake Ridge sediments.

Chapter 6

^{230}Th$_{xs}$ Normalization at Site 1061

6.1 Introduction

^{230}Th normalization has become a valuable tool to estimate the vertical flux of material to the sea-floor [e.g. *Francois et al.*, 2004; *Knudsen et al.*, 2007; *Marcantonio et al.*, 1999; *McManus et al.*, 1998]. In Chapter 4, ^{230}Th-normalization was used to derive an age model for the palaeomagnetic record of the Blake excursion (~125 ka) on the Blake-Bahama Outer Ridge in the western North Atlantic. Chapter 5 documents the Blake Ridge record of the later Laschamp excursion (~41 ka) but, rather than use ^{230}Th-normalization, a high-resolution correlation to the Antarctic NGRIP δ^{18}O [*Svensson et al.*, 2006] is used to construct the age model [*Bourne et al.*, 2013]. However, uranium-thorium measurements were also conducted on samples from the Laschamp interval at Site 1061. This chapter discusses these measurements and the reason why they were not used to construct the Site 1061 age model in Chapter 5.

The Blake Ridge is a hemipelagic sediment drift located in the western North Atlantic Ocean, characterized by particularly high sedimentation rates (> 40 cm kyr, see Section 5.5.2) between 50 and 40 ka. Ocean drilling program (ODP) Site 1061 is located on the tip of the Blake Ridge at a seawater depth of 4047 mbsl. Uranium-thorium measurements were made on the samples from ODP Site 1061 with the intention of constructing a high-resolution age model to constrain the temporal behaviour of the Earth's magnetic field during the Laschamp excursion.

6.2 $^{230}Th_{xs}$ Calculations and Results

Uranium and thorium measurements, including ^{230}Th, were carried out on 18 samples from ODP Hole 1061B, between 13.27 mcd and 17.27 mcd [*Shipboard Scientific Party*, 1998a]. For each sample, 0.1 g of dry sediment was dissolved following the method described in Section 2.5.1 [*Thomas et al.*, 2007]. For two of the samples (1H4-0270, 13.83 mcd; and 1H5-1180, 16.24 mcd), another 0.1 g was taken and dissolved separately to test repeatability. Column chemistry was used to separate uranium and thorium from the solutions. The samples were spiked with a mixed ^{229}Th and ^{236}U spike and concentrations of the isotopes ^{234}U and ^{238}U were measured statically and ^{230}Th and ^{232}Th were subsequently measured dynamically, on a Nu Instruments ICP-MS at the Department of Earth Sciences, University of Oxford. For a more complete description of the methods employed see Section 2.5.

Following the approach described in Chapter 3, the U-Th measurements were analysed using the XSage software. The contributions to the total ^{230}Th activity from ^{230}Th supported by detrital U ($^{230}Th_{det}$) and ^{230}Th ingrown from authigenic U ($^{230}Th_{auth}$) were calculated using XSage and subtracted from the total ^{230}Th concentration to determine the concentration of the $^{230}Th_{xs}$.

To correct for radioactive decay, a low-resolution age model was constructed for Hole 1061B using the correlation to GRIP. Rather than employing the full correlation outlined in Section 5.3.2, two age constrained boundaries were chosen to construct a simple age model (Figure 6.1). The younger age constraint was placed at 13.5±0.1 mcd and assigned an age of 38.2±0.7 ka on the NGRIP GICC05 age scale [*Svensson et al.*, 2006]. The older age constraint was placed at 17.1±0.1 mcd and assigned an age of 46.9±1.0 ka, also based on the NGRIP age scale. Using this age model as an initial input, the $^{230}Th_{xs}$ determined

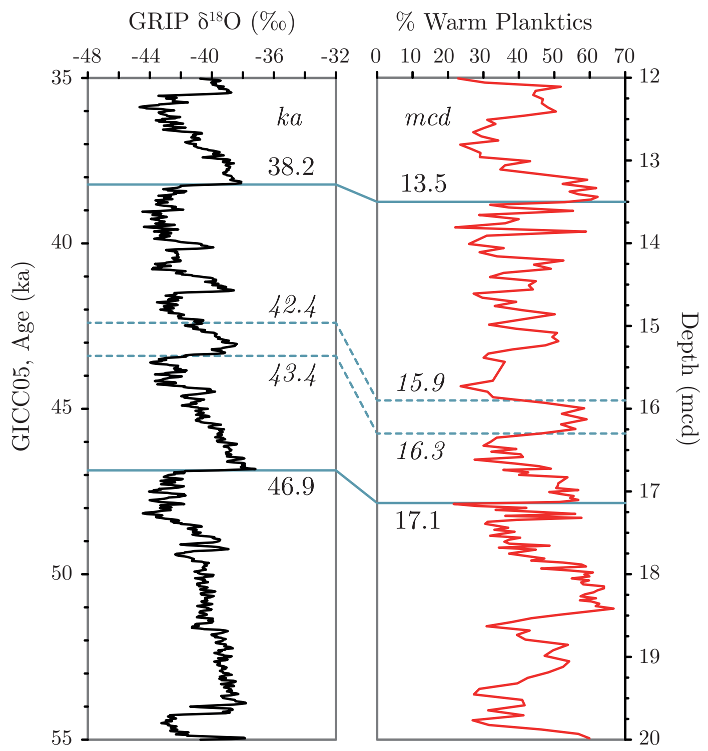

Figure 6.1: Chronology for Hole 1061B used to calculate $^{230}Th_{xs}$. Correlation between GRIP $\delta^{18}O$ record [*Johnsen et al.*, 1992] on the GICC05 timescale [*Svensson et al.*, 2006] and the abundance of warm planktic foraminefera [*Vautravers et al.*, 2004] on the Site 1061 (mcd) depth scale derived from the fully correlated age model determined in Section 5.3.2, achieved using the 'MATCH' protocol of *Lisiecki and Lisiecki* [2002]. The uppermost and lowermost stratigraphic bounds (labelled, solid blue lines) were used to determine a simple age model to calculate $^{230}Th_{xs}$ using XSage. Middle two stratigraphic bounds (dashed, italics) were used to calculate focussing within intermediate intervals.

for each sample was then corrected for its own decay via an iterative process to obtain the initial $^{230}Th^{0}_{xs}$ using the XSage program (Chapter 3). The measured uranium and thorium activities are presented in Table 6.1, along with the ^{230}Th components calculated using XSage.

The XSage calculations indicate that there is no ^{230}Th derived from authigenic uranium in the samples measured. This is expected as most deep sea sediments deposited under oxic conditions tend not to accumulate authigenic uranium [*Francois et al.*, 2004]. Samples for which repeat measurements were made gave $^{230}Th_{xs}$ determinations within

Sample ID	Depth	Measured Activities										XSage Calculations			
	(mcd)	^{238}U	2 s.e.	^{234}U	2 s.e.	^{232}Th	2 s.e.	^{230}Th	2 s.e.	$^{234}U/^{238}U$	2 s.e.	$^{230}Th_{det}$	2 s.d.	$^{230}Th_{xs}$	2 s.d
1H3-1210	13.27	1.42	0.002	1.37	0.009	2.29	0.033	4.20	0.052	0.97	0.007	1.42	0.19	2.78	0.20
1H4-0110	13.67	1.85	0.005	1.78	0.015	2.58	0.040	3.94	0.060	0.96	0.009	1.60	0.22	2.35	0.23
1H4-0270	13.83	1.78	0.003	1.72	0.013	2.58	0.040	3.75	0.056	0.97	0.007	1.59	0.22	2.16	0.23
1H4-0270	13.83	1.80	0.002	1.73	0.011	2.62	0.037	3.82	0.055	0.96	0.006	1.62	0.22	2.20	0.23
1H4-0470	14.03	1.74	0.002	1.66	0.006	2.62	0.028	3.57	0.032	0.95	0.004	1.62	0.22	1.95	0.22
1H4-0670	14.23	1.70	0.003	1.63	0.012	2.61	0.035	3.41	0.045	0.96	0.007	1.61	0.22	1.80	0.22
1H4-0960	14.52	1.71	0.002	1.63	0.010	2.64	0.037	3.37	0.043	0.96	0.006	1.64	0.22	1.74	0.23
1H4-1260	14.82	1.54	0.003	1.47	0.013	2.49	0.023	3.88	0.033	0.96	0.009	1.54	0.21	2.34	0.21
1H5-0060	15.12	1.65	0.002	1.62	0.011	2.42	0.035	3.66	0.050	0.98	0.007	1.50	0.20	2.16	0.21
1H5-0360	15.42	1.62	0.002	1.55	0.011	2.50	0.031	3.98	0.039	0.96	0.007	1.55	0.21	2.43	0.21
1H5-0660	15.72	1.52	0.002	1.48	0.010	2.34	0.024	4.02	0.041	0.98	0.007	1.45	0.20	2.58	0.20
1H5-0980	16.04	1.69	0.003	1.64	0.014	2.49	0.038	4.11	0.049	0.97	0.008	1.54	0.21	2.57	0.21
1H5-1180	16.24	1.59	0.003	1.52	0.013	2.55	0.036	3.43	0.042	0.96	0.008	1.58	0.22	1.85	0.22
1H5-1180	16.24	1.60	0.003	1.54	0.014	2.52	0.033	3.53	0.045	0.96	0.009	1.56	0.21	1.97	0.22
1H5-1410	16.47	1.50	0.002	1.43	0.010	2.45	0.032	3.65	0.039	0.96	0.007	1.52	0.21	2.14	0.21
1H6-0110	16.67	1.24	0.001	1.21	0.007	2.23	0.028	3.39	0.046	0.98	0.006	1.38	0.19	2.01	0.19
1H6-0280	16.84	1.45	0.002	1.39	0.009	2.55	0.035	2.98	0.033	0.96	0.006	1.58	0.22	1.40	0.22
1H6-0710	17.27	1.59	0.002	1.55	0.012	2.44	0.036	3.67	0.054	0.98	0.008	1.51	0.21	2.16	0.21

Table 6.1: Measured isotope activities and activity ratios and ^{230}Th components calculated using XSage. Isotopic activities given in dpm g^{-1}

Sample						Interval			
ID	Depth (mcd)	$^{230}Th^0_{xs}$ (dpm g^{-1})	2 s.d.	Age (ka)	2 s.d.	Upper (rmcd)	Lower (rmcd)	Sed. Rate (cm kyr^{-1})	2 s.d.
1H3-1210	13.27	3.91	0.28	37.58	1.52	13.27	13.47	37.16	2.37
1H4-0110	13.67	3.35	0.33	38.68	1.58	13.47	13.75	43.59	2.65
1H4-0270	13.83	3.09	0.32	39.08	1.59	13.75	13.93	47.23	2.87
1H4-0270	13.83	3.15	0.33	39.08	1.59	13.75	13.93	46.38	2.79
1H4-0470	14.03	2.82	0.32	39.52	1.62	13.93	14.13	52.05	3.06
1H4-0670	14.23	2.61	0.33	39.93	1.64	14.13	14.38	56.34	3.69
1H4-0960	14.52	2.53	0.33	40.49	1.66	14.38	14.67	58.06	3.97
1H4-1260	14.82	3.44	0.32	41.17	1.70	14.67	14.97	42.69	2.49
1H5-0060	15.12	3.21	0.31	41.91	1.73	14.97	15.27	46.01	2.79
1H5-0360	15.42	3.64	0.33	42.68	1.77	15.27	15.57	40.60	2.44
1H5-0660	15.72	3.90	0.31	43.53	1.81	15.57	15.88	37.99	2.40
1H5-0980	16.04	3.93	0.34	44.46	1.86	15.88	16.14	37.80	2.39
1H5-1180	16.24	2.86	0.34	44.97	1.89	16.14	16.36	52.13	3.35
1H5-1180	16.24	3.03	0.34	44.97	1.89	16.14	16.36	49.07	3.06
1H5-1410	16.47	3.31	0.33	45.50	1.92	16.36	16.57	45.04	2.73
1H6-0110	16.67	3.13	0.31	45.98	1.94	16.57	16.75	47.67	2.98
1H6-0280	16.84	2.19	0.33	46.31	1.96	16.75	17.06	68.38	5.76
1H6-0710	17.27	3.42	0.33	47.20	2.01	17.06	17.27	43.79	2.82

Table 6.2: Calculated $^{230}Th^0_{xs}$ activity (dpm g^{-1}) and thorium normalized sedimentation rate for Hole 1061B. Calculated age (ka) is determined using only the simple two-point age model and the ^{230}Th-normalized sedimentation rate.

6% of one another, within the reported ∼10% 2σ uncertainties for the $^{230}Th_{xs}$.

The sedimentation rate for each depth interval was then calculated (Table 6.2, Figure 6.2a) using the following expression:

$$F_n = F_a \times \frac{\overline{Th}}{Th_n} \quad . \tag{6.1}$$

where F_n is the sedimentation rate for the sample interval; Th_n is the concentration of $^{230}Th^0_{xs}$ in that sample interval; F_a is the average sedimentation rate in cm kyr^{-1} between the tie-points; and $\overline{Th}$ is the depth-interval-weighted average concentration of $^{230}Th^0_{xs}$ between the tie-points.

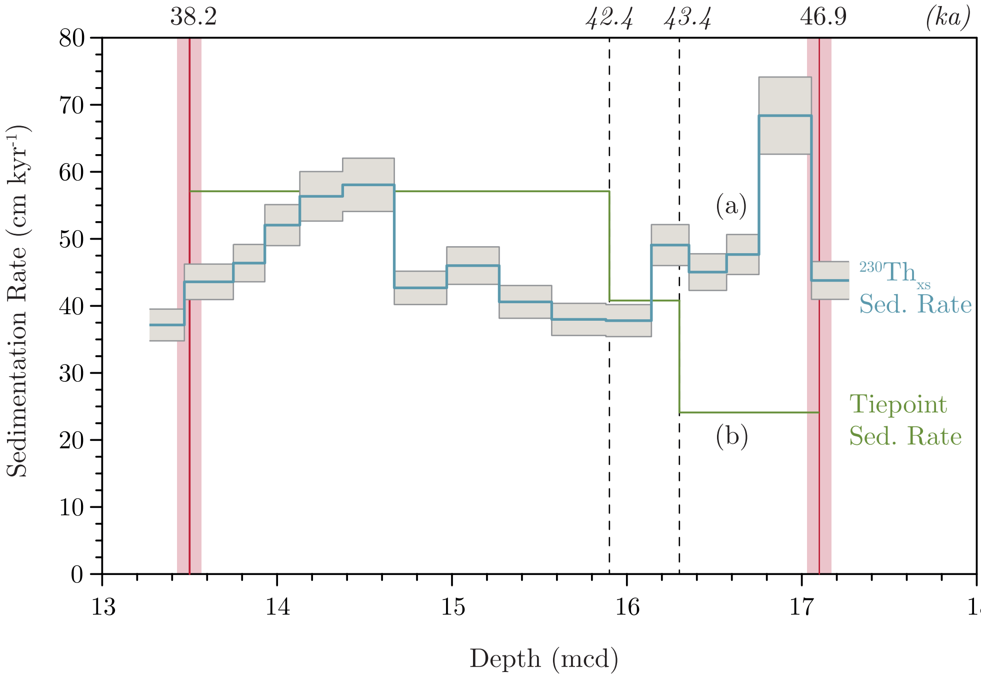

Figure 6.2: Sedimentation rates derived using ^{230}Th-normalization (blue line, with uncertainties shaded in grey) using only the uppermost and lowermost tie-points (indicated by red lines with pink bars to indicate uncertainties) and (b) using all the tie-points (additional two tie-points indicated by dashed lines and labelled in italics) but without ^{230}Th-normalization (green line). Tie-point ages given above in ka.

6.3 Discussion

One of the principal assumptions of using ^{230}Th to reconstruct sedimentation rate is that the focussing remains constant between the selected tie-points (see Section 3.2.3). Across the interval 13.30–17.14 mcd (38.2–46.9 ka), the calculated focussing factor (Eq. 1.43), Ψ, is equal to 9.5. That is, that the total amount of $^{230}Th^0_{xs}$ in the sediment column is 9.5 times greater than that produced in the equivalent time interval in the water column above. Focussing during this interval is therefore high: more than 90% of the sediment is transported laterally to the site. This would not be reflected in sedimentation rates calculated using ^{230}Th-normalization as any laterally transported sediment would have a similar $^{230}Th^0_{xs}$ concentration to that sourced from the water column above [*Francois et al.*, 2004; *Lyle et al.*, 2005].

Significant variation in sediment focussing might be predicted for this interval. Unlike marine isotope stage (MIS) 5 (see Chapter 4), the period 60-30 ka, MIS 3, is characterized by a dynamic, rapidly changing climatic system, particularly in the North Atlantic [*Dansgaard et al.*, 1993; *Rahmstorf*, 2002]. The drift sediments at the Blake-Bahama Ridge are created by deposition of material by the contour-hugging Western Boundary Undercurrent (Figure 4.2a) [*Heezen et al.*, 1966]. Changes in the flow-speeds of this deep current could affect the degree of focussing at the Blake-Bahama Ridge sites. Grain-size variation studies suggest that the vigour of the bottom-water flow was significantly increased between 60 and 35 ka, with associated large-scale variability [*Hoogakker et al.*, 2007; *Johnson et al.*, 1988]. Such conditions are unlikely to provide an environment where the degree of focussing remains constant.

One way by which sediment focussing may be constrained is by the use of additional dated stratigraphic intervals, not used to determine the ^{230}Th-normalized age model, which can be used to indicate whether focussing is variable at a site with time or changes in climate. The existence of an independent high-resolution age model across the interval, using the correlation of the abundance of warm planktic foraminifer [*Vautravers et al.*, 2004] to the NGRIP δ^{18}O record [*Svensson et al.*, 2006] (Chapter 5), allows us to test whether focussing has remained constant throughout the Laschamp interval at Site 1061. Two additional tie-points from the GICC05 age model in Chapter 5 (15.9 $\pm$ 0.1 mcd, 42.4 $\pm$ 0.9 ka; and 16.3 $\pm$ 0.1 mcd, 43.4 $\pm$ 0.9 ka, see Figure 6.1) may then be used to constrain the focussing within three intervals (Table 6.3).

As Table 6.3 demonstrates, the focussing factor in the youngest interval (42.4–38.2 ka) is 12.5, more than double the focussing factor of 4.6 in the oldest interval (46.9–43.4 ka). As a result, the effective sedimentation rate is more than doubled during the youngest interval compared to the oldest (using the NGRIP correlation) expanding this interval proportionally (as may be seen in Figure 6.1). The different estimates of sedimentation rate derived using the tie-points and ^{230}Th-normalization are presented in Figure 6.2. ^{230}Th-normalization, using only the original two tie-points, is 'blind' to the change in

Top Depth (mcd)	Age (ka)	Bottom Depth (mcd)	Age (ka)	Tiepoint Sed. Rate (cm kyr^{-1})	$^{230}Th_{xs}$ Sed. Rate (cm kyr^{-1})	focussing Factor Ψ
13.5	38.2	15.9	42.4	57.1	42.3	12.5
15.9	42.4	16.3	43.4	40.8	38.9	9.7
16.3	43.4	17.1	46.9	22.8	47.5	4.6

Table 6.3: Average sedimentation rates for three intervals in Hole 1061B derived firstly, using the two additional intermediate NGRIP tie-points and secondly, using the ^{230}Th-normalized sedimentation rates. Focussing factors were calculated for intermediate intervals using the additional stratigraphic tie-points.

focussing and so the sedimentation rates originally calculated fail to record the dramatic change in sedimentation rate.

6.4 Conclusions

Sediment focussing was found to vary significantly within the studied interval of Hole 1061B. Thorium normalization was therefore not a robust means to constrain the sedimentation rates in Hole 1061B. The age model determined using ^{230}Th-normalized sedimentation rates for this core is therefore unreliable and offers no advantage over the NGRIP correlation achieved in Chapter 5. The age model determined using the full NGRIP correlation was therefore used to calculate the duration of the Laschamp excursion.

A constant focussing factor is a primary assumption used in ^{230}Th-normalization. This chapter highlights the importance of ensuring that the degree of focussing has remained constant through time within the interval of study. Where possible, one of the easiest and robust means of testing this assumption is to use additional stratigraphic tie-points not used to calculate the thorium-normalized sedimentation rates.

Chapter 7

Pacific Cores

7.1 Introduction

A geographically distributed set of observations are required to examine the global character of the geomagnetic field during an excursion. If excursions result from a similar mechanism to that which causes secular variation it is likely that reversed polarities could be relatively localised features, where the local field in one region may be simultaneously in the opposite polarity to that in another [*Whitney*, 1971]. Alternatively, globally reversed VGPs, occurring simultaneously in both hemispheres, indicate a reversed dipole field and are likely to be the result of a completely different mechanism to that controlling secular variation [*Brown et al.*, 2007; *Merrill et al.*, 1996]. What constitutes the required amount of evidence to confirm either possibility remains controversial. *Merrill and McFadden* [1994] and *Laj and Channell* [2007], for example, consider the Laschamp excursion (∼41 ka) as a reversal excursion and as a polarity interval respectively.

In contrast to the Laschamp excursion, the Blake excursion (∼125 ka) is relatively poorly documented. Two records of the Blake excursion, one observed in marine sediments from the Mediterranean [*Tric et al.*, 1991] and the other in lacustrine sediments from Pringle Falls, Oregon [*Herrero-Bervera and Helsley*, 1993], showed VGPs that could be correlated between the two sites. The distance between these sites, combined with the similarity of the records, prompted the authors to suggest that the transitional field contained a significant dipolar component during the Blake excursion [*Tric et al.*, 1991] and that the Blake excursion could, and should, be used as a global stratigraphic marker [*Herrero-Bervera and Helsley*, 1993]. Although the record of the Blake excursion from Site 1062 on the Blake Ridge [*Bourne et al.*, 2012a, see Chapter 4] suggests that there may be a dipole component during at least the reversed phase, these early attempts to determine the global nature of the Blake excursion, on the basis of two sites, were perhaps rather premature. The spatial distribution of currently available data and the relatively poor age-control means that no firm conclusions can be drawn as to the global field during the Blake event. Global coverage has historically been rather limited, with a particular paucity of sites from the Southern Hemisphere [*Roberts*, 2008]. To complement the Atlantic records of the Blake excursion obtained from Leg 172 (see Chapter 4), a number of cores were sampled from Ocean Drilling Program (ODP) Sites located in the Pacific Ocean. By obtaining widely-distributed, high-resolution palaeomagnetic records, accurately constrained in time, we hope to construct a global picture of geomagnetic field behaviour during the Blake excursion and more clearly resolve the nature of this episode.

7.2 Core Choice

A survey was conducted to determine which marine sediment cores would be of interest for detailed palaeomagnetic study of the Blake excursion. Potential cores for sampling were selected on criteria intended to provide the highest-resolution, well-dated, palaeomagnetic records of the Blake excursion.

A number of factors control the quality of the palaeomagnetic record. Typically, sediments with a high terrigenous input provide the best mineralogy for recording the Earth's magnetic field because they contain a high proportion of fine-grained magnetic minerals. Carbonate dominated sediments are poor recorders of the geomagnetic field

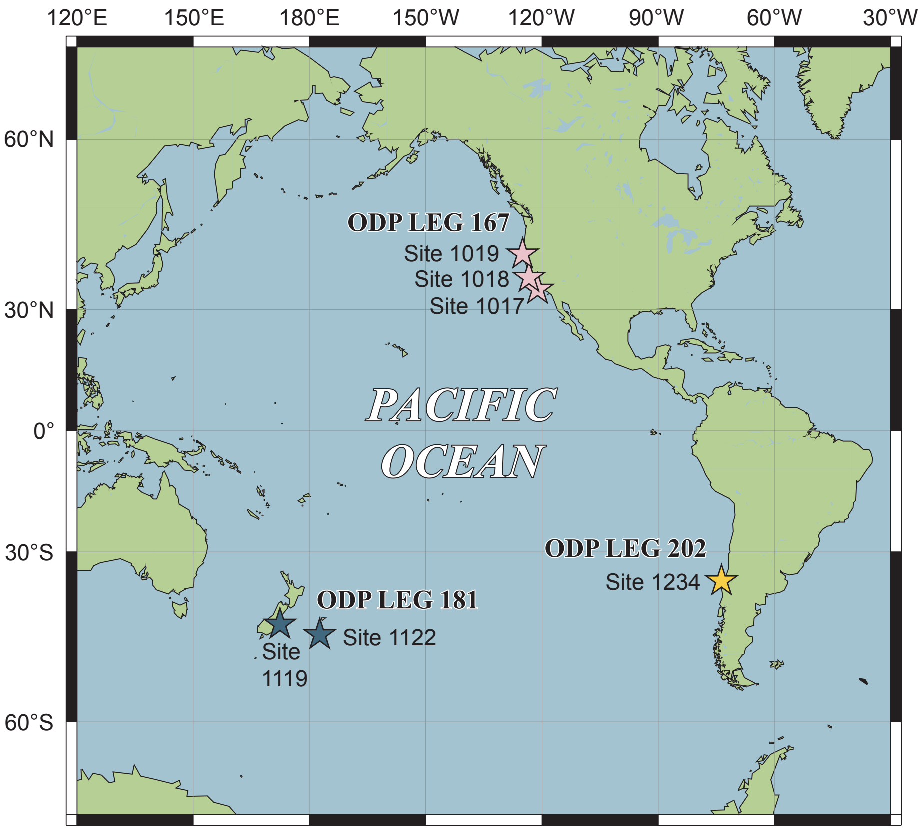

Figure 7.1: Location map of the three Pacific legs sampled in this study.

because they have a low concentration of magnetic grains and therefore a low intensity of magnetization. However, sediments with very low carbonate content are far harder to date accurately, as the absence of sufficient carbonate material precludes the determination of an oxygen isotope stratigraphy [e.g. *Vautravers et al.*, 2004]. Therefore, although cores with a high proportion of detrital material were selected for sampling, these were limited to those for which the potential to construct oxygen isotope stratigraphies had already been demonstrated.

A high sedimentation rate is vital in order to record high-frequency secular variation signals such as short-duration geomagnetic excursions. *Lund and Keigwin* [1994] observed that even at moderate rates of sedimentation (on the order of 10 cm ka^{-1}) that the PDRM process can act as a low-pass filter thereby smoothing the record. At sedimentation rates less than 1-3 cm ka^{-1} the smoothing effect is so dramatic that no excursions are recorded [*Roberts*, 2006; *Roberts and Winklhofer*, 2004].

Drilling of the cores can impart a secondary overprint obscuring the primary magnetization. The drill-overprint is most likely an isothermal remanent magnetization (IRM) produced by exposure to a magnetized steel core barrel during drilling. It is a common feature of samples from oceanic boreholes and was first noticed in Deep-Sea Drilling Project (DSDP) cores [*Ade-Hall and Johnson*, 1976]. Preliminary ship-board measurements can indicate the efficacy of alternating frequency (AF) demagnetization to isolate the primary magnetization. Cores in which AF demagnetization appeared to only have a limited effect on any secondary overprint were generally avoided.

Apparent excursions in a single hole record may be the result of sedimentary disturbance or other localised physical effects rather than a regional or global magnetic event at the time of deposition [*Channell et al.*, 2012]. Unfortunately, sediments with high sedimentation rates are often those dominated by sediment slumping and turbiditic deposition [e.g. ODP 181 *Shipboard Scientific Party*, 2000]. Therefore, it is important that neighbouring holes should have palaeomagnetic records and sedimentary rates suitable for corroborating records. Corroborating records from multiple holes at a particular site and multiple sites from a particular leg would demonstrate that the observed excursions are truly geomagnetic phenomena rather than anomalies arising from sedimentary processes or disturbance. Sites with multiple suitable holes were preferentially selected.

The initial reports from Ocean Drilling Program (ODP) and Integrated Ocean Drilling Program (IODP) expeditions since ODP Leg 160 (Spring 1995) were examined. Of the 69 legs examined, 3 appeared to provide suitable holes from localities in the Pacific Ocean. Continuous half-core and whole-core palaeomagnetic measurements of the sediments made on-board ship were used, in conjunction with published biostratigraphic age models, to determine which core sections were of particular interest. This extensive

Leg 167	*California Margin*		
Hole	Long.	Lat.	Water Depth (m)
1017B	121°6.360'W	34°32.094'N	966
1017C	121°6.420'W	34°32.094'N	956
1017D	121°6.420'W	34°32.088'N	955
1018A	123°16.620'W	36°59.298'N	2477
1018D	123°16.500'W	36°59.394'N	2487
1019E	124°55.980'W	41°40.962'N	978

Leg 181	*SW Pacific Gateways*		
Hole	Long.	Lat.	Water Depth (m)
1119B	172°23.598'E	44°45.332'S	393
1119C	172°23.614'E	44°45.331'S	393
1122A	177°23.611'W	46°34.781'S	4432
1122C	177°23.622'W	46°34.780'S	4432

Leg 202	*SE Pacific Palaeoceanography*		
Hole	Long.	Lat.	Water Depth (m)
1234A	73°40.909'W	36°13.153'S	1015

Table 7.1: Pacific Sites from which samples were collected to study the Blake Excursion.

survey of ODP literature revealed only a few potential sampling targets (Table 7.1 and Figure 7.1).

7.3 ODP Leg 167 - California Margin

Ocean Drilling Program Leg 167 drilled sites along the California Margin in an attempt to characterise the response of the California Current system to climate change [*Lyle et al.*, 2000a]. Three sites were selected for sampling, representing those with the highest sedimentation rates on the margin: Sites 1017, 1018 and 1019 (Table 7.1, Figure 7.2).

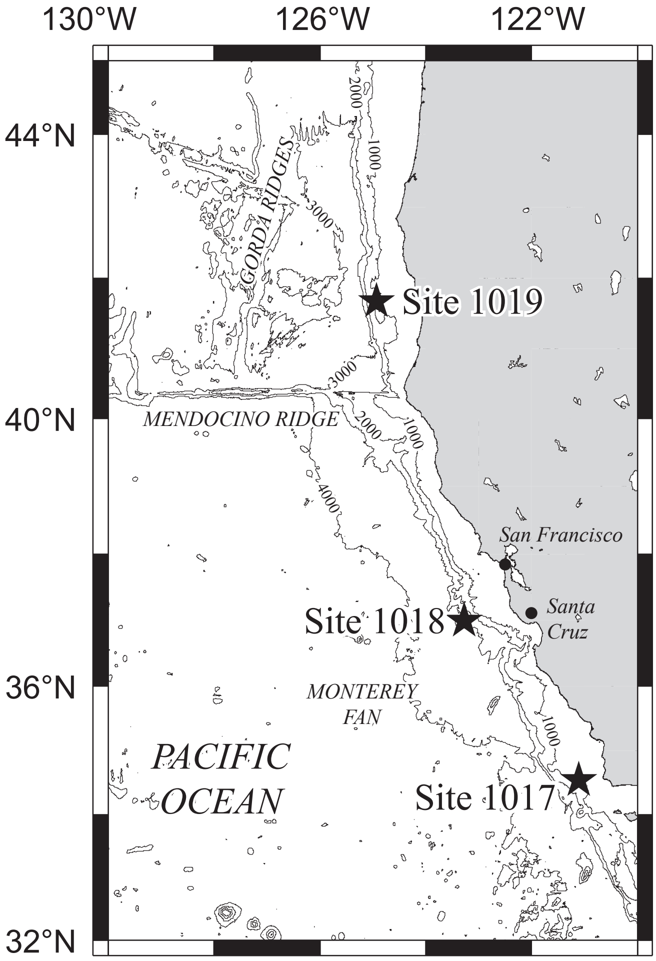

Figure 7.2: Location map of the three sites sampled from ODP Leg 167 (Sites 1017, 1018 and 1019) in this study. Bathymetry contours at 1000 m intervals.

7.3.1 Depositional Setting

Site 1017

Site 1017 is situated on the continental slope, south of Santa Lucia Bank, 50 km west of Point Arguello (Figure 7.2). The water depth at this site is roughly 960 metres below sea level (mbsl). The sedimentary sequence comprises hemipelagic, fine-grained terrigenous sediments accumulated during the Quaternary [*Shipboard Scientific Party*, 1997a]. During the late Quaternary, sedimentation rates exceed 15 cm kyr^{-1} [*Cannariato and Kennett*, 2005; *Kennett et al.*, 2000]. The high sedimentation rate is reflected in a corresponding decrease in carbonate content of the sediment as the carbonate material is diluted by increased siliciclastic input. The sampled section comprises greenish grey silty clay although there are some indications of thin turbidite layers within the sedimentary sequence.

Three holes with almost continuous recovery were selected for sampling at this site; 1017B, C, and D.

Site 1018

Site 1018 is situated further North than Site 1017, on a sediment drift at a water depth of 2477 mbsl (Figure 7.2). The site is just south of the Guide Seamount and approximately 75 km west of Santa Cruz, California [*Shipboard Scientific Party*, 1997b]. Site 1018 is a high resolution, lower Pliocene to Holocene sediment section that records the evolution of the California current. The fine-grained, siliciclastic sediments are typical of drift sediments, containing only small to moderate amounts of siliceous and calcareous biogenic components. Similarly, high sedimentation rates ($\sim$ 20 cm kyr^{-1}) support a drift sediment origin, although again they may potentially be inflated by turbidite deposition.

Two holes were selected for sampling at this site; 1018A and D.

Site 1019

Site 1019 is the northernmost of the Leg 167 sites and is located in the Eel river basin, 60 km west of Crescent City, California at a water depth of ~978 mbsl [*Shipboard Scientific Party*, 1997c] (Figure 7.2). Site 1019 similarly represents a thick sequence of Quaternary siliciclastic sediments with only minor amounts of siliceous and calcareous biogenic components. Thin sand beds, likely deposits from turbidity currents originating at the ridge, occur within the sequence until ~ 100 ka.

Only one hole was sampled from this site; 1019E.

7.3.2 Sampling

In all, 415 samples were collected from 6 ODP Leg 167 Sites. Collected samples are summarised below:

Table 7.2: Samples taken from ODP Leg 167 to study the Blake Excursion.

Leg 167	*California Margin*						
	No. of	Top Depth		Bottom Depth		Samples	Mean NRM
Hole	Samples	(mbsf)	(mcd)	(mbsf)	(mcd)	Analysed	(mAm^{-1})
1017B	70	13.61	14.31	28.16	31.35	all	1.41
1017C	61	11.85	13.55	26.39	31.00	all	1.15
1017D	68	11.04	14.46	27.61	31.65	all	1.57
1018A	64	11.885	12.925	26.06	30.47	all	1.46
1018D	84	12.35	12.76	28.00	29.51	all	2.74
1019E	68	5.17	5.07	16.715	16.985	all	12.5

7.3.3 Age Models

Site 1017

To improve upon the correlation between holes from Site 1017 achieved using the ODP composite depth scale (mcd), a revised depth scale was determined by correlating all records (1017C, D, & E) to their equivalent depth in Hole 1017B (mbsf) [*Shipboard Scientific Party*, 1997a]. Shipboard measurements of magnetic susceptibility were cross correlated between Holes 1017B, C, D and E (Figure 7.3).

The 'MATCH 2.3.1' protocol of *Lisiecki and Lisiecki* [2002], which utilizes dynamic programming, was used to determine the best correlation between all the records. The protocol compares possible alignments of the records to determine a realistic and optimal match. The records are similar but lack many well-defined features. Therefore, only a reasonably good, low-resolution match was achieved between the records.

A published age model, based on oxygen isotope stratigraphy, exists for Hole 1017E [*Cannariato and Kennett*, 2005; *Kennett et al.*, 2000]. To transfer the age model for 1017E to the sampled holes at Site 1017, the shipboard magnetic susceptibility record of 1017E (mbsf) was correlated to the magnetic susceptibility record of Hole 1017B (mbsf) (as described above). The transferred age model is displayed in Figure 7.4. The age model was then transferred to the other holes via their correlation to 1017B.

Site 1018

An age model based on an oxygen isotope stratigraphy from Holes 1018C and D is published in the ODP Initial Reports for Site 1018 [*Shipboard Scientific Party*, 1997b]. The ODP composite depth scale (mcd) for Site 1018 was found to provide a good correlation between all the holes at the site. Therefore, the age model was transferred to the sampled holes using the ODP composite depth scale (mcd) for Site 1018 (Figure 7.5). The palaeomagnetic records from Hole 1018A are subsequently given on the age model transferred using the ODP Site 1018 composite depth scale (mcd).

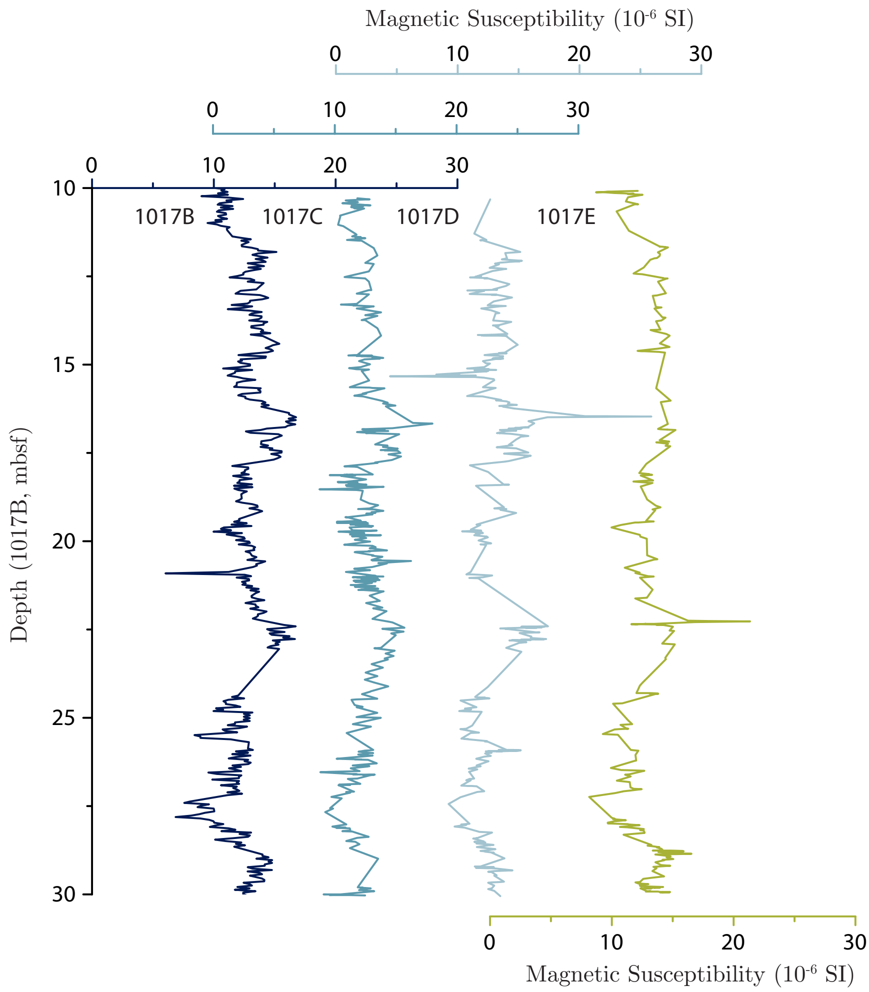

Figure 7.3: Site 1017 hole correlation. Holes 1017B, C, D &E were cross correlated using shipboard ODP measurements of magnetic susceptibility [*Shipboard Scientific Party*, 1997a]. All records are shown correlated to their equivalent depth in Hole 1017B (mbsf).

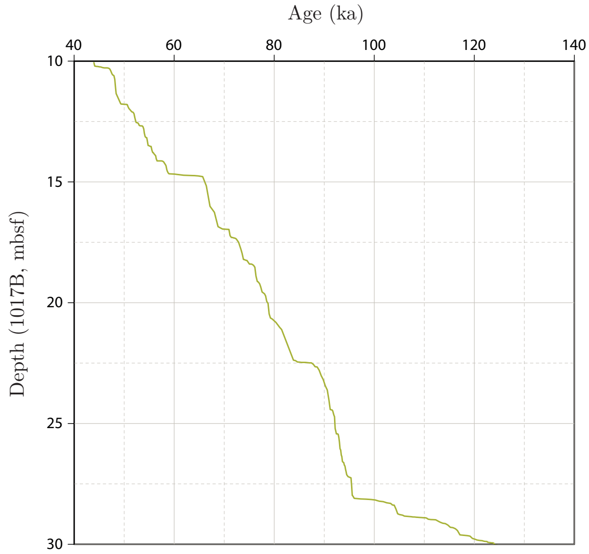

Figure 7.4: Age model for Site 1017. Depth given is that in Hole 1017B (mbsf). The age model is based on an oxygen isotope stratigraphy determined by *Kennett et al.* [2000].

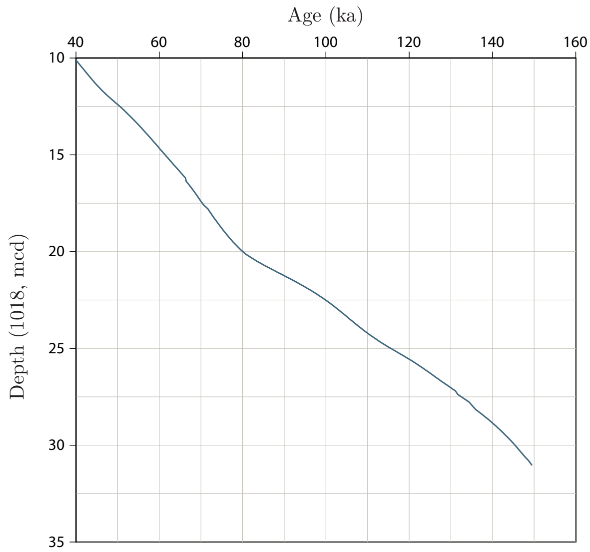

Figure 7.5: Age model for Site 1018. Depth given is the ODP composite depth scale (mcd) for Site 1018. The age model is based on an oxygen isotope stratigraphy from Holes 1018C & D [*Shipboard Scientific Party*, 1997b].

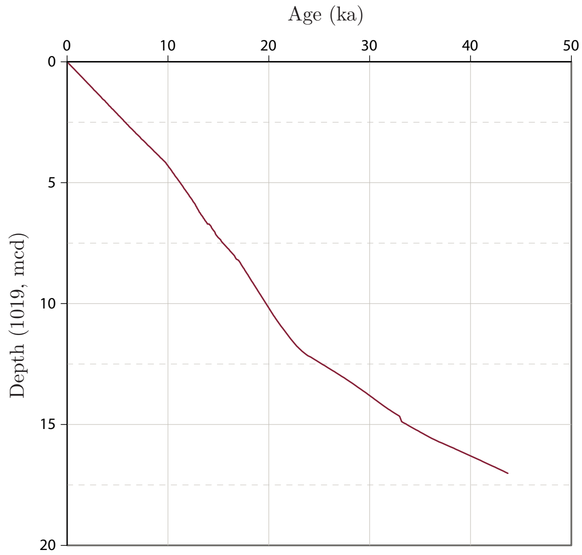

Figure 7.6: Age model for Site 1019. Depth given is the ODP composite depth scale (mcd) for Site 1019. The age model is based on an oxygen isotope stratigraphy from Holes 1019C & E [*Lyle et al.*, 2000b].

Site 1019

For sampling purposes, the stratigraphic age model reported in the ODP Initial Reports was used to determine the interval of interest at Site 1019 [*Shipboard Scientific Party*, 1997c]. However, a revised age model based on an oxygen isotope stratigraphy from Holes 1019C and E was also published in the ODP Scientific Reports for Site 1019 [*Lyle et al.*, 2000b]. The revised age model was not consulted prior to sampling. Unfortunately, the revised age model is very different from that in the Initial Reports and the sampled interval was found to be significantly younger than intended. The ODP composite depth scale (mcd) for Site 1019 was found to provide a good correlation between all the holes at the site. The revised age model was therefore transferred to the sampled holes using the ODP composite depth scale (mcd) for Site 1019 (Figure 7.6). The palaeomagnetic records from Hole 1019E are subsequently given on the revised age model transferred using the ODP Site 1019 composite depth scale (mcd) [*Lyle et al.*, 2000b].

7.3.4 Palaeomagnetic Measurements

All samples were subjected to a 17 step alternating field (AF) demagnetization procedure. After initial measurement of the Natural Remanent Magnetization (NRM) the samples were subjected step-wise to alternating fields of maximum amplitudes 3, 6, 9 , 12, 15, 20, 25, 30, 35, 40, 50, 60, 70, 80, 90, and 100 mT.

Representative orthogonal demagnetization diagrams from Site 1017 are shown in Figure 7.7 and representative diagrams from Sites 1018 and 1019 are shown in Figure 7.8. Many samples displayed a lower coercivity component that was typically removed by an applied peak AF of 20 mT. This lower coercivity component was assumed to be an artifact isothermal remanent magnetization (IRM) induced by exposure to the magnetized steel core barrel during drilling [*Ade-Hall and Johnson*, 1976]. The resulting demagnetization vectors were analysed using Principal Component Analysis (PCA) to determine the Characteristic Remanent Magnetization (ChRM) of the samples.

The results of the PCA for Sites 1017, 1018 and 1019 are shown in Figures 7.9, 7.10 and 7.11 respectively.

The inclination records for the three holes, 1017B, C and D, are shown in the left-hand panel of Figure 7.9. The sampled interval is unfortunately younger (∼50-105 ka) than intended. The three holes appear to show little coherence with each other. This would appear to be the result of very low concentrations of high-coercivity grains. The remanence of the samples appears to mainly be carried by low-coercivity grains as may be seen in the intensity graphs of the samples during demagnetization (Figure 7.7). These low-coercivity grains are particularly susceptible to overprinting by the magnetized steel core barrel during drilling. Once the drilling overprint has been removed by AF demagnetization, the samples' magnetizations were very weak (less than 4×10^{-4} Am^{-1}) such that the reliability of the signal is very low (reflected in the high MAD values ($\sim 10-40$) (Figure 7.9). The directional signals recorded by the samples taken from Site 1017 were therefore deemed unreliable and no further analysis was carried out on these samples.

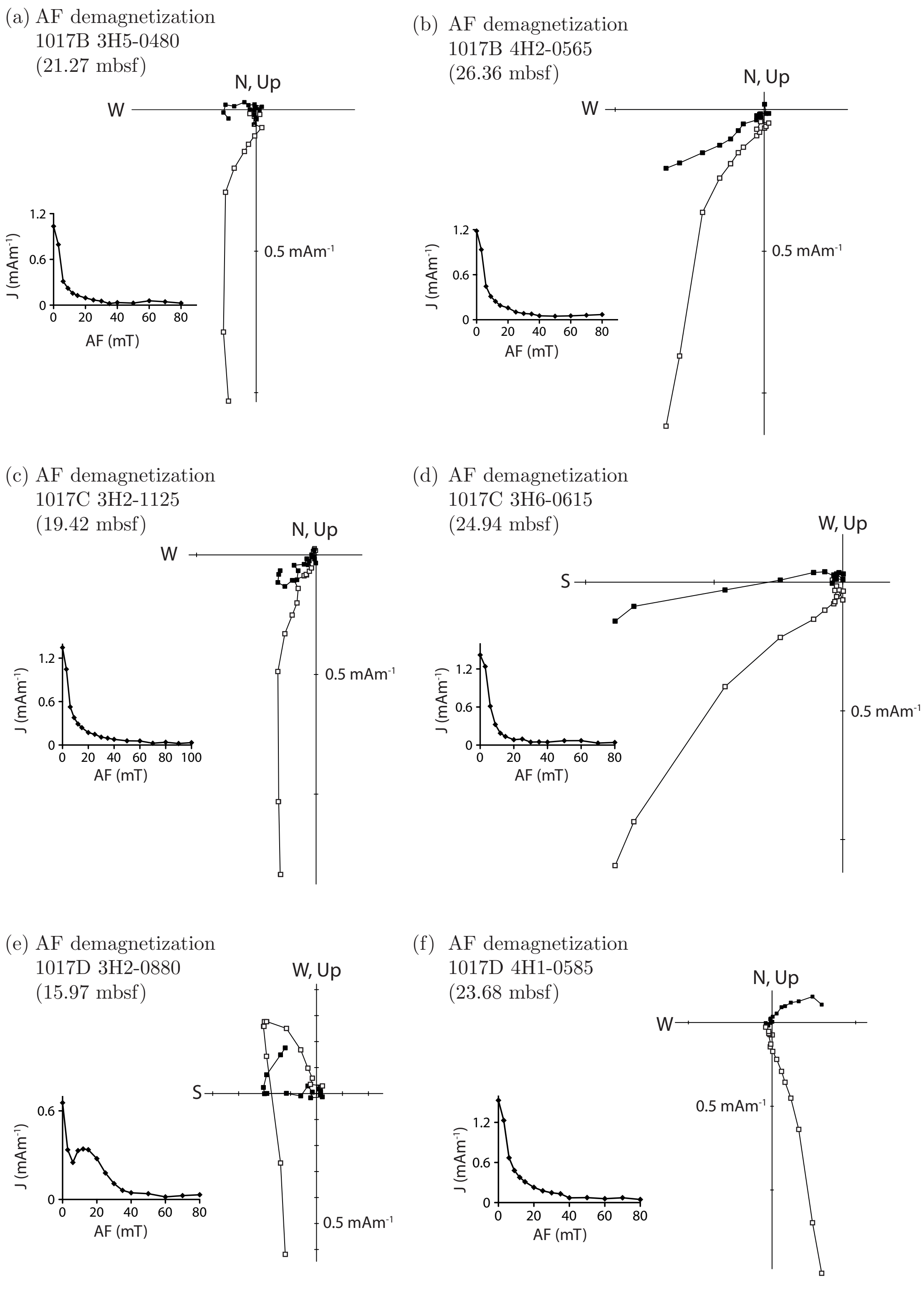

Figure 7.7: Representative Zijderveld diagrams for samples from Holes 1017B, C and D showing the results of alternating field (AF) demagnetization. White (black) squares indicate the projection on the horizontal (vertical) plane. See text for further discussion.

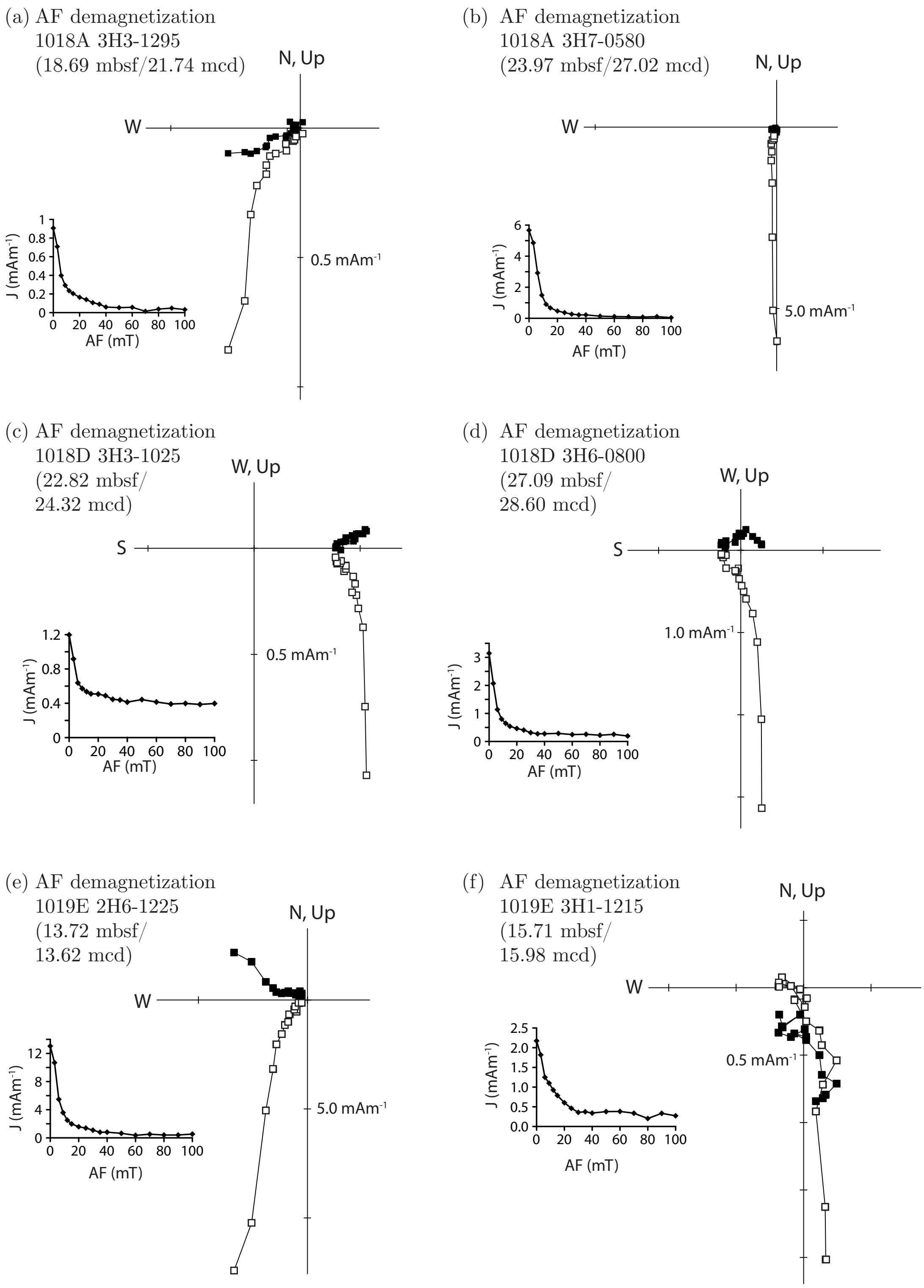

Figure 7.8: Representative Zijderveld diagrams for samples from Holes 1018A, 1018D and 1019E showing the results of alternating field (AF) demagnetization. White (black) squares indicate the projection on the horizontal (vertical) plane. See text for further discussion.

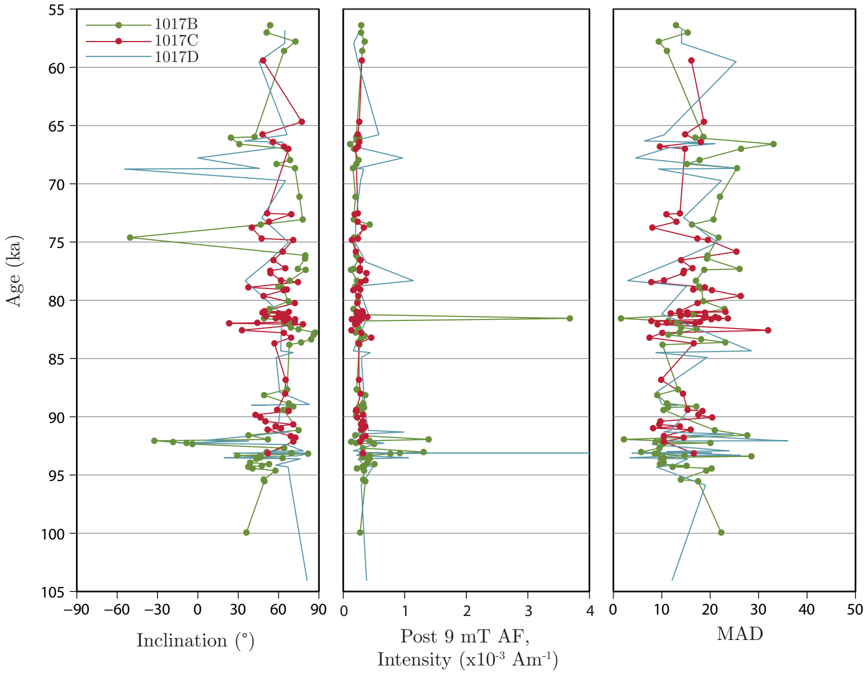

Figure 7.9: Inclination (left), Magnetization Intensity (middle) following 9 mT AF demagnetization to remove the drilling overprint, and MAD (right) for samples from Site 1017.

A similar situation was observed for samples collected from Site 1018A. The ages of the samples collected from Site 1018A range from ∼50-150 ka, across the interval we might expect to see the Blake excursion. The remanence of the samples appears to be carried principally by low-coercivity grains (Figure 7.8). Again, once the drilling overprint was removed by AF demagnetization, the samples' magnetization was very weak (less than $1{\times}10^{-3}$ Am^{-1}) such that the reliability of the signal is very low (reflected in the high MAD values ($\sim 10-30$) (Figure 7.9). Samples from 1018D failed to demagnetize completely after application of a 100 mT alternating field (Figure 7.8c & d). The remaining high coercivity remanence is orientated horizontally north-south. As the samples from 1018A were dominated by low-coercivity grains and the samples from 1018D did not completely demagnetize, the directional signals recorded by the samples taken from Site 1018 were therefore deemed unreliable. No further analysis was carried out on these samples.

The sampling interval for Site 1019 was found to be significantly younger than intended

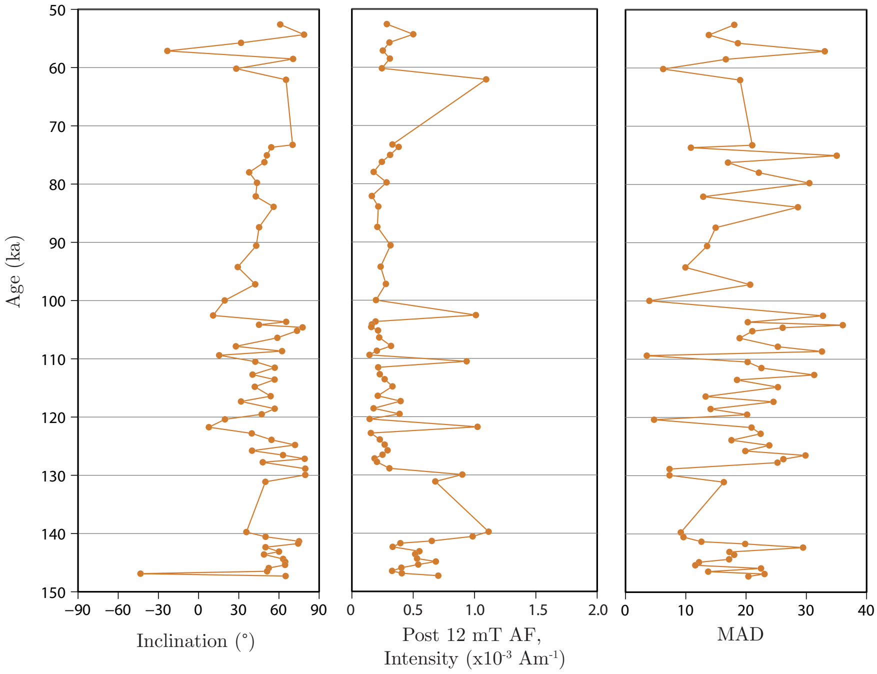

Figure 7.10: Inclination (left), Magnetization Intensity (middle) following 12 mT AF demagnetization to remove the drilling overprint, and MAD (right) for samples from Hole 1018A.

(< 45 ka) (Figure 7.6). Although this meant that the Blake excursion could not be identified in this interval, the interval does encompass the time period during which the Laschamp Excursion is believed to have occurred (∼41 ka). The inclination record in Figure 7.11 appears to show an anomalous feature beginning at 39 ka. Almost fully reversed directions appear to be recorded at 37-36 ka. However, on closer examination, this feature corresponds to an interval of very low magnetization intensity (less than 5×10^{-4} Am^{-1}) and very high MAD values (20-40).

We must therefore conclude that the directional signals recorded by the samples taken from Site 1019 are similarly unreliable and no further analysis was carried out on these samples. Sampling from Leg 167 was therefore unsuccessful in providing a record of the Blake excursion. In summary, this was the result of poorly recorded signals and of sampling intervals incorrectly identified as containing the Blake interval.

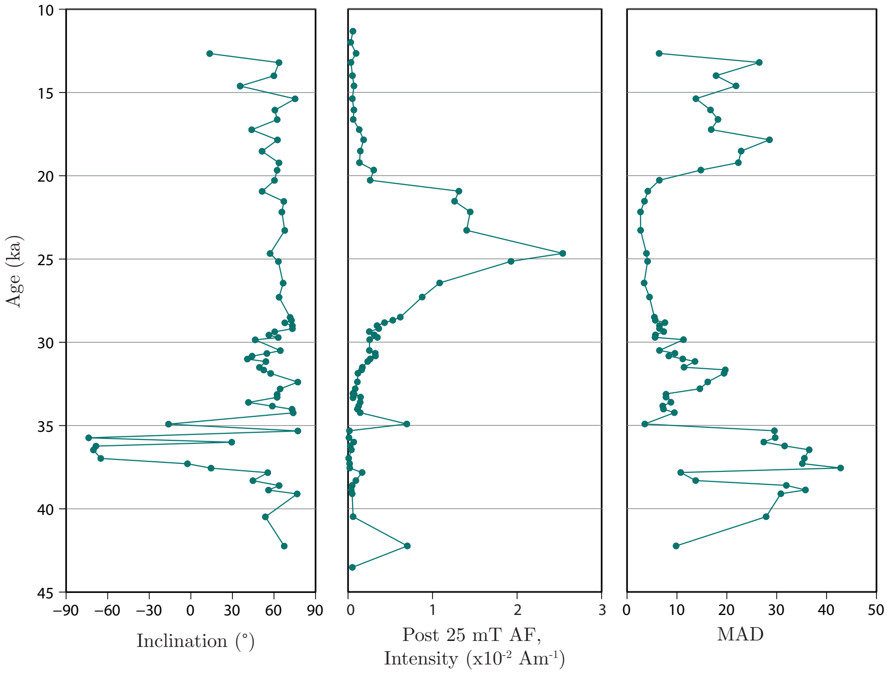

Figure 7.11: Inclination (left), Magnetization Intensity (middle) following 25 mT AF demagnetization to remove the drilling overprint, and MAD (right) for samples from Hole 1019E.

7.4 ODP Leg 181 - South-West Pacific Gateways

Drilling on ODP Leg 181 was undertaken in the eastern New Zealand region with the intention of reconstructing the development of the Antarctic Circumpolar Current (ACC) and the Deep Western Boundary Current (DWBC) [*Richter*, 2004]. Such an investigation requires drill sites through thick, undisturbed and fine-grained sediment masses formed under the influence of the currents. Leg 181 holes were therefore drilled through a series of sediment drifts on the eastern edge of the New Zealand Plateau (Figure 7.12).

7.4.1 Depositional Setting

Site 1119

ODP Site 1119 is situated on the upper continental slope, east of South Island, New Zealand at a water depth of 395 mbsl [*Shipboard Scientific Party*, 1999] (Figure 7.12).

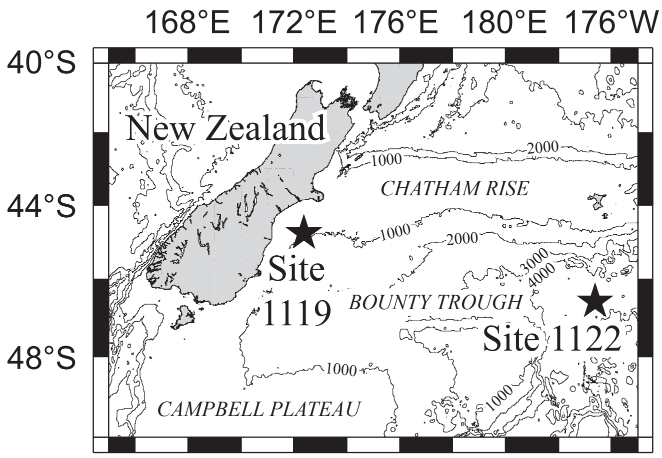

Figure 7.12: Location map of the two sites sampled from ODP Leg 181 (Sites 1119 and 1122) in this study. Bathymetry contours at 1000 m intervals.

The drilled holes sample a series of prograding mud foresets on the slope.The site is characterised, like many of the continental slope settings around New Zealand, by alternating sequences of glacial sands and interglacial clay-silt beds. The slope sands result from interglacial highstands during which the site was starved of terrigenous material. The sands themselves are likely the product of reworked material from the edge of the shelf. The glacial periods are characterised by high sediment supply to the slope, resulting in the formation of thick greenish gray silty clay beds. Interglacial intervals have sedimentation rates ranging between 5 and 32 cm kyr^{-1} whilst glacial intervals have much higher sedimentation rates ($\sim$ 70 cm kyr^{-1} during Stage 6).

Two holes were sampled from this site; 1119B and C.

Site 1122

Site 1122 was drilled on the north bank levee of the abyssal Bounty Fan at a depth of 4432 mbsl [*Shipboard Scientific Party*, 2000] (Figure 7.12). Bounty fan receives sediment from the Southern Alps in New Zealand. Periodically, sediment near the shelf edge is mobilized, travelling some 900 km to the fan. The sediment sequences are therefore dominated by turbidite sedimentation characterised by greenish gray clays interbedded with sandy turbidites.

Although two holes were sampled from this site; 1122A and C; the presence of turbidites made recovery of a robust palaeomagnetic signal unlikely and no measurements were conducted on the collected samples from Site 1122.

7.4.2 Sampling

In all, 319 samples were collected from 4 ODP Leg 181 Sites. Collected samples are summarised below:

Table 7.3: Samples taken from ODP 181 to study the Blake Excursion.

Leg 181	*SW Pacific Gateways*						
	No. of	Top Depth		Bottom Depth		Samples	Mean NRM
Hole	Samples	(mbsf)	(mcd)	(mbsf)	(mcd)	Analysed	(mAm^{-1})
1119B	67	15.15	16.39	49.87	52.85	16	5.01
1119C	94	16.99	16.75	49.67	51.93	8	3.07
1122A	91	6.90	14.78	29.655	37.555	none	-
1122C	67	14.06	14.70s	31.585	32.515	none	-

7.4.3 Palaeomagnetic Measurements

Demagnetization of Remanence

At these Southern Hemisphere sites the expected NRM direction is inclined approximately $\sim 63°$ in the negative direction (i.e. upwards) during the Brunhes Chron. Initially, 16 discrete samples (8 from 1119B and 8 from 1119C, in both cases at regular intervals across the sampled interval) were subjected to full stepwise AF demagnetization (examples shown in Figures 7.13a,b). Samples had NRM intensities typically between 10^{-4} and 10^{-2} Am^{-1}. The resulting demagnetization vectors were noisy and in general the AF

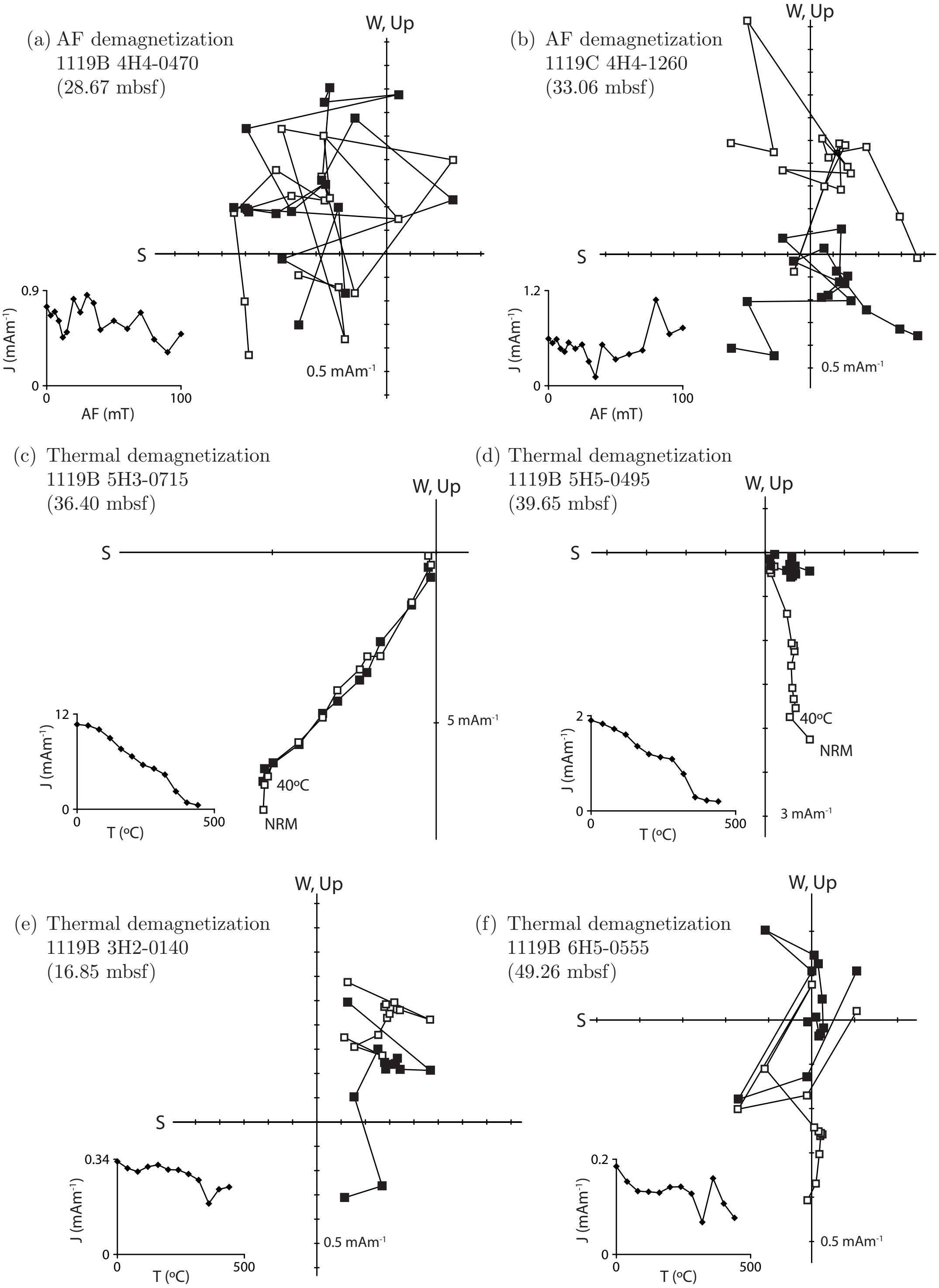

Figure 7.13: Representative Zijderveld diagrams for samples from Holes 1119B and 1119C. (a-b) show the results of alternating field (AF) demagnetization whilst (d-f) show the results of thermal demagnetization. White (black) squares indicate the projection on the horizontal (vertical) plane. See text for further discussion.

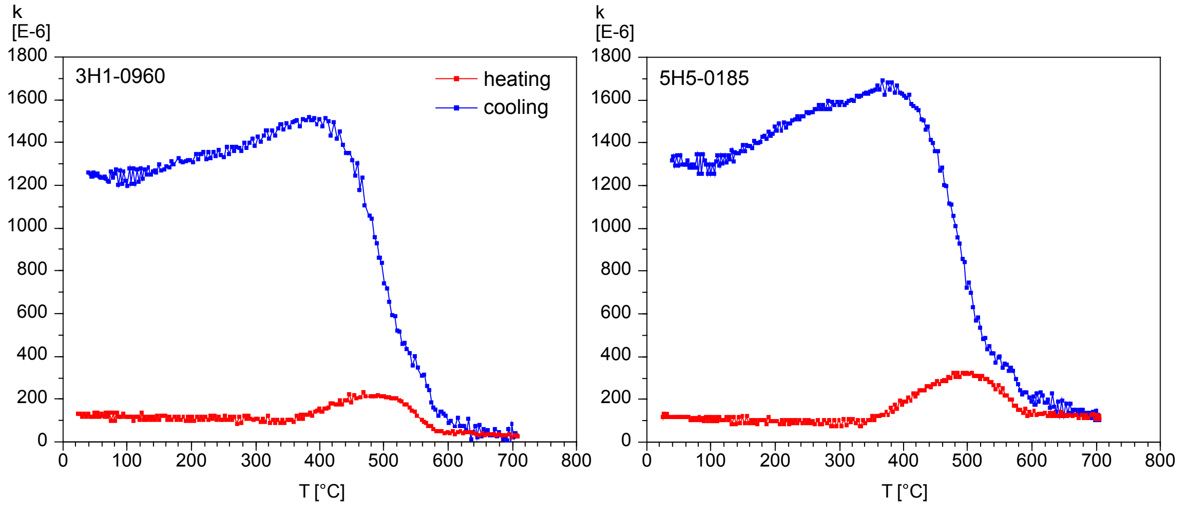

Figure 7.14: Measurements of the thermal dependency of magnetic susceptibility (k). Representative heating and cooling curves of two samples from Hole 1119B: 3H1-0960 (15.16 mbsf) and 5H5-0185 (39.35 mbsf).

was ineffective in demagnetizing the samples (Figure 7.13a,b). Determination of a remanence direction using AF demagnetization was therefore not possible. This was similarly observed on-board ship [*Shipboard Scientific Party*, 1999].

To investigate whether thermal demagnetization might be appropriate for isolating a magnetic remanence in the samples, 8 representative discrete samples from 1119B were subjected to an investigation into the effect of thermal changes on their magnetic susceptibility. Samples were powdered and $\sim$ 0.5 cm^3 volumes of powder were measured using the CS-2 apparatus and KLY-2 Kappabridge. The samples were heated, in air, from room temperature up to 700°C and subsequently cooled back to room temperature. Figure 7.14 shows typical thermomagnetic heating and cooling curves for these samples. The increase in magnetic susceptibility after 400°C indicates mineral alteration, probably due the formation of magnetite from other weakly magnetic phases. The very different cooling curve is indicative of the presence of magnetic alteration products. IRM acquisition profiles for 8 samples from 1119C (examples shown in Figure 7.15) indicate that remanence saturation is achieved when applied fields reach 200-500 mT, whilst H_{cr} values

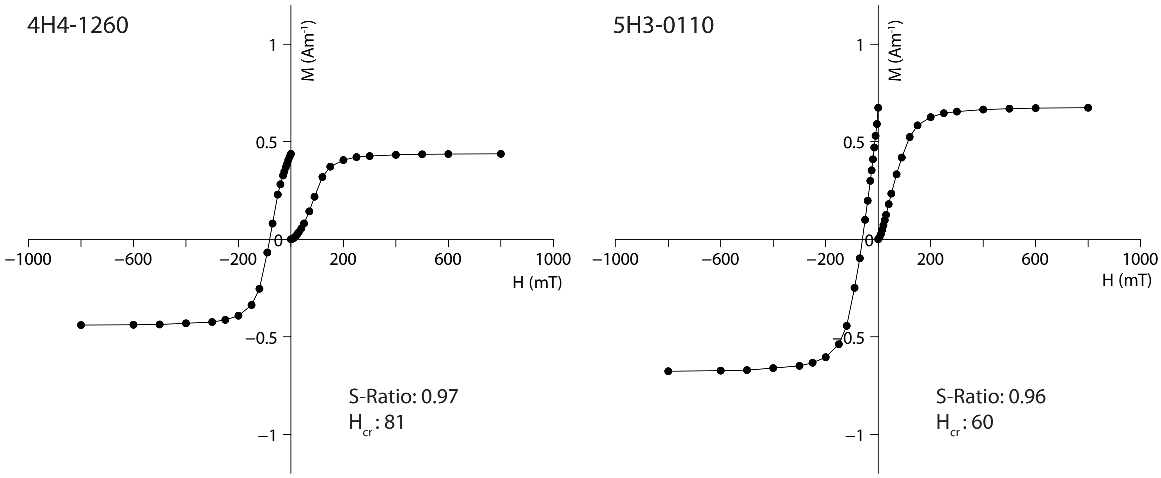

Figure 7.15: Example isothermal remanent magnetization (IRM) acquisition profiles for samples from Hole 1119C: 4H4-1260 (33.06 mbsf) and 5H3-0110 (39.91 mbsf)

range between 20 and 85 mT.

Subsequently, a further 8 discrete samples from 1119B were subjected to stepwise thermal demagnetization but only up to 400°C to ascertain whether this might be effective in isolating a ChRM. The sediment samples were carefully removed from their plastic cubes and wrapped in aluminium foil before being placed in the furnace. Of the 8 samples, 3 revealed stable demagnetization vectors (e.g. Figure 7.13c,d). These samples had initial NRM intensities greater than 2×10^{-4} Am^{-1} and displayed a steeply positive (pointing vertically downcore), essentially univectorial remanence (examples shown in Figures 7.13c,d). This is most likely attributable to a drill-string-induced IRM that obscures any natural remanence. These samples were demagnetized at 400°C. For the remaining 5, the NRM intensities were very low ($< 2\times10^{-4}$ Am^{-1}) such that noise obscured any NRM direction (examples shown in Figures 7.13e,f). Thermal demagnetization therefore also failed to reveal stable remanence directions. The low unblocking temperature, coupled with the low SIRM (200-500 mT), H_{cr} values between 20 and 85 mT, and mineral alteration to magnetite above 400°C, suggests that the main remanence carrier is probably a ferrimagnetic iron sulphide mineral [*Roberts et al.*, 2011]. Similar observations were

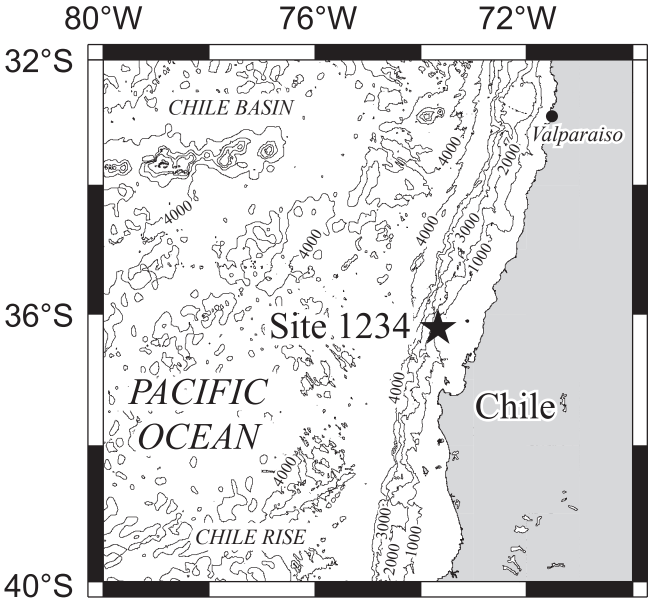

Figure 7.16: Location map of Site 1234 from ODP Leg 202 sampled in this study. Bathymetry contours at 1000 m intervals.

made on board ship and are supported by the presence of pyrite [*Shipboard Scientific Party*, 1999].

The unfortunate difficulties in measuring a stable remanence in these cores rendered them unsuitable for further study.

7.5 ODP Leg 202 - Southeast Pacific Transects

ODP Leg 202 drilled 11 sites of relatively continuous sediment sequences in the the southeast and equatorial Pacific in order to study climatic records on a number of temporal scales [*Tiedemann et al.*, 2007]. Only one site, 1234, was sampled for this study (Figure 7.16).

7.5.1 Depositional Setting

Site 1234

Site 1234 was recovered from the central Chile margin, from the middle of the continental slope, at 1015 m water depth [*Shipboard Scientific Party*, 2003a] (Figure 7.16). The core is principally hemipelagic sediment with a dark gray, silty clay lithology, with high fluvial sediment input from the Chilean Coastal Range and the Andes. Site 1234 was suggested as potentially providing the 'highest-resolution long-term record of palaeomagnetic secular variation (PSV) and excursional field behaviour ever recovered' [*Shipboard Scientific Party*, 2003b]. Samples were taken from Hole 1234A.

7.5.2 Sampling

In all, 43 samples were collected from Hole 1234A from ODP Leg 202. Collected samples are summarised below:

Table 7.4: Samples taken from ODP 202 to study the Blake Excursion.

Leg 202	*SE Pacific Palaeoceanography*						
	No. of	Top Depth		Bottom Depth		Samples	Mean NRM
Hole	Samples	(mbsf)	(mcd)	(mbsf)	(mcd)	Analysed	(mAm^{-1})
1234A	43	42.56	45.78	74.18	86.75	none	-

However, during sampling it was found that the intervals of particular interest had already been sampled heavily by other studies. A 4-5 m sampling gap across the potential Blake interval resulted in the decision not to undertake any further work on this hole.

7.6 Conclusion

Our study of ODP cores from the Pacific Ocean failed to provide any record of the Blake Excursion. This was primarily the result of three major factors:

- Poor magnetic remanence and mineralogy characteristics of the selected cores precluded the isolation of a stable remanence signal in many cores.
- Core intervals in some circumstances were not from the time-period intended and were in some cases significantly younger.
- Previous sampling of the cores by other studies prevented high resolution sampling across the interval of interest.

Chapter 8

Conclusion

8.1 ^{230}Th$_{xs}$-Normalization

Age models for marine sediments are often constructed using techniques such as oxygen isotope stratigraphy. However, where such models are constructed using relatively widely-spaced tie-points, ages between the tie-points are underconstrained and may be affected by unrecognised variations in sedimentation rate. ^{230}Th$_{xs}$ normalization has long been used by researchers to reconstruct oceanic particle fluxes into marine sediments [e.g. *Francois et al.*, 2004; *Henderson and Anderson*, 2003; *Marcantonio et al.*, 1999; *McManus et al.*, 1998]. ^{230}Th$_{xs}$-normalization can be used to reconstruct relative variations in total sedimentation rate. By combining traditional oxygen isotope stratigraphy with sedimentation rates derived from measurements of ^{230}Th$_{xs}$, the ages and durations within these intervals may be determined with improved accuracy. ^{230}Th$_{xs}$ normalization therefore presents an opportunity to more accurately constrain the durations of comparatively 'short' (several thousands of years) events such as geomagnetic excursions recorded in marine cores.

8.1.1 A Modified Approach

Determination of $^{230}Th_{xs}$ requires that a number of corrections are made to the total measured ^{230}Th before $^{230}Th_{xs}$-normalization may be used to constrain sedimentation rates. Chapter 3 suggests a number of improvements to the corrections applied to the total measured ^{230}Th used to obtain $^{230}Th^0_{xs}$ activities. By making a localized estimate of $(^{238}U/^{232}Th)_{det}$, the uncertainty associated with the assumption of a ocean basin-wide $(^{238}U/^{232}Th)_{det}$ estimate may be reduced. A localized estimate of $(^{238}U/^{232}Th)_{det}$ may be achieved by identifying samples that are unlikely to contain authigenically derived uranium and taking the mean of their $^{238}U/^{232}Th$. The traditional assumption that the detrital component is in secular equilibrium is also challenged and modified to take into account the effects of alpha-recoil as the ^{238}U decays to ^{230}Th. Lastly, a means by which the value for the initial $(^{234}U/^{238}U)$ of authigenic uranium used in the correction for $^{230}Th_{auth}$ is also suggested.

Previous published measurements have tended to avoid sediments where the authigenic or detrital corrections amount to a significant proportion of the total ^{230}Th, because their associated uncertainties are poorly constrained. Therefore, the difference between these new corrections and the previous approach are relatively minor, when applied to previously obtained records. However, the revised approach, with better estimation of uncertainties, opens the possibility of using sites in the future where the authigenic correction is larger (where the age of the sediment is greater) or at sites with a larger detrital input.

8.1.2 XSage Software

My development of the MATLAB XSage routine incorporates these adaptations to the traditional technique [*Bourne et al.*, 2012b]. XSage allows the rapid calculation of $^{230}Th^0_{xs}$ activities using measured total uranium and thorium isotopic activities. Using the calculated $^{230}Th^0_{xs}$ and a simple age model, XSage can also determine variations in sedimentation rate which in turn can be used to refine the age model for a core.

The complexity and inter-dependence of the various equations involved in calculating $^{230}\mathrm{Th}^0_{xs}$ makes the use of classical error propagation difficult when attempting to determine the uncertainty on calculated sedimentation rates, age models and interval durations. XSage therefore employs a Monte Carlo approach to calculate uncertainties associated with the $^{230}\mathrm{Th}^0_{xs}$ activity estimates, sedimentation rates, individual ages, and interval durations. This approach provides a more complete assessment of uncertainties than in most previous ^{230}Th-normalization work.

XSage presents many advantages over traditional techniques for calculating $^{230}\mathrm{Th}^0_{xs}$. It allows quick and flexible comparison between different approaches and assumptions. The ability to recalculate answers using different data or stratigraphic age boundaries is fast and convenient compared to using spreadsheet software. Furthermore, by employing a Monte-Carlo approach, uncertainties can be reliably propagated from the interdependent input variables and parameters to the final calculations.

8.1.3 Sediment Focussing

In an attempt to improve the age model for the Laschamp excursion record from Site 1061, $^{230}\mathrm{Th}_{xs}$-normalization was employed to constrain relative variations in sedimentation rate (Chapter 6). However, using the age model derived from the NGRIP time-scale, sediment focussing was found to vary dramatically by at least a factor of 2. Variation in sediment focussing is not unexpected during this period. Unlike marine isotope stage (MIS) 5, (during which the Blake excursion occurred), the period 60-30 ka (MIS 3) is characterized by a dynamic, rapidly changing climatic system, particularly in the North Atlantic. A constant sediment focussing factor [*Francois et al.*, 2004] is a primary assumption used in $^{230}\mathrm{Th}_{xs}$-normalization. Where sediment focussing varies, the total sedimentation rates derived by $^{230}\mathrm{Th}_{xs}$-normalization are unreliable and fail to capture changes in lateral transport of sediment. The $^{230}\mathrm{Th}_{xs}$-normalized sedimentation rates were therefore not used to construct the age model for Site 1061 and constrain the timing and duration of the Laschamp excursion. This study therefore highlights the importance of constraining any potential variation in sediment focussing where $^{230}Th_{xs}$-normalization of sedimentation rates is to be used. This is most readily achieved by using additional, independent stratigraphic age boundaries, not used to calculate the $^{230}Th_{xs}$-normalized sedimentation rates, within the studied interval. Constraining focussing by other means remains a difficult problem, however, and development of proxies that may indicate changing lateral deposition, such as sortable silt analysis [e.g. *McCave and Hall*, 2006; *McCave et al.*, 1995] or magnetic grain-size proxies [e.g. *Banerjee et al.*, 1981; *Stanford et al.*, 2011], could allow a more flexible approach to constraining focussing where age-constrained stratigraphic tie-points are sparse.

8.2 Geomagnetic Excursions

This thesis presents two records of geomagnetic excursions obtained from the Blake-Bahama Outer Ridge in the western North Atlantic. In Chapter 4, a high-resolution record of the Blake excursion (~125 ka) is presented from Ocean Drilling Program (ODP) Site 1062 on the Blake-Bahama Outer Ridge and in Chapter 5, a high-resolution record for the Laschamp excursion (~41 ka) is presented from the same site and neighbouring ODP Site 1061 on the Blake Ridge. Both of these sites are in close proximity to a further record of the Iceland Basin excursion from ODP Site 1063 on the Bermuda Rise [*Knudsen et al.*, 2006, 2007]. This collection of records allows the direct comparison of multiple excursions at the same location, thereby excluding potential differences in geometric effects due to site location [*Brown et al.*, 2007].

The Blake-Bahama Outer Ridge record of the Blake excursion (ODP Site 1062) indicates that the geomagnetic field deviated from directions expected during 'normal' secular variation for 6.5 ± 1.3 kyr between 128.5 ± 4.0 ka and 122.0 ± 3.9 ka. Using an oxygen isotope stratigraphy, $^{230}Th_{xs}$-normalization and the new approach described in Chapter 3, the duration and timing of the event at this location may be accurately constrained and an estimate made of their associated uncertainties. The Blake excursion at this location was characterised by rapid transitions (less than 500 years in duration) between the normal polarity and a single fully-reversed polarity interval. Unlike records of the Blake from the Mediterranean [*Tric et al.*, 1991] and Chinese Loess [*Fang et al.*, 1997; *Zhu et al.*, 1994]; the cores from Site 1062 do not record multiple reversed intervals during the Blake Excursion. This new record therefore suggests that multiple reversed intervals should not be considered characteristic of the Blake excursion.

At the Blake Ridge, a chronology linked to the NGRIP GICC05 δ^{18}O time-scale [*Johnsen et al.*, 1992; *Svensson et al.*, 2006, 2008] is applied to a new palaeomagnetic record of the Laschamp excursion. The well-dated record shows that the midpoint of the Laschamp excursion occurred at 41.3 ka, in good agreement with the most recent estimates for the age of the excursion from volcanic lava and sedimentary archives [*Channell et al.*, 2012; *Nowaczyk et al.*, 2012; *Singer et al.*, 2009], and contemporaneous with a high in ^{10}Be production [*Ménabréaz et al.*, 2011, 2012; *Muscheler et al.*, 2004]. Here, the intensity low associated with the geomagnetic excursion has a duration of less than 2000 years, whilst the duration of the directional excursion is much shorter, lasting ~250 years.

8.2.1 Duration of Geomagnetic Excursions

Excursions have often been presented as 'short' events lasting less than 3000 years, exemplified in particular by the Laschamp excursion [e.g. *Channell et al.*, 2012; *Laj et al.*, 2000]. This is in agreement with the theory presented by *Gubbins* [1999], whereby excursions can not last longer than a certain cut-off duration before the geodynamo achieves stability and the excursion instead becomes a full reversal. However, whilst the Laschamp excursion was certainly less than 2000 years long (with a directional excursion duration of less than ~250 years) the Blake excursion [*Bourne et al.*, 2012a] and Iceland Basin excursion [*Knudsen et al.*, 2007], with durations of 6.5 ± 1.3 kyr and 6.8 ± 0.5 kyr respectively, do not fit so simply into this narrative. These relatively long durations suggest that excursions do not necessarily have short durations (i.e. <3 kyr) but instead occupy a continuous range of durations. Furthermore, the maintenance of fully reversed directions for a long duration (greater than the time-scale of secular variation) implies the presence of a weakly reversed dipole during the excursion [*Valet et al.*, 2008].

These longer duration excursions alone are not necessarily in direct opposition to the idea that the magnetic inertia of the inner core is the primary control on distinguishing geomagnetic excursions and reversals. The estimated figure of 3 kyr (see Appendix A for a derivation) for the inner-core's e-folding time [*Gubbins*, 1999; *Hollerbach*, 1993] has a large associated uncertainty. *Gubbins* [1999] states that this e-folding time-scale could theoretically allow for excursions with durations of up to 6 kyr. However, the combination of more than one excursion approaching this theoretical maximum, and modelling studies suggesting that the conductivity of the inner core has little influence on the geodynamo [*Wicht*, 2002], must lead us to seriously question the idea that the inner core conductivity is a major factor controlling the evolution of the excursional geomagnetic field.

8.2.2 Rapid Transitions

The records of both the Blake excursion and the Laschamp excursion from the Blake-Bahama Ridge sites show rapid transitions to excursional VGPs (less than 500 years). The failure of the cores to record the transitional field in any detail, despite relatively high sedimentation rates (> 10cm kyr^{-1}), demonstrates how sedimentation rate is a limiting factor in many studies of geomagnetic field behaviour [*Roberts and Winklhofer*, 2004]. Such rapid transitions correspond to a VGP transition rate of $\sim$180° kyr^{-1}. Current orthodoxy suggests that full reversal transitions can take $\sim$5 kyr, corresponding to a rate of only 18° kyr^{-1} [*Clement*, 2004]. Although one recent study has suggested that full reversals may also be rapid [*Valet et al.*, 2012], there is little data to confirm this assertion. On the basis of present evidence, any mechanism or mechanisms to explain excursions and reversals must be able to account for (or resolve) the apparent significant difference in transition rate between the two.

8.2.3 Palaeomagnetic Measurements

The differences between the whole-core palaeomagnetic measurements and the final measurements of discrete samples in the Laschamp study (Chapter 5) demonstrates the importance of careful analysis of palaeomagnetic features observed in continuous palaeomagnetic measurements. As documented by *Lund et al.* [2001b], spurious palaeomagnetic features may occur in long-core and u-channel measurements that are not observed in discrete samples. The origin of these features is not entirely clear but appears to be the result of incomplete demagnetization due to fast translation speeds of samples through the demagnetizing coil [*Brachfeld et al.*, 2004] and edge effects associated with deconvolution [*Roberts et al.*, 1996]. Therefore, any excursional palaeomagnetic signal recorded solely in continuous data should be treated with caution before the result is verified by further analysis.

8.2.4 A Global Perspective

The two new high-resolution records of geomagnetic excursions from the Blake-Bahama Outer Ridge represent some of the first steps towards constructing a global dataset of high-quality palaeomagnetic data with precise chronological control. Much of recent palaeoceanographic and palaeoclimatic research has focussed on the North Atlantic and, as a result, marine sediment palaeomagnetic records, which depend upon the same high-resolution cores, are predominately from the North Atlantic [e.g. *Channell*, 1999, 2006; *Channell et al.*, 1997; *Laj et al.*, 2004], although a few exist from the South Atlantic [*Stoner et al.*, 2002, 2003]. In Chapter 7, a number of ODP cores from the Pacific Ocean were studied in an attempt to move the focus of study away from the North

Atlantic and provide a more global perspective on the most recent excursions. Despite the apparent abundance of suitable ODP sites [*Lund et al.*, 2006], this study failed to provide any record of the Blake excursion. Poor magnetic remanence and magnetic mineralogy characteristics precluded the isolation of a stable remanence signal in many of the cores. This work therefore demonstrates the difficulties associated with obtaining high-quality palaeomagnetic records. Geochemical diagenesis and sediment disturbance can easily compromise potential marine geomagnetic records. Therefore, even with high-sedimentation rate cores [*Roberts and Winklhofer*, 2004], marine cores may not always provide high-quality palaeomagnetic records.

Our understanding of geomagnetic field behaviour during geomagnetic excursions is severely limited by the paucity of globally distributed data for any but the most recent of excursions. We still can not effectively distinguish between competing theories of dipole rotation [*Merrill and McFadden*, 1994] or collapse (an 'aborted reversal' scenario) [*Valet et al.*, 2008] during excursions. If we wish to understand the global coherence or incoherence of any geomagnetic signal then high-quality records are required from a number of locations across the world [*Roberts*, 2008]. In particular, the paucity of Southern Hemisphere palaeomagnetic records must be addressed in any future work. *Clement* [2004] raised the possibility of full reversal transition duration varying with latitude, it would be an interesting exercise to see whether any latitudinal-dependent behaviour is also characteristic of excursions.

Bibliography

Acton, G. D., M. Okada, B. M. Clement, S. P. Lund, and T. Williams (2002), Paleomagnetic overprints in ocean sediment cores and their relationship to shear deformation caused by piston coring, *J. Geophys. Res.*, *107*, B42,067, doi: 10.1029/2001JB000518.

Ade-Hall, J. M., and P. J. Johnson (1976), Review of magnetic properties of basalts and sediments, Leg 34, in *Proc. ODP, Init. Repts., Leg 34*, edited by R. S. Yeats, S. R. Hart, J. M. Ade-Hall, M. N. Bass, W. E. Benson, R. A. Hart, P. G. Quilty, H. M. Sachs, M. H. Salisbury, and T. L. Vallier, pp. 769–777, Washington (U.S. Government Printing Office), doi: 10.2973/dsdp.proc.34.165.1976.

Adkins, J., P. DeMenocal, and G. Eshel (2006), The African humid period and the record of marine upwelling from excess ^{230}Th in Ocean Drilling Program Hole 658C, *Paleoceanography*, *21*(4), 1–14, doi: 10.1029/2005PA001200.

Alfvén, H. (1942), Existence of electromagnetic-hydrodynamic waves, *Nature*, *150*(3805), 405–406.

Amit, H., and P. Olson (2010), A dynamo cascade interpretation of the geomagnetic dipole decrease, *Geophys. J. Int.*, *181*, 1411–1427, doi: 10.1111/j.1365-246X.2010.04596.x.

Amit, H., R. Leonhardt, and J. Wicht (2010), Polarity reversals from paleomagnetic observations and numerical dynamo simulations, *Space Science Reviews, 155*, *1*(4), 293–335, doi: 10.1007/s11214-010-9695-2.

Andersen, K. K., N. Azuma, J.-M. Barnola, M. Bigler, P. Biscaye, N. Caillon, J. Chappellaz, H. B. Clausen, D. Dahl-Jensen, H. Fischer, J. Flückiger, D. Fritzsche, Y. Fujii, K. Goto-Azuma, K. Grø nvold, N. S. Gundestrup, M. Hansson, C. Huber, C. S. Hvidberg, S. J. Johnsen, U. Jonsell, J. Jouzel, S. Kipfstuhl, A. Landais, M. Leuenberger, R. Lorrain, V. Masson-Delmotte, H. Miller, H. Motoyama, H. Narita, T. Popp, S. O. Rasmussen, D. Raynaud, R. Rothlisberger, U. Ruth, D. Samyn, J. Schwander, H. Shoji, M.-L. Siggard-Andersen, J. P. Steffensen, T. Stocker, a. E. Sveinbjörnsdóttir, A. Svensson, M. Takata, J.-L. Tison, T. Thorsteinsson, O. Watanabe, F. Wilhelms, and J. W. C. White (2004), High-resolution record of Northern Hemisphere climate extending into the last interglacial period, *Nature*, *431*(7005), 147–51, doi: 10.1038/nature02805.

Andersen, K. K., A. Svensson, S. J. Johnsen, S. O. Rasmussen, M. Bigler, R. Röthlisberger, U. Ruth, M.-L. Siggaard-Andersen, J. r. Peder Steffensen, and D. Dahl-Jensen (2006), The Greenland ice core chronology 2005, 15-42ka. Part 1: constructing the time scale, *Quat. Sci. Rev.*, *25*(23-24), 3246–3257, doi: 10.1016/j.quascirev.2006.08.002.

Andersen, M. B., C. H. Stirling, B. Zimmermann, and a. N. Halliday (2010), Precise determination of the open ocean $^{234}U/^{238}U$ composition, *Geochem. Geophys. Geosyst.*, *11*(12), doi: 10.1029/2010GC003318.

Anderson, R. F., and A. P. Fleer (1982), Determination of natural actinides and plutonium in marine particulate material, *Analytical Chemistry*, *54*(7), 1142–1147, doi: 10.1021/ac00244a030.

Aubert, J., J. Aurnou, and J. Wicht (2008), The magnetic structure of convection-driven numerical dynamos, *Geophys. J. Int.*, *172*(3), 945–956, doi: 10.1111/j.1365-246X.2007.03693.x.

Bacon, M. P. (1984), Glacial to interglacial changes in carbonate and clay sedimentation in the Atlantic Ocean estimated from ^{230}Th measurements, *Chem. Geol.*, *46*(2), 97–111, doi: 10.1016/0009-2541(84)90183-9.

Bacon, M. P., and R. F. Anderson (1982), Distribution of thorium isotopes between dissolved and particulate forms in the deep sea, *J. Geophys. Res.*, *87*(C3), 2045–2056, doi: 10.1029/JC087iC03p02045.

Bacon, M. P., C.-a. Huh, A. P. Fleer, and W. G. Deuser (1985), Seasonality in the flux of natural radionuclides and plutonium in the deep Sargasso Sea, *Deep Sea Research Part A. Oceanographic Research Papers*, *32*(3), 273–286, doi: 10.1016/0198-0149(85)90079-2.

Banerjee, S. K., J. King, and J. Marvin (1981), A rapid method for magnetic granulometry with applications to environmental studies, *Geophys. Res. Lett.*, *8*(4), 333–336, doi: 10.1029/GL008i004p00333.

Bateman, H. (1910), Solution of a system of differential equations occurring in the theory of radio-active transformations, *Proc. Cambridge Phil. Soc.*, *15*, 423–427.

Belshaw, N., P. Freedman, R. O'Nions, M. Frank, and Y. Guo (1998), A new variable dispersion double-focusing plasma mass spectrometer with performance illustrated for Pb isotopes, *International Journal of Mass Spectrometry*, *181*(1-3), 51–58, doi: 10.1016/S1387-3806(98)14150-7.

Bendat, J. S., and A. G. Piersol (1986), *Random Data: analysis and measurement procedures*, 2nd ed., John Wiley & Sons.

Berner, R. A. (1984), Sedimentary pyrite formation: An update, *Geochim. Cosmochim. Acta*, *48*(4), 605–615, doi: 10.1016/0016-7037(84)90089-9.

Bloxham, J., and D. Gubbins (1986), Geomagnetic field analysis? IV. Testing the frozen-flux hypothesis, *Geophys. J. R. Astr. Soc.*, *84*(1), 139–152, doi: 10.1111/j.1365-246X.1986.tb04349.x.

Bonhommet, N., and J. Babkin (1967), Sur la presence d'aimantation inversees dans la Chaine des Puys, *C. R. Acad. Sci. Paris*, *264*, 92–94.

Bonhommet, N., and J. Zähringer (1969), Paleomagnetism and potassium argon age determinations of the Laschamp geomagnetic polarity event, *Earth Planet. Sci. Lett.*, *6*(1), 43–46, doi: 10.1016/0012-821X(69)90159-9.

Bourdon, B., S. Turner, G. M. Henderson, and C. C. Lundstrom (2003), Introduction to U-series Geochemistry, in *Rev. Mineral. Geochem.*, vol. 52, edited by B. Bourdon, G. M. Henderson, C. C. Lundstrom, and S. Turner, pp. 1–20, Geochemical Society.

Bourne, M., C. Mac Niocaill, A. L. Thomas, M. F. Knudsen, and G. M. Henderson (2012a), Rapid directional changes associated with a 6.5kyr-long Blake geomagnetic excursion at the Blake-Bahama Outer Ridge, *Earth Planet. Sci. Lett.*, *333-334*, 21–34, doi: 10.1016/j.epsl.2012.04.017.

Bourne, M. D., A. L. Thomas, C. Mac Niocaill, and G. M. Henderson (2012b), Improved determination of marine sedimentation rates using $^{230}Th_{xs}$, *Geochem. Geophys. Geosyst.*, *13*, Q09,017, doi: 10.1029/2012GC004295.

Bourne, M. D., C. Mac Niocaill, A. L. Thomas, and G. M. Henderson (2013), High-resolution record of the Laschamp geomagnetic excursion at the Blake-Bahama Outer Ridge, *Geophys. J. Int.*, *in revisio*, doi: 10.1093/gji/ggt327.

Brachfeld, S. A., C. Kissel, C. Laj, and A. Mazaud (2004), Behavior of u-channels during acquisition and demagnetization of remanence: implications for paleomagnetic and rock magnetic measurements, *Phys. Earth Planet. Inter.*, *145*(1-4), 1–8, doi: 10.1016/j.pepi.2003.12.011.

Brown, M. C., R. Holme, and A. Bargery (2007), Exploring the influence of the non-dipole field on magnetic records for field reversals and excursions, *Geophys. J. Int.*, *168*(2), 541–550, doi: 10.1111/j.1365-246X.2006.03234.x.

Brunhes, B. (1906), Recherches sur la direction de l'aimentation des roches volcaniques, *Journal de Physique*, *5*, 705–724.

Bullard, E. C. (1949), The magnetic field within the Earth, *Proceedings of the Royal Society A: Mathematical, Physical and Engineering Sciences*, *197*(1051), 433–453, doi: 10.1098/rspa.1949.0074.

Burgess, S., G. M. Henderson, and B. Hall (2010), Reconstructing Holocene conditions under the McMurdo Ice Shelf using Antarctic barnacle shells, *Earth Planet. Sci. Lett.*, *298*(3-4), 385–393, doi: 10.1016/j.epsl.2010.08.015.

Butler, R. F. (1992), *Paleomagnetism - Magnetic Domains to Geologic Terranes*, Blackwell Scientific Publications.

Cande, S. C., and D. V. Kent (1992), A new geomagnetic polarity time scale for the late Cretaceous and Cenozoic, *J. Geophys. Res.*, *97*(B10), 13,917–13,951, doi: 10.1029/92JB01202.

Cande, S. C., and D. V. Kent (1995), Revised calibration of the geomagnetic polarity timescale for the Late Cretaceous and Cenozoic, *J. Geophys. Res.*, *100*(B4), 6093, doi: 10.1029/94JB03098.

Cannariato, K. G., and J. P. Kennett (2005), Structure of the penultimate deglaciation along the California margin and implications for Milankovitch theory, *Geology*, *33*(2), 157, doi: 10.1130/G21065.1.

Carter-Stiglitz, B., J. P. Valet, and M. LeGoff (2006), Constraints on the acquisition of remanent magnetization in fine-grained sediments imposed by redeposition experiments, *Earth Planet. Sci. Lett.*, *245*(1-2), 427–437, doi: 10.1016/j.epsl.2006.03.002.

Cassata, W., B. S. Singer, and J. Cassidy (2008), Laschamp and Mono Lake geomagnetic excursions recorded in New Zealand, *Earth Planet. Sci. Lett.*, *268*, 76–88, doi: 10.1016/j.epsl.2008.01.009.

Cassidy, J., and M. J. Hill (2009), Absolute palaeointensity study of the Mono Lake excursion recorded by New Zealand basalts, *Phys. Earth Planet. Inter.*, *172*(3-4), 225–234, doi: 10.1016/j.pepi.2008.09.018.

Chabaux, F. (2003), U-Th-Ra fractionation during weathering and river transport, *Reviews in Mineralogy and Geochemistry*, *52*(1), 533–576, doi: 10.2113/0520533.

Chaisson, W. P., M. Poli, and R. C. Thunell (2002), Gulf Stream and Western Boundary Undercurrent variations during MIS 10-12 at Site 1056, Blake-Bahama Outer Ridge, *Mar. Geol.*, *189*(1-2), 79–105, doi: 10.1016/S0025-3227(02)00324-9.

Champion, D., M. Lanphere, and M. Kuntz (1988), Evidence for a new geomagnetic reversal from lava flows in Idaho: discussion of short polarity reversals in the Brunhes and late Matuyama polarity chrons, *J. Geophys. Res.*, *93*(B10), 11,667–11,680, doi: 10.1029/JB093iB10p11667.

Channell, J. E. T. (1999), Geomagnetic paleointensity and directional secular variation at Ocean Drilling Program (ODP) Site 984 (Bjorn Drift) since 500 ka: Comparisons with ODP Site 983 (Gardar Drift), *J. Geophys. Res.*, *104*(B10), 22,937–22,951, doi: 10.1029/1999JB900223.

Channell, J. E. T. (2006), Late Brunhes polarity excursions (Mono Lake, Laschamp, Iceland Basin and Pringle Falls) recorded at ODP Site 919 (Irminger Basin), *Earth Planet. Sci. Lett.*, *244*(1-2), 378–393, doi: 10.1016/j.epsl.2006.01.021.

Channell, J. E. T., and C. Xuan (2009), Self-reversal and apparent magnetic excursions in Arctic sediments, *Earth Planet. Sci. Lett.*, *284*(1-2), 124–131, doi: 10.1016/j.epsl.2009.04.020.

Channell, J. E. T., D. A. Hodell, and B. Lehman (1997), Relative geomagnetic paleointensity and $\delta^{18}O$ at ODP Site 983 (Gardar Drift, North Atlantic) since 350 ka, *Earth Planet. Sci. Lett.*, *153*(1-2), 103–118, doi: 10.1016/S0012-821X(97)00164-7.

Channell, J. E. T., J. S. Stoner, D. A. Hodell, and C. D. Charles (2000), Geomagnetic paleointensity for the last 100 kyr from the sub-antarctic South Atlantic: a tool for inter-hemispheric correlation, *Earth Planet. Sci. Lett.*, *175*(1-2), 145–160, doi: 10.1016/S0012-821X(99)00285-X.

Channell, J. E. T., J. H. Curtis, and B. P. Flower (2004), The Matuyama-Brunhes boundary interval (500-900 ka) in North Atlantic drift sediments, *Geophys. J. Int.*, *158*(2), 489–505, doi: 10.1111/j.1365-246X.2004.02329.x.

Channell, J. E. T., C. Xuan, and D. A. Hodell (2009), Stacking paleointensity and oxygen isotope data for the last 1.5 Myr (PISO-1500), *Earth Planet. Sci. Lett.*, *283*(1-4), 14–23, doi: 10.1016/j.epsl.2009.03.012.

Channell, J. E. T., D. A. Hodell, and J. H. Curtis (2012), ODP Site 1063 (Bermuda Rise) revisited: oxygen isotopes, excursions and paleointensity in the Brunhes Chron, *Geochem. Geophys. Geosyst.*, *13*(1), Q02,001, doi: 10.1029/2011GC003897.

Chen, J., R. Lawrence Edwards, and G. Wasserburg (1986), ^{238}U, ^{234}U and ^{232}Th in seawater, *Earth Planet. Sci. Lett.*, *80*(3-4), 241–251, doi: 10.1016/0012-821X(86)90108-1.

Cheng, H., R. Edwards, J. Hoff, C. Gallup, D. Richards, and Y. Asmerom (2000), The half-lives of uranium-234 and thorium-230, *Chemical Geology*, *169*(1-2), 17–33, doi: 10.1016/S0009-2541(99)00157-6.

Cheng, H., R. L. Edwards, W. S. Broecker, G. H. Denton, X. Kong, Y. Wang, R. Zhang, and X. Wang (2009), Ice age terminations., *Science*, *326*(5950), 248–52, doi: 10.1126/science.1177840.

Christensen, U., P. Olson, and G. A. Glatzmaier (1999), Numerical modelling of the geodynamo: a systematic parameter study, *Geophys. J. Int.*, *138*(2), 393–409, doi: 10.1046/j.1365-246X.1999.00886.x.

Christensen, U. R. (2011), Geodynamo models: tools for understanding properties of Earths magnetic field, *Phys. Earth Planet. Inter.*, *187*(3-4), 157–169, doi: 10.1016/j.pepi.2011.03.012.

Christensen, U. R., and J. Aubert (2006), Scaling properties of convection-driven dynamos in rotating spherical shells and application to planetary magnetic fields, *Geophys. J. Int.*, *166*(1), 97–114, doi: 10.1111/j.1365-246X.2006.03009.x.

Christl, M., C. Strobl, and A. Mangini (2003), Beryllium-10 in deep-sea sediments: a tracer for the Earth's magnetic field intensity during the last 200,000 years, *Quat. Sci. Rev.*, *22*, 725–739, doi: 10.1016/S0277-3791(02)00195-6.

Chulliat, A., and N. Olsen (2010), Observation of magnetic diffusion in the Earth's outer core from Magsat, Ørsted, and CHAMP data, *J. Geophys. Res.*, *115*(B5), 1–13, doi: 10.1029/2009JB006994.

Cisowski, S., and F. Hall (1997), An examination of the paleointensity record and geomagnetic excursions recorded in Leg 155 cores, in *Proc. ODP, Sci. Results, Leg 155*, vol. 155, pp. 231–243, College Station, TX (Ocean Drilling Program), doi: 10.2973/odp.proc.sr.155.214.1997.

Clement, B. M. (2004), Dependence of the duration of geomagnetic polarity reversals on site latitude., *Nature*, *428*(6983), 637–40, doi: 10.1038/nature02459.

Coe, R. S., and G. a. Glatzmaier (2006), Symmetry and stability of the geomagnetic field, *Geophysical Research Letters*, *33*(21), L21,311, doi: 10.1029/2006GL027903.

Collinson, D. W. (1965), Depositional remanent magnetization in sediments, *J. Geophys. Res.*, *70*(18), 4663–4668, doi: 10.1029/JZ070i018p04663.

Collinson, D. W. (1983), *Methods in rock magnetism and palaeomagnetism : techniques and instrumentation*, Chapman and Hall, London; New York.

Cox, A. (1970), Latitude dependence of the angular dispersion of the geomagnetic field, *Geophys. J. R. Astr. Soc.*, *20*, 253–269, doi: 10.1111/j.1365-246X.1970.tb06069.x.

Cox, S. E., K. A. Farley, and S. R. Hemming (2012), Insights into the age of the Mono Lake Excursion and magmatic crystal residence time from (U-Th)/He and ^{230}Th dating of volcanic allanite, *Earth Planet. Sci. Lett.*, *319-320*, 178–184, doi: 10.1016/j.epsl.2011.12.025.

Craig, H., and L. I. Gordon (1965), Deuterium and oxygen-18 variations in the oceans and marine atmosphere, in *Stable Isotopes in Oceanographic Studies and Paleotemperatures*, edited by E. Tongiorgi, Spoleto, Consiglio Nazionale delle Ricerche, Laboratorio di Geologica Nucleare, Piza.

Creer, K. M. (1962), The dispersion of the geomagnetic field due to secular variation and its determination for remote times from paleomagnetic data, *J. Geophys. Res.*, *67*(9), 3461–3476, doi: 10.1029/JZ067i009p03461.

Cutler, K., R. Edwards, F. Taylor, H. Cheng, J. Adkins, C. Gallup, P. Cutler, G. Burr, and A. L. Bloom (2003), Rapid sea-level fall and deep-ocean temperature change since the last interglacial period, *Earth Planet. Sci. Lett.*, *206*(3-4), 253–271, doi: 10.1016/S0012-821X(02)01107-X.

Dansgaard, W., S. J. Johnsen, H. B. Clausen, D. Dahl-Jensen, N. S. Gundestrup, C. U. Hammer, C. S. Hvidberg, J. P. Steffensen, A. E. Sveinbjörnsdottir, J. Jouzel, and G. Bond (1993), Evidence for general instability of past climate from a 250-kyr ice-core record, *Nature*, *364*(6434), 218–220, doi: 10.1038/364218a0.

De Bièvre, P., and G. Debus (1965), Precision mass spectrometric isotope dilution analysis, *Nuclear Instruments and Methods*, *32*(2), 224–228, doi: 10.1016/0029-554X(65)90516-1.

Dekkers, M. J. (1997), Environmental magnetism : an introduction, *Geologie en Mijnbouw*, *76*(1-2), 163–182, doi: 10.1023/A:1003122305503.

DeMenocal, P. B., W. F. Ruddiman, and D. V. Kent (1990), Depth of post-depositional remanence acquisition in deep-sea sediments: a case study of the Brunhes-Matuyama reversal and oxygen isotopic Stage 19.1, *Earth Planet. Sci. Lett.*, *99*(1-2), 1–13, doi: 10.1016/0012-821X(90)90066-7.

Denham, C. R., and A. Cox (1971), Evidence that the Laschamp polarity event did not occur 13300-30400 years ago, *Earth Planet. Sci. Lett.*, *13*(1), 181–190, doi: 10.1016/0012-821X(71)90122-1.

DePaolo, D. J., K. Maher, J. N. Christensen, and J. McManus (2006), Sediment transport time measured with U-series isotopes: Results from ODP North Atlantic drift site 984, *Earth Planet. Sci. Lett.*, *248*(1-2), 394–410, doi: 10.1016/j.epsl.2006.06.004.

Dormy, E., J. P. Valet, and V. Courtillot (2000), Numerical models of the geodynamo and observational constraints, *Geochem. Geophys. Geosyst.*, *1*(10), 1037, doi: 10.1029/2000GC000062.

Drysdale, R. N., J. C. Hellstrom, G. Zanchetta, a. E. Fallick, M. F. Sánchez Goñi, I. Couchoud, J. McDonald, R. Maas, G. Lohmann, and I. Isola (2009), Evidence for obliquity forcing of glacial Termination II., *Science*, *325*(5947), 1527–31, doi: 10.1126/science.1170371.

Dunk, R., R. Mills, and W. Jenkins (2002), A reevaluation of the oceanic uranium budget for the Holocene, *Chemical Geology*, *190*(1-4), 45–67, doi: 10.1016/S0009-2541(02)00110-9.

Dunlop, D. J., and O. Ozdemir (1997), *Rock Magnetism: fundamentals and frontiers*, Cambridge University Press, Cambridge, New York.

Elsasser, W. (1946), Induction effects in terrestrial magnetism. Part I. Theory, *Physical Review*, *69*(3-4), 106–116, doi: 10.1103/PhysRev.69.106.

Elsasser, W., E. P. Ney, and J. R. Winckler (1956), Cosmic-ray intensity and geomagnetism, *Nature*, *178*(4544), 1226–1227, doi: 10.1038/1781226a0.

Emiliani, C. (1955), Pleistocene temperatures, *Journal of Geology*, *63*(6), 538–578, doi: 10.1086/626295.

Epstein, S., R. Buchsbaum, H. A. Lowenstam, and H. C. Urey (1953), Revised carbonate-water isotopic temperature scale, *Geological Society of America Bulletin*, *64*(11), 1315–1325, doi: 10.1130/0016-7606(1953)64.

Evans, M., and F. Heller (2001), Magnetism of loess/palaeosol sequences: recent developments, *Earth-Sci. Rev.*, *54*(1-3), 129–144, doi: 10.1016/S0012-8252(01)00044-7.

Fagaly, R. L. (2006), Superconducting quantum interference device instruments and applications, *Review of Scientific Instruments*, *77*(10), 101,101, doi: 10.1063/1.2354545.

Fang, X., J. Li, R. Vandervoo, C. Mac Niocaill, X. Dai, R. Kemp, E. Derbyshire, J. Cao, J. Wang, and G. Wang (1997), A record of the Blake Event during the last interglacial paleosol in the western Loess Plateau of China, *Earth Planet. Sci. Lett.*, *146*(1-2), 73–82, doi: 10.1016/S0012-821X(96)00222-1.

Fisher, N. I., T. Lewis, and M. E. Willcox (1981), Tests of discordancy for samples from Fisher's distribution on the sphere, *Applied Statistics*, *30*(3), 230, doi: 10.2307/2346346.

Fisher, R. (1953), Dispersion on a sphere, *Proceedings of the Royal Society A: Mathematical, Physical and Engineering Sciences*, *217*(1130), 295–305, doi: 10.1098/rspa.1953.0064.

Francois, R., M. Frank, M. M. Rutgers Van Der Loeff, and M. P. Bacon (2004), ^{230}Th normalization: an essential tool for interpreting sedimentary fluxes during the late Quaternary, *Paleoceanography*, *19*(1), PA1018, doi: 10.1029/2003PA000939.

Francois, R., M. Frank, M. Rutgers van der Loeff, M. P. Bacon, W. Geibert, S. Kienast, R. F. Anderson, L. Bradtmiller, Z. Chase, G. M. Henderson, F. Marcantonio, and S. E. Allen (2007), Comment on Do geochemical estimates of sediment focusing pass the sediment test in the equatorial Pacific? by M. Lyle et al., *Paleoceanography*, *22*(1), 1–5, doi: 10.1029/2005PA001235.

Frank, M., B. Schwarz, S. Baumann, P. W. Kubik, M. Suter, and A. Mangini (1997), A 200 kyr record of cosmogenic radionuclide production rate and geomagnetic field intensity from ^{10}Be in globally stacked deep-sea sediments, *Earth Planet. Sci. Lett.*, *149*(1-4), 121–129, doi: 10.1016/S0012-821X(97)00070-8.

Frank, U., and N. R. Nowaczyk (2008), Mineral magnetic properties of artificial samples systematically mixed from haematite and magnetite, *Geophysical Journal International*, *175*(2), 449–461, doi: 10.1111/j.1365-246X.2008.03821.x.

Gee, J. S., S. C. Cande, J. a. Hildebrand, K. Donnelly, and R. L. Parker (2000), Geomagnetic intensity variations over the past 780 kyr obtained from near-seafloor magnetic anomalies., *Nature*, *408*(6814), 827–32, doi: 10.1038/35048513.

Gilbert, W. (1600), *De magnete, magneticisque corporibus, et de magno magnete tellure: physiologia noua plurimis et argumentis, et experimentis demonstrata*, Petrus Short, London.

Gillson, G. R., D. J. Douglas, J. E. Fulford, K. W. Halligan, and S. D. Tanner (1988), Nonspectroscopic interelement interferences in inductively coupled plasma mass spectrometry, *Analytical Chemistry*, *60*(14), 1472–1474, doi: 10.1021/ac00165a024.

Giosan, L., R. D. Flood, J. Grützner, S.-O. Franz, M.-s. Poli, and S. Hagen (2001), High-Resolution Carbonate Content Estimated from Diffuse Spectral Reflectance for Leg 172 Sites, in *Proc. ODP, Sci. Results, Leg 172*, edited by L. D. Keigwin, D. Rio, G. D. Acton, and E. Arnold, August 1999, Ocean Drilling Program, College Station, TX, doi: 10.2973/odp.proc.sr.172.210.2001.

Glatzmaier, G. A. (2002), Geodynamo simulations - how realistic are they?, *Annual Review of Earth and Planetary Sciences*, *30*(1), 237–257, doi: 10.1146/annurev.earth.30.091201.140817.

Glatzmaier, G. A., and R. S. Coe (2007), Magnetic reversals in the core, in *Treatise on Geophysics, vol. 8*, edited by P. Olson, pp. 283–299, Elsevier B.V.

Glatzmaier, G. A., and P. H. Roberts (1995a), A three-dimensional self-consistent computer simulation of a geomagnetic field reversal, *Nature*, *377*(6546), 203–209, doi: 10.1038/377203a0.

Glatzmaier, G. A., and P. H. Roberts (1995b), A three-dimensional convective dynamo solution with rotating and finitely conducting inner core and mantle, *Physics of The Earth and Planetary Interiors*, *91*, 63–75, doi: 10.1016/0031-9201(95)03049-3.

Grützner, J., L. Giosan, S. O. Franz, R. Tiedemann, E. Cortijo, W. P. Chaisson, R. D. Flood, S. Hagen, L. D. Keigwin, S. Poli, D. Rio, and T. Williams (2002), Astronomical age models for Pleistocene drift sediments from the western North Atlantic (ODP Sites 1055-1063), *Mar. Geol.*, *189*(1-2), 5–23, doi: 10.1016/S0025-3227(02)00320-1.

Gubbins, D. (1999), The distinction between geomagnetic excursions and reversals, *Geophys. J. Int.*, *137*(1), F1–F4, doi: 10.1046/j.1365-246x.1999.00810.x.

Guillou, H., B. S. Singer, C. Laj, C. Kissel, S. Scaillet, and B. R. Jicha (2004), On the age of the Laschamp geomagnetic excursion, *Earth Planet. Sci. Lett.*, *227*, 331–343, doi: 10.1016/j.epsl.2004.09.018.

Guyodo, Y., and J. P. Valet (1999), Global changes in intensity of the Earth's magnetic field during the past 800 kyr, *Nature*, *399*(6733), 249–252, doi: 10.1038/20420.

Heezen, B. C., C. D. Hollister, and W. F. Ruddiman (1966), Shaping of the Continental Rise by deep geostrophic contour currents, *Science*, *152*(3721), 502–508.

Henderson, G. M. (2002), Seawater (^{234}U/^{238}U) during the last 800 thousand years, *Earth Planet. Sci. Lett.*, *199*(1-2), 97–110, doi: 10.1016/S0012-821X(02)00556-3.

Henderson, G. M., and R. F. Anderson (2003), The U-series Toolbox for Paleoceanography, in *Rev. Mineral. Geochem.*, vol. 52, edited by B. Bourdon, G. M. Henderson, C. C. Lundstrom, and S. Turner, pp. 493–531, Geochemical Society, doi: 10.2113/0520493.

Henderson, G. M., C. Heinze, R. Anderson, and A. Winguth (1999), Global distribution of the ^{230}Th flux to ocean sediments constrained by GCM modelling, *Deep Sea Research Part I: Oceanographic Research Papers*, *46*(11), 1861–1893, doi: 10.1016/S0967-0637(99)00030-8.

Henderson, G. M., N. C. Slowey, and M. Q. Fleisher (2001), U-Th dating of carbonate platform and slope sediments, *Geochim. Cosmochim. Acta*, *65*(16), 2757–2770, doi: 10.1016/S0016-7037(01)00621-4.

Herrero-Bervera, E., and C. E. Helsley (1993), Global paleomagnetic correlation of the Blake geomagnetic polarity episode, *Applications of Paleomagnetism to Sedimentary Geology, SEPM Special Publication*, *49*, 71–82.

Heslop, D. (2009), On the statistical analysis of the rock magnetic S-ratio, *Geophys. J. Int.*, *178*(1), 159–161, doi: 10.1111/j.1365-246X.2009.04175.x.

Heslop, D., C. Langereis, and M. Dekkers (2000), A new astronomical timescale for the loess deposits of Northern China, *Earth Planet. Sci. Lett.*, *184*(1), 125–139, doi: 10.1016/S0012-821X(00)00324-1.

Heslop, D., M. J. Dekkers, P. P. Kruiver, and I. H. M. van Oorschot (2002), Analysis of isothermal remanent magnetization acquisition curves using the expectation-maximization algorithm, *Geophys. J. Int.*, *148*(1), 58–64, doi: 10.1046/j.0956-540x.2001.01558.x.

Heumann, K. G., S. M. Gallus, G. Rädlinger, and J. Vogl (1998), Precision and accuracy in isotope ratio measurements by plasma source mass spectrometry, *Journal of Analytical Atomic Spectrometry*, *13*(9), 1001, doi: 10.1039/a801965g.

Higgins, S. M., W. Broecker, R. Anderson, D. C. McCorkle, and D. Timothy (1999), Enhanced sedimentation along the Equator in the western Pacific, *Geophys. Res. Lett.*, *26*(23), 3489, doi: 10.1029/1999GL008331.

Hollerbach, R. (1993), A geodynamo model incorporating a finitely conducting inner core, *Phys. Earth Planet. Inter.*, *75*(4), 317–327, doi: 10.1016/0031-9201(93)90007-V.

Hollerbach, R., and C. A. Jones (1995), On the magnetically stabilizing role of the Earth's inner core, *Physics of The Earth and Planetary Interiors*, *87*(3-4), 171–181, doi: 10.1016/0031-9201(94)02965-E.

Holt, J. W., and J. L. Kirschvink (1996), Geomagnetic field inclinations for the past 400 kyr from the 1-km core of the Hawaii Scientific Drilling Project, *J. Geophys. Res.*, *101*(B5), 11,655–11,663, doi: 10.1029/95JB03843.

Hoogakker, B. A. A., I. McCave, and M. J. Vautravers (2007), Antarctic link to deep flow speed variation during Marine Isotope Stage 3 in the western North Atlantic, *Earth Planet. Sci. Lett.*, *257*(3-4), 463–473, doi: 10.1016/j.epsl.2007.03.003.

Hospers, J. (1953), Reversals of the main geomagnetic field I, II, *Proc. Kon. Nederl. Akad. Wetensch., B.*, *56*, 467–491.

Hospers, J. (1955), Rock magnetism and polar wandering, *The Journal of Geology*, *63*(1), 59–74, doi: 10.1086/626226.

Imbrie, J., A. McIntyre, and A. C. Mix (1984), Oceanic response to orbital forcing in the late Quaternary: observational and experimental strategies, in *Climate and Geosciences, A Challenge for Science and Society in the 21st Century*, edited by A. Berger, S. H. Schneider, and J.-C. Duplessy, D. Reidal Publishing Company.

Irving, E. (1964), *Paleomagnetism and its Application to Geological and Geophysical Problems*, John Wiley, New York.

Irving, E., and A. Major (1964), Post-depositional detrital remanent magnetization in a synthetic sediment, *Sedimentology*, *3*(2), 135–143, doi: 10.1111/j.1365-3091.1964.tb00638.x.

Jackson, A., A. Jonkers, and M. Walker (2000), Four centuries of geomagnetic secular variation from historical records, *Philos. Trans. R. Soc. Lond. A*, *358*(1768), 957.

Johnsen, S. J., H. B. Clausen, W. Dansgaard, K. Fuhrer, N. Gundestrup, C. U. Hammer, P. Iversen, J. Jouzel, B. Stauffer, and J. P. Steffensen (1992), Irregular glacial interstadials recorded in a new Greenland ice core, *Nature*, *359*(6393), 311–313, doi: 10.1038/359311a0.

Johnson, C. L., C. G. Constable, L. Tauxe, R. Barendregt, L. L. Brown, R. S. Coe, P. Layer, V. Mejia, N. D. Opdyke, B. S. Singer, H. Staudigel, and D. B. Stone (2008), Recent investigations of the 0-5 Ma geomagnetic field recorded by lava flows, *Geochem. Geophys. Geosyst.*, *9*(4), doi: 10.1029/2007GC001696.

Johnson, E. A., T. Murphy, and O. W. Torreson (1948), Pre-history of the Earth's magnetic field, *J. Geophys. Res.*, *53*(4), 349–372, doi: 10.1029/TE053i004p00349.

Johnson, T. C., E. L. Lynch, W. J. Showers, and N. C. Palczuk (1988), Pleistocene fluctuations in the western boundary undercurrent on the Blake Outer Ridge, *Paleoceanography*, *3*(2), 191–207, doi: 10.1029/PA003i002p00191.

Kageyama, A., and T. Sato (1995), Computer simulation of a magnetohydrodynamic dynamo. II, *Physics of Plasmas*, *2*(5), 1421, doi: 10.1063/1.871485.

Katari, K., L. Tauxe, and J. King (2000), A reassessment of post-depositional remanent magnetism: preliminary experiments with natural sediments, *Earth Planet. Sci. Lett.*, *183*(1-2), 147–160, doi: 10.1016/S0012-821X(00)00255-7.

Kawamura, K., F. Parrenin, L. Lisiecki, R. Uemura, F. Vimeux, J. P. Severinghaus, M. a. Hutterli, T. Nakazawa, S. Aoki, J. Jouzel, M. E. Raymo, K. Matsumoto, H. Nakata, H. Motoyama, S. Fujita, K. Goto-Azuma, Y. Fujii, and O. Watanabe (2007), Northern Hemisphere forcing of climatic cycles in Antarctica over the past 360,000 years., *Nature*, *448*(7156), 912–916, doi: 10.1038/nature06015.

Keigwin, L. D., and G. A. Jones (1994), Western North Atlantic evidence for millennial-scale changes in ocean circulation and climate, *J. Geophys. Res.*, *99*(C6), 12,397–12,410, doi: 10.1029/94JC00525.

Keigwin, L. D., W. B. Curry, S. J. Lehman, and S. J. Johnsen (1994), The role of the deep ocean in North Atlantic climate change between 70 and 130 kyr ago, *Nature*, *371*(6495), 323–326, doi: 10.1038/371323a0.

Kennett, J. P., E. B. Roark, K. G. Cannariato, B. L. Ingram, and R. Tada (2000), Latest Quaternary Paleoclimatic and Radiocarbon Chronology, Hole 1017E, Southern Californian Margin, in *Proc. ODP, Sci. Results, Leg 167*, edited by M. Lyle, I. Koizumi, C. Richter, and R. J. Behl, pp. 249–254, Ocean Drilling Program, College Station, TX, doi: 10.2973/odp.proc.sr.167.212.2000.

King, J., S. K. Banerjee, J. Marvin, and O. Özdemir (1982), A comparison of different magnetic methods for determining the relative grain size of magnetite in natural materials: some results from lake sediments, *Earth Planet. Sci. Lett.*, *59*(2), 404–419, doi: 10.1016/0012-821X(82)90142-X.

King, J. W., and J. E. Channell (1991), Sedimentary magnetism, environmental magnetism, and magnetostratigraphy, *Rev. Geophys. Supp. April, U.S. Natl. Rep. IUGG 1987-1990*, *29*, 358–370.

King, J. W., S. K. Banerjee, and J. Marvin (1983), A new rock-magnetic approach to selecting sediments for geomagnetic paleointensity studies: application to paleointensity for the last 4000 years, *J. Geophys. Res.*, *88*(B7), 5911–5921.

Kirschvink, J. L. (1980), The least-squares line and plane and the analysis of palaeomagnetic data, *Geophys. J. R. Astr. Soc.*, *62*(3), 699–718, doi: 10.1111/j.1365-246X.1980.tb02601.x.

Kissel, C., H. Guillou, C. Laj, J. Carracedo, S. Nomade, F. Perez-Torrado, and C. Wandres (2011), The Mono Lake excursion recorded in phonolitic lavas from Tenerife (Canary Islands): paleomagnetic analyses and coupled K/Ar and Ar/Ar dating, *Phys. Earth Planet. Inter.*, *187*(3-4), 232–244, doi: 10.1016/j.pepi.2011.04.014.

Klinkhammer, G., and M. Palmer (1991), Uranium in the oceans: where it goes and why, *Geochim. Cosmochim. Acta*, *55*(7), 1799–1806, doi: 10.1016/0016-7037(91)90024-Y.

Knudsen, M. F., C. Mac Niocaill, and G. M. Henderson (2006), High-resolution data of the Iceland Basin geomagnetic excursion from ODP sites 1063 and 983: existence of intense flux patches during the excursion?, *Earth Planet. Sci. Lett.*, *251*(1-2), 18–32, doi: 10.1016/j.epsl.2006.08.016.

Knudsen, M. F., G. M. Henderson, C. Mac Niocaill, and A. J. West (2007), Seven thousand year duration for a geomagnetic excursion constrained by $^{230}\mathrm{Th}_{xs}$, *Geophys. Res. Lett.*, *34*(22), 1–6, doi: 10.1029/2007GL031090.

Knudsen, M. F., G. M. Henderson, M. Frank, C. Mac Niocaill, and P. Kubik (2008), In-phase anomalies in Beryllium-10 production and palaeomagnetic field behaviour during the Iceland Basin geomagnetic excursion, *Earth Planet. Sci. Lett.*, *265*(3-4), 588–599, doi: 10.1016/j.epsl.2007.10.051.

Korte, M. (2005), Continuous geomagnetic field models for the past 7 millennia: 1. A new global data compilation, *Geochem. Geophys. Geosyst.*, *6*(2), Q02H16, doi: 10.1029/2004GC000800.

Krishnaswami, S. (1976), Authigenic transition elements in Pacific pelagic clays, *Geochim. Cosmochim. Acta*, *40*(4), 425–434, doi: 10.1016/0016-7037(76)90007-7.

Kruiver, P. P., M. J. Dekkers, and D. Heslop (2001), Quantification of magnetic coercivity components by the analysis of acquisition curves of isothermal remanent magnetisation, *Earth Planet. Sci. Lett.*, *189*(3-4), 269–276, doi: 10.1016/S0012-821X(01)00367-3.

Ku, T.-L. (1965), An evaluation of the U^{234}/U^{238} method as a tool for dating pelagic sediments, *J. Geophys. Res.*, *70*(14), 3457–3474, doi: 10.1029/JZ070i014p03457.

Kuang, W., and J. Bloxham (1997), An Earth-like numerical dynamo model, *Nature*, *389*(6649), 371–374, doi: 10.1038/38712.

Kukla, G., F. Heller, L. Ming, X. Chun, L. Sheng, and A. Sheng (1988), Pleistocene climates in China dated by magnetic susceptibility, *Geology*, *16*(9), 811–814, doi: 10.1130/0091-7613(1988)016¡0811.

Kutzner, C., and U. R. Christensen (2002), From stable dipolar towards reversing numerical dynamos, *Physics of The Earth and Planetary Interiors*, *131*(1), 29–45, doi: 10.1016/S0031-9201(02)00016-X.

Kutzner, C., and U. R. Christensen (2004), Simulated geomagnetic reversals and preferred virtual geomagnetic pole paths, *Geophys. J. Int.*, *157*(3), 1105–1118, doi: 10.1111/j.1365-246X.2004.02309.x.

Laj, C., and J. E. T. Channell (2007), Geomagnetic Excursions, in *Treatise on Geophysics: Geomagnetism*, vol. 5, edited by G. Schubert, D. Bercovici, A. Dziewonski, T. Herring, H. Kanamori, M. Kono, P. L. Olson, G. D. Price, B. Romanowicz, T. Spohn, D. Stevenson, and A. B. Watts, pp. 373–416, Elsevier B.V., Amsterdam.

Laj, C., C. Kissel, A. Mazaud, J. E. T. Channell, and J. Beer (2000), North Atlantic palaeointensity stack since 75ka (NAPIS-75) and the duration of the Laschamp event, *Philos. Trans. R. Soc. Lond. A*, *358*(1768), 1009–1025, doi: 10.1098/rsta.2000.0571.

Laj, C., C. Kissel, and J. Beer (2004), High resolution global paleointensity stack since 75 kyr (GLOPIS-75) calibrated to absolute values, in *Timescales of the Paleomagnetic Field, Geophys. Monogr.*, vol. 145, edited by J. Channell, D. Kent, W. Lowrie, and J. Meert, pp. 255–265, AGU, Washington, D.C.

Laj, C., C. Kissel, and A. P. Roberts (2006), Geomagnetic field behavior during the Iceland Basin and Laschamp geomagnetic excursions: a simple transitional field geometry?, *Geochem. Geophys. Geosyst.*, *7*(3), Q03,004, doi: 10.1029/2005GC001122.

Laj, C., C. Kissel, C. Davies, and D. Gubbins (2011), Geomagnetic field intensity and inclination records from Hawaii and the Réunion Island: geomagnetic implications, *Phys. Earth Planet. Inter.*, *187*(3-4), 170–187, doi: 10.1016/j.pepi.2011.05.007.

Langereis, C., M. J. Dekkers, G. J. Lange, M. Paterne, and P. J. M. Santvoort (1997), Magnetostratigraphy and astronomical calibration of the last 1.1 Myr from an eastern Mediterranean piston core and dating of short events in the Brunhes, *Geophys. J. Int.*, *129*(1), 75–94, doi: 10.1111/j.1365-246X.1997.tb00938.x.

Langmyhr, F., and S. Sveen (1965), Decomposability in hydrofluoric acid of the main and some minor and trace minerals of silicate rocks, *Analytica Chimica Acta*, *32*, 1–7, doi: 10.1016/S0003-2670(00)88885-6.

Liddicoat, J. C., and R. S. Coe (1979), Mono Lake geomagnetic excursion, *J. Geophys. Res.*, *84*(B1), 261–271, doi: 10.1029/JB084iB01p00261.

Lisiecki, L. E., and P. A. Lisiecki (2002), Application of dynamic programming to the correlation of paleoclimate records, *Paleoceanography*, *17*(4), 14–23, doi: 10.1029/2001PA000733.

Lisiecki, L. E., and M. E. Raymo (2005), A Pliocene-Pleistocene stack of 57 globally distributed benthic δ^{18}O records, *Paleoceanography*, *20*, PA1003, doi: 10.1029/2004PA001071.

Loubere, P., F. Mekik, R. Francois, and S. Pichat (2004), Export fluxes of calcite in the eastern equatorial Pacific from the Last Glacial Maximum to present, *Paleoceanography*, *19*(2), doi: 10.1029/2003PA000986.

Lovlie, R. (1974), Post-depositional remanent magnetization in a re-deposited deep-sea sediment, *Earth Planet. Sci. Lett.*, *21*(3), 315–320, doi: 10.1016/0012-821X(74)90167-8.

Lund, S. P., and L. Keigwin (1994), Measurement of the degree of smoothing in sediment paleomagnetic secular variation records: an example from late Quaternary deep-sea sediments of the Bermuda Rise, western North Atlantic Ocean, *Earth Planet. Sci. Lett.*, *122*(3-4), 317–330, doi: 10.1016/0012-821X(94)90005-1.

Lund, S. P., G. Acton, B. Clement, M. Hastedt, M. Okada, and T. Williams (1998), Geomagnetic field excursions occurred often during the last million years, *Eos Trans. AGU*, *79*, 178–179.

Lund, S. P., T. Williams, G. Acton, B. Clement, and M. Okada (2001a), Brunhes Chron magnetic-field excursions recovered from Leg 172 sediments, in *Proc. ODP, Sci. Results, Leg 172*, edited by L. D. Keigwin, D. Rio, G. D. Acton, and E. Arnold, Ocean Drilling Program, College Station, TX, doi: 10.2973/odp.proc.sr.172.216.2001.

Lund, S. P., G. D. Acton, B. Clement, M. Okada, and T. Williams (2001b), Paleomagnetic Records of Stage 3 Excursions, Leg 172, in *Proc. ODP, Sci. Results, Leg 172*, edited by L. Keigwin, D. Rio, G. Acton, and E. Arnold, Ocean Drilling Program, College Station, TX, doi: 10.2973/odp.proc.sr.172.2001.

Lund, S. P., M. Schwartz, L. Keigwin, and T. Johnson (2005), Deep-sea sediment records of the Laschamp geomagnetic field excursion (∼41,000 calendar years before present), *J. Geophys. Res.*, *110*, B04,101, doi: 10.1029/2003JB002943.

Lund, S. P., J. E. T. Channell, J. S. Stoner, and G. Acton (2006), A summary of Brunhes paleomagnetic field variability recorded in Ocean Drilling Program cores, *Phys. Earth Planet. Inter.*, *156*, 194–204, doi: 10.1016/j.pepi.2005.10.009.

Lyle, M., I. Koizumi, C. Richter, and T. Moore (Eds.) (2000a), *Proceedings of the Ocean Drilling Program, 167 Scientific Results*, Ocean Drilling Program, College Station, TX, doi: 10.2973/odp.proc.sr.167.2000.

Lyle, M., A. Mix, A. C. Ravelo, D. Andreasen, L. Heusser, and A. Olivarez (2000b), Millennial-scale $CaCO_3$ and C_{ORG} events along the northern and central California Margins: stratigraphy and origins, in *Proc. ODP, Sci. Results, Leg 167*, edited by M. Lyle, I. Koizumi, C. Richter, and R. J. Behl, Ocean Drilling Program, College Station, TX.

Lyle, M., N. Mitchell, N. Pisias, A. Mix, J. I. Martinez, and A. Paytan (2005), Do geochemical estimates of sediment focusing pass the sediment test in the equatorial Pacific?, *Paleoceanography*, *20*, PA1005, doi: 10.1029/2004PA001019.

Maher, K., D. J. DePaolo, and J. C.-F. Lin (2004), Rates of silicate dissolution in deep-sea sediment: in situ measurement using $^{234}U/^{238}U$ of pore fluids, *Geochim. Cosmochim. Acta*, *68*(22), 4629–4648, doi: 10.1016/j.gca.2004.04.024.

Marcantonio, F., K. K. Turekian, S. Higgins, R. F. Anderson, M. Stute, and P. Schlosser (1999), The accretion rate of extraterrestrial ^{3}He based on oceanic ^{230}Th flux and the relation to Os isotope variation over the past 200,000 years in an Indian Ocean core, *Earth Planet. Sci. Lett.*, *170*(3), 157–168, doi: 10.1016/S0012-821X(99)00100-4.

Marcantonio, F., R. F. Anderson, S. Higgins, M. Stute, P. Schlosser, and P. Kubik (2001), Sediment focusing in the central equatorial Pacific Ocean, *Paleoceanography*, *16*(3), 260, doi: 10.1029/2000PA000540.

Marchal, O., R. François, T. F. Stocker, and F. Joos (2000), Ocean thermohaline circulation and sedimentary ^{231}Pa/^{230} Th ratio, *Paleoceanography*, *15*(6), 625, doi: 10.1029/2000PA000496.

Mason, A. J., and G. M. Henderson (2010), Correction of multi-collector-ICP-MS instrumental biases in high-precision uranium-thorium chronology, *Int. J. Mass Spectrom.*, *295*(1-2), 26–35, doi: 10.1016/j.ijms.2010.06.016.

Matyuama, M. (1929), On the direction of magnetization of basalt in Japan, Tyosen and Manchuria, *Proceedings of the Imperial Academy of Japan*, *5*, 203–205.

McCave, I. N. (2002), Paleoclimate. A poisoned chalice?, *Science*, *298*(5596), 1186–1187, doi: 10.1126/science.1076960.

McCave, I. N., and I. R. Hall (2006), Size sorting in marine muds: processes, pitfalls, and prospects for paleoflow-speed proxies, *Geochem. Geophys. Geosyst.*, *7*(10), Q10N05, doi: 10.1029/2006GC001284.

McCave, I. N., B. Manighetti, and S. G. Robinson (1995), Sortable silt and fine sediment size/composition slicing: parameters for palaeocurrent speed and palaeoceanography, *Paleoceanography*, *10*(3), 593, doi: 10.1029/94PA03039.

McElhinny, M., P. McFadden, and R. Merrill (1996), The time-averaged paleomagnetic field 0-5 Ma, *J. Geophys. Res.*, *101*(B11), 25,007–25.

McElhinny, M. W., and P. L. McFadden (1997), Palaeosecular variation over the past 5 Myr based on a new generalized database, *Geophys. J. Int.*, *131*, 240–252, doi: 10.1111/j.1365-246X.1997.tb01219.x.

McElhinny, M. W., P. L. McFadden, R. Dmowska, J. R. Holton, and H. T. Rossby (1999), *Paleomagnetism: Continents and Oceans*, International Geophysics, Academic Press.

McElhinny, W. (1973), *Palaeomagnetism and Plate Tectonics*, Cambridge Earth Science Series, Cambridge University Press.

McManus, J. F., R. F. Anderson, W. S. Broecker, M. Q. Fleisher, and S. M. Higgins (1998), Radiometrically determined sedimentary fluxes in the sub-polar North Atlantic during the last 140,000 years, *Earth Planet. Sci. Lett.*, *155*(1-2), 29–43, doi: 10.1016/S0012-821X(97)00201-X.

Ménabréaz, L., N. Thouveny, G. Camoin, and S. P. Lund (2010), Paleomagnetic record of the late Pleistocene reef sequence of Tahiti (French Polynesia): a contribution to the chronology of the deposits, *Earth Planet. Sci. Lett.*, *294*(1-2), 58–68, doi: 10.1016/j.epsl.2010.03.002.

Ménabréaz, L., N. Thouveny, D. Bourlès, P. Deschamps, B. Hamelin, and F. Demory (2011), The Laschamp geomagnetic dipole low expressed as a cosmogenic ^{10}Be atmospheric overproduction at ∼41 ka, *Earth Planet. Sci. Lett.*, *312*(3-4), 305–317, doi: 10.1016/j.epsl.2011.10.037.

Ménabréaz, L., D. L. Bourlès, and N. Thouveny (2012), Amplitude and timing of the Laschamp geomagnetic dipole low from the global atmospheric ^{10}Be overproduction: contribution of authigenic ^{10}Be/^{9}Be ratios in west equatorial Pacific sediments, *J. Geophys. Res.*, *117*, B11,101, doi: 10.1029/2012JB009256.

Merrill, R. T., and P. L. McFadden (1994), Geomagnetic field stability: reversal events and excursions, *Earth Planet. Sci. Lett.*, *121*(1-2), 57–69, doi: 10.1016/0012-821X(94)90031-0.

Merrill, R. T., and P. L. McFadden (1999), Geomagnetic polarity transitions, *Rev. Geophys.*, *37*(2), 201, doi: 10.1029/1998RG900004.

Merrill, R. T., M. W. McElhinny, and D. Stevenson (1979), Evidence for long-term asymmetries in the Earth's magnetic field and possible implications for dynamo theories, *Phys. Earth Planet. Inter.*, *20*(2-4), 75–82, doi: 10.1016/0031-9201(79)90029-3.

Merrill, R. T., M. W. McElhinny, and P. L. McFadden (1996), *The magnetic field of the earth : paleomagnetism, the core, and the deep mantle (Series: International geophysics series ; v. 63)*, Academic Press, San Diego; London.

Mitra, R., and L. Tauxe (2009), Full vector model for magnetization in sediments, *Earth Planet. Sci. Lett.*, *286*(3-4), 535–545, doi: 10.1016/j.epsl.2009.07.019.

Muscheler, R., J. Beer, G. Wagner, C. Laj, C. Kissel, G. M. Raisbeck, F. Yiou, and P. W. Kubik (2004), Changes in the carbon cycle during the last deglaciation as indicated by the comparison of ^{10}Be and ^{14}C records, *Earth Planet. Sci. Lett.*, *219*(3-4), 325–340, doi: 10.1016/S0012-821X(03)00722-2.

Muscheler, R., J. Beer, P. W. Kubik, and H.-A. Synal (2005), Geomagnetic field intensity during the last 60,000 years based on ^{10}Be and ^{36}Cl from the Summit ice cores and ^{14}C, *Quat. Sci. Rev.*, *24*(16-17), 1849–1860, doi: 10.1016/j.quascirev.2005.01.012.

Nagata, T. (1961), *Rock Magnetism*, 2nd ed., Maruzen Company Ltd., Tokyo.

Néel, L. (1949), Théorie du traînage magnétique des ferromagnétiques en grains fins avec applications aux terres cuites, *Ann. Géophys.*, *5*, 99–136.

Nowaczyk, N. R. (1997), High-resolution magnetostratigraphy of four sediment cores from the Greenland Sea-II. Rock magnetic and relative palaeointensity data, *Geophys. J. Int.*, *131*(2), 325–334, doi: 10.1111/j.1365-246X.1997.tb01225.x.

Nowaczyk, N. R., and M. Antonow (1997), High-resolution magnetostratigraphy of four sediment cores from the Greenland Sea-I. Identification of the Mono Lake excursion, Laschamp and Biwa I/Jamaica geomagnetic polarity events, *Geophys. J. Int.*, *131*(2), 310–324, doi: 10.1111/j.1365-246X.1997.tb01224.x.

Nowaczyk, N. R., and J. Knies (2000), Magnetostratigraphic results from the eastern Arctic Ocean: AMS ^{14}C ages and relative palaeointensity data of the Mono Lake and Laschamp geomagnetic reversal excursions, *Geophys. J. Int.*, *140*(1), 185–197, doi: 10.1046/j.1365-246x.2000.00001.x.

Nowaczyk, N. R., T. W. Frederichs, A. Eisenhauer, and G. Gard (1994), Magnetostratigraphic data from late Quaternary sediments From the Yermak Plateau, Arctic Ocean: evidence for four geomagnetic polarity events within the last 170 ka of the Brunhes Chron, *Geophys. J. Int.*, *117*(2), 453–471, doi: 10.1111/j.1365-246X.1994.tb03944.x.

Nowaczyk, N. R., H. Arz, U. Frank, J. Kind, and B. Plessen (2012), Dynamics of the Laschamp geomagnetic excursion from Black Sea sediments, *Earth Planet. Sci. Lett.*, *351-352*, 54–69, doi: 10.1016/j.epsl.2012.06.050.

Olson, P. (2011), Laboratory Experiments on the Dynamics of the Core, *Phys. Earth Planet. Inter.*, *187*(3-4), 139–156, doi: 10.1016/j.pepi.2011.08.006.

Olson, P., P. Driscoll, and H. Amit (2009), Dipole collapse and reversal precursors in a numerical dynamo, *Phys. Earth Planet. Inter.*, *173*(1-2), 121–140, doi: 10.1016/j.pepi.2008.11.010.

Opdyke, N. D., and J. E. Channell (1996), *Magnetic Stratigraphy*, 346 pp., Academic Press, San Diego, Calif.

Opdyke, N. D., and K. W. Henry (1969), A test of the dipole hypothesis, *Earth Planet. Sci. Lett.*, *6*, 139–151, doi: 10.1016/0012-821X(69)90132-0.

Osete, M.-L., J. Martín-Chivelet, C. Rossi, R. L. Edwards, R. Egli, M. B. Muñoz García, X. Wang, F. J. Pavón-Carrasco, and F. Heller (2012), The Blake geomagnetic excursion recorded in a radiometrically dated speleothem, *Earth Planet. Sci. Lett.*, *353-354*, 173–181, doi: 10.1016/j.epsl.2012.07.041.

Osmond, J. K., and M. Ivanovich (1992), Uranium Series mobilization and surface hydrology, in *Uranium Series disequilibrium - applications to earth, marine, and environmental sciences*, edited by M. Ivanovich and R. S. Harmon, pp. 259–289, Clarendon Press, Oxford.

Otofuji, Y.-i., and S. Sasajima (1981), A magnetization process of sediments: laboratory experiments on post-depositional remanent magnetization, *Geophys. J. Int.*, *66*(2), 241–259, doi: 10.1111/j.1365-246X.1981.tb05955.x.

Palmer, M., and J. Edmond (1993), Uranium in river water, *Geochim. Cosmochim. Acta*, *57*(20), 4947–4955, doi: 10.1016/0016-7037(93)90131-F.

Parés, J. M., R. Van der Voo, M. Yan, and X. Fang (2004), After the dust settles: why is the Blake event imperfectly recorded in the Chinese Loess?, in *AGU Geophysical Monograph, 145: Timescales of the Paleomagnetic Field*, edited by J. E. Channell, D. V. Kent, W. Lowrie, and J. Meert, pp. 191–204, AGU, Washington, D.C.

Plenier, G., J. P. Valet, G. Guerin, J. Lefevre, M. Legoff, and B. Carter-Stiglitz (2007), Origin and age of the directions recorded during the Laschamp event in the Chaîne des Puys (France), *Earth Planet. Sci. Lett.*, *259*(3-4), 414–431, doi: 10.1016/j.epsl.2007.04.039.

Potts, P. J. (1987), *Handbook of Silicate Rock Analysis*, 1st ed., Blackie, Glasgow.

Pozzo, M., C. Davies, D. Gubbins, and D. Alfè (2012), Thermal and electrical conductivity of iron at Earths core conditions, *Nature*, *485*, 355–358, doi: 10.1038/nature11031.

Proudman, I. (1956), The almost-rigid rotation of viscous fluid between concentric spheres, *Journal of Fluid Mechanics*, *1*, 505–516, doi: 10.1017/S0022112056000329.

Quidelleur, X., J. P. Valet, V. Courtillot, and G. Hulot (1994), Long term geometry of the geomagnetic field for the last five million years: an updated secular variation database, *Geophys. Res. Lett.*, *21*(15), 1639, doi: 10.1029/94GL01105.

Rahmstorf, S. (2002), Ocean circulation and climate during the past 120,000 years., *Nature*, *419*(6903), 207–14, doi: 10.1038/nature01090.

Raisbeck, G. M., F. Yiou, O. Cattani, and J. Jouzel (2006), ^{10}Be evidence for the Matuyama-Brunhes geomagnetic reversal in the EPICA Dome C ice core, *Nature*, *444*(7115), 82–4, doi: 10.1038/nature05266.

Rehkämper, M., M. Schönbächler, and C. H. Stirling (2001), Multiple collector ICP-MS: introduction to instrumentation, measurement techniques and analytical capabilities, *Geostandards and Geoanalytical Research*, *25*(1), 23–40, doi: 10.1111/j.1751-908X.2001.tb00785.x.

Richter, C. (Ed.) (2004), *Proceedings of the Ocean Drilling Program, 181 Scientific Results*, Ocean Drilling Program, College Station, TX, doi: 10.2973/odp.proc.sr.181.2004.

Roberts, A. P. (2006), High-resolution magnetic analysis of sediment cores: Strengths, limitations and strategies for maximizing the value of long-core magnetic data, *Phys. Earth Planet. Inter.*, *156*(3-4), 162–178, doi: 10.1016/j.pepi.2005.03.021.

Roberts, A. P. (2008), Geomagnetic excursions: knowns and unknowns, *Geophys. Res. Lett.*, *35*, L17,307, doi: 10.1029/2008GL034719.

Roberts, A. P., and M. Winklhofer (2004), Why are geomagnetic excursions not always recorded in sediments? Constraints from post-depositional remanent magnetization lock-in modelling, *Earth Planet. Sci. Lett.*, *227*(3-4), 345–359, doi: 10.1016/j.epsl.2004.07.040.

Roberts, A. P., J. S. Stoner, and C. Richter (1996), Coring-induced magnetic overprints and limitations of the long-core paleomagnetic measurement technique: some observations from Leg 160, eastern Mediterranean sea, in *Proc. ODP, Init. Repts., Leg 160*, vol. 160, edited by K.-C. Emeis, A. H. F. Robertson, C. Richter, and M.-M. Blanc-Valleron, pp. 497–505, College Station TX (Ocean Drilling Program), doi: 10.2973/odp.proc.ir.160.115.1996.

Roberts, A. P., L. Chang, C. J. Rowan, C.-S. Horng, and F. Florindo (2011), Magnetic properties of sedimentary greigite (Fe_3S_4): An update, *Reviews of Geophysics*, *49*(1), doi: 10.1029/2010RG000336.

Roberts, A. P., L. Tauxe, and D. Heslop (2013), Magnetic paleointensity stratigraphy and high-resolution Quaternary geochronology: successes and future challenges, *Quat. Sci. Rev.*, *61*, 1–16, doi: 10.1016/j.quascirev.2012.10.036.

Roberts, P. H. (1967), *An introduction to magnetohydrodynamics*, American Elsevier Pub. Co.

Robertson, D., and D. France (1994), Discrimination of remanence-carrying minerals in mixtures, using isothermal remanent magnetisation acquisition curves, *Phys. Earth Planet. Inter.*, *82*(3-4), 223–234, doi: 10.1016/0031-9201(94)90074-4.

Robinson, L. F., N. S. Belshaw, and G. M. Henderson (2004), U and Th concentrations and isotope ratios in modern carbonates and waters from the Bahamas, *Geochim. Cosmochim. Acta*, *68*(8), 1777–1789, doi: 10.1016/j.gca.2003.10.005.

Rowan, C. J., and A. P. Roberts (2006), Magnetite dissolution, diachronous greigite formation, and secondary magnetizations from pyrite oxidation: unravelling complex magnetizations in Neogene marine sediments from New Zealand, *Earth Planet. Sci. Lett.*, *241*(1-2), 119–137, doi: 10.1016/j.epsl.2005.10.017.

Rutherford, E., and F. Soddy (1902), LXXXIV. - The radioactivity of thorium compounds. II. The cause and nature of radioactivity, *Journal of the Chemical Society, Transactions*, *81*, 837–860, doi: 10.1039/ct9028100837.

Schubert, G., and K. Zhang (2001), Effects of an electrically conducting inner core on planetary and stellar dynamos, *The Astrophysical Journal*, *557*(2), 930–942, doi: 10.1086/321687.

Schwartz, M., S. P. Lund, and T. C. Johnson (1996), Environmental factors as complicating influences in the recovery of quantitative geomagnetic-field paleointensity estimates from sediments, *Geophys. Res. Lett.*, *23*(19), 2693–2696.

Schwartz, M., S. P. Lund, D. E. Hammond, R. Schwartz, and K. Wong (1997), Early sediment diagenesis on the Blake/Bahama Outer Ridge, North Atlantic Ocean, and its effects on sediment magnetism, *J. Geophys. Res.*, *102*(B4), 7903–7914.

Schwartz, M., S. P. Lund, and T. C. Johnson (1998), Geomagnetic field intensity from 71 to 12 ka as recorded in deep-sea sediments of the Blake Outer Ridge, North Atlantic Ocean, *J. Geophys. Res.*, *103*(B12), 30,407–30,416, doi: 10.1029/1998JB900003.

Shackleton, N. (1967), Oxygen isotope analyses and Pleistocene temperatures re-assessed, *Nature*, *215*(5096), 15–17.

Shackleton, N., R. Fairbanks, T.-C. Chiu, and F. Parrenin (2004), Absolute calibration of the Greenland time scale: implications for Antarctic time scales and for Δ^{14}C, *Quat. Sci. Rev.*, *23*(14-15), 1513–1522, doi: 10.1016/j.quascirev.2004.03.006.

Shipboard Scientific Party (1997a), Site 1017, in *Proc. ODP, Init. Repts., Leg 167*, edited by M. Lyle, I. Koizumi, and C. Richter, Ocean Drilling Program, College Station, TX, doi: 10.2973/odp.proc.ir.167.111.1997.

Shipboard Scientific Party (1997b), Site 1018, in *Proc. ODP, Init. Repts., Leg 167*, edited by M. Lyle, I. Koizumi, and C. Richter, Ocean Drilling Program, College Station, TX, doi: 10.2973/odp.proc.ir.167.111.1997.

Shipboard Scientific Party (1997c), Site 1019, in *Proc. ODP, Init. Repts., Leg 167*, edited by M. Lyle, I. Koizumi, and C. Richter, Ocean Drilling Program, College Station, TX, doi: 10.2973/odp.proc.ir.167.113.1997.

Shipboard Scientific Party (1998a), Deep Blake Bahama Outer Ridge, Sites 1060, 1061, and 1062, in *Proc. ODP, Init. Repts., Leg 172*, edited by L. Keigwin, D. Rio, and G. Acton, pp. 157–250, Ocean Drilling Program, College Station, TX, doi: 10.2973/odp.proc.ir.172.1998.

Shipboard Scientific Party (1998b), Explanatory Notes, in *Proc. ODP, Init. Repts., Leg 172*, edited by L. Keigwin, D. Rio, and G. Acton, Proceedings of the Ocean Drilling Program, pp. 13–29, College Station TX (Ocean Drilling Program), doi: 10.2973/odp.proc.ir.172.1998.

Shipboard Scientific Party (1999), Site 1119: Drift Accretion on Canterbury Slope, in *Proc. ODP, Init. Repts., Leg 181*, edited by R. M. Carter, I. McCave, C. Richter, and L. Carter, Ocean Drilling Program, College Station, TX, doi: 10.2973/odp.proc.ir.181.103.2000.

Shipboard Scientific Party (2000), Site 1122: Turbidites with a Contourite Foundation, in *Proc. ODP, Init. Repts., Leg 181*, edited by R. Carter, I. McCave, C. Richter, and L. Carter, Ocean Drilling Program, College Station, TX, doi: 10.2973/odp.proc.ir.181.106.2000.

Shipboard Scientific Party (2003a), Site 1234, in *Proc. ODP, Init. Repts., Leg 202*, edited by A. Mix, R. Tiedemann, and P. Blum, Ocean Drilling Program, College Station, TX, doi: 10.2973/odp.proc.ir.202.105.2003.

Shipboard Scientific Party (2003b), Leg 202 Summary, in *Proc. ODP, Init. Repts., Leg 202*, edited by A. C. Mix, R. Tiedemann, and P. Blum, Proceedings of the Ocean Drilling Program, Ocean Drilling Program, College Station, TX, doi: 10.2973/odp.proc.ir.202.101.2003.

Siddall, M., R. F. Anderson, G. Winckler, G. M. Henderson, L. I. Bradtmiller, D. McGee, A. Franzese, T. F. Stocker, and S. a. Müller (2008), Modeling the particle flux effect on distribution of ^{230}Th in the equatorial Pacific, *Paleoceanography*, *23*(2), 1–17, doi: 10.1029/2007PA001556.

Singer, B. S., H. Guillou, B. R. Jicha, C. Laj, C. Kissel, B. L. Beard, and C. M. Johnson (2009), ^{40}Ar/^{39}Ar, K–Ar and ^{230}Th–^{238}U dating of the Laschamp excursion: a radioisotopic tie-point for ice core and climate chronologies, *Earth Planet. Sci. Lett.*, *286*(1-2), 80–88, doi: 10.1016/j.epsl.2009.06.030.

Singer, B. S., H. Guillou, B. R. Jicha, E. Zanella, and P. Camps (2013), Refining the Quaternary Geomagnetic Instability Time Scale (GITS): Lava flow recordings of the Blake and Post-Blake excursions, *Quaternary Geochronology*, *in press*, doi: 10.1016/j.quageo.2012.12.005.

Smith, J. D., and J. H. Foster (1969), Geomagnetic reversal in Brunhes normal polarity epoch., *Science*, *163*(3867), 565–567, doi: 10.1126/science.163.3867.565.

Spassov, S., F. Heller, M. E. Evans, L. P. Yue, and T. V. Dobeneck (2003), A lock-in model for the complex Matuyama-Brunhes boundary record of the loess/palaeosol sequence at Lingtai (Central Chinese Loess Plateau), *Geophysical Journal International*, *155*(2), 350–366, doi: 10.1046/j.1365-246X.2003.02026.x.

Stanford, J., E. Rohling, S. Bacon, A. P. Roberts, F. Grousset, and M. Bolshaw (2011), A new concept for the paleoceanographic evolution of Heinrich event 1 in the North Atlantic, *Quat. Sci. Rev.*, *30*(9-10), 1047–1066, doi: 10.1016/j.quascirev.2011.02.003.

Stoner, J. S., C. Laj, J. E. T. Channell, and C. Kissel (2002), South Atlantic and North Atlantic geomagnetic paleointensity stacks (0–80ka): implications for inter-hemispheric correlation, *Quat. Sci. Rev.*, *21*(10), 1141–1151, doi: 10.1016/S0277-3791(01)00136-6.

Stoner, J. S., J. E. T. Channell, D. a. Hodell, and C. D. Charles (2003), A 580 kyr paleomagnetic record from the sub-Antarctic South Atlantic (Ocean Drilling Program Site 1089), *J. Geophys. Res.*, *108*(B5), 1–19, doi: 10.1029/2001JB001390.

Suman, D. O., and M. P. Bacon (1989), Variations in Holocene sedimentation in the North American Basin determined from ^{230}Th measurements, *Deep Sea Research Part A. Oceanographic Research Papers*, *36*(6), 869–878, doi: 10.1016/0198-0149(89)90033-2.

Svensson, A., K. K. Andersen, M. Bigler, H. B. Clausen, D. Dahl-Jensen, S. M. Davies, S. J. Johnsen, R. Muscheler, S. O. Rasmussen, R. Röthlisberger, J. r. P. Steffensen, and B. M. Vinther (2006), The Greenland Ice Core Chronology 2005, 15–42 ka. Part 2: comparison to other records, *Quat. Sci. Rev.*, *25*(23-24), 3258–3267, doi: 10.1016/j.quascirev.2006.08.003.

Svensson, A., K. K. Andersen, M. Bigler, H. B. Clausen, D. Dahl-Jensen, S. M. Davies, S. J. Johnsen, R. Muscheler, F. Parrenin, S. O. Rasmussen, R. Röthlisberger, I. Seierstad, J. P. Steffensen, and B. M. Vinther (2008), A 60 000 year Greenland stratigraphic ice core chronology, *Clim. Past*, *4*(1), 47–57, doi: 10.5194/cp-4-47-2008.

Tarduno, J. A., W. Tian, and S. Wilkison (1998), Biogeochemical remanent magnetization in pelagic sediments of the western equatorial Pacific Ocean, *Geophys. Res. Lett.*, *25*(21), 3987–3990, doi: 10.1029/1998GL900079.

Tauxe, L. (1993), Sedimentary records of relative paleointensity of the geomagnetic field: theory and practice, *Rev. Geophys.*, *31*(3), 319–354, doi: 10.1029/93RG01771.

Tauxe, L., and G. Wu (1990), Normalized remanence in sediments of the western equatorial Pacific: relative paleointensity of the geomagnetic field?, *J. Geophys. Res.*, *95*(B8), 12,337–12,350, doi: 10.1029/JB095iB08p12337.

Tauxe, L., T. Herbert, and N. Shackleton (1996), Astronomical calibration of the Matuyama-Brunhes boundary: consequences for magnetic remanence acquisition in marine carbonates and the Asian loess, *Earth Planet. Sci. Lett.*, *140*(1-4), 133–146, doi: 10.1016/0012-821X(96)00030-1.

Tauxe, L., J. Steindorf, and A. Harris (2006), Depositional remanent magnetization: toward an improved theoretical and experimental foundation, *Earth Planet. Sci. Lett.*, *244*(3-4), 515–529, doi: 10.1016/j.epsl.2006.02.003.

Teanby, N., C. Laj, D. Gubbins, and M. Pringle (2002), A detailed palaeointensity and inclination record from drill core SOH1 on Hawaii, *Phys. Earth Planet. Inter.*, *131*(2), 101–140, doi: 10.1016/S0031-9201(02)00032-8.

Thomas, A. L. (2006), Variations in past and present ocean circulation assessed with U-series nuclides, Ph.D. thesis, University of Oxford.

Thomas, A. L., G. M. Henderson, and L. F. Robinson (2006), Interpretation of the ^{231}Pa/^{230}Th paleocirculation proxy: New water-column measurements from the southwest Indian Ocean, *Earth Planet. Sci. Lett.*, *241*(3-4), 493–504, doi: 10.1016/j.epsl.2005.11.031.

Thomas, A. L., G. M. Henderson, and I. N. McCave (2007), Constant bottom water flow into the Indian Ocean for the past 140 ka indicated by sediment ^{231}Pa/^{230}Th ratios, *Paleoceanography*, *22*(4), PA4210, doi: 10.1029/2007PA001415.

Thomas, A. L., G. M. Henderson, P. Deschamps, Y. Yokoyama, A. J. Mason, E. Bard, B. Hamelin, N. Durand, and G. Camoin (2009), Penultimate deglacial sea-level timing from uranium/thorium dating of Tahitian corals., *Science*, *324*(5931), 1186–1189, doi: 10.1126/science.1168754.

Thomson, D. (1982), Spectrum estimation and harmonic analysis, *IEEE Proc.*, *70*(9), 1055–1096, doi: 10.1109/PROC.1982.12433.

Tiedemann, R., A. Mix, C. Richter, and W. Ruddiman (Eds.) (2007), *Proceedings of the Ocean Drilling Program, 202 Scientific Results*, Ocean Drilling Program, College Station, TX, doi: 10.2973/odp.proc.sr.202.2007.

Tric, E., C. Laj, J. P. Valet, P. Tucholka, M. Paterne, and F. Guichard (1991), The Blake geomagnetic event: transition geometry, dynamical characteristics and geomagnetic significance., *Earth Planet. Sci. Lett.*, *102*(1), 1–13, doi: 10.1016/0012-821X(91)90013-8.

Tucholka, P., M. Fontugne, F. Guichard, and M. Paterne (1987), The Blake magnetic polarity episode in cores from the Mediterranean Sea, *Earth Planet. Sci. Lett.*, *86*(2-4), 320–326, doi: 10.1016/0012-821X(87)90229-9.

Urey, H. C., H. A. Lowenstam, S. Epstein, and C. R. Mckinney (1951), Measurement of paleotemperatures and temperatures of the upper Cretaceous of England, Denmark, and the southeastern United States, *Geological Society of America Bulletin*, *62*(4), 399, doi: 10.1130/0016-7606(1951)62[399:MOPATO]2.0.CO;2.

Valet, J. P., and L. Meynadier (1993), Geomagnetic field intensity and reversals during the past four million years, *Nature*, *366*(6452), 234–238, doi: 10.1038/366234a0.

Valet, J. P., and G. Plenier (2008), Simulations of a time-varying non-dipole field during geomagnetic reversals and excursions, *Phys. Earth Planet. Inter.*, *169*(1-4), 178–193, doi: 10.1016/j.pepi.2008.07.031.

Valet, J. P., L. Meynadier, and Y. Guyodo (2005), Geomagnetic dipole strength and reversal rate over the past two million years, *Nature*, *435*(7043), 802–805, doi: 10.1038/nature03674.

Valet, J. P., G. Plenier, and E. Herrero-Bervera (2008), Geomagnetic excursions reflect an aborted polarity state, *Earth Planet. Sci. Lett.*, *274*(3-4), 472–478, doi: 10.1016/j.epsl.2008.07.056.

Valet, J. P., A. Fournier, V. Courtillot, and E. Herrero-Bervera (2012), Dynamical similarity of geomagnetic field reversals, *Nature*, *490*(7418), 89–93, doi: 10.1038/nature11491.

Vandamme, D. (1994), A new method to determine paleosecular variation, *Phys. Earth Planet. Inter.*, *85*, 131–142, doi: 10.1016/0031-9201(94)90012-4.

Vautravers, M. J., N. J. Shackleton, C. Lopez-Martinez, and J. O. Grimalt (2004), Gulf Stream variability during marine isotope stage 3, *Paleoceanography*, *19*, PA2011, doi: 10.1029/2003PA000966.

Verosub, K. L. (1977), Depositional and postdepositional processes in the magnetization of sediments, *Reviews of Geophysics*, *15*(2), 129, doi: 10.1029/RG015i002p00129.

Watkins, N. D. (1973), Brunhes epoch geomagnetic secular variation on Reunion Island, *J. Geophys. Res.*, *78*(32), 7763–7768.

Whitney, J. (1971), Investigations of some magnetic and mineralogical properties of the Laschamp and Olby flows, France, *Quaternary Research*, *1*, 511–521, doi: 10.1016/0033-5894(71)90061-5.

Wicht, J. (2002), Inner-core conductivity in numerical dynamo simulations, *Physics of The Earth and Planetary Interiors*, *132*(4), 281–302, doi: 10.1016/S0031-9201(02)00078-X.

Wicht, J. (2005), Palaeomagnetic interpretation of dynamo simulations, *Geophys. J. Int.*, *162*(2), 371–380, doi: 10.1111/j.1365-246X.2005.02665.x.

Wicht, J., and P. Olson (2004), A detailed study of the polarity reversal mechanism in a numerical dynamo model, *Geochem. Geophys. Geosyst.*, *5*, Q03H10, doi: 10.1029/2003GC000602.

Wicht, J., S. Stellmach, and H. Harder (2009), Numerical models of the Geodynamo: from fundamental Cartesian models to 3D simulations of field reversals, in *Geomagnetic Field Variations - Space-Time Structure, Processes, and Effects on Systen Earth*, edited by H. Glassmeier, H. Soffel, and J. Negendank, pp. 107–158, Springer, Berlin.

Wilson, R. L. (1970), Permanent aspects of the Earth's non-dipole magnetic field over Upper Tertiary times, *Geophys. J. Int.*, *19*(4), 417–437, doi: 10.1111/j.1365-246X.1970.tb06056.x.

Wilson, R. L., and J. M. Ade-Hall (1970), Palaeomagnetic indications of a permanent aspect of the non-dipole field, in *Palaeogeophysics*, edited by S. K. Runcorn, pp. 307–312, Academic, San Diego, Calif.

Wilson, R. L., P. Dagley, and A. G. McCormack (1972), Palaeomagnetic evidence about the source of the geomagnetic field, *Geophys. J. R. Astr. Soc.*, *28*, 213–224, doi: 10.1111/j.1365-246X.1972.tb06124.x.

Wollin, G., D. Ericson, W. Ryan, and J. Foster (1971), Magnetism of the earth and climatic changes, *Earth Planet. Sci. Lett.*, *12*(2), 175–183, doi: 10.1016/0012-821X(71)90075-6.

Xuan, C., and J. E. T. Channell (2010), Origin of apparent magnetic excursions in deep-sea sediments from Mendeleev-Alpha Ridge, Arctic Ocean, *Geochem. Geophys. Geosyst.*, *11*(2), Q02,003, doi: 10.1029/2009GC002879.

Yamazaki, T., and P. Solheid (2011), Maghemite-to-magnetite reduction across the Fe-redox boundary in a sediment core from the Ontong-Java Plateau: influence on relative palaeointensity estimation and environmental magnetic application, *Geophys. J. Int.*, *185*, 1243–1254, doi: 10.1111/j.1365-246X.2011.05021.x.

Yu, E. F., R. Francois, M. P. Bacon, and A. P. Fleer (2001), Fluxes of ^{230}Th and ^{231}Pa to the deep sea : implications for the interpretation of excess ^{230}Th and ^{231}Pa/^{230}Th profiles in sediments, *Earth Planet. Sci. Lett.*, *191*, 219–230.

Zhu, R., L. Zhou, C. Laj, A. Mazaud, and Z. Ding (1994), The Blake geomagnetic polarity episode recorded in Chinese loess, *Geophys. Res. Lett.*, *21*(8), 697–697.

Zhu, R., R. S. Coe, B. Guo, R. Anderson, and X. Zhao (1998), Inconsistent palaeomagnetic recording of the Blake event in Chinese loess related to sedimentary environment, *Geophys. J. Int.*, *134*(3), 867–875, doi: 10.1046/j.1365-246x.1998.00599.x.

Zhu, R., Y. Pan, and R. S. Coe (2000), Paleointensity studies of a lava succession from Jilin Province, northeastern China: evidence for the Blake event, *J. Geophys. Res.*, *105*(B4), 8305–8317, doi: 10.1029/1999JB900448.

Ziegler, L. B., C. G. Constable, C. L. Johnson, and L. Tauxe (2011), PADM2M: a penalized maximum likelihood model of the 0-2 Ma palaeomagnetic axial dipole moment, *Geophys. J. Int.*, *184*(3), 1069–1089, doi: 10.1111/j.1365-246X.2010.04905.x.

Zimmerman, S. H., S. R. Hemming, D. V. Kent, and S. Y. Searle (2006), Revised chronology for late Pleistocene Mono Lake sediments based on paleointensity correlation to the global reference curve, *Earth Planet. Sci. Lett.*, *252*(1-2), 94–106, doi: 10.1016/j.epsl.2006.09.030.

Appendices

Appendix A

Free Decay Time of the Earth's Inner Core

A.1 Introduction

Gubbins [1999] proposed a hypothesis to explain why the field rapidly returned to its previous polarity following an excursion, rather than remain in the opposite state, as in a reversal. The conjecture, based upon numerical simulations conducted by [*Hollerbach*, 1993], emphasizes the stabilizing influence of the inner core on the geomagnetic field. Whilst the magnetic field of the liquid outer core can change by fluid flow within 500 years, the field in the inner, solid core can only change via a process of diffusion, on a 'free decay' time-scale of approximately 3 kyr [*Hollerbach and Jones*, 1995]. Decay times are usually quoted as being the time within which the field will decay to $1/e$ of its initial intensity. This appendix presents a simplified model proposed by *Roberts* [1967] that provides an insight into the order of magnitude of the free-decay time for the Earth's magnetic field in the solid inner core.

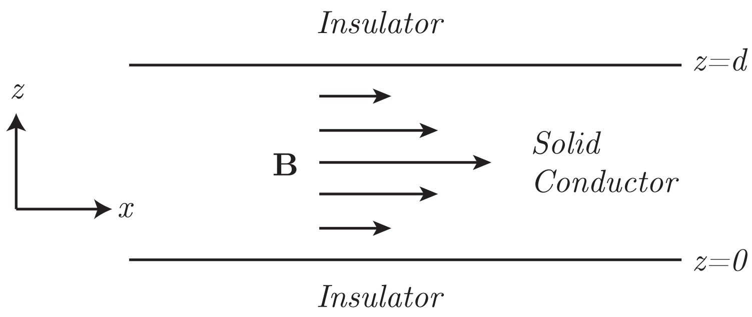

Figure A.1: Magnetic field decay in a solid conductor. A solid conducting region is encompassed by two insulating regions at $z = 0$ and $z = d$. The magnetic field, $\mathbf{B}(z,t)$, is confined within the conductor.

A.2 Decay of Magnetic Fields in a Solid Conductor

Roberts [1967] demonstrated an idealised 2D model that allows insight into the free decay of the Earth's magnetic field. The model presents a planar conducting region between two insulators (Fig. A.1). Let $0 \leq z \leq d$ be a stationary conductor in which the magnetic Reynolds number is very small, such that there is no convection term in the magnetic induction equation:

$$\partial \mathbf{B}/\partial t = k_m \nabla^2 \mathbf{B} \quad (R_m \ll 1) \quad , \tag{A.1}$$

where k_m, the 'magnetic diffusivity', is equal to $1/\mu_\circ \sigma$.

The conductor is surrounded by insulating regions $z > d$ and $z < 0$. Suppose that at time, $t = 0$ the magnetic field in the slab is:

$$\mathbf{B}_\circ = (b_\circ(z), 0, 0) \quad (t = 0; 0 \leq z \leq d) \quad , \tag{A.2}$$

and the current density is:

$$\mathbf{J}_\circ = \left(0, \frac{1}{\mu} b_\circ(z), 0\right) \quad (t = 0; 0 \leq z \leq d) \quad . \tag{A.3}$$

We must suppose that the net current flowing in the layer is zero, and that:

$$b_\circ(0) = b_\circ(d) = 0; \quad (t = 0) \quad . \tag{A.4}$$

The current and field will decay in time in the absence of any applied potential difference. The fields B_y and B_z are zero everywhere for all time, and in the insulator B_x must all be zero for all time, so that:

$$B_x(0, t) = B_x(d, t) = 0 \quad . \tag{A.5}$$

The conditions of A.5 are satisfied by each term of the fourier sine decomposition of B_x:

$$B_x = \sum_{n=1}^{\infty} B_{xn}(t) \sin\left(\frac{n\pi z}{d}\right) \quad . \tag{A.6}$$

We may then determine the differential equation that describes the decay of the nth fourier component B_{xn}(t), from A.1 and A.6:

$$\begin{aligned}
\frac{\partial}{\partial t}\left(B_{xn}(t) \sin\left(\frac{n\pi z}{d}\right)\right) &= k_m \frac{\partial^2}{\partial z^2}\left(B_{xn}(t) \sin\left(\frac{n\pi z}{d}\right)\right) \\
\sin\left(\frac{n\pi z}{d}\right) \frac{\partial B_{xn}}{\partial t} &= k_m \frac{\partial^2}{\partial z^2} \sin\left(\frac{n\pi z}{d}\right) \\
&= -k_m \left(\frac{n\pi z}{d}\right)^2 B_{xn} \sin\left(\frac{n\pi z}{d}\right) \\
\frac{\partial B_{xn}}{\partial t} &= -k_m \left(\frac{\pi n}{d}\right)^2 \; B_{xn} \quad .
\end{aligned} \tag{A.7}$$

We can then integrate to find the decay of B_{xn} with time:

$$\int \frac{1}{\mathrm{B}_{xn}}\,\mathrm{dB}_{xn} = -\int k_m \left(\frac{\pi n}{d}\right)^2\,\mathrm{d}t$$

$$\ln \mathrm{B}_{xn} = -k_m \left(\frac{\pi n}{d}\right)^2 t + C$$

$$\mathrm{B}_{xn} = Ce^{-k_m\left(\frac{\pi n}{d}\right)t}$$

$$\text{at } t = 0,\ C = \mathrm{B}_{xn(\circ)}$$

$$\mathrm{B}_{xn} = \mathrm{B}_{xn(\circ)} e^{-k_m\left(\frac{\pi n}{d}\right)^2 t} \quad . \tag{A.8}$$

On examining A.8 we see that the amplitude of each fourier component falls exponentially to zero, its rate of decay being proportional to n^2. The lowermost harmonic, $n = 1$, has the slowest rate of decay. Decay times are usually quoted as being the time in which the field will decay away to $1/e$ of its intial intensity in some time, the 'e-folding time', τ:

$$\mathrm{B}_{xn}(\tau) = \frac{\mathrm{B}_{xn(\circ)}}{e} = \mathrm{B}_{xn(\circ)} e^{-k_m\tau\left(\frac{\pi n}{d}\right)^2}$$

$$\tau = \left(\frac{d}{n\pi}\right)^2 \left(\frac{1}{k_m}\right) \quad . \tag{A.9}$$

A.3 Decay Time of Earth's Inner Core

Calculations involving spherical geometry are more complicated but yield similar results. Applying the simple model to the inner core, the characteristic length used is the radius of the inner core, $d = 1.23 \times 10^6$ m. The permittivity of free space, $\mu_\circ$ is equal to $4\pi \times 10^{-7}$ NA^{-2}. The conductivity, σ, of the Earth's core at the inner core boundary has been estimated, based on core mixtures, as $1.25 \times 10^6\ \Omega\ \mathrm{m}^{-1}$ [*Pozzo et al.*, 2012].

Thus, for the inner core:

$$\tau_{n=1} = \left(\frac{1.23 \times 10^6}{\pi}\right)^2 \left(4\pi \times 10^{-7} \times 1.25 \times 10^6\right)$$

$$= 2.4 \times 10^{11} \text{ s} \approx \mathbf{7.7\ kyr} \quad . \tag{A.10}$$

Using the simple model of *Roberts* [1967], the estimate obtained for the inner core e-folding decay time is very much an order-of magnitude estimate. In part, this is because the inner core is not surrounded by an insulator, but instead is encompassed by the conducting (and convecting) fluid outer core. However, the result obtained is very similar to results obtained using spherical geometry [*Hollerbach and Jones*, 1995] and illustrates schematically how such a value may be calculated.

Appendix B

Software Manual for XSage 1.9.2

If you use this software, please include the citation:

Bourne, M, Thomas, AL, Mac Niocaill, CM, Henderson GM, (2012) Improved determination of marine sedimentation rates using $^{230}Th_{xs}$, *Geochemistry, Geophysics, Geosystems*, DOI:10.1029/2012GC004295

B.1 Overview

Measuring sediment fluxes of ^{230}Th and ^{231}Pa have been invaluable in sedimentation rates and palaeoceanography. XSage 1.9 is a fully interactive MATLAB script that takes measured uranium and thorium and optionally protactinium data to calculate the input components of the isotopes into the sediment and using a Monte Carlo approach it also calculates the associated uncertainties.

Using the variation in the concentration of Thorium-230-excess ($^{230}Th_{xs}$), a constant flux proxy, the variation in sedimentation rate between two points of known ages in a core can be calculated. Assuming a relatively constant sedimentation regime, the relationship between Thorium-230-excess and sedimentation rate may be extrapolated beyond the tie-points. The variable sedimentation rate can then be used to calculate an age model for the core. This script has been designed to aid in the calculations of $^{230}Th_{xs}$-normalized age models for sedimentary cores.

Combining the measured data and known tie-points, the script can determine accurate age models using a Monte-Carlo approach to determine the associated uncertainties. Furthermore the age and durations of arbitrary intervals (e.g particular events) can be also be calculated by the script. A Monte-Carlo approach is employed as the equations used are not independent and therefore the uncertainties are difficult to propagate through the calculation using classical error propagation methods.

B.2 Installation

MATLAB is required to run this script. The script was written and tested in MATLAB R2011a. Installation is relatively straightforward. Download the compressed file and extract the contents to a folder in a location of your choice. The script should be ready to run. Note that the installation procedure is essentially the same under Linux, Mac and Windows.

B.3 Preparing Data for Use

For any one core, the script requires two user-prepared files in order to calculate the age and duration of an event using thorium-normalized sedimentation rates:

1. **Tie-points:** The first file contains the ages and depths of the tie-points to be used in the core and can optionally also contain the depths of the boundaries of event intervals.

2. **U-Th Data:** The second file contains the measured uranium, thorium and optionally protactinium measurements for samples at varying depths in the core.

Examples of both files are included in the installation folder. They are in CSV format and may be edited using a spreadsheet software package.

Tie-points File

The tie-points file contains the ages and depths of the tie-points determined by an independent stratigraphy such as, for example, an oxygen-isotope stratigraphy or tephrochronology. The file provides depths and ages for the tie-points as well as their respective uncertainties.

If you wish to calculate the age and duration of particular intervals, the depths of the intervals may also be entered in this file. If no interval depths are given, then the script does not calculate the duration of any interval. An example tie-points file is included as *tiepoints.csv* in the *Example* folder.

When the Monte-Carlo method is used, the ages and depths of the tie-points are varied within the ranges given for each evaluation. The tie-points file also contains an option labelled `Gaussian`. If this is set to 0, the Monte-Carlo simulation will model the age and depths of the tie-points as 'top-hat' distributions whereby the uncertainties set the minima and maxima for the ages and depths and the probability of any value between the bounds is equally likely. Otherwise, if the `Gaussian` option is set to 1 then the age and depths are modelled as Gaussian probability distributions with one standard deviations equal to the uncertainties provided.

U-Th-Pa Data File

The second data file contains the uranium and thorium and optional protactinium data used to calculate the the input components of Thorium (and Protactinium) and a ^{230}Th-normalized sedimentation rate. The file may be supplied with all the measured U-Th activities (and optional Pa activities) OR just the final $^{230}\mathrm{Th}^{o}_{xs}$ (and $^{231}\mathrm{Pa}^{o}_{xs}$). For the first option, if (^{234}U) has not been measured, retain this column but set all values to zero.

The samples must be given in depth order (from shallowest to deepest). Repeat measurements may also be provided.

If the measured U-Th(-Pa) activities are supplied in the data-file, the script calculates the authigenic, detrital and excess components of thorium-230 (and protactinium-231), and using the tie-points provided, normalized sedimentation rates and an age model. An example file is included in the *Example* folder as *uthdata.csv*. For each sample measurement, the file can either contain:

Columns	Description
`depth`	sample depth in the core (m)
`uranium238ActivityTotal`	total ^{238}U activity (dpm g^{-1})
`uranium238ActivityTotal_sd`	1σ total ^{238}U activity
`uranium234ActivityTotal`	total ^{234}U activity (dpm g^{-1})
`thorium230ActivityTotal`	total ^{230}Th activity (dpm g^{-1})
`thorium230ActivityTotal_sd`	1σ total ^{230}Th activity
`thorium232ActivityTotal`	total ^{232}Th activity (dpm g^{-1})
`thorium232ActivityTotal_sd`	1σ total ^{232}Th activity
Optional	
`protactinium231ActivityTotal`	total ^{231}Pa activity (dpm g^{-1})
`protactinium231ActivityTotal_sd`	1σ total ^{231}Pa

OR

`depth`	sample's depth in the core (m)
`thorium230ActivityExcessInit`	init. ^{230}Th$_{xs}$ activity (dpm g^{-1})
`thorium230ActivityExcessInit_sd`	1σ init. excess ^{230}Th activity
Optional	
`protactinium231ActivityExcessInitial`	init. ^{231}Pa$_{xs}$ activity (dpm g^{-1})
`protactinium231ActivityExcessInitial_sd`	1σ init. excess ^{231}Pa activity

The samples can have depths shallower or deeper than the uppermost and lowermost tie-points respectively.

When the Monte-Carlo method is used in the script, a dataset is created for each evaluation, whereby each isotope activity is generated as a sample from a normal distribution determined by the respective mean and standard deviation supplied. When the data-file contains the full U-Th data, $^{230}Th_{xs}$ (and $^{231}Pa_{xs}$) is calculated from the supplied data for each evaluation.

When only $^{230}Th^{o}_{xs}$ (and $^{231}Pa^{o}_{xs}$) is supplied, each evaluation generates a value for $^{230}Th^{o}_{xs}$ (and $^{231}Pa^{o}_{xs}$) by sampling from a normal distribution using the given mean and standard deviation. Note however, that this is inherently less realistic and the answers returned may be less reliable. Furthermore, the values for $^{230}Th^{o}_{xs}$ (and $^{231}Pa^{o}_{xs}$) may have been calculated using a different age model (to account for decay over time since deposition). However, this feature does allow the user to estimate the importance of the position and age of the tie-points on the final calculation.

Saving the Files

The files can have any name but must be in csv format.

CONSTANTS file

If the user wishes to check or adjust the half-lives (in years) of the thorium and uranium isotopes used in the calculations these may be changed by editing the `CONSTANTS.CONF` in the XSage folder using a simple text editor.

B.4 Running the Script

Navigate to the folder where XSage is installed within MATLAB. To run the script type `xsage` at the MATLAB command line. All prompts have a default setting which is used if the user does not enter an input before pressing return.

File Identification

1. On running XSage you will be presented with the opening lines and an open-file dialog box asking for a file. Open the tie-points file you have created.
2. XSage will then prompt for the data-file. Open the file containing the U-Th data.
3. XSage will then ask whether the data-file contains ^{231}Pa data.
4. XSage will then ask whether ^{230}Th$_{xs}$ is already calculated. If ^{230}Th$_{xs}$ has not been calculated previously (as in the first table above) type `N`. If the file contains only a previously calculated ^{230}Th$_{xs}$ (as in the second table above) dataset type `Y`.

U-Th(-Pa) Calculations

Detrital and Seawater Ratios

If the data-file contains the full uranium and thorium data, XSage will then ask if the user wants to use the data to make a local estimate of the (^{238}U)/(^{232}Th) value, if `N` is given, a value for the detrital ratio can be entered manually (default: 0.6 ± 0.1 - appropriate for Atlantic).

Otherwise, using the default option (`Y`), XSage will use the measured U-Th Data to determine an estimate for the detrital (^{238}U)/(^{232}Th) as follows:

- If (^{234}U) has been supplied by the user, XSage presents a graph of (^{234}U)/(^{238}U) for all the samples. Use the mouse cross-hair to indicate a divide between those samples with and without authigenic input (very roughly those with (^{234}U)/(^{238}U)>1 and <1 respectively) (Figure B.1). Samples with a (^{234}U)/(^{238}U) activity ratio less than the value determined by the cross-hair will be assumed to contain **no** thorium component formed from the decay of authigenic uranium. The selected samples will then be shown (Fig. B.2). XSage will also give the (^{238}U)/(^{232}Th) calculated from the average of those samples that do not appear to have an authigenic component. To continue and confirm the selection press `ENTER`.

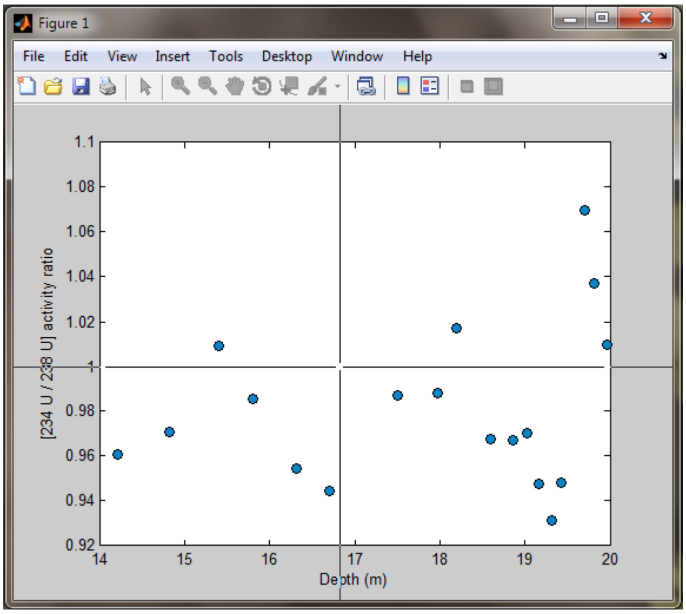

Figure B.1: Place the mouse cross-hair to divide the samples into those with and those without authigenic input.

- Alternatively, if (^{234}U) data is absent (i.e. all values in this column are zeros, see Section B.3) XSage presents a graph of (^{238}U)/(^{232}Th) for all the samples. Use the mouse cross-hair to indicate a divide between those samples with and without authigenic input (Figure B.3). Samples with a (^{238}U)/(^{232}Th) activity ratio less than the value determined by the cross-hair will be assumed to contain **no** thorium component formed from the decay of authigenic uranium. The selected results will then be shown (Fig. B.4). To continue and confirm the selection press `ENTER`.

XSage will then ask for the assumed lithogenic (^{230}Th)/(^{238}U) ratio and the uncertainty on this value (default is 0.96±0.04).

XSage will then ask for the assumed initial seawater (^{234}U)/(^{238}U) ratio and the uncertainty on this value (default assumes 1.147). This ratio is used in the calculation of the authigenic ^{230}Th component.

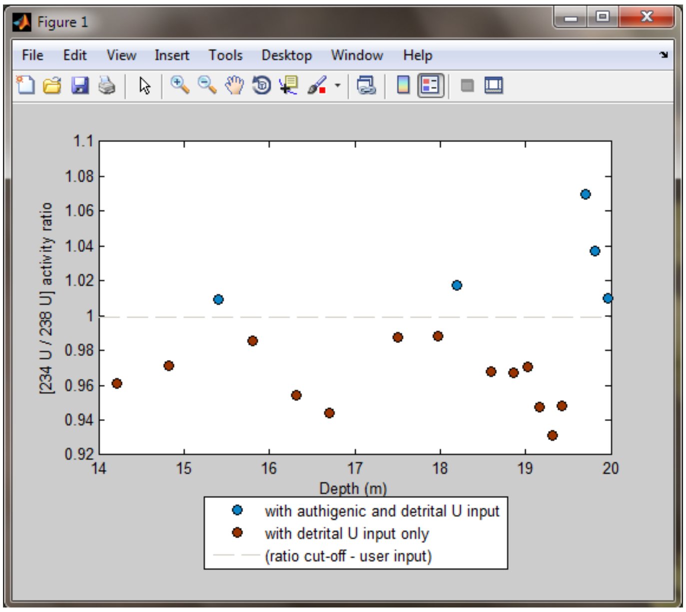

Figure B.2: Result of selection in Fig. B.1.

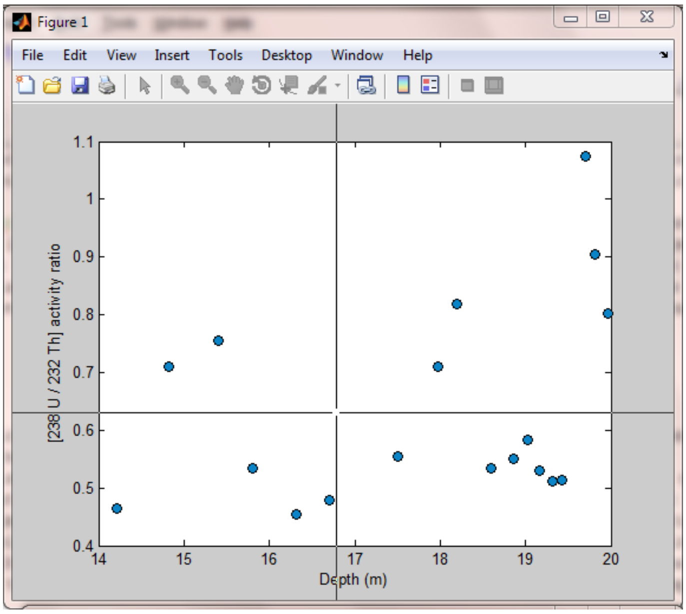

Figure B.3: Place the mouse cross-hair to divide the samples into those with and those without authigenic input.

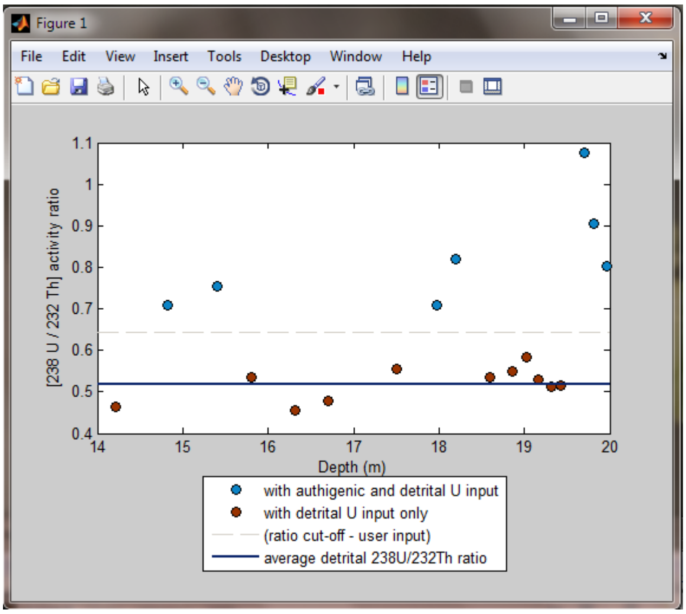

Figure B.4: Result of selection in Fig. B.3.

Monte Carlo Method

XSage will then ask if you want to calculate the duration using the Monte Carlo method. If you answer yes, `Y`, the script will calculate the ^{230}Th (and ^{231}Pa) component activities and an age model (as well as the age and duration of any defined event) n number of times by random sampling from probability distributions for each variable. Where n is specified by the user at a subsequent prompt.

Varying Detrital and Seawater Ratios

If the Monte Carlo method is used, then the script will prompt first to ask whether the 'constant' ratios (the initial seawater (^{234}U)/(^{238}U) and the specified detrital (^{238}U)/(^{232}Th) and (^{238}U)/(^{230}Th) ratios) should be varied between samples.

- The default (N) calculates each Monte-Carlo iteration such that the ratios are constant across all samples for that iteration. This first case essentially assumes that the uncertainties specified in the ratios are an uncertainty on a theoretically unchanging value (systematic error).

- Alternatively, if the ratios are allowed to vary (randomly) between each sample and are not constant within each iteration then the script is effectively assuming that the uncertainties specified for the input ratios actually represent temporal variations in these values (random error).

Tie-Points

The script will then ask whether the tie-points should be kept fixed or varied, and then for the number of evaluations, n.

- If the tie-points are kept fixed, the midpoints of the ranges supplied for the age and depths of the tie-points will be used for all evaluations whilst randomized datasets are generated from normal probability distributions for the isotope activities and the detrital and seawater ratios. The results therefore reflect the uncertainty associated with varying only the isotope data.
- If the tie-points are not kept fixed, the script will randomly sample ages and depths (independently) between the ranges supplied for the ages and depths of the tie-points *as well as* varying the isotope activities . For each evaluation, XSage determines which of the sample measurements are relevant as the movement of the tie-points can result in more or fewer data points being used.

Iterations

Typically around 10,000 evaluations achieves a stable answer with the example data provided. If the calculation takes too long, it may be cancelled using the key combination `CTRL+C`.

Non-Monte Carlo Evaluation

If the Monte Carlo Method is not used, the script will calculate the U-Th(-Pa) activities and age model using the midpoints of the ranges for the age and depths of the tie-points and the means of the U-Th(-Pa) activities and U-Th(-Pa) ratios supplied. In this case, the uncertainties are not calculated.

B.5 Results

Once the calculations are complete the script will display a set of results appropriate to the calculations conducted according to the user's parameters.

If specific intervals of interest have been defined (see *Tie-Points File*) then the ages and durations for the intervals will be calculated.

- Durations and ages for the intervals will be calculated assuming a constant average sedimentation rate between the tie-points.
- Secondly, a duration and age will be calculated using the $^{230}Th_{xs}$-normalized sedimentation rate. If the Monte-Carlo method has been used, a histogram of the calculated interval durations showing the distribution and plausibility of different duration estimates (Fig. B.5) will be presented (note that if more than three intervals are specified this will not be displayed).

In all cases:

- A $^{230}Th_{xs}$-normalized age model (age/depth relationship) is presented in graphical form (Fig. B.6) with the associated uncertainties on the ages of the age-model depths.
- A further figure of the $^{230}Th_{xs}$-normalized sedimentation rate is presented. The dashed lines indicate the associated uncertainties (Fig. B.7).
- To save the results file enter a `Y` when asked whether you'd like to save the results and press `ENTER`. The file, containing all the data used and the resulting sedimentation rates, ages and their associated uncertainties, can then be saved using the save-dialog box. Note that the contents of this file will vary depending upon whether any U/Th/Pa calculations were carried out and whether the Monte-Carlo method was used.

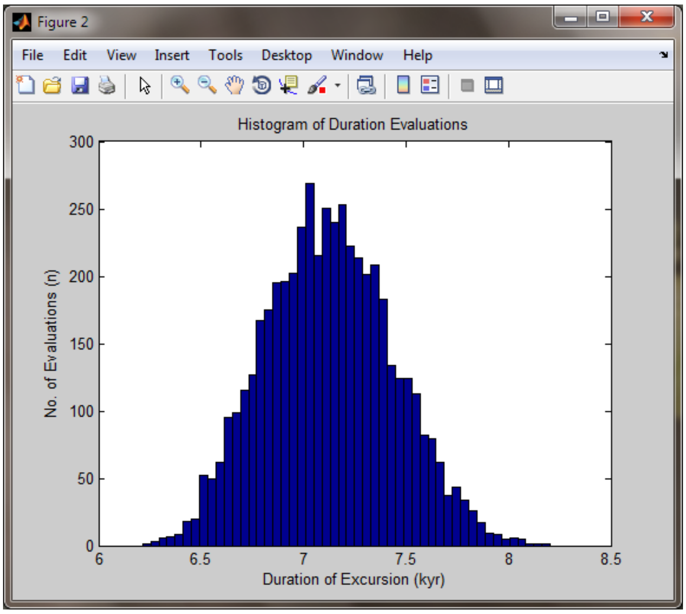

Figure B.5: Monte-Carlo model histogram of the calculated event durations.

- XSage will ask if you wish to save the age model (depths, ages and, if the Monte-Carlo method was used, the uncertainty on the ages). The intervals between the depths represent regions assumed to have a constant sedimentation rate by the calculations and thus the depths and their respective ages can be used to interpolate (or extrapolate) the ages for other depths.

- Finally, XSage will ask if you wish to save the interval calculations (depths, ages and durations and, if the Monte-Carlo method was used, the uncertainty on these values).

Note that the normalized sedimentation rate in the *XSResults* file is the average instantaneous sedimentation rate at the depth of that sample. The normalized sedimentation rate in the *XSAgeModel* file is the average sedimentation rate across the interval indicated. The graph of sedimentation rate generated by XSage therefore uses the same sedimentation rate data as the *XSAgeModel* file.

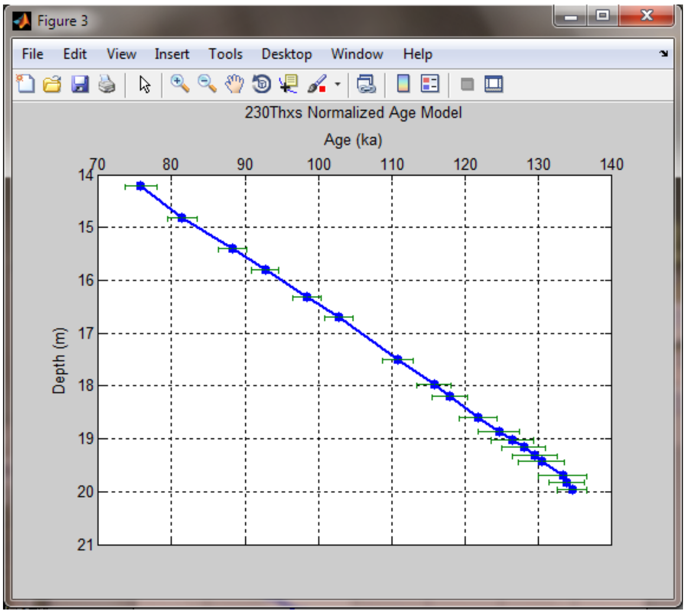

Figure B.6: ^{230}Th$_{xs}$-normalized age model (age/depth relationship).

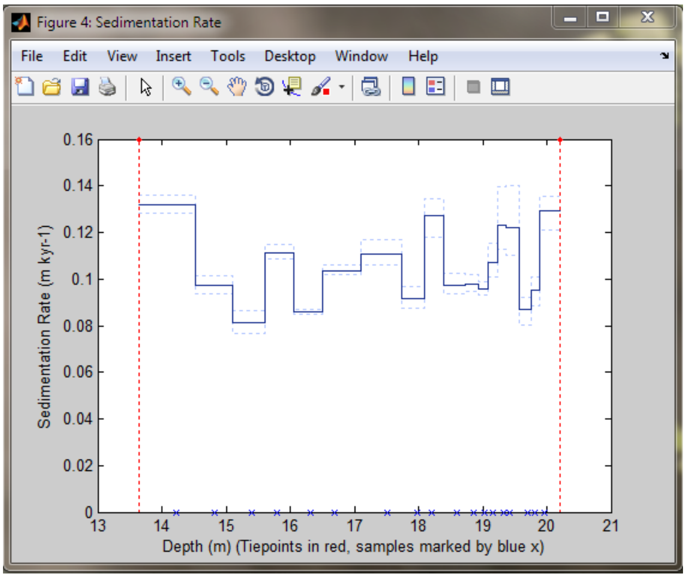

Figure B.7: ^{230}Th$_{xs}$-normalized Sedimentation Rate.

B.6 Known Issues

- If the standard deviations are very large when using pre-calculated $^{230}Th_{xs}$ values, the probability distribution can generate negative values. To avoid creating impossible age models, the script assumes that the negative concentrations are equal to zero. If this has happened the user is warned.
- If specified input files are open in other software, or unavailable for access for any other reason, the script will terminate.

Please feel free to use this software and contact mark.bourne@earth.ox.ac.uk if you have any comments or discover bugs.